Cavity QED with Exciton Polaritons Using Two-Dimensional Coherent Spectroscopy

by

Travis Autry

B.S., University of Texas Austin, 2011

M.S., University of Colorado Boulder, 2014

A thesis submitted to the
Faculty of the Graduate School of the
University of Colorado in partial fulfillment
of the requirements for the degree of
Doctor of Philosophy
Department of Physics
2017

This thesis entitled:
Cavity QED with Exciton Polaritons Using Two-Dimensional Coherent Spectroscopy
written by Travis Autry
has been approved for the Department of Physics

Steven T. Cundiff

Markus B. Raschke

Date __________________

The final copy of this thesis has been examined by the signatories, and we find that both the content and the form meet acceptable presentation standards of scholarly work in the above mentioned discipline.

Autry, Travis (Ph.D., Physics)

Cavity QED with Exciton Polaritons Using Two-Dimensional Coherent Spectroscopy

Thesis directed by Prof. Steven T. Cundiff

In semiconductors the band edge absorption properties are dominated by Coulomb bound electron-hole pairs known as excitons. In an isotropic ideal infinite crystal such as a bulk semiconductors the exciton does not decay to a ground state but instead exchanges energy with the internal modes of the electromagnetic field found from the same boundary conditions as the crystal. It is only the leakage of photons out of the crystal due to real crystals having finite size that allows the exciton-light field to decay. This exchange of energy led to the concept of the exciton-polariton which represents the coupled system of exciton and light.

In this work we bring novel insight into the behavior of excitons and exciton-polaritons using a new tool for performing of multidimensional coherent spectroscopy (MDCS) experiments. We first present a new realization of MDCS using a collinear approach to record a nonlinear wave-mixing signal as a photocurrent. This approach has many advantages over conventional approaches to MDCS as it allows for microscopy and the study of single nano-objects while recording the phase and amplitude of these signals.

To achieve the strong coupling regime in semiconductors a semiconductor microcavity is often grown around a quantum well. When optically excited the quantum well exciton exchanges energy with the electromagnetic field resulting in new normal modes. These normal modes are called exciton-polaritons. The strong coupling regime is typically characterized by an avoided crossing measured as a function of exciton-cavity detuning. In polariton systems, the new normal modes result in quasiparticles with very small mass due to the photonic component of the system. As a result the detuning becomes a dispersion relation. We explore the higher lying dispersion curves of exciton-polaritons in a semiconductor microcavity by utilizing a pulse sequence that creates higher order coherences, i.e. coherences between states with an energy difference of $\Delta n > 1$. By recording this coherence as a function of detuning we are able to map out the strong coupling for these higher lying states bringing new insight into the nature of strong coupling and the bosonic nature of polaritons.

Dedication

This thesis is dedicated to my wonderful wife Jennifer. You are an unbelievable partner.

Acknowledgements

I would first like to thank Steve Cundiff for giving me the opportunity to work in his lab. I have learned an enormous amount while working for him. I would like to especially thank him for keeping my experiment at JILA while I finished my Ph.D. . This meant the world to me.

I would like to thank all of the individuals I have had the pleasure to work with during my graduate career. In particular Gaël Nardin is a great friend and mentor who taught me so much. I have also learned from and become friends with the 2D team of Galan Moody, Hebin Li, Takeshi Suzuku, Eric Martin, Bo Sun, Bachana Lomsadze, Mark Siemens, Chris Smallwood and Diogo Almeida. In addition it was pleasure to discuss quantum optics with Marc Aβmann and George Roumpos. Andy Almand-Hunter was always available for a quick question and helped in particular on the surface plasmon polariton project with Megan Ives. I have also enjoyed mentoring the undergraduates Matt Day, Megan Ives and Connor Awe. I have had the opportunity to collaborate with other groups such as Jacqueline Bloch's group at CRNS. They provided us with a one-of-a kind exction-polariton diode that I studied for most of my thesis. Additionally, the Raschke group provided us with AFM tip samples and allowed us to provide proof of principle FWM from an AFM tip. I would also like to acknowledge the amazing support staff at JILA especially Kim Hagen and Hans Green in the machine shop, Terry Brown and Carl Sauer in the electronics shop, J. R. Raith and Corey Keasling for computing help. Finally, I would like to thank my family and friends for their continued support and encouragement over the years.

Contents

Chapter

Appendix

Tables

Table

Figures

Figure

Chapter 1

Introduction to Excitons and Exciton-Polaritons

In semiconductors, the band edge absorption properties are dominated by Coulomb bound electron-hole pairs known as excitons. The band-edge optical absorption of semiconductors, as determined by excitons, was formally developed by Elliot [1]. Since the pioneering work of Hopfield these excitons have been considered a special class of the quantized polarization field in an insulating crystal. In an isotropic ideal infinite crystal, such as a bulk semiconductors, the exciton does not decay to a ground state but instead exchanges energy with the internal modes of the electromagnetic field found from the same boundary conditions as the crystal. It is only the leakage of photons out of the crystal due to real crystals having finite size that allows the exciton-light field to decay. This exchange of energy led to the concept of the exciton-polariton which represents the coupled system of exciton and light.

When studying semiconductor nanostructures we generally refer to excitons when the light-matter coupling is not strong and exciton-polaritons when the light-matter coupling is sufficiently strong to observe new normal modes. Both excitons and exciton-polaritons represent collective excitations of semiconductor crystals that have been extensively studied over the last few decades. Historically, these studies have progressed from bulk semiconductor experiments to experiments where the exciton is confined in a semiconductor nanostructure and the light field is confined in a microcavities.

The work conducted in this thesis was performed on semiconductor quantum wells or quantum wells strongly coupled to a microcavity. In these systems the lifetimes and dephasing of the excitons are on the order of $\sim$ 10ps. This requires ultrafast techniques to study their dynamical response. In this chapter we review the properties of direct-gap semiconductors near the band edge as well as nanostructures that confine the exciton, and microcavities that confine the light field.

1.1 Classifying Materials and Semiconductor Band Structure

Semiconductors are a class of materials that are "between" a conductor and an insulator. They are characterized by electronic structure known as the valence and conduction bands that describe electronic single-particle states. The valence bands are of lower energy while the conduction bands are higher energy. Because only partially filled bands can conduct [2], the electron occupation of the bands is critical to understanding the material properties. Metals conduct well because their conduction band is partially occupied. Semiconductors and insulators do not have a partially filled conduction band, typically requiring the absorption of light or the application of an applied field to make them conduct. The distinction between semiconductors and insulators rests in the energy difference between the valence and conduction bands (bandgap), as a smaller bandgap makes a material correspondingly easier to conduct. Quantitatively, the occupation probability of a state is described by the Fermi-Dirac distribution

$$f(\epsilon) = \frac{1}{1 + e^{\frac{\epsilon - \mu}{kT}}} \tag{1.1}$$

where ϵ is the energy level of an electron state, μ is the Fermi level, k is the Boltzmann constant and T is the temperature. For a fixed temperature and energy level it is the Fermi level that determines the occupation of the conduction band. In metals the Fermi level lies within the conduction band leading to occupation of these higher lying states by electrons. For insulators the Fermi level typically lies in between the conduction band and valence band and this bandgap is typically quite large leading to poor electrical conductivity. Semiconductors are like insulators in that the Fermi level lies between the conduction and valence bands. However, unlike insulators the bandgap is much smaller making it relatively easier to partially occupy the conduction band.

The origin of the band structure begins with the the Schrodinger equation for an electron in a periodic potential.

$$[\frac{-\hbar^2}{2m^*}\boldsymbol{\nabla}^2 + U(\vec{r})]\Psi(\vec{r}) = E\Psi(\vec{r}) \tag{1.2}$$

where E is the energy level, m^* is the effective mass, $U(\vec{r})$ is the potential and $\Psi(\vec{r})$ is the electron wavefunction. In a crystal the repeating pattern of the unit cell, the smallest arrangement of atoms, results in a periodic potential $U(\vec{r})$. For a lattice vector $\vec{R}$, $U(\vec{r})$ is periodic with $U(\vec{r}) = U(\vec{r}+\vec{R})$. Due to the periodicity of the potential, the wavefunctions are $\Psi(\vec{r}) = e^{i\vec{k}\cdot\vec{r}}u_{nk}(\vec{r})$ where $u_{nk}(\vec{r}) = u_{nk}(\vec{r}+\vec{R})$. This directly provides Bloch's theorem that $\Psi(\vec{r}+\vec{R}) = \Psi(\vec{r})e^{i\vec{k}\cdot\vec{r}}$ [2]. These solutions have important physical consequences for electrons in solids. The description of the electron as a plane wave implies that it is delocalized over the entire crystal and that it propagates without scattering. This is only true, however, under the condition that the electron has a state to move into. In the context of the Fermi-Dirac distribution (Eq. 1.1), if a band is completely occupied by electrons then there is no free state for it to move into and it will have infinite resistivity and be termed an insulator or semiconductor. Conversely, metals conduct because the electrons in a crystal propagate without scattering and because there are unoccupied states available for it to move to [3]. In general, the Bloch wavefunction defines the electronic envelope and additional calculations are needed to find the interactions of the lattice with the electrons. These interaction give the electrons dispersion and determine the effective mass of electron-quasiparticles in a band.

For semiconductors a tight binding model is often used to find the band structure dispersion. This model assumes that the crystal Hamiltonian is $H = H_{at} + \Delta U(r)$ where H_{at}

is the atomic Hamiltonian at the lattice point while $\Delta U(r)$ is a correction term allowing the atomic potential to satisfy the periodic potential of a crystal. Using separation of variables gives $\Psi(\vec{r}) = \sum_R e^{i\vec{k}\cdot\vec{r}}\phi(\vec{r}-\vec{R})$ with the term $\phi(\vec{r}) = \sum_n b_n\psi_n(r)$ where $\psi_n(r)$ are the localized atomic wavefunctions. For the semiconductors discussed in this thesis (GaAs,InGaAs) the outer shell electrons are predominately s and p type. Given a particular tight binding Hamiltonian, this method can be used to calculate the dispersion of the semiconductor band structure. A prototypical band structure for a direct gap semiconductor (GaAs) is presented in Fig. 1.4.

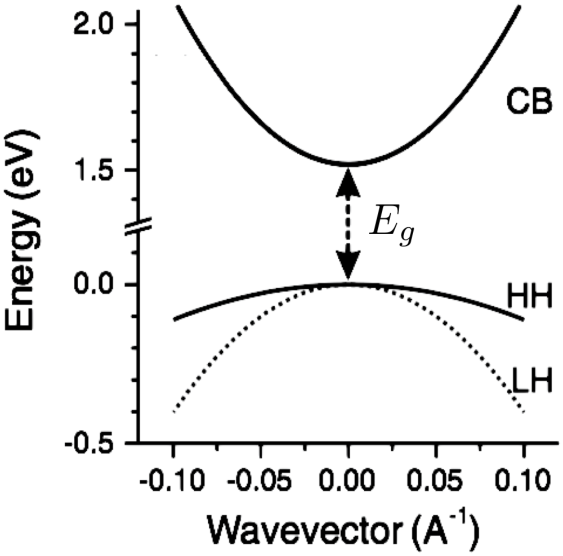

Figure 1.1: The bulk band structure of GaAs. At the Γ point in GaAs a direct bandgap occurs in which the conduction band (CB) and the degenerate valence bands (HH) and (LH) have vertices. The bandgap energy of GaAs of $1.5eV$ E_g is depicted with the double arrow. Figure adapted from Ref. [4].

In GaAs at the Γ point ($k = 0$) three bands occur (Fig. 1.1), one conduction band (CB) and the two degenerate hole bands (HH and LH) [3]. A hole occurs when an electron with wavevector k_e has been promoted from the valence band to the conduction band leaving the valence band with net wavevector $k_h = -k_e$. The hole has opposite charge, has the opposite sign of energy and has the negative mass with respect to the electron mass in the valence band [5]. Fig. 1.1 refers to a valence and conduction band. In a picture where the hole exists the hole band is the valence band. This is often confusing. To convert to a hole-picture it is implicitly understood the x axis is increasing from left-right for the electron and decreasing from left-right for the hole bands. Additionally, for the hole, the sign of the y axis has the opposite sign and holes increase in energy the lower they occur in the plot. In the tight binding picture, at the Γ point, the CB band is predominately an s type wave function with orbital angular momentum $(L) = 0$ and spin angular momentum $(S) = \frac{\hbar}{2}$. The total angular momentum of the CB is $J = L + S = \frac{\hbar}{2}$ with a total angular momentum wavefunction $\chi_{CB} = |\frac{1}{2}, \pm\frac{1}{2}\rangle$. The degenerate hole bands are p type wavefunctions with $L = 1$, giving these bands total angular momentum $J = \frac{3\hbar}{2}$. The heavy-hole band (HH) band is characterized by $m_j = \frac{3}{2}$ with the wavefunction $\chi_{HH} = |\frac{3}{2}, \pm\frac{3}{2}\rangle$. The light-hole band (LH) band is characterized by $m_j = \frac{1}{2}$ with the wavefunction $\chi_{LH} = |\frac{3}{2}, \pm\frac{1}{2}\rangle$. Near $k = 0$ an effective mass

$$m^* = \hbar^2 (\frac{\partial^2 E}{\partial k^2})^{-1} \tag{1.3}$$

can be defined for the different bands. Due to the difference in curvature between the LH and HH band, these bands have different effective masses hence their naming convention. A semiconductor is termed *direct* or *indirect* depending on the whether the critical points of the electronic bands occur at the same k vector (Fig. 1.2a-b). Whether or not a semiconductor is direct or indirect significantly modifies its optical properties. In direct gap semiconductors an electron can be promoted from the valence band to the conduction band with the absorption of a photon equal to the bandgap energy (Fig. 1.2a). Indirect semiconductors require the emission of a phonon in order to absorb light at the bandgap energy. The phonon provides a large wavevector with a negligible energy contribution (Fig. 1.2b). When considering the inverse of the absorption process, the emission of light, this effect is even more pronounced. In indirect semiconductors, the phonon requirement makes the recombination rate much slower and subsequently radiative recombination is not a dominant relaxation process.

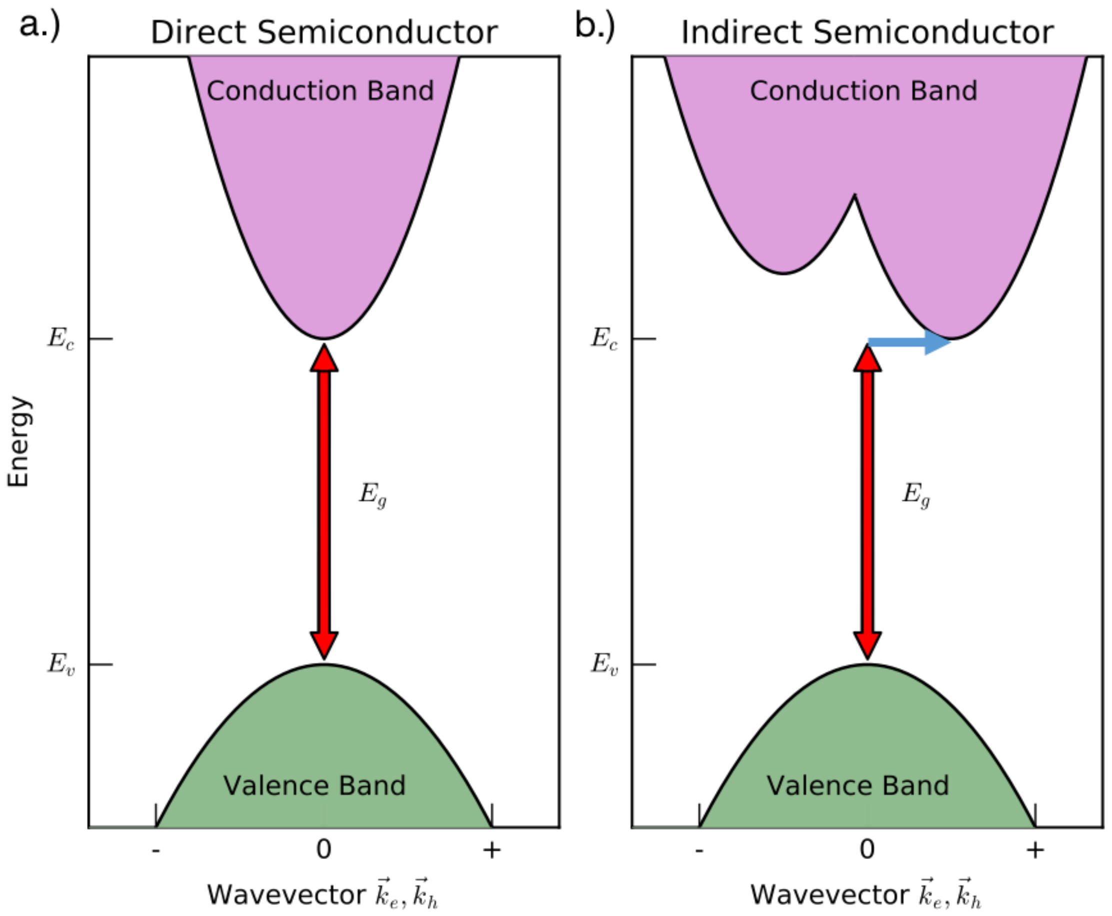

Figure 1.2: Difference between a direct and indirect semiconductor. a.) In a direct gap semiconductor the critical points of both the conduction and valence bands occur at the same wavevector k_e. Optical absorption (red line) occurs at the bandgap energy E_g. b.) In indirect gap semiconductors the critical points of the conduction and valence bands do not occur at the same wavevector k_e. Optical absorption in indirect semiconductors typically involves a phonon emission (blue arrow) and the absorption of a photon at the bandgap energy E_g in order to satisfy wavevector conservation.

1.2 Bulk Excitons

At the band edge of a semiconductor, the electronic band structure describes the electrons in the conduction band and the holes in the valence band. However, the semiconductor optical properties are not determined by this single particle picture of the semiconductor.

The absorption of a photon promotes an electron with wavevector k_e leaving behind a hole with wavevector $k_h = -k_e$. This is a significant simplification of the absorption process as an electron in the conduction band will interact with the valence band hole through the Coulomb interaction. In semiconductors the Coulomb interaction dominates the band edge optical response. Let us consider a two-band direct gap semiconductor without spin and follow the approach of [6] to find the Coulomb corrected picture of a semiconductor. The Hamiltonian for an interacting electron-hole is:

$$H = \int d^3x \Psi^\dagger(x) H_0(x) \Psi(x) + \int d^3x d^3y \Psi^\dagger(x) \Psi^\dagger(y) V(x-y) \Psi^\dagger(y) \Psi(x) \tag{1.4}$$

where H_0 is the single electron Hamiltonian and $V(x) = \frac{e^2}{|x|}$ is the Coulomb interaction. The wavefunctions for this Hamiltonian can be written

$$\Psi(x) = \sum_{j=c,v} a_{k,j} \mu_{kj}(x) \frac{e^{ik \cdot x}}{\sqrt{N}} \tag{1.5}$$

where $a_{k,j}$ and $a^\dagger_{k,j}$ are Fermi annihilation and creation operators for the valence and conduction band and $\mu_{kj}(x)\frac{e^{ik\cdot x}}{\sqrt{N}}$ is the eigenfunction for an electron with wavevector k in the energy band j. The wavefunction $\mu_{k,j}(x)$ is the Bloch wavefunction and N is the number of unit cells. The expression $\mu_{kj}(x)\frac{e^{ik\cdot x}}{\sqrt{N}}$ in Eq. 1.5 is itself a wavefunction $\psi_{k,j} = \mu_{kj}(x)\frac{e^{ik\cdot x}}{\sqrt{N}}$ that satisfies $H_0\psi_{k,j}(x) = E^0_{kj}\psi_{k,j}$ the Hamiltonian for single electrons. At this point some limits should be taken. In Eq. 1.4 if $V(x-y) = 0$ the crystal ground state is given by the electron-hole states discussed above that satisfy the Bloch theorem. However, if $V \neq 0$ then these electron states are not the eigenstates of the crystal. This equation can only be solved analytically in certain approximations, but the Coulomb interaction will repel charges of like charge and attract charges of opposite charge. Since the absorption of a photon involves creating an electron and a hole and does not involve creating an electron-electron, or hole-hole these same-charge effects are typically considered of secondary importance. For the rest of this thesis the screening of the Coulomb potential, and the repulsive interactions will be termed "residual Coulomb" or many-body effects. Consider the case of an electron in the conduction band and a hole in the valence band separated by a distance larger than a unit cell. In this case the Coulomb and plane wave factors are slowly varying as in the original approximations of Wannier [7]. In this limit and by invoking the effective-mass approximation near the band edge, the Hamiltonian (Eq. 1.4) can be reduced to:

$$H = \frac{p_e^2}{2m_e} + \frac{p_h^2}{2m_h} + \frac{1}{4\pi\epsilon\epsilon_0|x_e - x_h|} + E_g. \tag{1.6}$$

Here $p_e(p_h)$ is the momentum of the electron(hole), $m_e(m_h)$ is the effective mass of the electron(hole), ϵ is the dielectric constant of the material, E_g is the band gap energy, and $\vec{x_e}(\vec{x_h})$ are the positions of the electron(hole). The Hamiltonian, (Eq. 1.6) is reminiscent of a Hydrogenic system except that the proton(hole) is not treated as stationary. We introduce the relative electron-hole coordinate $\vec{r} = \vec{x_e} - \vec{x_h}$ with relative wavevector $\vec{l} = \frac{m_h}{M}k_e + \frac{m_e}{M}\vec{k_h}$ where $k_e(k_h)$ represent the electron(hole) wavevector. We further introduce the center of mass coordinate $\vec{R} = \frac{m_h}{M}\vec{x_e} + \frac{m_e}{M}\vec{x_h}$ (CM wavevector $\vec{K}$) and $M = m_e + m_h$ so that the center of mass motion and relative motion can be separated. From this an excitonic-wavefunction can be written as

$$\phi(x_e, x_h) = \psi_n(r)e^{iK\cdot R}. \tag{1.7}$$

In the relative basis and introducing the reduced mass $m_r = \frac{m_e m_h}{M}$ the Schrodinger equation becomes:

$$[\frac{p_r^2}{2m_r} - \frac{e^2}{4\pi\epsilon\epsilon_0 r}]\psi_n(r) = E_{ex}\psi_n(r). \tag{1.8}$$

In this expression we have grouped E_g into E_{ex} as it is just a constant. Solving this equation results in a Hydrogenic series with energy levels denoted by the Rydberg index n [8]. The total energy of the electron-hole pair includes the plane wave dispersion $\frac{\hbar K^2}{2M}$ so that the total energy of the exciton is

$$E_{exciton}(n, K) = \frac{\hbar K^2}{2M} + E_g - \frac{E_R}{n^2}. \tag{1.9}$$

Here the excitonic Rydberg Energy is

$$E_R = \frac{e^2}{8\pi\epsilon_0\epsilon a_0} \tag{1.10}$$

where a_0 is the Bohr radius of the exciton given by

$$a_0 = \frac{4\pi\epsilon_r\epsilon_0\hbar^2}{e^2 M}. \tag{1.11}$$

In GaAs based systems discussed in this text the bulk exciton binding energy has been found to be 4.2meV with a bandgap of 1.52eV [9] and a Bohr radius $\sim$ 10nm. The exciton as a bound electron-hole pair represents the Coulomb corrected eigenstates of the crystal. The crystal is considered to be in an excitation vacuum in the absence of an exciton and the first Rydberg state of the exciton is the first excited state of the crystal (Fig. 1.3a). The exciton energy structure consists of a series of Rydberg states below the bandgap of the semiconductor. Optical excitation can either excite unbound Coulomb interacting electron-hole pairs (excitonic continuum) or bound exciton states. As a result of the exciton mass only a select range of wavevectors are accessible with optical excitation, those near $K = 0$. The expected absorption spectrum of excitons in a direct gap semiconductor is shown in (Fig. 1.3b). In this spectrum the Rydberg exciton-states are labeled by n below the electron-hole continuum.

From these simplifying equations and dispersion relation an excitonic creation operator $C^\dagger$ can be written in terms of the electron Pauli operators $a(a^\dagger)$ and the hole Pauli operators $b(b^\dagger)$

$$C^\dagger_{K,n} = \sum_{k_e,k_h} \delta_{K,k_e+k_h}\psi_n(l)a^\dagger_{k_e}b^\dagger_{k_h}. \tag{1.12}$$

These exciton creation and annihilation operators commute with the relationship

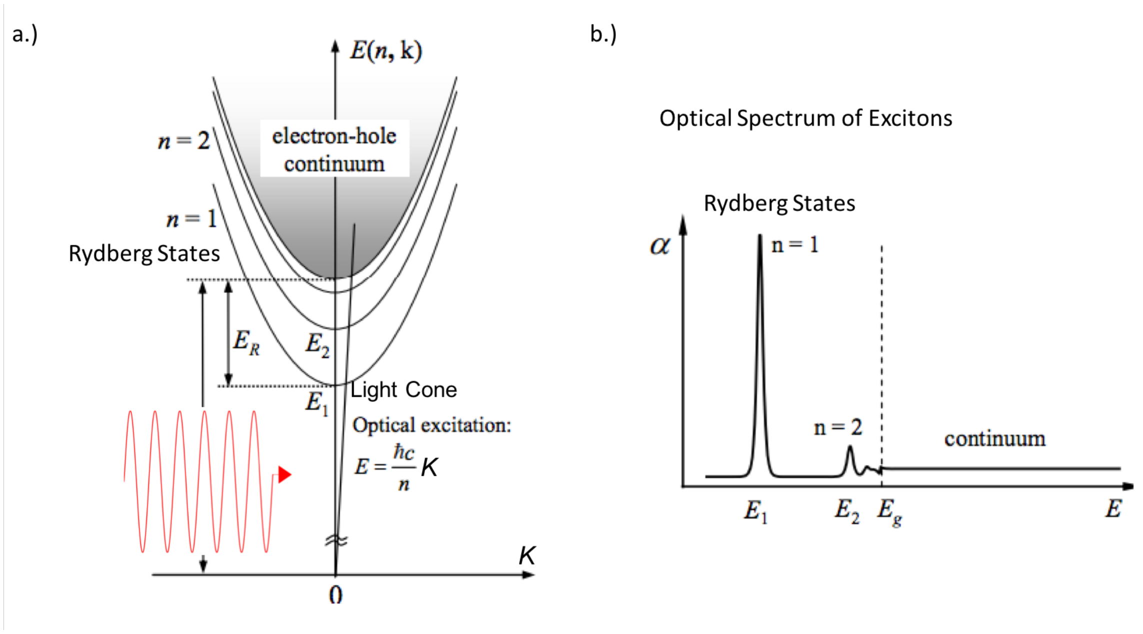

Figure 1.3: a.) Exciton energy structure and dispersion relation. The exciton-spectrum provides bound electron-hole states below the bandgap of the semiconductor (electron-hole continuum) in this picture. b.) The expected optical spectrum of excitons in a direct gap semiconductor. The Rydberg states are labeled be n while the electron-hole continuum is at higher energy. Figure adapted from Ref. [10].

$$[C_{K',n'}, C^\dagger_{K,n}] = \delta_{K,K'}\delta_{n,n'} + \mathcal{O}(na_0^3). \tag{1.13}$$

If we remember that bosons with annihilation(creation) operators $d(d^\dagger)$ have the commutation relation $[d_i, d_j^\dagger] = \delta_{i,j}$ then it is apparent from (Eq. 1.13) that excitons can be considered bosons provided that the volume of excitations is small compared to a_0^3. As this density increases exciton-exciton interactions become increasingly important. From (Eq. 1.12) it is apparent that the exciton represents the number-state basis of the semiconductor polarization field [6, 11, 12]. As the eigenbasis of the polarization field, excitons determine the absorption properties of semiconductors which at low densities are similar to that of a quantum harmonic oscillator [13].

1.3 Absorption of Bulk Semiconductors: Exciton-Polaritons

Early on a significant issue in calculating the optical properties of semiconductors was how to calculate the radiative lifetime of the exciton. The principle issue that Hopfield [11] realized was that the electromagnetic field modes must satisfy the same boundary conditions as the crystal. For an exciton with wavevector K to radiatively decay into a crystal-mode photon with wavevector K and for that energy to be lost; the energy must escape the crystal. Thus for a finite sized crystal, in an infinitely large volume, the radiative lifetime must be determined by the electromagnetic field leakage out of the crystal. As the crystal becomes large (as solid state physics often assumes) the radiative decay out of the crystal must go to zero. This means that both the exciton and the photonic lifetime in the crystal must become infinite in the limit of an infinitely sized crystal. Because the exciton is radiating and absorbing light from the optical-crystal mode the two modes are coherently exchanging energy. When the rate of energy exchange exceeds the loss rate the exciton and field become strongly coupled leading to the exciton-polariton. As a result for an infinitely large crystal Hopfield realized the energy sink that caused absorption and energy loss must come from many-body interactions, phonon interactions etc. The the full light matter interaction for a semiconductor in the rotating wave approximation is

$$H = \sum_k \hbar\omega_X b_k^\dagger b_k^\dagger + \sum_k \hbar\omega_\gamma a_k^\dagger a_k^\dagger + \sum_k g_0(a_k^\dagger b_k + b_k^\dagger a_k) + H_{int}. \tag{1.14}$$

Here a slight change of notation occurs. The exciton center of mass wavevector is k with excitonic operators b, while the electromagnetic field operators are a, the excitonic energy is $\hbar\omega_X$ (Eq. 1.9) and the electromagnetic field energy is $\hbar\omega_\gamma$. The many-body interactions and loss mechanism are determined by H_{int}. The electromagnetic field also obeys a dispersion in k space $E_\gamma = \frac{\hbar c|k|}{n}$ where n is the index of refraction. The Hamiltonian (Eq. 1.14) is that of two coupled harmonic oscillators. The Hamiltonian can be diagonalized to find the new normal modes with operators

$$P_k = X_k b_k^\dagger + C_k a_k^\dagger$$
$$Q_k = X_k b_k^\dagger - C_k a_k^\dagger.$$

With this description the diagonalized Hamiltonian becomes

$$H = \sum_k E_{LP}(k) P_k^\dagger P_k^\dagger + \sum_k E_{UP}(k) Q_k^\dagger Q_k^\dagger. \tag{1.15}$$

Here $E_{LP}(E_{UP})$ represent new normal modes found from the coherent exchange of the exciton and electromagnetic field. As a result of the coupling these states split by the coherent exchange rate $\Omega = 2g_0$ and form a low energy mode E_{LP} and a higher energy mode E_{UP} that are the lower and upper polariton. The lower polariton operators are P_k while the upper polariton operators are Q_k. The coefficients X_k and C_k are known as the Hopfield coefficients [11, 14] with

$$|X_k|^2 + |C_k|^2 = 1. \tag{1.16}$$

These coefficients relate the exciton and photon components of the wavefunction. As the new modes of the system, the exciton-polaritons are the dressed states of the exciton. When the coupling constant g_0 is larger than the electromagnetic field leakage rate, these new normal modes can be observed through an avoided crossing in wavevector k. When this coupling constant is smaller than the leakage rate, we continue to describe the system by excitons and their interaction with a classical radiation field.

1.4 Semiconductor Quantum Wells

A modern approach to the study of excitons is to confine them into $1, 2$ or 3d confined nanostructures. Doing this modifies the electron-hole density of states. For excitons the effect of confinement is to increase the exciton binding energy making them accessible at higher temperatures.

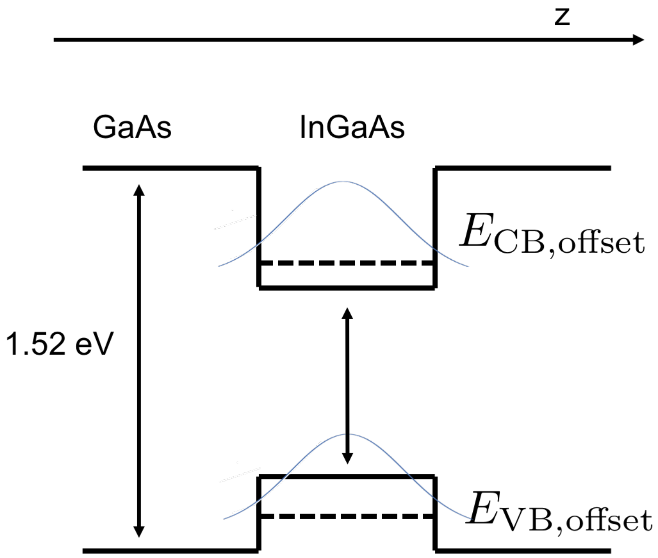

Figure 1.4: The quantum confinement of electrons and holes in semiconductor quantum wells. Shown are the electron and heavy hole n=1 states for $\mathrm{In_xGa_{1\text{-}x}As}$/GaAs quantum wells. E_{VB} and E_{CB} correspond to the valence and conduction band offsets. The bandgap of $\mathrm{In_xGa_{1\text{-}x}As}$ is (x) dependent.

Of interest to this thesis is the confinement of excitons in 1d semiconductor nanostructures called quantum wells. Quantum wells are grown by either molecular beam epitaxy or metal-organic chemical vapor deposition. A prototypical quantum well might consist of a small layer of $\mathrm{In_xGa_{1\text{-}x}As}$ grown in between two larger layers of GaAs. Due to adding fractional amounts (x) of indium the bandgap of the $\mathrm{In_xGa_{1\text{-}x}As}$ will be smaller than that of the GaAs. This gives a confinement potential that is equal for the the conduction and valence bands provided that the chemical potential of GaAs is the same as $\mathrm{In_xGa_{1\text{-}x}As}$. In actuality these materials have slightly different chemical potentials giving the confinement energies an offset $E_{\mathrm{CB,offset}}$ for the conduction band and $E_{\mathrm{VB,offset}}$ for the valence band as shown in Fig. 1.4. In InGaAs quantum wells the light-hole is typically not confined[15, 16]. This leaves the confinement of just the electron and heavy-hole justifying the use of a two band picture.

The electrons and holes are confined in the growth direction (z direction) but free to move in-plane. With the introduction of the Coulomb interaction an in-plane exciton is formed that is confined in the growth direction. This makes the hydrogenic solution to the Coulomb potential cylindrical [17] and increases the binding energy of the exciton due to the increased proximity of the electron to the hole in the z direction. In order to achieve any significant increase in the exciton binding energy the well width needs to be on the order of the Bohr radius of the exciton $\sim$ 10nm in GaAs. The binding energy of a heavy-hole $\mathrm{Al_xGaAs_{1\text{-}x}}$/GaAs exciton as a function of well width is shown in Fig. 1.5.

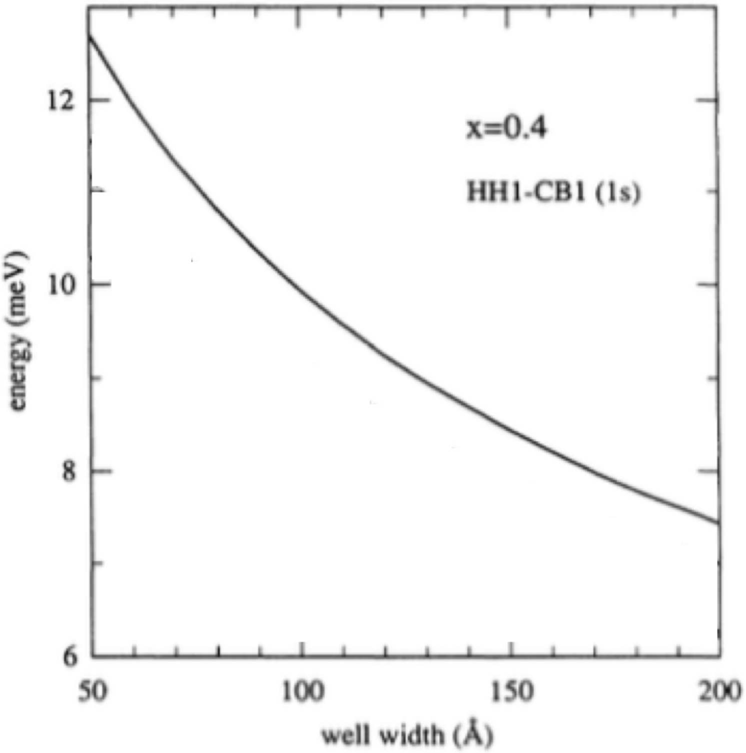

Figure 1.5: The calculated binding energy for quantum confined heavy-hole excitons in $\mathrm{Al_xGaAs_{1\text{-}x}}$/GaAs quantum wells as a function of well width. Figure adapted from [17].

In an excitonic picture the exciton binding energy again shifts the resonance below the electron-hole states. The main difference with bulk excitons is that in a quantum well a series of electron and hole sub-bands exist. As a result a series of confined excitonic states exist below these confined energy levels.

The bulk polaritonic effects no longer apply for quantum-well excitons as the electromagnetic field modes are defined by the quantum well. These electromagnetic field modes that coherently oscillate with the exciton have significant leakage out of the quantum well and the quantum well exciton will be in the weak-coupling regime. In an excitonic basis the band-edge Hamiltonian neglecting many-body interactions is

$$H = \sum_{k_{||}} \hbar\omega_X b^\dagger_{k_{||}} b^\dagger_{k_{||}} + \sum_{k_{||}} g_0 (E^*_{k_{||}} b_{k_{||}} + b^\dagger_{k_{||}} E_{k_{||}}). \tag{1.17}$$

This equation is the same as Eq. 1.14 except that the exciton wavevector is defined to be in-plane $k_{||}$ and the electromagnetic field is written classically with electric field components E^*, E.

1.5 Semiconductor Microcavities

Modern semiconductor heterostructure growth techniques have enabled the growth of high quality Bragg mirrors. Bragg mirrors consist of material grown with a modulated index of refraction. Each modulation layer has an optical thickness of $\frac{\lambda}{4}$ as shown in Fig. 1.6. This modulation is designed to ensure constructive interference in the reflected direction. If two DBR mirrors are spaced $\frac{\lambda_c}{2}$ or an integer multiple of $\frac{\lambda_c}{2}$ a microcavity is formed, where λ_c is the optical wavelength.

The transmission coefficient describing such a microcavity [14] is

$$T = \frac{(1 - R_1)(1 - R_2)}{[1 - \sqrt{R_1 R_2}]^2 + 4\sqrt{R_1 R_2}\sin^2(\phi/2)}. \tag{1.18}$$

Here R_1 and R_2 are the reflectances of the two DBR's and ϕ is the cavity round trip phase shift of a photon. The "Q" factor is a characteristic parameter that determines how underdamped a resonator is. For a cavity this quantity is

$$Q = \frac{\lambda_c}{\Delta\lambda_c} = \frac{\pi (R_1 R_2)^{1/4}}{1 - (R_1 R_2)^{1/2}}. \tag{1.19}$$

The Q factor of semiconductor microcavities is $4000 - 6000$ and for a $\frac{\lambda_c}{2}$ cavity can be thought of as the number of round trips light makes in the cavity. A very high Q micro-cavity means

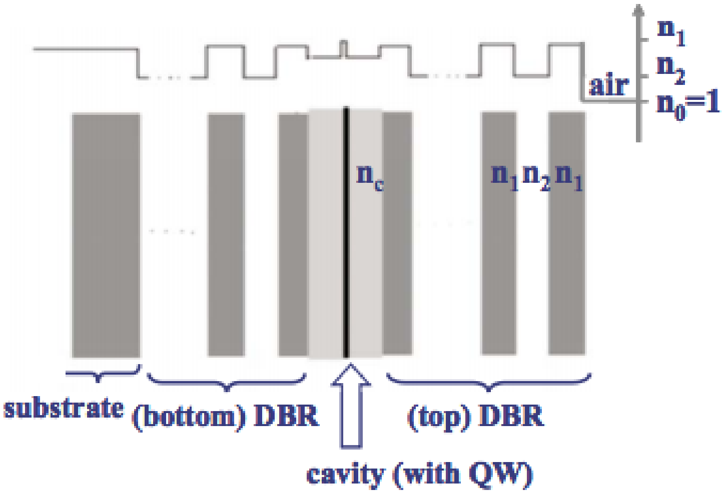

Figure 1.6: A prototypical microcavity structure with a quantum well at the cavity antinode. Index modulation ensures high reflectivity of the top and bottom DRB while a quantum well is grown at the center of the dialectric stack. This figure is from [14].

that it acts as a high quality stop-band for all incident light not at λ_c as shown in Fig. 1.7a. Other microcavity designs have achieved higher Q [18] but for this thesis Bragg mirror microcavities are discussed. The Bragg microcavity confines light in the growth direction of a semiconductor structure and achieves an antinode at the center of the cavity as shown in Fig. 1.7b.

The effective cavity length can be varied by varying the incident excitation wavevector k. As a result the cavity has an energy dispersion

$$E_{cavity} = \frac{\hbar c}{n_c}\sqrt{k_{||}^2 + k_{\perp}^2}. \tag{1.20}$$

Here $k_{||}$ and $k_{\perp}$ are the in plane and out of plane wavevectors. The out of plane wavevector is $k_{\perp} = n_c 2\pi/\lambda_c$ while in the small in-plane wavevector limit $k_{||} \sim \frac{2\pi}{\lambda}$. In the small wavevector limit the energy dispersion relation is parabolic [14] with a dispersion

$$E_{cavity} = E_{cavity}(k_{||} = 0) + \frac{\hbar^2 k_{||}^2}{2m_{cavity}}. \tag{1.21}$$

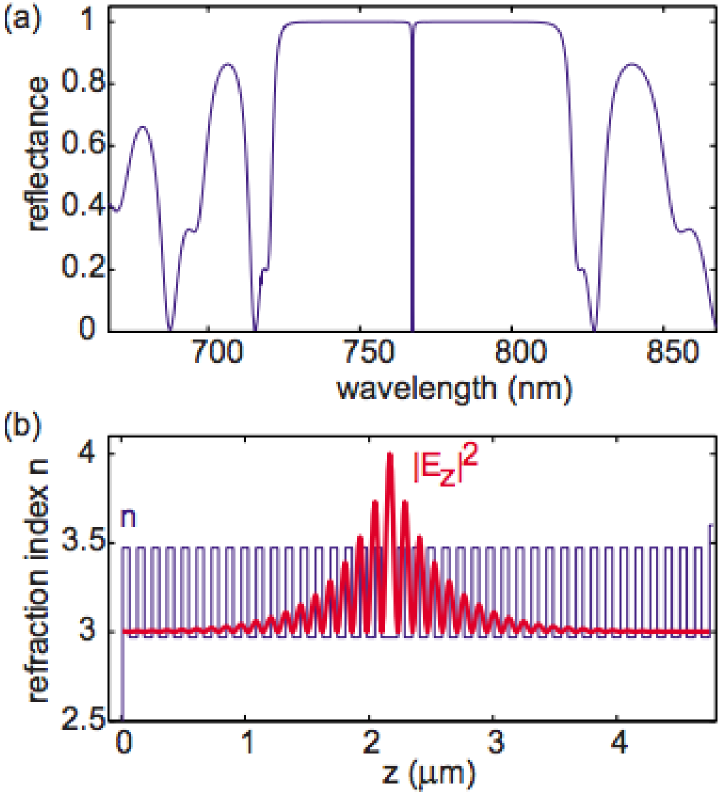

Figure 1.7: a.) The reflection spectrum of an empty Bragg microcavity with Q$\sim$ 4000. b.) The field distribution in the microcavity exhibits an antinode at the center of the cavity due to the modulation of the refractive index n. This figure is from [14].

The effective "cavity photon mass" is:

$$m_{cavity} = \frac{E_{cavity}(k_{||} = 0)}{c^2/n_c^2}. \tag{1.22}$$

This dispersion relation allows for the tuning of the optical cavity by varying the incident excitation wavevector. If an absorbing medium (such as a quantum well) is grown at the antinode of the cavity the electromagnetic field interaction can be tuned onto resonance with the absorbing medium. Due to the field distribution in the cavity the electromagnetic field interaction is enhanced at the cavity antinode. The presence of a semiconductor quantum well at the antinode of the cavity can lead to enhanced field-exciton interaction strength and create an enhanced strong coupling regime where the semiconductor quantum well exciton is strongly coupled to the cavity mode. The new eigenmodes that result from this coupling are analogous to the bulk exciton-polariton discussed previously. The primary difference is that instead of an infinite crystal providing the mechanism for strong coupling it is the microcavity that is preventing the electromagnetic field from leaking out of the semiconductor [19]. The semiconductor quantum well exciton-polariton will be discussed in detail in this thesis.

Chapter 2

Theoretical Background for Coherent and MDCS Spectroscopy

Spectroscopy is a tool to characterize the optical response of an absorbing medium. Basic spectroscopy techniques such as photoluminescence or linear absorption provide information about resonant energies of absorbing media and their absorption strengths. However, basic techniques are insufficient for understanding inhomogeneity, collective resonances, and coherent many-body interactions. Fortunately, *nonlinear* spectroscopy can provide insight into these phenomena [4].

Nonlinear spectroscopies are divided into two classes - coherent and incoherent spectroscopies. The simplest and thus most commonly used type are the incoherent techniques. Incoherent techniques such as pump-probe spectroscopy optically excite a sample with a strong pump and then probe the absorption(or reflection) with a probe beam. These techniques are sensitive to changes in the population/excitation density. Measuring the population dynamics can provide information about many effects, including multiphoton transitions [20, 21], electron thermalization in metals [22, 23], tunneling times in semiconductor heterostructures [24], optical gain [25, 26] and can also be used to classically dress absorbing semiconductor nanostructures [27, 28].

Alternatively, coherent nonlinear spectroscopy is a technique that is sensitive to coherences in the sample. In the coherent picture of light-matter interactions, the matter-resonance oscillates in a quantum mechanical superposition state with a phase defined by the incident light and resonant transition energy. The evolution of this phase encodes both the resonant energy shifts and dephasing, making coherent spectroscopy an ideal tool to measure these dynamic properties.

One of the main advantages of coherent nonlinear spectroscopy is its sensitivity to many-body interactions. This advantage is because many-body interactions result in resonant energy shifts and additional dephasing in excitonic systems. In particular, excitons can scatter off of each other by interacting through residual Coulomb interactions, exchange interactions, and Pauli blocking. Because exciton-exciton scattering depends on the density of excitons, the scattering energy that modifies the resonant exciton energy are termed excitation induced shifts (EIS) [29]. If the exciton-exciton scattering interrupts the coherent evolution of the excitons, additional dephasing will be observed in the coherent evolution. Therefore, the irreversible broadening resulting from this scattering is termed excitation induced dephasing (EID) [30, 31].

In this chapter I review the theoretical concepts of coherent spectroscopy building towards a theoretical understanding of multidimensional coherent spectroscopy and the information encoded in a MDCS spectrum. I begin with a historical discussion of MDCS. I then review absorption and the role of phase in coherent spectroscopy for non-interacting systems. Next, the optical Bloch equations and spectroscopy Feynman diagrams are discussed in the impulsive limit in order to discuss the perturbation theory and perturbative wave-mixing. Finally, the three types of third-order MDCS spectra, rephasing, nonrephasing, and two-quantum are simulated and discussed.

2.0.1 Historical Development of MDCS

Historically, multidimensional spectroscopy developed with NMR [32] where two pulses were used to probe nuclear spins. In these experiments the signal was recorded as a function of τ the time between pulses and t^* the time after the second pulse. The signals were then Fourier transformed with respect to these two time axes. It became apparent that more information about spin coupling was available from MDCS than in simple time-domain or one-dimensional experiments [33]. The success of MDCS in NMR led to the technique being extended to the microwave [34], to the infrared regime [35] and to study optical-raman spectra [36]. The infrared regime has become particularly important with the ability to study the ultrafast vibrational couplings and structure of molecules [37–39]. Relatively recently, MDCS was extended by the Jonas and coworkers [40] to the electronic regime to study the dye IR144.

In the time since its demonstration for electronic MDCS it has been used to study many-body interactions in quantum wells [41, 42], multiphoton absorption in organic dyes [43], coupling between isolated excitonic transitions [44], coherent coupling between quantum dots in a microcavity [45], collective resonances in atomic vapors [46] and quantum wells [47],corrugated plasmonic resonances in silver [48], quantum-dot based solar cells [49], THz spectroscopy of phonon-coupled quantum wells [50] and cyclotron motion in semiconductors using optically generated THz pulses [51]. While this list is not comprehensive it does demonstrate that MDCS has become in most cases the tool-of-choice to study coherent light-matter interactions in the optical regime. In the following sections we describe a perturbative approach to understand most MDCS experiments in the perturbative regime of light-matter interactions.

2.1 Coherent Spectroscopy of Model Systems: Theory

2.1.1 Optical Absorption

Absorbing media such as semiconductor excitons, atoms, and molecules often exhibit an optical resonance at the transition energy between two quantum mechanical states. When excited by an electric field, on resonance, an induced material polarization oscillates out of phase with the driving field. This dipole radiates and destructively interferes with the driving field to cause absorption. From a quantum mechanical point of view the radiating polarization comes from transitions between states. The time evolution of the quantum states is described by the Schrodinger equation. Environmental coupling and many-body interactions requires a formalism capable of describing dynamic decaying processes. A description which can describe classical and quantum states as well as this environmental coupling is given by the density matrix. The time evolution of the density matrix is

$$\frac{d\rho}{dt} = \frac{-i}{\hbar}[H, \rho] + L(\rho). \tag{2.1}$$

Here ρ is a density matrix describing the evolution of the quantum states and H is a Hamiltonian and $L(\rho)$ describes decay terms. The first part of this equation is often referred to as the Von-Neumann equation. When $L(\rho)$ is derived from first principles (Eq. 2.1) is often called a "master equation". When this equation is expanded into a matrix basis to include all states and energies and phenomenological dephasing/population decay, the equations are called the optical Bloch equations. The diagonal elements of the density matrix correspond to populations (for a single atom, the probability it is excited) while the off diagonal elements correspond to coherences (the system is evolving from one state to another with a defined phase). The conventional coherent nonlinear spectroscopy experiments discussed in this chapter measure coherent radiation arising from the sum of the off diagonal elements of the density matrix times the dipole transition matrix. In our experiment the signal arises from the trace of the density matrix multiplied by the excitation matrix. As an ideal model system consider a two level system with the density matrix

$$\begin{pmatrix} \rho_{gg} & \rho_{ge} \\ \rho_{eg} & \rho_{ee} \end{pmatrix} \tag{2.2}$$

where ρ_{gg} and ρ_{ee} denote the population in the ground and excited states, and ρ_{eg} and ρ_{ge} are complex conjugates and denote a coherent superposition between the two states. The properties of incoherent vs coherent states can be understood by considering the temporal evolution of these density matrix elements given some initial conditions $\rho_{ij}(t = 0)$ and a radiative lifetime T_1 and dephasing time T_2.

The temporal evolution of the excited state density matrix element is:

$$\rho_{ee}(t) = \rho_{ee}(0)e^{-\frac{t}{T_1}}. \tag{2.3}$$

This element decays without a phase and thus characteristic of population decay. In contrast the temporal evolution of a coherence has a phase and evolves as

$$\rho_{eg}(t) = \rho_{eg}(0)e^{-i\omega t-\frac{t}{T_2}}. \tag{2.4}$$

The difference between these two cases is that coherences develop phase as they evolve in time while populations do not. Importantly, the T_1 time constant refers to dissipation of the system while the T_2 time corresponds to decoherence. The limiting relationship between T_1 and T_2 is determined by the dissipation rate. Thus in a closed system the dephasing time is

$$T_2 = 2T_1. \tag{2.5}$$

This relationship can be understood intuitively and generalized by realizing that diagonal density matrix elements decay as $\rho_{n,n} = |C_n|^2 e^{-\frac{t}{T_n}}$ where C_n is the wavefunction amplitude and T_n is the population lifetime of state n. In contrast the off-diagonal density matrix elements correspond to $\rho_{n,m} = C_n^* C_m e^{-\frac{t}{2}(\frac{1}{T_n}+\frac{1}{T_m})}$ and thus the factor of two arises naturally. Generally (Eq. 2.5) does not hold as additional dephasing can occur. This *pure* dephasing does not involve additional population decay. This additional loss of phase memory can come from phonons, exciton-exciton scattering, etc and modifies the T_2 time as

$$\frac{1}{T_2} = \frac{1}{2T_1} + \frac{1}{T_2^*} \tag{2.6}$$

where T_2^* represents the additional dephasing. The inverse of the T_2 time is often called the homogeneous linewidth because it corresponds to the resonance linewidth in the absence of inhomogeneous broadening.

2.1.2 Role of Phase in Pulsed Experiments

In order to understand coherent spectroscopy in the context of MDCS it is helpful to review Ramsey spectroscopy where the role of phase becomes clear. The textbook-picture of Ramsey spectroscopy, is the interaction of a two-state system with two temporally separated driving pulses. Each pulse has a pulse duration σ as shown in Fig. 2.1a. When the transition probability of the system is plotted as a function of detuning Δ or pulse separation τ an oscillatory pattern is observed called Ramsey fringes [52–54] (Fig. 2.1b).

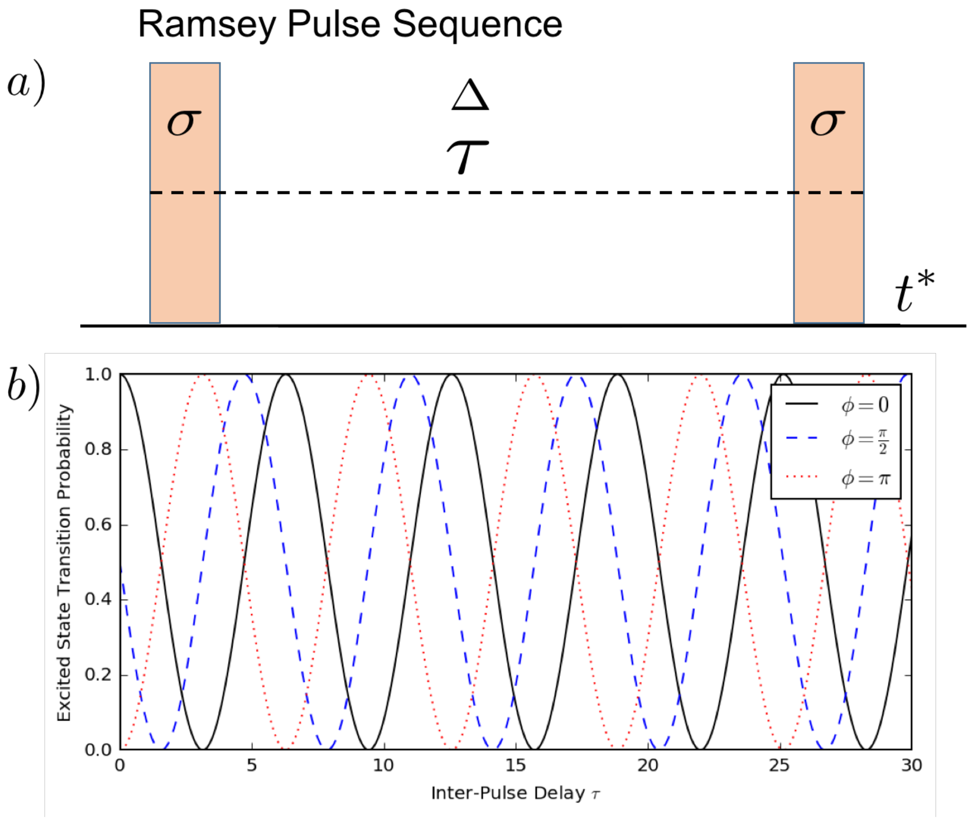

Figure 2.1: a) Ramsey pulse sequence of two pulses of width σ and detuning Δ with inter-pulse delay τ. b.) Plot of the two-level transition probability as a function of interpulse delay τ. When the relative phase ϕ between pulses is varied the Ramsey fringes are altered.

To understand Ramsey spectroscopy, is it sufficient to consider a system initially in an initial state $|g\rangle$ with an excited state $|e\rangle$ unpopulated. The first pulse will excite the system into a quantum superposition between the ground and excited state which will evolve during

τ and develop a phase as $\psi = 2\pi\delta\tau$ where $\delta = v_e - v_g$ is the transition frequency between the two states. The second pulse will interrupt this evolution and subsequent measurement with a state sensitive detector will project this superposition state into one of the two eigenstates of the system. Critically, this projection depends on ψ, the accumulated phase, and ϕ, the relative phase, between pulses as shown in Fig. 2.1b. In this sense the Ramsey fringes are an interference pattern between which quantum states the system projects into.

In general coherent ultrafast spectroscopy is concerned with understanding and characterizing coherences which are characterized by the phase evolution ψ of a quantum system. The techniques are typically a generalization of or related to Ramsey spectroscopy. Ramsey spectroscopy has many uses of which an important one is precision measurement [55–57]. However, in the context of this thesis its most important use is to understand and quantify ψ and thus quantum coherence and decoherence [58–60].

In the original Ramsey pulse sequence, the rate at which the system evolved from one state to another (the Rabi frequency Ω) times the pulse duration σ defined a phase called the pulse area $\theta = \Omega\sigma$. Using a pulse area of $\frac{\pi}{2}$ equally weights the superposition state, while a pulse area of π transitions the initially unexcited population into a fully excited population. Historically, a pulse area of $\frac{\pi}{2}$ was used for the "Ramsey pulse sequence" but this is not a requirement for observing Ramsey fringes as a different value will reduce the fringe contrast. The pulse area θ is a phase that relates the weighting of the state of the system after the pulse, while the relative phase ϕ deals with the phase evolution and readout of the system.

The Ramsey fringe contrast is greatly reduced if a strongly inhomogeneously broadened ensemble is considered. Inhomogeneity means that each oscillator has a slightly different transition frequency. The first pulse will put each oscillator in an identical quantum superposition state from which they will each evolve and accumulate their own phase $\psi_i = 2\pi\delta_i\tau$. It should be clear that larger transition frequencies will accumulate phase faster, and as a result the ensemble will dephase as each oscillator accumulates an independent phase. This will reduce the fringe contrast when the second pulse reads out the Ramsey fringes. Essentially, the fringes of Fig. 2.1b become averaged as τ increases and the read-out probability asymptotes to $\frac{1}{2}$.

While this dephasing may at first glance appear irreversible, each oscillator still retains phase even though the ensemble has dephased. If instead of the second pulse having pulse area $\frac{\pi}{2}$, it had a pulse area of π the phase evolution of the ensemble will "reverse" and accumulate phase as $\psi_i = -2\pi\delta_i t^*$ where t^* is the time after the second pulse. At a later time t^* will equal τ and the ensemble will rephase emitting a "pulse" leading to a spin-echo in NMR experiments and a photon-echo in optics [61, 62].

These examples show that role of phase in *isolated non-interacting quantum systems* and why it is critical to understanding and measuring the coherent response of quantum systems. When vibrational, electronic or spin couplings are introduced these interactions modify the coherences in observable ways, and it is these couplings that motivates MDCS.

2.1.3 Optical Bloch Equations and Feynman Diagrams

To calculate the optical response of a system the optical Bloch equations (Eq. 2.1) are typically used. The Hamiltonian is typically notated $H = H_0 + H_{int}$ where H_0 describes the energy eigenstates and H_{int} describes the interacting electric field. Written explicitly for a two level system these equations are:

$$\dot{\rho_{11}} = \frac{i}{\hbar}(H_{12}\rho_{12} - \rho_{21}H_{12}) - \gamma_{11}\rho_{11} \tag{2.7}$$

$$\dot{\rho_{22}} = \frac{-i}{\hbar}(H_{12}\rho_{12} - \rho_{21}H_{12}) - \gamma_{22}\rho_{22} \tag{2.8}$$

$$\dot{\rho_{12}} = \frac{-i}{\hbar}(H_{21}\rho_{22} - \rho_{11}H_{12}) - \gamma_{12}\rho_{12} - i\omega_{12}\rho_{12}. \tag{2.9}$$

$$\tag{2.10}$$

Here H_{ij} is a Hamiltonian matrix element, ρ is a density matrix, and γ_{ij} is the radiative decay or dephasing rate from $L(\rho)$ all indexed by $i = 1, 2$. For the responses measured in optical coherent spectroscopy the interaction Hamiltonian $H_{int} = -\hat{\mu} \cdot \hat{E}(t)$ describes the off-diagonal Hamiltonian matrix elements. The interaction Hamiltonian describes the driving field interacting with the system and is perturbative to H_0, the systems undriven Hamiltonian that describes the diagonal Hamiltonian matrix elements. The interaction Hamiltonian is characterized by $\hat{\mu}$ the dipole operator and $\hat{E}$ the electric field operator. For a two level system with a density matrix given by Eq. 2.2 the dipole operators are:

$$\hat{\mu} = \mu_0(|e\rangle\langle g| + |g\rangle\langle e|) \tag{2.11}$$

where μ_0 represents the transition dipole moment and $|e\rangle\langle g| + c.c.$ are the raising-lowering operators. Accordingly, the electric field in a Dirac delta (impulsive) approximation for n pulses is

$$E(t) = \sum_{i=1}^{n} \frac{E_0 \mu}{2} \delta(t - t_i)(e^{i\omega_L(t-t_i)-i\phi} + e^{-i\omega_L(t-t_i)-i\phi}). \tag{2.12}$$

Here E_0 is the field amplitude, $\delta(t - t_i)$ is the impulsive field distribution, ω_L is the pulse carrier frequency, ϕ is the pulse phase, and t_i is the time at which the ith pulse arrives. On comparison of Eq. 2.11 and Eq. 2.12 it is clear that the product $\hat{\mu} \cdot \hat{E}(t)$ has four terms times a pulse envelope term. A unitary transformation $U = e^{i\omega_0 t|e\rangle\langle e|} = |g\rangle\langle g| + e^{i\omega_0 t}|e\rangle\langle e|$ transforms the interaction Hamiltonian into a rotating frame where only two terms are near stationary and the other terms oscillate much faster than the transition frequency ω_0. Although not strictly valid in the impulsive limit, the rotating wave approximation is valid for Gaussian envelopes of finite width. As the Gaussian bandwidth increases they become increasingly better approximations of the impulsive limit; without necessarily having the bandwidth to invalidate the rotating-wave approximation. Keeping the faster rotating terms leads to the Bloch-Seigert shift which is rarely observed. After dropping the faster oscillating terms and transforming back into the Schrodinger picture, the interaction Hamiltonian is

$$H_I = -\sum_i^n \frac{E_0\mu_0}{2}\delta(t-t_i)(|e\rangle\langle g|e^{-i\omega_L(t-t_i)-i\phi} + |g\rangle\langle e|e^{i\omega_L(t-t_i)+i\phi}). \tag{2.13}$$

In the impulsive limit $E(t) = E_0\delta(t)$. This convention allows us to define the Rabi frequency Ω, that describes the rate at which the system will evolve from it's ground state to an excited state and vice versa. In a rotating frame the Rabi frequency is

$$\Omega = \frac{\mu_0 E_0}{2\hbar}. \tag{2.14}$$

The Rabi frequency is a parameter that describes the coupling strength of the interaction Hamiltonian, i.e. ,the rate at which the system is driven from one state to the other. This is understood since H_{int} only provides off-diagonal matrix elements, coupling the diagonal matrix elements H_0 to the off-diagonal elements. Provided H_{int} is perturbative we can consider the situation when there is only one pulse. Then the density matrix can be expanded in terms of a dimensionless parameter $\Omega \rightarrow \lambda\Omega$ which can vary from $0-1$.

$$\rho_{ij} = \rho_{ij}^0 + \lambda\rho_{ij}^1 + \lambda^2\rho_{ij}^2 + \lambda^3\rho_{ij}^3 + \lambda^4\rho_{ij}^4 + ... \tag{2.15}$$

Usually after the expansion λ is set to one. Odd orders in perturbation theory will describe the polarization while even orders will describe a system's population. In general for resonant transition frequency $\omega_{ij} = \omega_i - \omega_j$ the perturbation expansion of the density matrix is

$$\dot{\rho_{ij}}^{(n)} = -(i\omega_{ij} + \gamma_{ij})\rho_{ij}^{(n)} - \frac{i}{\hbar}[H_{int}, \rho^{(n-1)}]_{ij} \tag{2.16}$$

where n denotes the order to which the expansion occurs. As we will see in the following section there is a diagrammatic way to solve the OBE's perturbativey using "Feynman diagrams" which allows spectroscopists to analytically deal with multilevel systems and effects like quantum interference, Raman coherences, multi-quantum coherences etc.

2.1.4 Feynman Diagrams for the OBEs

In order to solve the optical Bloch equations analytically to some order n in perturbation theory, a diagrammatic approach has been developed that allows spectroscopists to easily capture multi-energy levels and quantum interference. Each diagram represents a "quantum pathway" which represents how states are excited/dexcited and how these states transfer energy. The wave-mixing signal of interest is represented by the sum of all permutations of these diagrams.

For a given resonance the complex resonant frequency is denoted $\Omega_{ij} = \omega_i - \omega_j - i\gamma_{ij}$ (note this is not a Rabi frequency Ω). The transition dipole moment μ_{kl} represents the transition dipole moment for the $|k\rangle \rightarrow |l\rangle$ transition. In the diagramatic approach to the OBEs each pulse is assumed to be time-ordered such that each pulse is not coincident or overlapping in time with the other pulses. In this way the response of the system for any given pulse can be calculated independently. In the limit that each pulse interacts with the system "linearly" then a defined order in perturbation theory appears from the density matrix where each pulse increases the perturbation order by one.

In this way the nth order density matrix can be calculated after the nth pulse excites the system. Each pulse excites the system with a phase ϕ_n that does not need to be identical. For instance, if each pulse excites the system from a particular direction $\phi_n = \hat{k_n} \cdot \hat{x}$ or if each pulse had a different carrier frequency then $\phi_n = \omega_n \cdot t$. Such phases provide Ramsey fringes in the form of a "transient population grating" for $\phi_n = \hat{k_n} \cdot \hat{x}$ and a temporal population modulation for $\phi_n = \omega_n \cdot t$.

In order to calculate an nth order response each of these diagrams is "stacked" with time increasing vertically and n integrals must be evaluated. Electric fields E^* provide "arrows" that point to the left (providing the conjugate action of the electric field) while electric fields E act to the right of the diagrams (providing the non-conjugate action of the electric field). Both conjugate and non-conjugate fields can excite or de-excite the system. Experiments

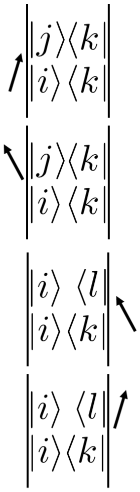

$$\rho^{(n)}_{jk} = \frac{i\mu_{ji}}{2\hbar} e^{i\phi_n} \int_{-\infty}^{t} E_n(t') e^{-i\omega_n t'} e^{-i\Omega_{jk}(t-t')} \rho^{(n-1)}_{ik}(t') dt'$$

$$\rho^{(n)}_{jk} = \frac{i\mu_{ji}}{2\hbar} e^{-i\phi_n} \int_{-\infty}^{t} E^{*}_n(t') e^{i\omega_n t'} e^{-i\Omega_{jk}(t-t')} \rho^{(n-1)}_{ik}(t') dt'$$

$$\rho^{(n)}_{il} = \frac{-i\mu_{kl}}{2\hbar} e^{-i\phi_n} \int_{-\infty}^{t} E^{*}_n(t') e^{i\omega_n t'} e^{-i\Omega_{il}(t-t')} \rho^{(n-1)}_{ik}(t') dt'$$

$$\rho^{(n)}_{il} = \frac{-i\mu_{kl}}{2\hbar} e^{i\phi_n} \int_{-\infty}^{t} E_n(t') e^{-i\omega_n t'} e^{-i\Omega_{il}(t-t')} \rho^{(n-1)}_{ik}(t') dt'$$

Figure 2.2: Feynman Diagrams with their corresponding integral to evaluate the density matrix element $\rho^{(n)}_{ij}$. Time increases in the vertical direction, arrows to the left indicate conjugate phase/fields while arrows to the right indicate positive phase/fields.

will use a phase modulation or phase matching condition to select processes based on the time-ordering of these conjugate vs. non-conjugate pulses. A common initial condition is that the system starts in the ground state $\rho^{(0)}_{gg} = 0$. The primary observables in spectroscopy are population as with Ramsey fringes or coherent light which is re-radiated in the form of a macroscopic polarization. The macroscopic polarization $P = tr(\hat{\mu}\hat{\rho})$ radiates into the electric field $E_{rad} \sim iP$ where it can be detected on a photodetector-spectrometer. In our experiments, we measure an excitation level $S \sim tr(\hat{n}\hat{\rho})$ as a photocurrent. The difference in these measurements is the order of perturbation required. Both detection approaches are interested in measuring coherences, however from Eq. 2.16 the first order correction to the density matrix involves coherences/off-diagonal elements while second order corrections involve populations/diagonal elements.

This creates a difference in how many diagrams need to be considered for a measurement that records coherences vs populations. A measurement recording polarization up to nth order in perturbation will have m diagrams while a population measurement will have $2m$ diagrams. This is understood by realizing that an additional pulse is needed to 'map' the polarization into a population state. However, nothing fundamental changes about the quantum pathways or diagrams, it is simply the final state that needs to be considered.

2.1.5 Types of 2D Spectra

There are a variety of different MDCS spectra that can be obtained. The type of MDCS spectra measured depends on the ordering of the pulse phases in Fig. 2.2. In general there are many possibilities but in third order perturbation theory there exist primarily three pulse sequences that are of interest due to having three pulses interact with the sample as in Fig. 2.3. In order to generate a MDCS spectrum the signal is Fourier transformed with respect to two of the three time axis in Fig. 2.3.

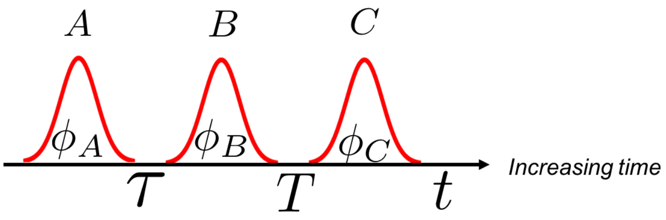

Figure 2.3: In third order MDCS three pulses are used to excite the sample, each with relative phase $\phi_{A,B,C}$. The time ordering of the pulses A, B, C is such that A arrives first and C last.

The three pulses are labeled by their relative phases, if we denote the time ordering of the pulses A, B, C where A comes first and C last then the three pulse sequences of interest are given by:

$$\phi_{S_I} = -\phi_A + \phi_B + \phi_C \tag{2.17}$$

$$\phi_{S_{II}} = \phi_A - \phi_B + \phi_C \tag{2.18}$$

$$\phi_{S_{III}} = \phi_A + \phi_B - \phi_C. \tag{2.19}$$

The S_I pulse sequence refers to rephasing pulse sequences in which the first pulse is oppositely phased with respect to the second two. Because of the opposite phase of the exciting pulse A relative to the next two pulse phases this pulse sequence will reverse the coherent phase evolution created by the first pulse. For fixed T at some point $\tau = t$ an inhomogeneously broadened ensemble will "rephase" leading to a photon echo in an inhomogeneously broadened system.

The S_{II} pulse sequence is a non-rephasing pulse sequence in which the first and third pulses are oppositely phased with respect to the second. In this situation, unlike that of $S1$, the second and third pulses are oppositely phased effectively causing an inhomogeneously broadened ensemble to decay by its free induction decay.

The S_{III} pulse sequence is a multi-quantum pulse sequence. This name arises from the additive nature of the first and second pulse phases. The phase evolution after the first pulse is given by $\phi_\tau = \omega\tau$ where ω is the resonant frequency. The second pulse will attempt to "kick" the resonance again so that it accumulates phase twice as fast during inter-pulse delay T with $\phi_T = 2\omega T$. For a single two level resonance this pulse sequence will provide no signal due to destructive interference of the quantum pathways. For multi-level resonances such as a ladder type three-level system this pulse sequence effectively creates a coherence between the ground state and the doubly excited states. The multi-quantum coherence is particularly useful to investigate coupling between (for instance) two-coupled two level systems because it provides a direct probe of the coupled state.

2.1.5.1 Rephasing Spectra

A number of simulated rephasing MDCS spectra are plotted in Fig. 2.4 for model systems. The coherent signal recorded as a function of two time delays $S(\tau, T, t)$ is Fourier transformed with respect to τ and t. The rephasing y axis is plotted with negative frequencies to indicate the relative phase of the first pulse $-\phi_A$ and the subsequent negative phase evolution after the first pulse during time τ. The x axis is plotted with positive frequencies to indicate the coherent evolution after the third pulse ϕ_C during time t is opposite to that during τ. Because MDCS measures the phase and amplitude of the coherence it is customary to plot the absolute and real part of the MDCS as in Fig. 2.4.

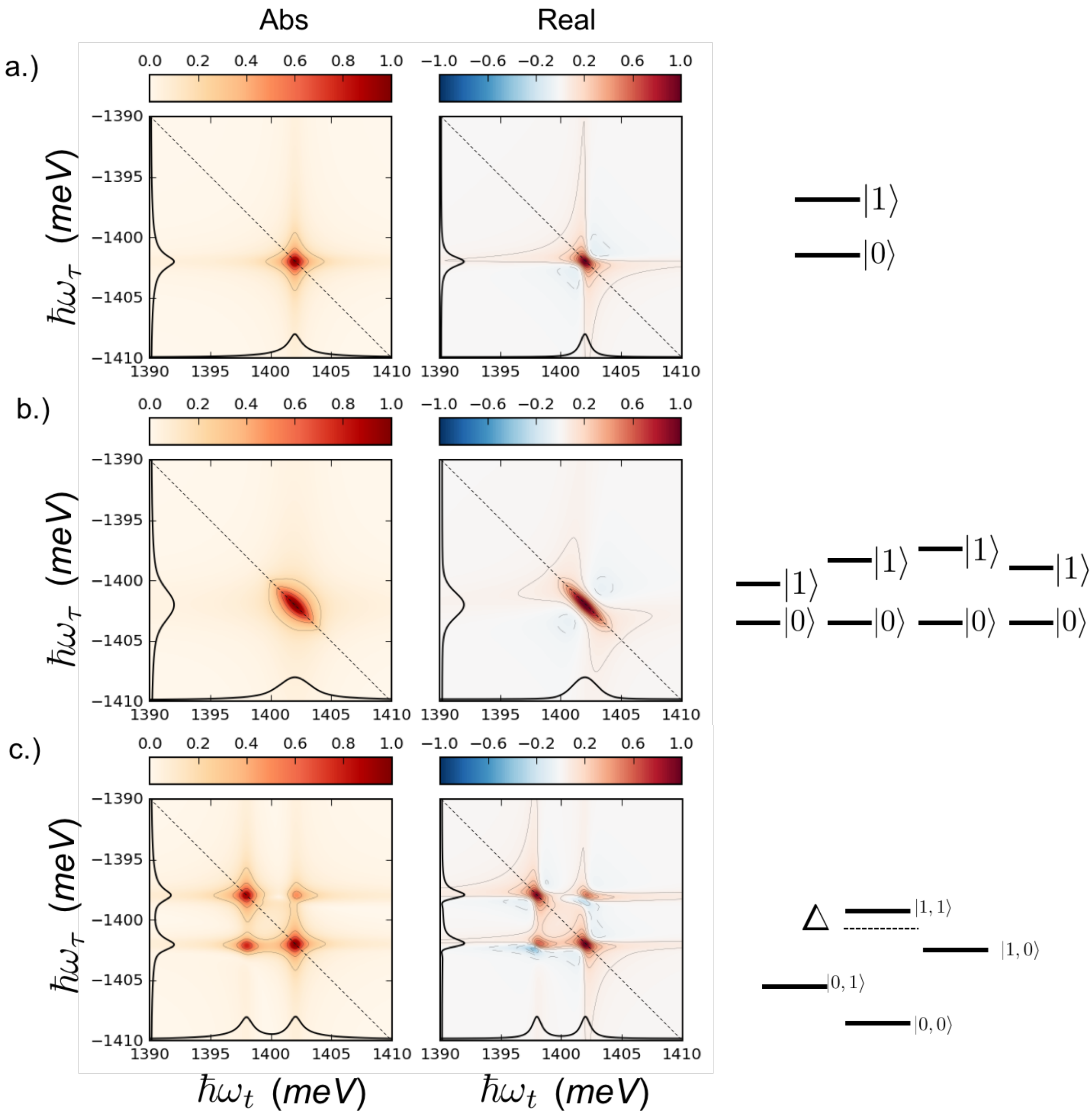

Figure 2.4: Simulated rephasing absolute and real part of MDCS spectra for a variety of physical systems. a.) The MDCS spectra of a homogeneously broadened resonances. b.) The MDCS spectra of a inhomogeneously broadened resonance that has a photon-echo. c.) The MDCS spectra of two coupled homogeneously broadened resonances with coupling energy Δ.

In Fig. 2.4a the MDCS spectra of a homogeneously broadened two-level system is plotted. The absolute spectrum demonstrates absorption at the resonant energy y axis and emission at the same energy x axis. The real part of this spectrum $2D$ is characterized as absorptive with a positive central peak along the diagonal (dotted line). Along the cross-diagonal the real part of the spectrum has negative lobes which are an artifact of the Fourier transform of τ from $0 \rightarrow \infty$ as opposed to $-\infty \rightarrow \infty$. Methods to correct this negative component include the correlation spectra which records both the rephasing and non-rephasing spectra [40] restoring the range $-\infty \rightarrow \infty$ along the τ dimension. For our measurements this is rarely done due to concern about the phase changes that occur due to many-body interactions [41, 63].

In Fig. 2.4b the MDCS spectra of an inhomogeneous ensemble of two-level systems is plotted. The absolute spectrum demonstrates absorption at the resonant energy y axis and emission at the same energy x axis. Unlike the homogeneous ensemble of Fig. 2.4a this peak is elongated along the diagonal. This occurs because in an inhomogeneously broadened ensemble the rephasing pulse sequence results in a photon echo. The homogeneous decay occurs along $t^{'} = t + \tau$ while the inhomogeneous decay occurs along $\tau^{'} = t - \tau$. In the Fourier transform these axis are given by the crossdiagonal and the diagonal slices [64–66]; and hence the inhomogeneity can be separated from the homogeneous linewidth [65, 67–69]. The separation of these linewidths potentially allows for coherent control of inhomogenously broadened ensembles [70].

In Fig. 2.4c the MDCS spectra of two homogeneous interacting resonances is plotted. The absolute spectrum demonstrates absorption at the two resonant energies y-axis and emission at the same two resonant energies. However the appearance of peaks off the diagonal line is indicative of coupling between the two diagonal resonances. In the absence of coupling the quantum pathway destructive-interference will only provide peaks along the diagonal. The presence of coupling will lift this destructive interference condition and provide a mechanism for energy transfer to the other states. This is visually represented by the crosspeaks which absorb energy at one resonance and transfer it at another where it re-radiates. The real-part of the crosspeaks can indicate the kind of coupling present. The two diagonal peaks appear absorptive as Figs.(2.4a-b) did, however the crosspeaks appear dispersive with a negative wing showing up for both crosspeaks towards the bottom left corner. This dispersive profile on the cross peak is indicative of an interaction with a negative interaction energy Δ.

2.1.5.2 Non-Rephasing Spectra

In addition to the rephasing-pulse sequence in which the second and third pulses are phased the same way, a pulse sequence exists in which the second and third pulses are oppositely phased. If the second and third pulses are commensurate in time then they destructively interfere and the system decays after the first pulse by free induction decay instead of rephasing. As a result, in this pulse sequence no photon-echo appears, the signal decays faster than in resphasing spectra and the frequency resolution is not as good due to this faster signal decay. Because of this, this is the least commonly studied type of MDCS spectrum. However, it commonly used to generate correlation spectra in which the rephasing and non-rephasing are added together to generate a purely absorptive phase profile [40, 71]. While advantageous for reducing Fourier transform artifacts, in correlation spectra peak oscillations can occur due to interference of the rephasing and non-rephasing spectra [72, 73]. This interference can complicates the interpretation of the MDCS spectra and has contributed to coherent energy transfer controversies in photosynthetic systems [72, 74–76].

In a non-rephasing pulse sequence (Fig. 2.5) both the y axis and the x axis have positive frequencies to indicate the coherent phase evolution ϕ is the same after the first pulse during time τ as after the third pulse $\phi = \omega t$. The non-rephasing homogeneous absolute spectrum (Fig. 2.5a) of a two-level system looks quite similar to to the homogeneous rephasing spectra (Fig. 2.4a). The differences between S_I and S_{II} appear in the real part of the spectrum where a relative rotation of ninety-degrees occurs. The result of this rotation is that negative side-lobes along the diagonal as opposed to off the diagonal as in the rephasing pulse sequence (Fig. 2.4a) and the absorptive peak is cross-diagonal as opposed to along the diagonal as

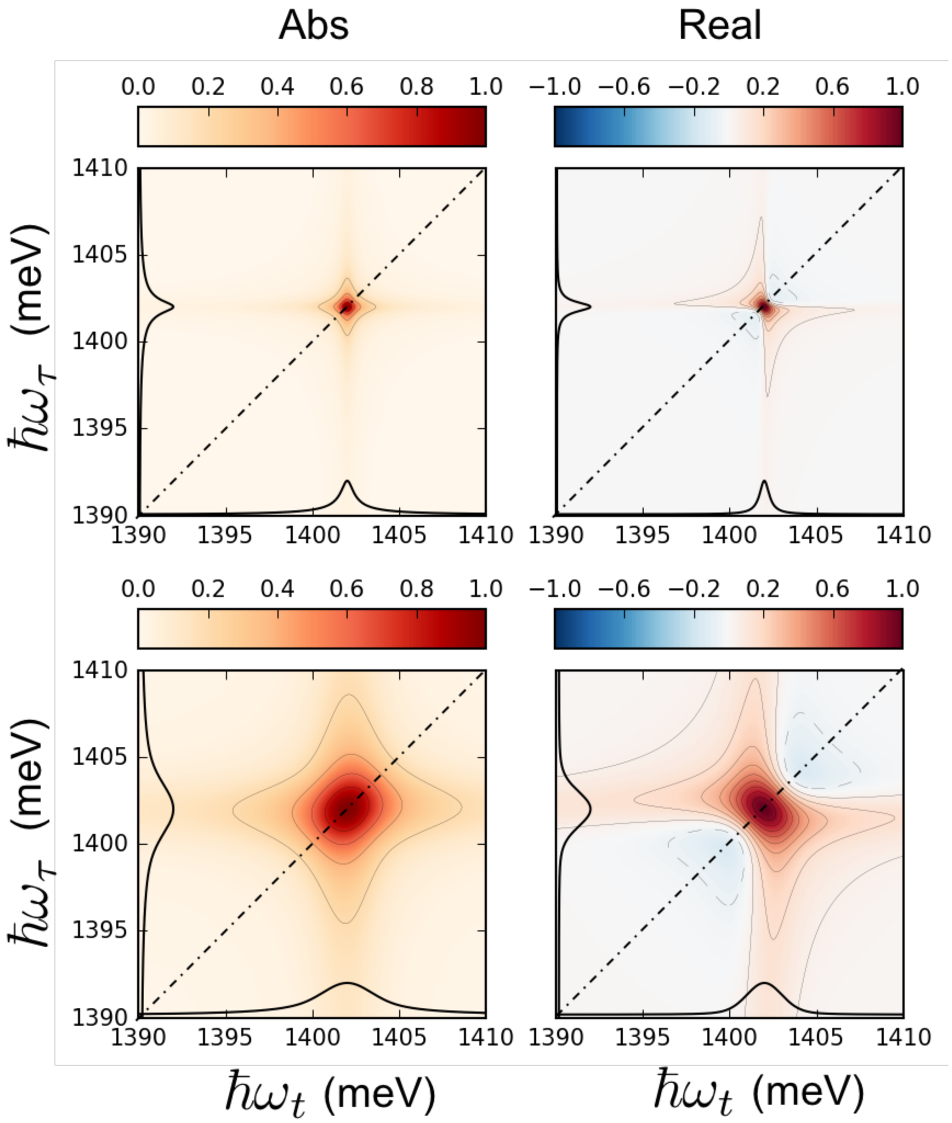

Figure 2.5: Simulated MDCS spectra for the non-rephasing pulse sequence for a two-level homogeneous and inhomogeneously broadened resonance.. a.) A homogeneously broadened non-rephasing spectrum. b.) An inhomogeneously broadened non-rephasing spectrum.

in the rephasing pulse sequence. Inhomogeneous broadening in the non-rephasing pulse sequence results in free-induction decay along both τ and t and broadens the spectrum while maintaining the same phase profile.

2.1.5.3 Two Quantum Spectra

The multi-quantum pulse sequence is of particular interest due to its ability to probe collective dynamics mediated through energy exchange/ many-body interactions [42, 46, 47]. The multi-quantum pulse sequences are unique as compared to the S_I, S_{II} pulse sequences in that for resonant excitation of a two level system no signal is present due to the lack of a second state at approximately double the excitation energy. A similar multiphoton pathway can exist in which two pulses at half the excitation energy excite a state [77].

For resonant excitation, this pulse sequence probes the states at approximately twice the excitation energy. This results in a requirement that the transition energy from the ground to first excited manifold and the transition energy from the first excited manifold to the second excited manifold be anharmonic or have different linewidths. In the context of many-body physics the system is described as a collective ensemble and the second excitation manifold consists of doubly excited states. As an example we consider a six-level system with doubly-excited anharmonicities Δ_i and γ_i as in Fig. 2.6.

In this model, there are three “red” transitions and three “blue” transitions. The state $|2\rangle$ corresponds to a single excitation of the red “mode” and the state $|3\rangle$ corresponds to a double excitation of the red mode. In order for the two-quantum spectra pathways to not destructively interfere anharmonicities Δ_i (resonant energy shift) and γ_i (excitation induced dephasing) are assigned to the doubly excited states. The first pulse creates a coherence between the first excited manifold and the ground state. This coherence acquires phase at the optical transition frequency $\phi = \omega_i \tau$. The second pulse converts the coherences created by the first pulse into multi-quantum coherences which acquire phase at $\phi = n\omega_i \tau$ where n is an integer detailing the order of the multi-quantum coherence. For the case of a two-quantum coherence $n = 2$. When the time after the second pulse T is Fourier transformed this phase evolves twice as fast resulting in a frequency axis at twice the optical transition frequency as in the y axis of Fig. (2.6).

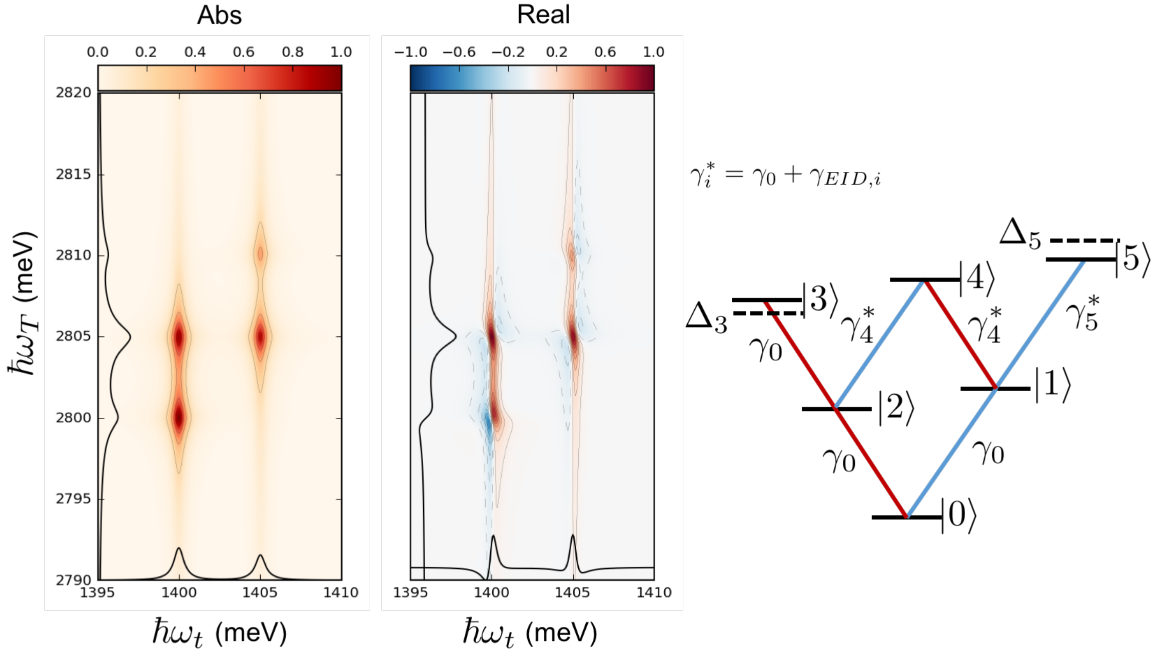

Figure 2.6: Two quantum absolute and real part of MDCS spectra for a six level system with different two-body interactions. In this example the homogeneous linewidth γ_0 of all resonances is the same however there can exist additional dephasing $\gamma_{EID,i}$ for the ith state and energy shifts Δ_i. In this example state $|3\rangle$ has a negative energy shift Δ_3, state $|4\rangle$ has only additional dephasing $\gamma_{EID,4}$ and state $|5\rangle$ has a positive energy shift Δ_5.

In the model of Fig. (2.6) state $|3\rangle$ has a negative energy shift of 10 ueV giving the real part of its spectra at 1400meV a dispersive profile with a negative lobe at lower energy (Fig. 2.6). The cross peaks absorbing at 2805meV and emitting at 1400meV and 1405meV are absorptive because the doubly excited state $|4\rangle$ has increased dephasing $\gamma_{EID,4}$. The state $|5\rangle$ has a positive energy shift of 10ueV and an increased dephasing of 10ueV resulting in a slightly dispersive peak at 2810meV and 1405meV with negative lobe toward higher energy.

Chapter 3

Development of Multidimensional Coherent Optical Photocurrent Spectroscopy

A common technique to study the ultrafast coherent evolution of a chemical or semiconductor system is a multi-pulse four-wave mixing (FWM) experiment. These techniques have been used extensively in semiconductors [78–80] to study the coherent response of excitons and quantum dots. In these experiments, optical coherences are measured as a function of inter-pulse delays.

Most FWM techniques are only sensitive to the magnitude of the coherent evolution of quantum states and do not record phase information. Therefore, the real and imaginary components of the complex FWM signal are unknown. To correctly disentangle these components, both the amplitude and the phase of the FWM signal need to be recorded as a function of inter-pulse delay. Then, the Fourier transform of the inter-pulse delays can be taken to generate an optical spectrum. By taking the Fourier transform with respect to two or more time delays, a multidimensional coherent spectrum can be generated.

Multidimensional coherent spectroscopy is not a new concept as it was first applied to Multidimensional Nuclear Magnetic Resonance (MD-NMR) experiments by Ernst [81]. The difference between the NMR and the optical regime is the comparative difficulty in measuring the phase. NMR experiments are conducted in the radio frequency regime where electronic instrumentation allows for precise control of the exciting pulses and where long dephasing rates allow radio-frequency detection to time resolve the emitted signal.

In contrast, optical experiments typically operate in an ultrafast regime, ∼ps, where electronics are not fast enough to resolve the emitted signal and square law detectors are insensitive to the phase. Additionally, the most important complication in the optical regime is phase-noise between pulses induced by interferometric fluctuations greater than $\frac{\lambda}{100}$ that degrades the phase measurement. In the last 18 years a variety of techniques have emerged both for vibrational and electronic spectroscopy that surmount these difficulties. In that time MDCS has proven to be one of the most powerful techniques for extracting information about the coherent evolution of quantum states [4, 10, 47, 82].

In this chapter, I discuss our development of a new way to record MDCS signals. The goal of our experiment was to bypass the limitations of standard, non-collinear FWM techniques to build an experiment suitable for studying single nano-objects. We achieve this by performing a type of dynamic phase cycling and recording an incoherent signal as a photocurrent. This approach has intrinsic phase stabilization due to our modulation scheme, allowing us to record both quadratures of a FWM signal while achieving long interpulse delays. We were able to successfully demonstrate MDCS on a single quantum well using this approach, we then used this setup for all other experiments discussed in this thesis.

3.0.1 Standard FWM Techniques for MDCS

Most methods for performing ultrafast FWM rely on non-collinear momentum/phase matching. A prototypical approach is to perform a time-integrated two-pulse measurement as shown in Fig. 3.1a. This experiment closely resembles a pump-probe experiment. In this experiment the first pulse A excites a sample while a pulse B excites the sample after some delay τ. The time delay τ is precisely stepped by a translation stage and the system response is recorded as a function of this delay. At each step of τ the signal is emitted in a background free direction $k_s = -k_A + 2k_B$ and recorded on a detector.

More elaborate FWM geometries often break pulse B into two pulses so that an interaction involves, pulse A,B and C. This provides a variety of phase matching conditions such as

$$k_{S_I} = -k_A + k_B + k_C$$
$$k_{S_{II}} = k_A - k_B + k_C$$
$$k_{S_{III}} = k_A + k_B - k_C.$$

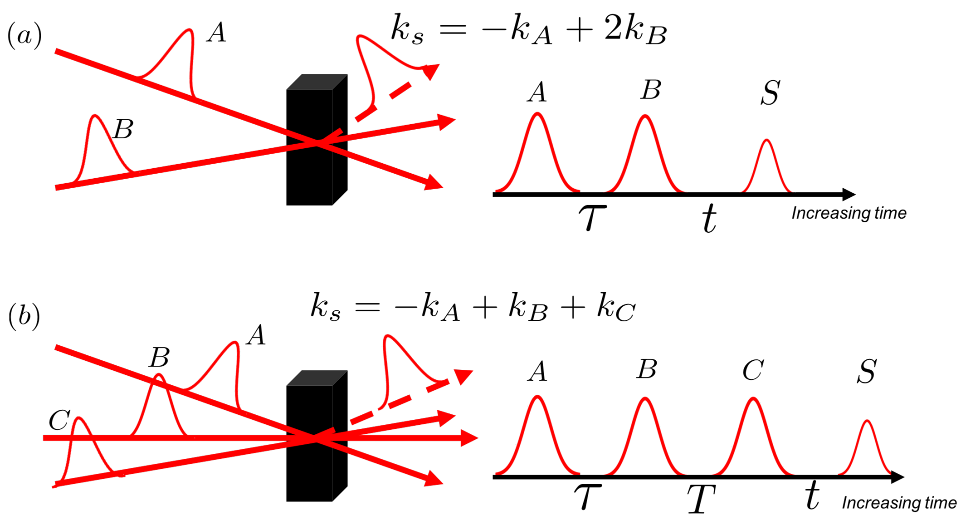

Figure 3.1: Different phase-matched FWM geometries. A two pulse experiment would resemble (a) in which the second pulse acts twice, while a three pulse experiment would resemble (b) in which each pulse drives the system linearly. The emission time for the signal S is t while the inter-pulse delays are τ, T

The implementation of a three-pulse FWM experiment Fig. 3.1b makes it easier to isolate these different phase matching conditions [4, 83]. This isolation is important as depending on this phase-matching condition the quantum coherences will evolve with different phase and exhibit different physics. For instance in an inhomogeneously broadened system the S_I signal will give rise to a "photon echo" while the S_{II} signal will not. Because of this difference the S_I signal is capable of isolating the homogeneous line width from an inhomogeneous system while the S_{II} is not [64, 65]. Just as in the two pulse version the signal is recorded as a function of interpulse delay.

In order to achieve a MDCS spectrum any of the above non-collinear techniques may be chosen as long as the signal is heterodyned with a local oscillator. The central problem in phase-resolved optical FWM is the issue of pulse-pulse phase stabilization. If any pulse acquires independent phase noise this will get mapped onto the coherent evolution of the quantum states and appear as a "real" phase when in fact it is just noise. If this noise is larger than a π phase , then the phase is completely unrecoverable. The standard requirement to claim phase resolved FWM is phase stabilization between pulses $\sim \frac{\lambda}{50}$. Typical phase noise arises from interferometer fluctuations due to mechanical vibrations. These interferometer fluctuations are on the order of 100 nm. Given $\lambda \sim$ 800nm the required interferometer stability is $(8 - 16)$nm. Addressing this issue requires either pulse shaping methods [84, 85] to achieve pulse-pulse phase stabilization, elaborate interferometer locking techniques [4, 83, 86] or the careful manipulation of wavefronts [87]. In the pulse-shaping case beam A is pulse shaped into two phase-locked beams with variable delay and the probe field acts as a local oscillator heterodyning with the signal. For the case of locked interferometers a local oscillator goes around the sample and heterodynes the emitted field. In this situation additional protocols must be followed to properly phase the FWM signal [88].

All of the above techniques rely on wave vector selection to isolate a FWM beam from other signals in the far field. This approach works for 3D systems such as dense atomic vapors, 2D systems such as quantum wells or dense ensembles of quantum dots. What 3D and 2D systems have in common is translational symmetry that allows for the formation of a beam in the far field. Single nano objects such as quantum dots, atomic-force microscope tips, and other single nano objects radiate as point sources preventing the formation of a well formed beam in the far field. Prior to our implementation, only two other FWM experiments were suitable for studying single nano objects [45, 48, 82]. One of these experiment makes a variety of assumptions about the phase evolution of the FWM signal in order to phase the spectrum. The other experiment is limited to studying surfaces with a few hundred fs time resolution.

In addition to non-collinear approaches there are two previous approaches to collinear population-readout MDCS. The first relies on a static phase modulation scheme, where the phases of three exciting pulses is modulated to coherently subtract out unwanted signal pathways from the MDCS signal. For the signal measurement, instead of an emitted coherent field, an incoherent photoluminescence is collected. In this way the second pulse acts as pulses B and C from the non-collinear schemes (Fig. 3.1a) while the third pulse converts the coherent signal into a population state; where it is read out as photoluminescence [43, 89] as shown in Fig. 3.2a. The second approach uses four collinear pulses A,B,C, and D and uses a dynamic phase cycling/modulation scheme to phase 2D spectra. Like the static scheme the coherence after pulse C is converted into an incoherent photoluminescence signal. However, in this scheme this incoherent signal is modulated at a specific detection frequency [90, 91] as shown in Fig. 3.2b.

3.0.2 Coherent Optical Photocurrent Spectroscopy

Inspired by the dynamic phase cycling schemes of [26, 90, 91] we implemented a dynamic phase cycling experiment [92] for performing multidimensional coherent optical photocurrent spectroscopy (MD-COPS) using photocurrent as an incoherent detection signal. The reason for this approach arises from a desire to record dephasing times $\sim$ 1ns in semiconductor single quantum dots and other nano-objects. Our experimental parameters preclude the use of pulse shaping, wavevector matching geometries and luminescence collection. Pulse shaping methods are limited to $\sim$ 10ps coherence times. Wavevector selection fails due to the lack of translational symmetry. Due to the index of refraction contrast between a semiconductor and air we expect that the incoherent, isotropic luminescence collection efficiency from a semiconductor to be poor. Furthermore, an intrinsic advantage of our approach is the realistic response of optoelectronic devices such as solar cells and and optical detectors. In this perspective a variety of single-nano objects have been embedded in Schottky or p-i-n diodes and studied with photocurrent spectroscopy. They include quantum wells [93, 94],

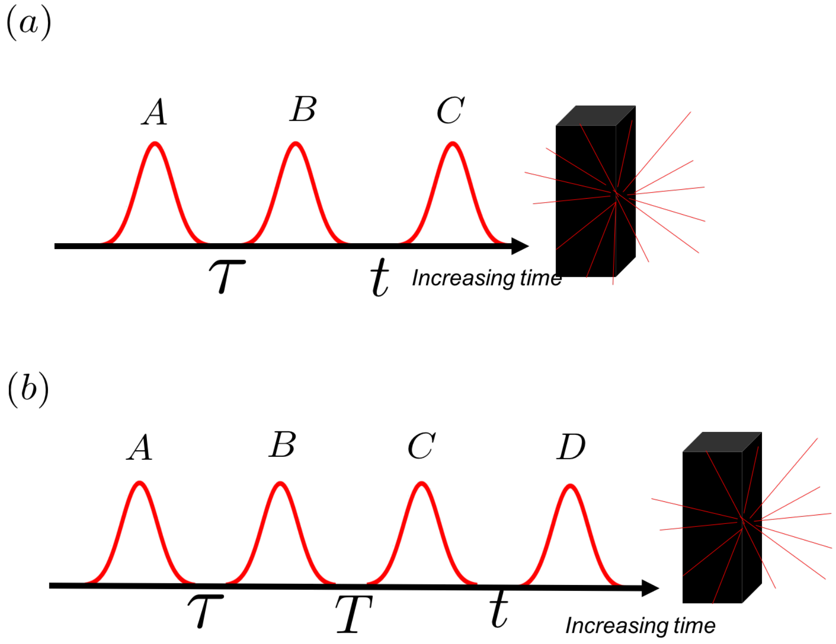

Figure 3.2: Different collinear FWM geometries. A three pulse experiment using static phase-cycling would resemble (a) in which the second pulse acts twice. A three pulse dynamic phase cycling experiment would resemble (b) in which each pulse drives the system linearly. In these schemes the polarization emitting after pulse B/C gets mapped onto an incoherent population with pulse C/D. The FWM signal is recorded as a function of inter-pulse delays τ, T, t

single and many quantum dots [95–103], quantum dot molecules [24, 104, 105] and carbon nanotubes [106].

Our experiment [92] consists of four excitation pulses A, B, C, D labeled in chronological order with A first as shown in Fig. 3.3a. The four pulses are prepared using two Mach-Zehnder interferometers nested within a larger Mach-Zehnder interferometer. Each interferometer contains a delay stage used for precisely stepping the interpulse delays (Fig. 3.3b). In each interferometer arm an Acoustic Optical Modulator (AOM) is driven by a phase locked direct-digital synthesizer (DDS). An AOM provides a radio-frequency defined diffraction grating due to the strain caused by a propagating acoustic wave. Thus unlike a typical diffraction grating the scattered light is doppler shifted by an integer times the driving frequency of the AOM. In each arm we take the 1st order diffracted beam and spatially block the other diffraction orders. Each AOM is driven by a different and unique radio frequency ω_i with $i = A, B, C, D$ on the order of 80 MHz. Using different radio frequencies (RF) therefore shifts each excitation pulses carrier frequency differently as $\omega'_{c,i} = \omega_c + \omega_i$. This frequency shift is insignificant compared to the optical carrier, but it's effect on the relative pulse trains between interferometer arms is significant. The linear and nonlinear signals recorded will occur at the "beatnote" between different pulse trains tagged by these radio frequencies.

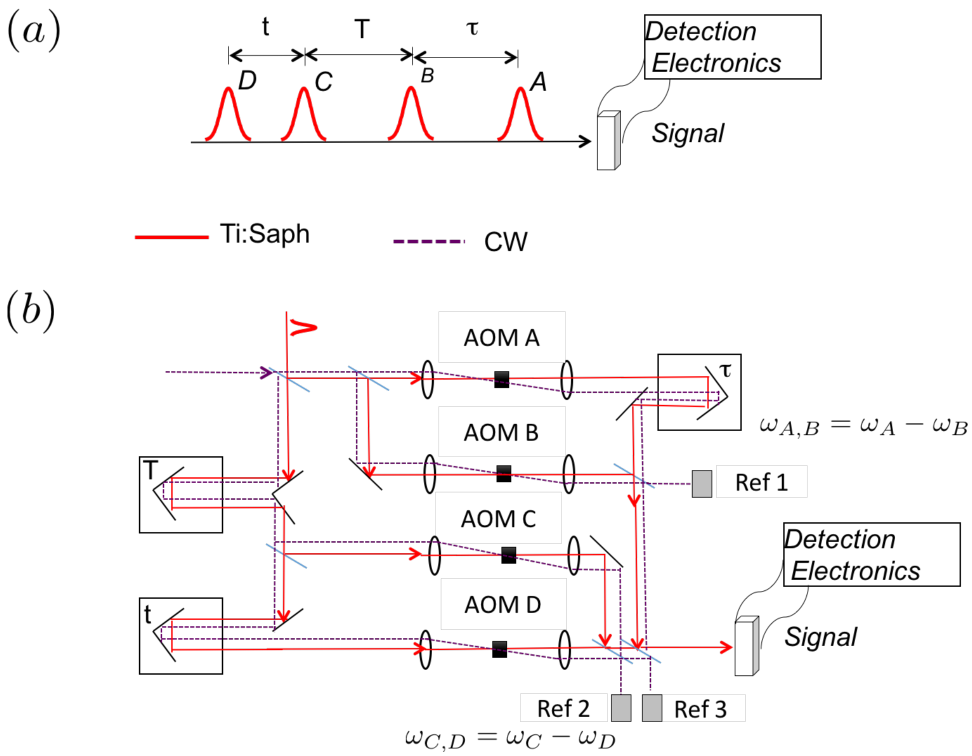

Figure 3.3: Experimental Apparatus for multidimensional photocurrent spectroscopy. a.) Shows the experimental pulse sequence with inter-pulse delays τ, T, t. The FWM signal is electrically collected in the form of a photocurrent. b.) The interferometer design of COPS experiments relies on four AOM's driven at unique and different frequencies. A CW laser propagates through the experiment spatially offset from the principal axis and is detected on reference detectors Ref $1, 2, 3$. This beatnote is sent as a reference to the lock-in detection signals where it is used for demodulation.

At the same time a reference continuous-wave laser is sent into the interferometer offset from the principal axis. This laser samples all of the same interferometer fluctuations that the mode-locked pulse trains sample since it is incident on the same optics. The reference laser beatnotes from each interferometer are detected on three reference detectors; where they are then mixed and sent as a reference for lock-in detection. Because of our modulation scheme the interferometer noise is removed as will be discussed in the following sections.

3.0.3 Dynamic Phase Cycling

In MDCS the FWM signal can be extracted from “static” phase cycling in which consecutive measurements are taken with different phase shifts applied to the exciting pulses [43, 48, 89, 107]. In our scheme each AOM is driven with a unique and different frequency. The beamsplitters make identical copies of the laser pulse train in each interferometer arm. Each AOM in each interferometer arm, with its unique driving frequency, then shifts the pulse-train carrier frequency so that they have non-identical carrier frequencies. The effect of this is to create a dynamic pulse to pulse phase cycling. Before entering the interferometers the pulse train is

$$\sum_n E(n,t^*) = a(t^* - nT_{rep})\cos(\omega_0 t^*) \tag{3.1}$$

where $T_{rep} = \frac{1}{f_{rep}}$ where f_{rep} is the laser repetition frequency $\sim 76MHz$, t^* is a real time, and w_0 is the optical carrier frequency. This carrier frequency ω_0 is given by $\omega_0 = 2\pi(Nf_{rep} + f_{ce})$ where N is an integer and f_{ce} is the carrier offset frequency. When f_{rep} and f_{ce} are stable the pulse-train can be thought of as a frequency comb [108]. The carrier offset frequency is due to a difference in group and phase velocities in the oscillator cavity and results in an intrinsic phase cycling in the pulse train i. This intrinsic phase cycling is given by $\Delta\phi_i = (\omega_i + 2\pi f_{CE})T_{rep}$.

When this pulse train enters the interferometers each pulse in this train is split into four identical copies. If we consider the n^{th} pulse in interferometer arm $i = A, B, C, D$ after going through the AOM it can be written

$$E(n,t^*)_i = a(t^* - nT_{rep}) \cos{(\omega_i^{'} t^*)} \tag{3.2}$$

where $\omega_i^{'}$ is shifted carrier frequency. The shifted carrier frequency is given by $\omega_i^{'} = \omega_0 + \omega_i$ where ω_i is the AOM driving frequency. Thus pulses in interferometer arm i develop a unique carrier frequency determined by the AOM driving frequency. When comparing the n_{th} pulses in interferometer arms i, j a clear pulse-to-pulse phase develops as

$$\Delta\phi_{i,j} = \omega_i^{'} - \omega_j^{'} = (\omega_i - \omega_j)(nT_{rep}). \tag{3.3}$$

With this in mind it becomes clear that each pair of pulses does not excite a sample the same way as the previous pair. The cycling frequency is given by the difference in the interferometer AOM driving frequency. The time domain picture of this process can be visualized in Fig. 3.4 for all four pulses.

An equivalent but different view of the phase cycling process is to consider the process in the frequency domain. In this picture the Fourier transform of a train of pulses is a frequency comb [108]. The AOM's shift each comb line by the AOM driving frequency. The "cw" comb lines can then beat in time with the other interferometer arm's comb lines which are shifted by the AOM driving frequency in its arm as shown in Fig. 3.5. This analogy is particularly helpful as it is analogous to how the reference laser beat note is generated.

3.0.4 Phase Stability and the Rotating Frame

For MDCS recording the phase of the FWM signal is critical. Generally, interferometer fluctuations scramble the phase of the FWM signal. Our approach to phase stability is to send a reference cw laser through the interferometers offset from the principal optical axis. The AOM's give the cw laser in arms A, B, C, D a relative frequency shift determined by the AOM driving frequency. The beatnote between the cw lasers is then collected on an the reference photodiodes (Fig. 3.3b). This cw laser samples the same interferometer fluctuations

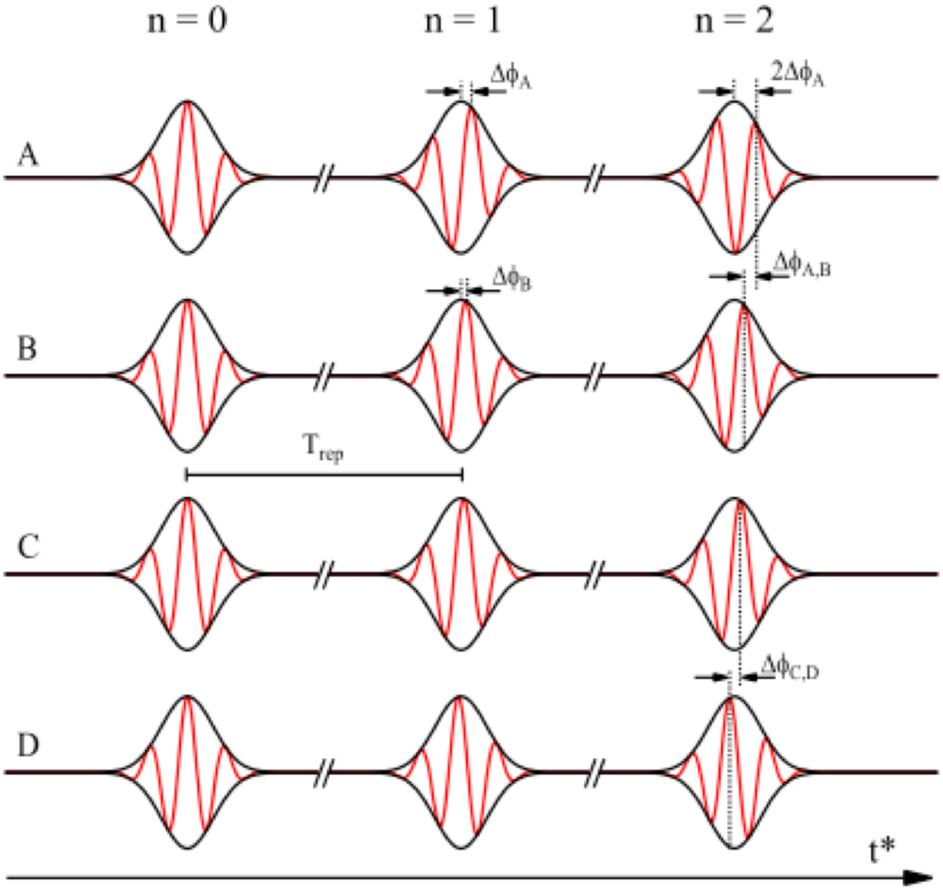

Figure 3.4: Time domain picture of dynamic phase cycling. On top of the intrinsic phase-shift of a mode locked laser due to its carrier offset frequency each interferometer arm acquires a new carrier frequency. This relative difference in carrier frequencies causes a pulse-pulse phase shift to develop between interferometer arms due to non-identical carrier frequencies. The rate at which the phase cycles is given by the difference in AOM driving frequencies. Here the interpulse delays τ, T, t have been set to zero. This figure is from [92].

as the primary pulsed laser system; and thus can be used to demodulate and remove those same interferometer fluctuations. A simple example of this can be understood by considering linear absorption in a two level system using two pulse trains in interferometer arms A, B and with a photocurrent readout of the population.

The two pulse trains (Eq. 3.2) from arm A, B in a delta-function limit are,

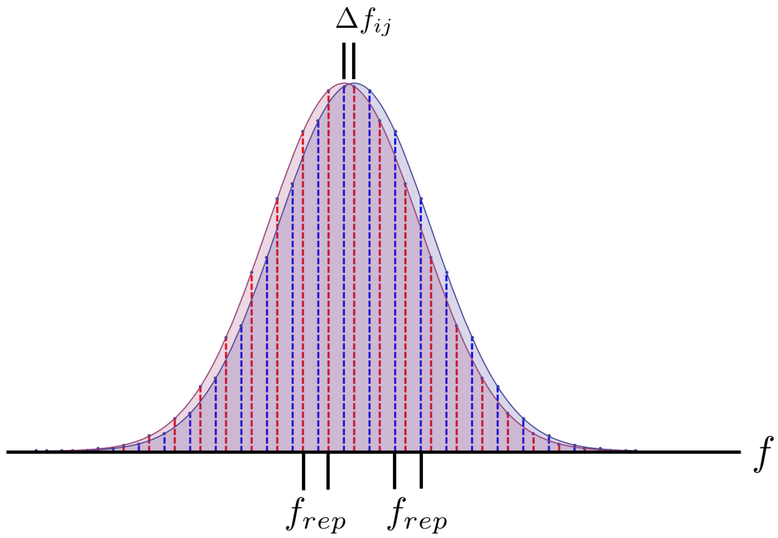

Figure 3.5: Two-pulse frequency domain picture of dynamic phase cycling. In the frequency domain the modulation scheme can be understood as the beating between each pair of comb lines shifted by the relative AOM frequencies. The comb line spacing is separated by the repetition rate of the laser. The comb lines in arm i are separated from the comb lines in arm j by the AOM difference frequency. Here the inter pulse delays τ, T, t have been set to zero.

$$E_A = e^{i(t^{'} - t_1 + nT_{rep})\omega^{'}_A}\delta(t^{'} - t_1) + c.c. \tag{3.4}$$

$$E_B = e^{i(t^{'} - t_2 + nT_{rep})\omega^{'}_B}\delta(t^{'} - t_2) + c.c. \tag{3.5}$$

$$\tag{3.6}$$

where $t^{'} = t^{*} - nT_{rep}$ is the real time τ is the pulse-pulse delay and $\omega_{A,B}$ are the shifted carrier frequencies. The linear absorption (photocurrent) signal will correspond to the response of the system encoded as a phase times a modulation term. The expression for the signal (ignoring the pulse train) is

$$S = DC + A\frac{-\mu^2}{4\hbar^2}e^{-\gamma_{11}(t-t2)}e^{-i(\omega_{01}-i\gamma_{01})\tau}\theta(\tau)e^{inT_{rep}(\omega_A-\omega_B)} + ... \tag{3.7}$$

where γ_{11} is the lifetime of the system, γ_{01} is the dephasing time, ω_{01} is the resonant frequency, μ is the transition dipole, DC corresponds to signals generated by one pulse acting twice and A is a constant that provides units of current. Note the DC term is actually at the repetition frequency of the laser but slow electronics effectively low pass this frequency to DC. The generated two-pulse signal is shown by Fig. 3.6.

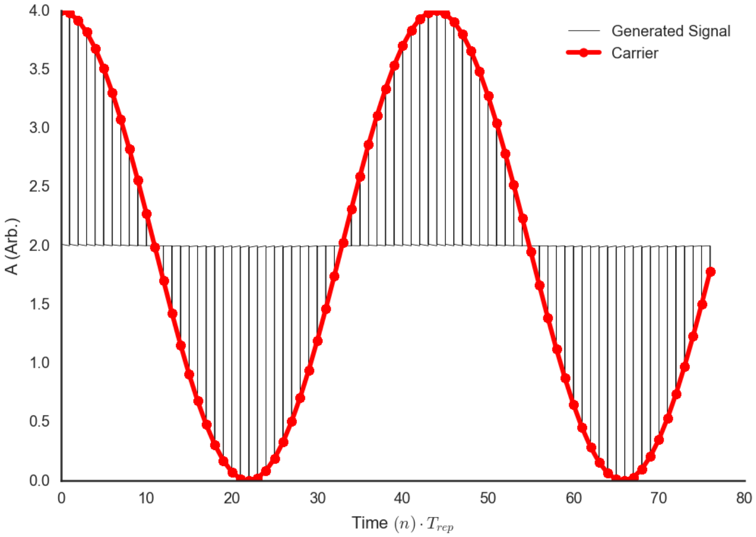

Figure 3.6: Two-pulse picture of COPS modulation signal for fixed inter-pulse delay τ. Note that the carrier frequency is much slower than the optical frequencies and that the signal is not centered around zero. The DC contributions come from each pulse acting twice.

Our detection scheme records this signal in a sample as a photocurrent where it is amplified and sent to a lock-in amplifier. In our experiment the cw laser is used to generate a lock-in reference that measures interferometer fluctuations. The cw fields in arms A, B develop a phase as

$$E_{ref,A} = e^{i(t^{*}-\tau)\omega_{ref,A}} + c.c. \tag{3.8}$$

$$E_{ref,B} = e^{i(t^{*})\omega_{ref,B}} + c.c.. \tag{3.9}$$

Here $E_{ref,A,B}$ is the reference laser's electric field in arm A, B, and $\omega_{ref,i} = \omega_{ref} + \omega_i$ which corresponds to the shifted reference laser frequency in each interferometer arm. The beatnote signal S_{ref} between the two cw lasers is given by $S_{ref} \sim [2 + 2\cos((\omega_{ref,B} - \omega_{ref,A})t^{*} + \omega_{ref,A}\tau)]$. This beatnote occurs at the AOM difference frequency in arms A, B.

The lock-in reference input triggers on the rising edges of this reference signal and will essentially discard the DC component.

Subsequently the input signal (Eq. 3.7) is demodulated by using this reference. The demodulation process moves the AC signal components to DC and the DC signals to AC. The final signal processing step is to low pass the demodulated signals. The end result is a signal of the form

$$S_{demod} \sim A(\tau)\cos\left(\tau(\omega_{ref,A} - \omega_{01})\right) + IA(\tau)\sin\left(\tau(\omega_{ref,A} - \omega_{01})\right). \tag{3.10}$$

The differential phase evolution as a function of inter-pulse delay $\phi = (\omega_{ref,A} - \omega_{01})\tau$ corresponds to measuring our FWM signal in the frame of the reference laser (a rotating frame). Because of the dual-quadrature nature of the measurement the complex signal can be recorded as a function of τ and Fourier transformed. This measurement requires that at each step phase stability is maintained. The signal error due to interferometer fluctuations $\Delta\tau$ is

$$\Delta S^2 = e^{-2\gamma\tau}(\gamma^2 + (\omega_0 - \omega_r)^2)\Delta\tau^2. \tag{3.11}$$

This signal error equation relates the total signal error. For MDCS we are primarily concerned with the phase error which is $\Delta\phi = (\omega_0 - \omega_r)\Delta\tau$. We recorded the fully sampled interferometer fluctuations at a fixed τ for each interferometer by setting $\omega_r = 0$ (an electronic reference) and observed path fluctuations $\sim$ 70nm as shown in Fig. 3.7a. A significant improvement is recorded when the interferometers are completely covered in order to prevent fluctuations (Fig. 3.7b) with the fluctuations dropping to $\sim$ 14nm. For signals measured in our experiment it is advantageous to have the reference laser near-commensurate to the optical transition wavelengths $\sim$ 10nm. For an interferometer fluctuation $\sim$ 100nm and $(\omega_0 - \omega_r) \sim 10$ THz the accumulated phase error is $\sim 1.1^\circ$ degrees.

Similar derivations can be worked out for our nonlinear-FWM schemes however there

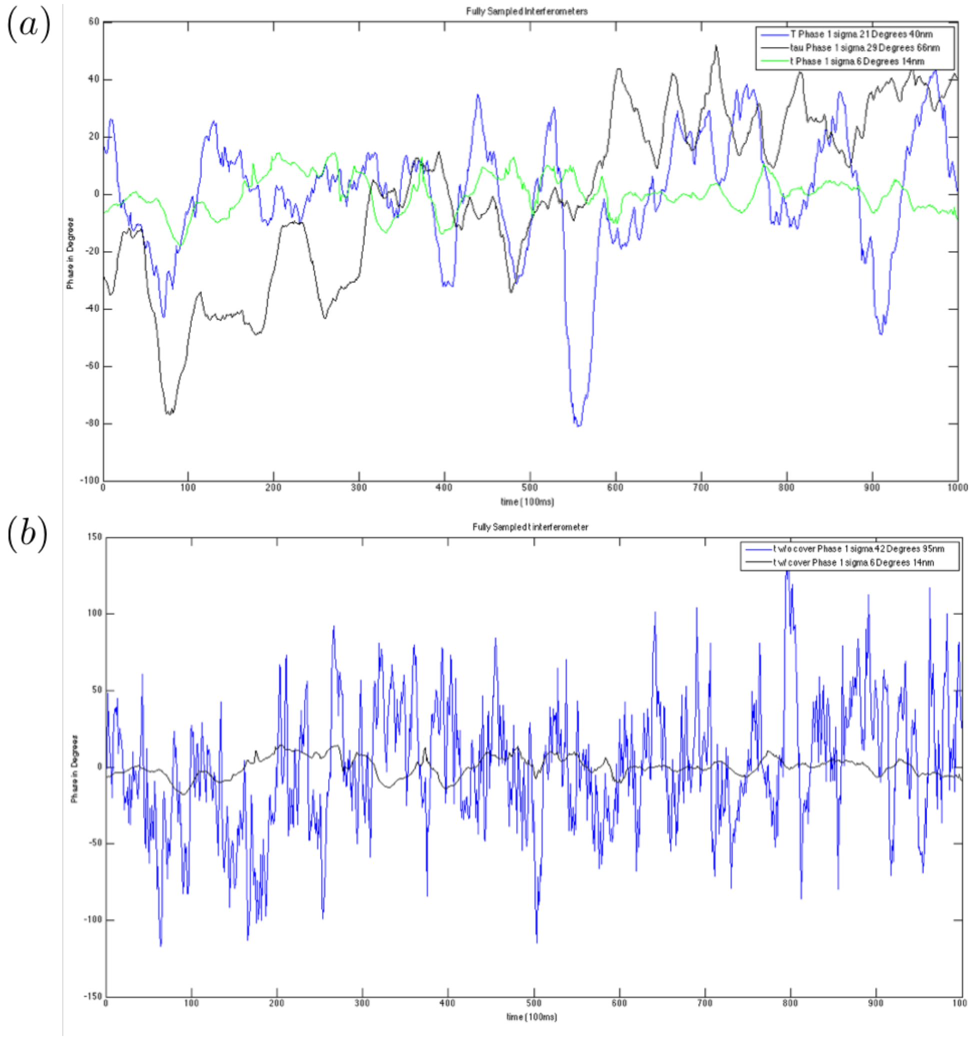

Figure 3.7: a.) Interferometer stability for each interferometer arm τ, T, t. This was recorded by using an electronic reference to demodulate the signal as opposed to an optical reference. b.) Interferometer stability for interferometer arm t with and without a cover on the experiment to dampen air fluctuations.

is an additional complication with respect to generating a reference signal for nonlinear signals. Our cw reference laser is not of sufficient intensity to generate nonlinear wave-mixing and therefore cannot directly generate a reference signal. In order to generate an appropriate reference we mix the linear output of two detectors REF 1, 2 (Fig. 3.3b) using single-side band mixing in a digital signal processor (DSP). Our mixing algorithm is to input the difference frequency beatnotes $\omega_{ref,AB} = \omega_{ref,A} - \omega_{ref,B}$ and $\omega_{ref,CD} = \omega_{ref,C} - \omega_{ref,D}$

and Hilbert transform them. A Hilbert transform shifts the phase of positive frequency by $\frac{\pi}{2}$. In doing so we are able to obtain the in-quadrature $\cos(\omega_{ref,ij})$ and in-phase components $\sin(\omega_{ref,ij})$ for the input beatnotes. We make use of the identity

$$\cos(\omega_{ref,AB} \pm \omega_{ref,CD}t^*) = \cos(\omega_{ref,AB}t^*)\cos(\omega_{ref,CD}t^*) \mp \sin(\omega_{ref,AB}t^*)\sin(\omega_{ref,CD}t^*) \tag{3.12}$$

to generate reference signals at the FWM beat frequencies

$$\omega_{ref,S1} = \omega_{CD} - \omega_{AB} \tag{3.13}$$

$$\omega_{ref,S2} = \omega_{CD} + \omega_{AB} \tag{3.14}$$

$$\tag{3.15}$$

for the resphasing ($S1$) and non-rephasing ($S2$) FWM signals. Using detector REF 3 we can also generate the n-quantum reference beatnotes after appropriate mixing and filtering. The use of frequency instead of wave-vector selection enables the simultaneous measurement of multiple FWM signals by using two lock-in detectors. The phase stability after the simultaneous measurement of $S1$ and $S2$ is shown in Fig. 3.8 where it is clear the demodulation process has effectively stabilized the interferometers $\sim$ 5nm.

3.0.5 Fourier Transform Spectroscopy: Physical Undersampling, Bandwidth and Resolution

An intrinsic advantage to our measurement approach is that we measure in a rotating frame, providing a “physical” undersampling to our signal. This is in contrast to more conventional methods of MDCS where the signal is measured relative to zero frequency. As a result of those conventional approaches it is a common to require very precise delay stepping. This is often achieved via birefringent delay lines [109] or with mechanical stages that

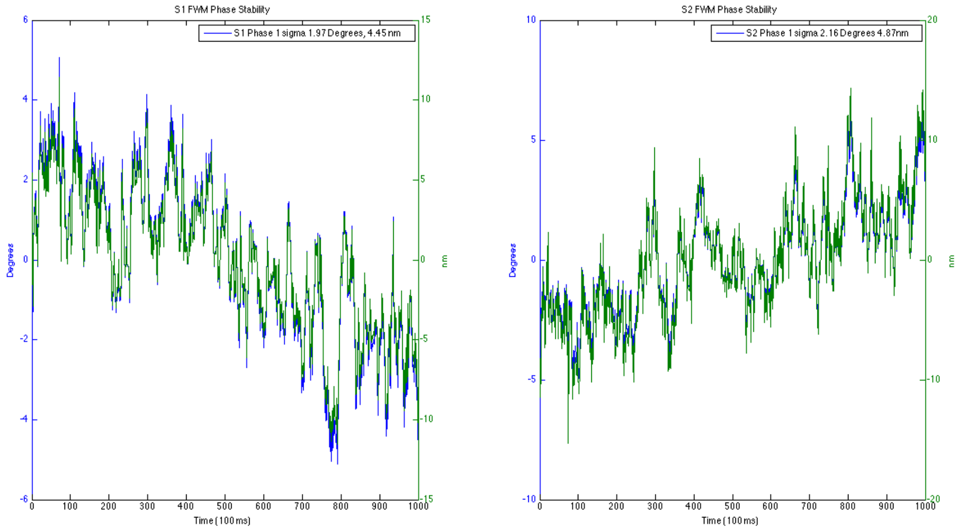

Figure 3.8: FWM Stability for fixed interpulse delay τ, T, t. Average fluctuations of both FWM signals is $\sim$ 4nm

step with a reference oscillators fringe spacing [4, 83]. This approach requires unnecessary bandwidth for fully-sampled signals $\sim$ 800THz which is significantly more than that of a 100fs pulse $\sim$ 20THz. In a rotating frame, to fully sample a signal the bandwidth requirements are relaxed and the stage stepping can be much larger $\sim$ 10um vs $\sim$ 150nm for fully sampled signals. Previous approaches to MDCS [90, 91] implemented their reference signal by temporally broadening their excitation pulses and using the beatnote between them as a reference. The frequency resolution in that approach is limited to $\sim \frac{1}{10ps}$ determined by their monochromator resolution. In our approach using an external cavity diode laser [92], the frequency resolution is limited to the linewidth of the external cavity diode laser $1-100$MHz and the mechanical delay stages length. The use of an auxiliary cw laser is particularly advantageous for studying quantum dots [110, 111] and other long coherence time objects.

3.0.6 Signal Amplification

A consequence of a photocurrent implementation to MDCS is that the measured signal to noise is not decoupled from the device physics of the sample. Issues such as device capacitance create non-ideal current sources, reducing the electronic bandwidth and adding additional noise due to impedance mismatch of the device and amplifier. Typically, an electronic amplifier is necessary for sensitive measurements of single nano-objects such as quantum dots [97, 100]. The issue of how to amplify or enhance weak electrical signals is an area of active research [103, 112–117] with no standard solution. Here we briefly discuss the model for a photodiode and the amplifier solution we implemented based off of bootstrapping concepts [118, 119].

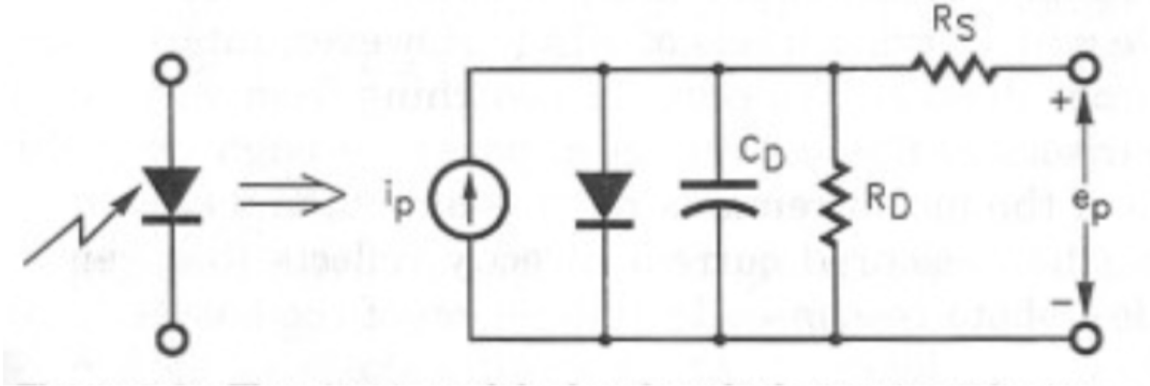

Figure 3.9: The model for a photodiode. This model consists of the signal current I_p generated by incident light, C_D the junction capacitance, R_D the shunt resistance and R_S the parasitic resistance. Figure originally from [118].

The model of a photodiode is shown by Fig. 3.9. This model consists of a consists of the signal current I_p generated by incident light, C_D the junction capacitance, R_D the shunt resistance and R_S the parasitic resistance. The shunt resistance R_D represents the resistance of the zero-biased diode junction and is usually (and ideally) large to the point of ignoring it. The parasitic resistance R_S represents the series resistance of the semiconductor material and the contacts and is often small in commercial diodes, but larger in our research-grade samples and should be considered. The junction capacitance represents the complicated capacitive behavior of diodes varying with both the area of the diode and the diode voltage. Larger diodes such as in our samples have larger junction capactiance which causes bandwidth, stability and noise issues in our experiments. Standard tricks to reduce the sample capacitance, such as reverse biasing a diode are not available to our experiments. The reason is that large reverse biases would cause tunneling of electrons/holes out of their respective quantum wells. Indeed we typically forward bias our samples to provide the smallest electric field possible while maintaining a field strong enough to collect charges.

In our samples, which were double quantum wells embedded in a p-i-n diode, the sample capacitance was very large due to the surface area of our diodes. Thus we estimated our sample capacitance to be on the order of 1μF leaving our current source with a source impedance $\sim$ 5 kOhm. In a traditional transimpedence amplifier the noise gain $NG = 1 + R_{feedback}/R_{source}$with a 1MOhm feedback resistor for our sample would be on the order of 230. This noise gain completely dominates the Johnson and shot noise. The amplifier noise is given by $NG * V_{noiseamplifier}$ with $V_{noiseamplifier} \sim 5 - 10\frac{nV}{Hz^{.5}}$. In order to deal with this issue we implemented the bootstrapping scheme of [119] (An application note on the LTC6244 operational amplifier). This circuit makes use of an ultra-low voltage noise JFET $\sim .8\frac{nV}{Hz^{.5}}$ to “drop” this large sample capacitance across the gate-source voltage of the JFET. The feedback resistor is then looking back into the JFET capacitance, some parasitic capacitance and the op-amp capacitance $\sim$ 10pF. Thus our source impedance is converted into a current noise as

$$I_{cnoise} = V_{noise_{JFET}}/Z_{capacitance} = 150\frac{fA}{Hz^{.5}}. \tag{3.16}$$

This current noise is subsequently multiplied by the feedback resistor providing noise of $\sim 150\frac{nV}{Hz^{.5}}$. Effectively though, the amplifier voltage noise has been replaced with the JFET voltage noise providing a factor of $\sim$ 10 improvement. While not discussed here this approach also dramatically improves the amplifier bandwidth from $\sim$ 50kHz to $\sim$ 350kHz. The total noise of the amplifier can be calculated as:

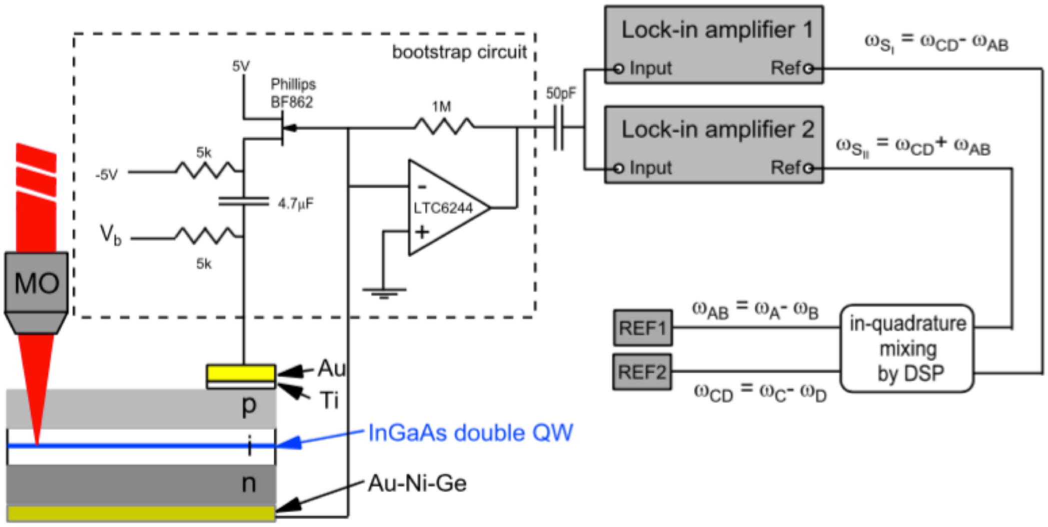

Figure 3.10: Our bootstrap implementation and other circuitry such as the digital signal processing. The circuit implementation makes use of a "bootstrap" design to isolate and deal with sample capacitance. Figure from [92].

$$V_{noise} = \sqrt{(I_{cnoise}R_F)^2 + (I_{shot}R_F)^2 + V^2_{Johnson,Rf}} * BW \tag{3.17}$$

where I_{shot} is the shot noise of the photocurrent, $V_{Johnson,Rf}$ is the feedback resistor and BW is the measurement bandwidth. Of course this is not the total noise in the system, this is merely the circuitry noise generated prior to the modulation discussed above. A full noise calculation should take into account the $\frac{1}{f}$ noise of the lock-in amplifiers, the interferometers, the delay between signal and reference and dark current.

Another issue that arises is that of population decay. Standard FWM techniques probe the lifetime of a quantum state by measuring S_I spectra as a function of T. In a diode with photocurrent readout, this approach is only sensitive to the charge lifetime in the device (i.e. the device bandwidth) and not the actual quantum state lifetime.

3.0.7 Demonstration of MDCS using a Photocurrent Readout

In order to demonstrate our technique we measured FWM signal from $\mathrm{In}_{0.2}\mathrm{Ga}_{0.8}\mathrm{As}/\mathrm{GaAs}$ double quantum wells embedded in a p-i-n diode. The sample consists of a 4.8nm thick QW and a 8nm thick QW separated by a 4nm barrier. A bottom contact of Au-Ni-Ge was deposited on the n-doped substrate while a top contact consisting of 5nm Ti and 200nm Au was deposited on the top. The quantum well resonances were recorded at $\sim$ 920nm and $\sim$ 950nm. This made simultaneous excitation of both quantum wells impossible with our laser bandwidth of $\sim$ 10nm. We excited the lowest energy excitonic quantum well structure with a total power of 250μ W and a $\sim 5\mu$m spot. Our photocurrent signal was split into two and fed into two lock-in amplifiers as shown in Fig. 3.10.

After recording the non-rephasing and rephasing signals as a function of interpulse delay τ, t the $S_I(\tau, T = 200, t)$ and $S_{II}(\tau, T = 200, t)$ signals were measured and fast Fourier transformed to generate a MDCS spectra as shown in Fig. 3.11. The absolute spectra (Fig. 3.11 a-c) show a slightly elongated peak on the diagonal. The real spectra (Fig. 3.11 b-d) are phased by removing the phase offset at $(\tau = 0, T = 200, t = 0)$ from the spectra. The spectra show a typical absorptive spectrum.

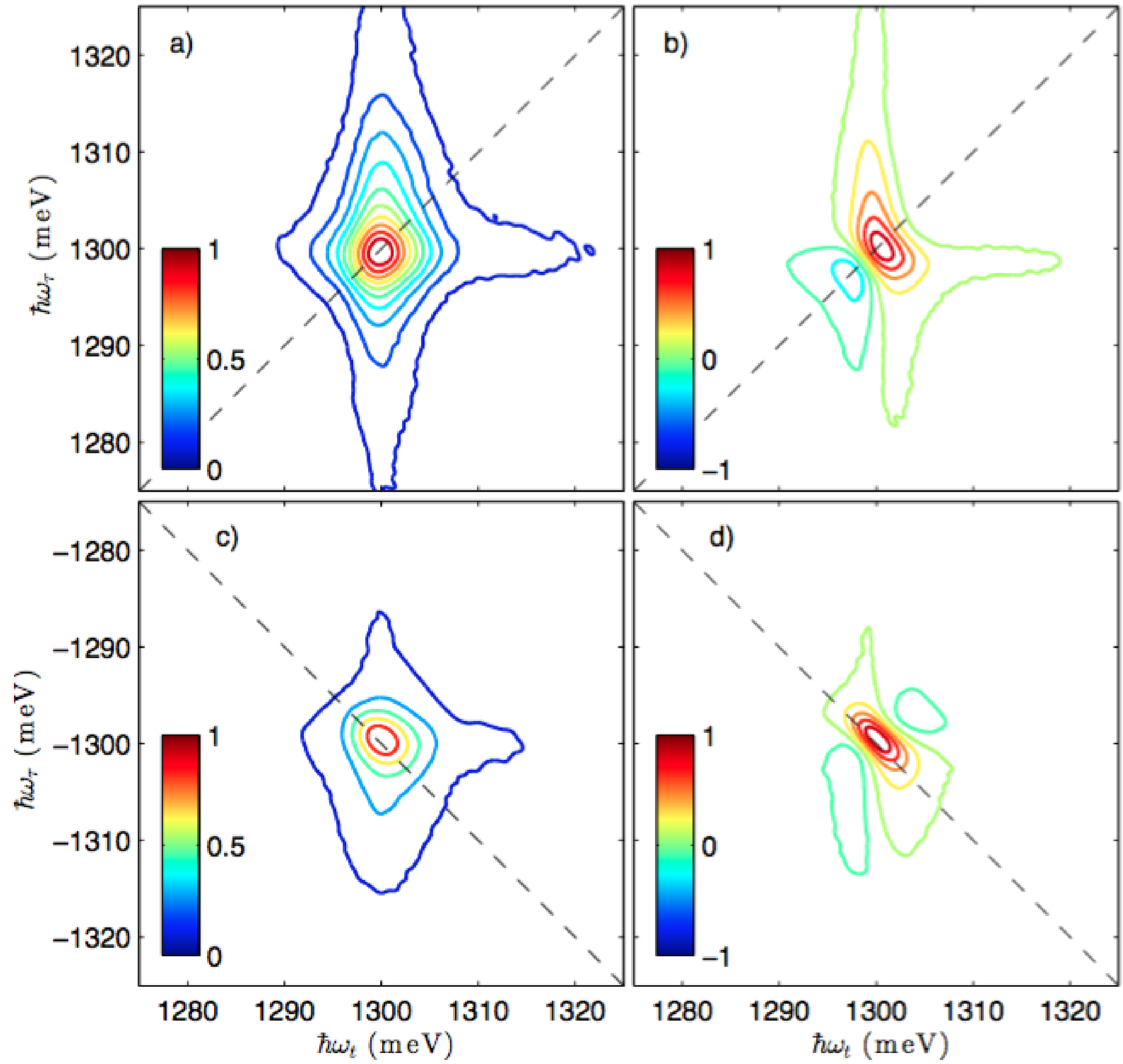

Figure 3.11: Photocurrent detected MDCS spectra plotted as a function of $\hbar\omega_{tau}$ (y-axis) and $\hbar\omega_t$ the (x-axis). a). Absolute value of non-rephasing $S_{II}(\hbar\omega_\tau, T = 200, \hbar\omega_t)$. b).The real part of the $S_{II}(\hbar\omega_\tau, T = 200, \hbar\omega_t)$ spectra. c). Absolute value of non-rephasing $S_I(\hbar\omega_\tau, T = 200, \hbar\omega_t)$. d).The real part of the $S_I(\hbar\omega_\tau, T = 200, \hbar\omega_t)$ spectra.

Chapter 4

Theoretical Modeling of Collective Systems

Many systems are composed of indistinguishable constituents, however discussing these individual constituents is not always helpful to understanding all of the dynamics or properties of interest. In such systems the individual constituents are said to be behaving *collectively*. Collective dynamics are a hallmark of both cold atom and many-body systems, and with appropriate engineering these dynamics are increasingly accessible with solid-state superconducting circuits.

In atomic systems, collective dynamics can be achieved via confining a gas of atoms to a region smaller than an optical wavelength. This is known as the Lamb-Dicke regime [120–124] and it achieves uniform coupling of each atom to the electromagnetic field in an indistinguishable fashion with respect to photon emission. This coupling leads to superradiance in which dipole correlations build up as an initially excited system begins to spontaneously decay. This collective effect results in an enhanced spontaneous emission rate that is N times faster than the spontaneous emission rate of a free-space atom [123]. The Dicke model serves as a basis for understanding many collective systems, and the advent of atom-cooling has opened up new regimes of collective physics [125–127] including a previously unobserved Dicke phase transition [128].

In semiconductors, the band edge optical response is dominated by excitonic physics. The exciton is a composite boson characterized by the Coulomb binding of an electron-hole pair. The spectrum of the exciton manifests as a series of hydrogenic transitions below the single particle band-gap energy. The Coulomb interaction also enhances the band-to-band transition strength by ensuring that the exciton is a *collective* quasiparticle. The collective behavior is best understood in the relative coordinate of the bound electron-hole pair where the hydrogenic wave function of an exciton is coherently distributed across the the band edge electron-hole states. By distributing excitations across many electron-holes states, the Coulomb interaction allows excitons to manifest collective attributes such as an enhanced dipole transition moment relative to that of just a single electron-hole transition moment as well as a superradiant decay in thin-film semiconductors [129–132].

Superconducting circuits have slowly built up the capability to create artificial microwave-regime two level systems through Josephenson junctions [133, 134]. By carefully engineering these qubits to be identical, collective dynamics have recently been achieved [135, 136].

Here we discuss collective coherent states composed of constituent two level systems. This presentation is motivated in two ways. First, the excitons and exciton-polaritons studied in this thesis constitute collective quasiparticles. Therefore we wish to establish a clear relationship between collective coherent states and excitons. Additionally, a satisfactory description of wave-mixing in a collective system, which explains the role of level truncation, many-body interactions and the collective dipole has not been established. This description should be related to both fermionic and bosonic models of exciton dynamics. Towards this end, we have extended existing theory to consider wave-mixing experiments in collective systems of constituent two-level systems. Our model can incorporate collective dipoles, explain how truncation can qualitatively match experiments and incorporate many-body interactions through a simple counting argument. We discuss certain limits to relate the model to fermionic and bosonic models of exciton dynamics. The issue of level truncation relates to the inability of a calculation to account for all states in a semiconductor due to the sheer number of them and causes truncation error in calculations. Importantly, we discuss physics beyond level truncation and how we expect our model can account for many-body effects that have previously been put in by hand.

Our discussion is organized as follows.

- We consider a simple two-level system driven by a pulse of electromagnetic radiation. We calculate the excitation properties of the system and consider effects that cause a variance in the polarization after the pulse. The causes of polarization variance include non-uniform excitation for an ensemble of two-level systems as well as statistical uncertainty.

- Secondly, we consider simple product states and discuss the two-level system picture for semiconductor excitons. We explicitly consider the averaging process in a product state basis and discuss the effect of the product basis on the dipole moment and wavefunctions.

- Thirdly, using the results from the previous section we develop a simplified excitation basis for two two-level systems. This exercise is performed in order to provide physical intuition for the process discussed in the fourth section.

- Fourthly, we develop a generalized excitation basis after an excitation pulse for the exciton. We relate these states to the coherent collective states of atomic physics and discuss limits in which basis appears “fermionic” versus “bosonic”.

- Fifthly, we explicitly consider a transformation of fermionic operators to bosonic operators for a collective ensemble. We arrive at a single-mode Hamiltonian that is equivalent to the single-mode bosonic-exciton Hamiltonian derived from the Wannier approximation in semiconductors. This Hamiltonian is functionally equivalent to the Dicke Hamiltonian for a collective ensemble of atoms, however it is has been modified to ensure the crystal vacuum of a semiconductor is correctly represented. We explicitly calculate the enhanced dipole moment in our model and then provide an estimate for $\frac{N}{A}$ the density of electrons that the exciton is distributed over.

- Sixthly, we consider the perturbative excitation of our model and find that the density matrix is non-perturbative in pulse-areas as the number of states becomes large. The density matrix is found to be non-perturbative despite the polarization remaining in a perturbative regime. We further find that the perturbative polarization can be correctly calculated from an expansion of the first few non-perturbative density matrix elements. We resolve this issue analytically and find that symmetry in the excitation ladder allows higher lying density matrix to provide the same polarization as the first few density matrix elements. This symmetry results in what is effectively a many-term polynomial approximating a few-term polynomial over a finite regime. Several limits are taken in order to resolve this and provide a physical intuition as to what states are actually contributing to the polarization.

- Seventhly, we numerically evaluate the polarization in the presence of many-body interactions. Our many-body model is motivated by simple counting arguments. We find that the results of our numerical calculation in combination with our analytical results justifies using a truncated level scheme in order to model collective systems.

- Finally, we consider a second interference effect that arises due to the methods used to measure wave-mixing in collective systems. We attempt to motivate how the previous calculations will differ from measurements by considering this process.

4.0.1 Pulsed Excitation of Ensembles of Two-Level Systems

Consider a initially unexcited $N = 1$ two-level system (TLS), where N represents the size of the ensemble, driven by a pulsed electromagnetic field, specifically a laser pulse of "short" duration. Here "short" means that the pulse interacts with the system in an impulsive limit. We calculate the excitation probability from the pulse area theorem, which accounts for the changing Rabi frequency $\Omega(t) = \frac{\mu}{\hbar}E(t)$, where $E(t)$ is the pulse amplitude and μ is the transition dipole moment, throughout the pulse duration. This approach leads to the concept of a phase known as the pulse area

$$\theta = \int_{t'} \Omega(t')dt'. \tag{4.1}$$

Since the Rabi frequency describes the rate at which the TLS evolves from unexcited to excited and vice versa, this phase determines the probability of finding the TLS excited after the driving pulse has passed. The density matrix, ρ, immediately after this driving pulse is [137],

$$\rho = \begin{pmatrix} \cos\left(\frac{\theta}{2}\right)^2 & e^{i\phi}\cos\left(\frac{\theta}{2}\right)\sin\left(\frac{\theta}{2}\right) \\ e^{-i\phi}\cos\left(\frac{\theta}{2}\right)\sin\left(\frac{\theta}{2}\right) & \sin\left(\frac{\theta}{2}\right)^2 \end{pmatrix}. \tag{4.2}$$

The probability of the single TLS being excited is $P_e = \sin\left(\frac{\theta}{2}\right)^2$, while the probability of the TLS remaining unexcited is $P_g = 1 - P_e$. Immediately after the driving pulse the TLS will have a polarization $p = \mathrm{tr}(\hat{\rho}\hat{\mu})$ and a phase ϕ determined from the incident radiation pulse. If the ensemble is rescaled to arbitrary N the macroscopic polarization is the average of these polarizations

$$P = N\langle p \rangle \tag{4.3}$$

as depicted in Fig. 4.1a for $N = 2$.

If each ensemble of TLS was excited non-uniformly, a variance in P will exist. This variance de-correlates the emitting dipoles and recovers the usual result that the response to driving radiation is determined by the response of the individual TLS in the ensemble (No collective effects). This variance can be understood to be creating an inhomogeneous distribution of polarization vectors. In atomic systems this variance can be caused by a relative phase across a spatially extended gas [122] while in excitonic systems this variance can be caused by disorder [131].

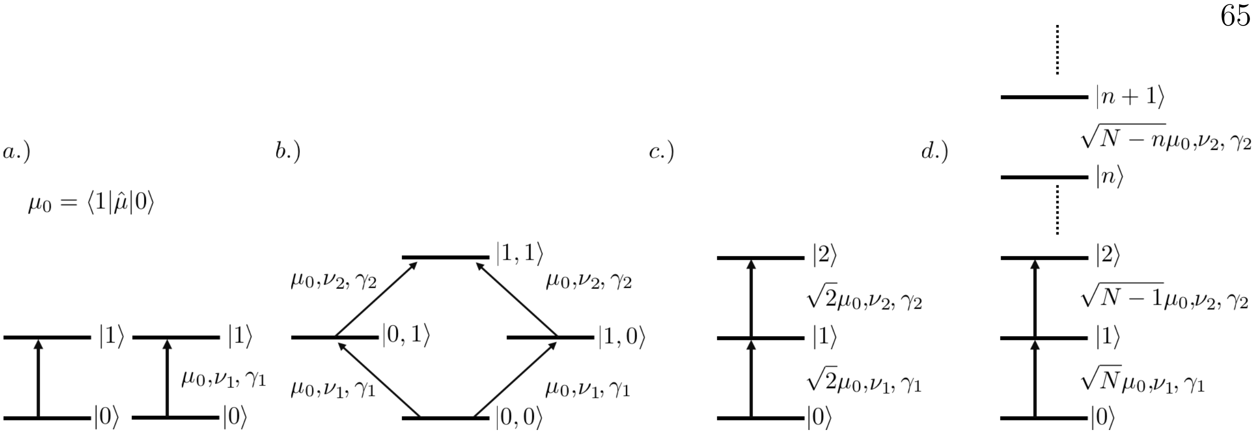

Figure 4.1: a.) Two independent TLS. b.) The product basis of two TLS. c.) An excitation-basis energy structure formed from two TLS. with excitation energy modified by the exciton binding energy. d.) An excitation-basis energy structure for all electron-hole transitions with excitation energy modified by the exciton binding energy.

However, in the limit that each TLS in the ensemble is excited uniformly collective effects appear and the concept of a collective Bloch vector becomes applicable [122, 137, 138]. The collective Bloch vector is the tip to tip addition of the Bloch vectors of the individual TLS that occurs when the vectors are the same amplitude and phase. The collective Bloch vector describes the state of the ensemble and not of an individual TLS. In this regime a statistical dispersion in how many TLS are excited appears due to the size of the ensemble itself. To understand this dispersion we consider the case where N is arbitrary and fixed and the field excites each TLS in the same way. This ensures the probability of any TLS becoming excited is the same. We then consider how many excitations exist in the ensemble. This situation is described by the binomial distribution $B(N,p)_n$ where $p = P_e$, with n representing the number of excitations in the ensemble after the pulse. Thus the probability of n excitations in an ensemble of N TLS after an excitation pulse (ignoring the phase ϕ) is

$$B(N, P_e)_n = \binom{N}{n}(P_e)^n(1-P_e)^{N-n}. \tag{4.4}$$

The binomial distribution tells us a number of things about the ensemble after being driven with a pulse. First, successive measurements with the same pulse area will map out an excitation distribution that is not the same as for the two level system with $N = 1$. Thus this distribution depends on the number of TLS. Secondly, the binomial coefficient calculates the number of ways in which the excitations can be distributed in the ensemble while providing no information about which TLS is excited. This is consistent with the TLS being indistinguishable.

4.0.2 Product Basis for Ensembles of Two-Level Systems

As a first attempt at building a model for an excitonic basis capturing the ensemble effects discussed earlier, we consider an approach that has previously been used to model many-body physics in semiconductors and atom ensembles. We consider product states $\rho = \rho_i \otimes \rho_j$ that exhibit no additional correlation [30]. To understand this basis we consider an ensemble of $N = 2$ as depicted in Fig. 4.1a-b. The Hamiltonian of each TLS is described by matrix H_i where ω_i is the transition energy of the ith system. A Hilbert transformation $H_{4,4} = H_{2,2} \otimes I_{2,2} + I_{2,2} \otimes H_{2,2}$, where $I_{x,x}$ is the identity matrix of size x, maps the two TLS into a combined product basis $|\psi_i\rangle|\psi_j\rangle$. The resulting Hamiltonian is

$$\mathbf{H} = \begin{pmatrix} 0 & 0 & 0 & 0 \\ 0 & \hbar\omega_i & 0 & 0 \\ 0 & 0 & \hbar\omega_j & 0 \\ 0 & 0 & 0 & \hbar\omega_i + \hbar\omega_j \end{pmatrix}. \tag{4.5}$$

The product basis conserves the number of states and is completely equivalent to two non-interacting TLS. An advantage of this picture is it easily allows the inclusion of interactions as has been recently demonstrated for Rydberg physics [126]. This process can be generalized to explicitly include an ensemble of size N [137].

This model type was introduced in phenomenological excitonic models [30, 42] to explain the biexciton, a molecular binding of two excitons that the semiconductor Bloch equations could not account for at the time [139–141]. In this case the ith and jth system represented oppositely polarized and thus distinguishable excitons. Many-body interactions are introduced by modifying the relative dephasing rates and energies of the transitions. The ensemble response was then that of Fig. 4.1b, averaged over N TLS. In the absence of an interaction energy this model effectively truncates to the first excited manifold. This transformation and truncation procedure has become extremely common in modeling the many-body physics of excitons [30, 46, 47, 79, 142–148]. Despite being a flawed model (as will be discussed), this picture remains incredibly useful and qualitatively calculates many of the correct results. The model we develop can be considered as a generalization of this phenomenological model after transforming into an excitation basis.

In such models, which are no longer just used to describe polarization effects, the inclusion of a many-body interaction term allows the doubly-excited state $|\psi_i\rangle|\psi_j\rangle = |1\rangle|1\rangle$ to develop a resonant energy shift Δ and an additional dephasing term $\gamma\prime$. In the context of excitonic physics, this approach is convenient. For instance, in GaAs only transition energies near the bandgap $K_x = 0$ need to be considered due to the large effective mass of the exciton. This approximation treats the bandgap as a transition between the $J_z = \pm\frac{1}{2}$ states in the conduction band and the $J_z = \pm\frac{1}{2}$(LH) and $J_z = \pm\frac{3}{2}$(HH) in the valence band. In the context of this model, the bandgap energy is corrected by the exciton binding energy. In this way the energy $\hbar\omega_k$ is simply the exciton transition energy (Eq. 1.9). The energy shifts Δ and γ then represent the two-body interactions manifesting as EID and EIS in the ensemble of bound electron-holes.

By considering the ΔJ_z transitions a clear two-level transition is established between the HH/LH and conduction band. The Coulomb interaction between the electron and hole is then considered to modify this transition energy by the exciton binding energy. While this two-level transition exists, this picture provides an unphysical and confusing picture of the exciton. At issue is that this model disregards the exciton as a coherent superposition of electron-hole states. It thus does not capture that the exciton transition dipole is larger than that of an electron-hole pair by M the number of unit cells [17, 129]. Thus a significant, flaw of this model is that 1.) The exciton should be a coherent superposition of the available states after a ΔJ_z transition. 2.) A collective dipole should be readily apparent.

Additionally, there are truncation-averaging issues with this model for excitonic physics. One issue is that in excitonic models the product basis describes an ensemble of two-level systems in a diamond structure. No attempt was made to modify the ensemble averaging process. In particular it is often assumed that $P \sim N\langle p\rangle$ when in fact this is only true for ground manifold - first excitation manifold P_{0-1} transitions. For transitions between the first excited manifold and doubly excited manifold the polarization should be averaged $P_{1-2} \sim N(N-1)\langle p\rangle$. The total polarization should then be the sum of these two polarizations. This can be simply argued based on the binomial coefficient. The confusion exists because this model encourages thinking of an ensemble ($N \gg 2$) as a two-level or four-level system. For the unphysical case that $N = 2$ both P_{0-1} and P_{0-2} become averaged over the same effective factor 2 and thus this effect is immaterial. The extent to which this truncation and averaging modifies the quantum pathway interference in coherent spectroscopy has not been explored and is addressed in this chapter. Our model can correctly account for these averaging issues as well as calculate the enhanced dipole moment of a collective system.

4.1 Excitation Basis and Excitonic Coherent States

4.1.1 An Excitation Basis for an Ensemble with $N = 2$

The product basis discussion of the previous section provides an immediate path to create an excitation basis for the exciton. Conceptually, this is important as the exciton should represent the quanta of the polarization field in a manner analogous to the Fock states of light [6, 137]. For a system with $N = 2$ the product basis gave the Hamiltonian (Eq. 4.5) with states $|\psi_i\rangle|\psi_j\rangle$. With identical TLS there are four states, two of which are degenerate with energy $\hbar\omega_i = \hbar\omega_j$. If these systems are indistinguishable then these states are entangled and the product basis does not accurately represent the system. In the excitation basis two manifolds of states are found. The first manifold of states consists of radiant states depicted in Fig. 4.1c and are

$$\begin{aligned}
|n=0\rangle &= |0\rangle_i|0\rangle_j \\
|n=1\rangle &= \frac{1}{\sqrt{2}}[|0\rangle_i|1\rangle_j + |1\rangle_i|0\rangle_j] \\
|n=2\rangle &= |1\rangle_i|1\rangle_j.
\end{aligned} \tag{4.6}$$

The other manifold consists of a sub-radiant state

$$|n=1\rangle = \frac{1}{\sqrt{2}}[|0\rangle_i|1\rangle_j - |1\rangle_i|0\rangle_j]. \tag{4.7}$$

It is worth noting that dipole operators allow transitions between adjacent states within a manifold, but do not allow transitions between manifolds. The fact that the ground state is an element of the radiant manifold therefore justifies its name [137]. Importantly, from Eq. 4.6 and $|n=1\rangle$ it is clear that a single excitation is shared between the different TLS. This begins to resemble the wavefunctions created by the excitonic operators Eq. 1.12. After exciting this system with a pulse the density matrix element of ρ_{ee} is determined by Eq. 4.4.

If the original TLS represent the unbound-electron-hole states at specific k then these transitions are between $|0\rangle$, the crystal vacuum (empty conduction band and full valence band), and the state $a_k^\dagger b_{k'}^\dagger|0\rangle$ where $a^\dagger/b^\dagger$ are the electron/hole raising operators. Then, this excitation basis recaptures the coherent superposition of electron-hole states at $n=1$ which make up the exciton. However, this basis still requires a correction not treated here in order to be fully correct. Because we are considering TLS and neglecting the Coulomb interaction the superposition of states is not weighted by the hydrogenic wavefunction from Eq. 1.12. Fortunately, if the exciton binding energy is then used to correct the $|n\rangle$ basis relative to the bandgap transition energy then these states can model the exciton. Therefore, we have provided a complete description for $N=2$ and in the next section we will generalize this to N TLS.

4.1.2 An Excitation Basis for a Collective Ensemble of Two Level Systems

As previously presented, after an exciting pulse there exists some probability of n excitations in an ensemble of TLS. Therefore, the resulting state of the system is a collective coherent state. These collective coherent states have previously been worked out by Arrechi [137] as an atomic analog to the Glauber-coherent states for light. Since we are interested in the optical response after a pulse, we ignore the sub-radiant states. The binomial distribution (Eq. 4.4) correctly describes the number of excitations and must also describe the density matrix elements of the collective system.

Remembering that the density matrix is $\rho = |\psi\rangle\langle\psi|$ a density matrix for the entire ensemble can be written by using Eq. 4.4 and Eq. 4.2. Each density matrix element after a pulse with pulse area θ can be written:

$$\rho_{n,n'} = |n\rangle\langle n^{'}| = \binom{N}{n}^{1/2}\binom{N}{n^{'}}^{1/2}\cos\left(\frac{\theta}{2}\right)^{2N-n-n^{'}}\sin\left(\frac{\theta}{2}\right)^{n+n^{'}}e^{i(n^{'}-n)}. \tag{4.8}$$

In an excitation basis for an ensemble with N TLS each diagonal element corresponds to the probability of some number of excitations. These excitations are distributed in an indistinguishable way amongst the different TLS in the ensemble, indicating that there is superposition of TLS as in Eq. 4.6. This is the N element density matrix extension to Eq. 4.6. The off-diagonal elements, $n \neq n^{'}$, correspond to optical coherences between the different diagonal elements. From these results as $N \to \infty$ the possible number of excitations goes to infinity and the energy levels of the system resemble that of a harmonic oscillator. The harmonic oscillator is the well known energy spectrum of a bosonic system and this relationship maps a collective ensemble of two-level fermions into a bosonic basis as shown in Fig. 4.1d. In contrast the system is most fermionic for $N = 1$ when only one excitation is allowed.

In the following section we formally develop a Hamiltonian capable of describing a system possessing these statistics and arriving at these density matrix elements.

4.1.3 The Dicke Hamiltonian and Collective Operators

The model so far has been argued on the basis of statistics in an ensemble of TLS and in analogy with the coherent states of atomic physics. In particular, since we are explicitly considering GaAs quantum wells and the exciton has a large mass, only the transitions near $K_X = 0$ need to be considered. It is then reasonable to introduce the Dicke model as an effective model of the exciton. As we will show, this model can be reduced to the single-mode exciton model at $K_X = 0$. The Dicke Hamiltonian is the sum of all of the two-level system Hamiltonians

$$H = \hbar\omega_a \frac{N}{2} + \sum_{i=1}^{N} \frac{\hbar\omega_a}{2}\sigma_{z,i} + \sum_{i=1}^{N} \hbar g(E^* \sigma_i^- + \sigma_i^\dagger E) \tag{4.9}$$

In this Hamiltonian $\sigma_{z,i}$ is the Pauli spin matrix of the ith electron-hole transition, $\hbar g$ is the dipole coupling strength of an individual TLS, E^*, E correspond to the electromagnetic field components, and $\sigma_i^\pm$ corresponds to the raising and lowering operator of the ith TLS. The constant energy term has been included to provide an offset energy appropriate for semiconductors. Because this Hamiltonian is expressed in terms of Pauli operators, this basis is fermionic. The collective operators of the ensemble can be defined as

$$\begin{aligned} S_z &= \sum_{i=1}^{N} \frac{1}{2}\sigma_{z,i} \\ S_+ &= \sum_{i=1}^{N} \sigma_i^\dagger \\ S_- &= \sum_{i=1}^{N} \sigma_i^- . \end{aligned} \tag{4.10}$$

There exists a basis transformation developed by Holstein and Primakoff [149, 150] that maps the Pauli matrices into a bosonic basis. Similiar transformations have been derived for both Frenkel and Wannier excitons [151–153], and for Frenkel excitons these transformations directly reduce to the Holstein-Primakoff transformation [152]. The sum of operators in Eq. 4.9 can be re-represented as collective operators. Applying the Holstein-Primakoff transformation maps the mode into a bosonic basis, which is indexed by excitation level $n = b^\dagger b$. This transformation is defined by:

$$S_- = (N - b^\dagger b)^{1/2} b, \tag{4.11}$$

$$S_+ = b^\dagger (N - b^\dagger b)^{1/2}, \tag{4.12}$$

$$S_z = b^\dagger b - \frac{N}{2}, \tag{4.13}$$

where b and $b^\dagger$ are bosonic raising and lowering operators for a collective ensemble of TLS. In the perturbative limit, the Holstein Primakoff transformation may be expanded based on the degree of excitation $b^\dagger b \ll N$. Applying this limit, these operators become:

$$S_- = (1 - \frac{b^\dagger b}{N})^{1/2} b\sqrt{N}, \sim b\sqrt{N} \tag{4.14}$$

$$S_+ = b^\dagger \sqrt{N} (1 - \frac{b^\dagger b}{N})^{1/2} \sim b^\dagger \sqrt{N}, \tag{4.15}$$

$$S_z = b^\dagger b - \frac{N}{2}. \tag{4.16}$$

The error in this expansion scales as $\frac{b^\dagger b}{N}$ where $b^\dagger b$ defines the number of excitations in the ensemble of TLS. This error provides a similar relation as Eq. 1.13, the bosonic operator error derived from the Wannier approximation. The Dicke Hamiltonian in the bosonic basis is then

$$H = \hbar\omega_a b^\dagger b + \hbar g \sqrt{N} (a^\dagger b + b^\dagger a). \tag{4.17}$$

This bosonization procedure results in an enhanced ensemble-electromagnetic field coupling strength $g\sqrt{N}$ which represents a collective Rabi frequency [154–157]. This dipole moment can be many orders of magnitude larger than the dipole moment of a single TLS leading to the concept of a "giant oscillator strength"[17, 158]. Note that this equation is equivalent to the single-mode form of Eq. 1.17. Therefore the Rabi frequency g_0 of Eq.

1.17 is a collective dipole that scales with $\sim g\sqrt{N}$. In semiconductor quantum wells there is no ability to change N. In order to know the collective enhancement of the exciton dipole moment, it must be calculated and then compared to a measured saturation density. To estimate N we consider a QW $1S$ exciton [17] and take the Fourier transform of Eq. 1.7 to find a wavefunction in relative k-space

$$FT[\phi_n(\vec{r})] = \phi(\vec{k_e}, \vec{k_h})_{n=1} = \frac{2}{a_0^2\left(\frac{1}{a_0^2} + \vec{l}^2\right)^{3/2}}. \tag{4.18}$$

Here a_0 is the exciton Bohr radius and $\vec{l} = \frac{m_h}{M}\vec{k_e} - \frac{m_e}{M}\vec{k_h}$, where $\vec{k_e}(\vec{k_h})$ are electron(hole) wavevectors and $M = m_e + m_h$. The plane wave decomposition of this wavefunction describes the exciton in relative k-space where it is distributed around multiple k-modes. Since we are considering the bandedge exciton in GaAs $K_x = 0$ which makes $k_e = -k_h$. Then the density of electron-hole states can be calculated by:

$$\frac{N}{A} = \langle k^2 \rangle = \int_0^\infty \phi_1(\vec{k_e}, \vec{k_h})\phi_1^*(\vec{k_e}, \vec{k_h})_{n=1} k^2 dk \tag{4.19}$$

$$= (\frac{1}{a_0})^2. \tag{4.20}$$

For the case of GaAs this value is $\sim 10^{12} cm^{-2}$ which agrees with experimentally measured values of the oscillator saturation density [158]. This enhanced dipole strength is graphically explained in Fig. 4.2a-b. An exciton with center of mass wavevector $\vec{K}_X \sim 0$ is distributed across many electron-hole pairs by the Fourier transform of the hydrogenic wavefunction. The distribution across many electron-hole pairs causes a collective enhancement of the exciton dipole with respect to a single electron-hole transition. The large effective mass of an exciton in GaAs ensures that $\vec{K}_X = 0$.

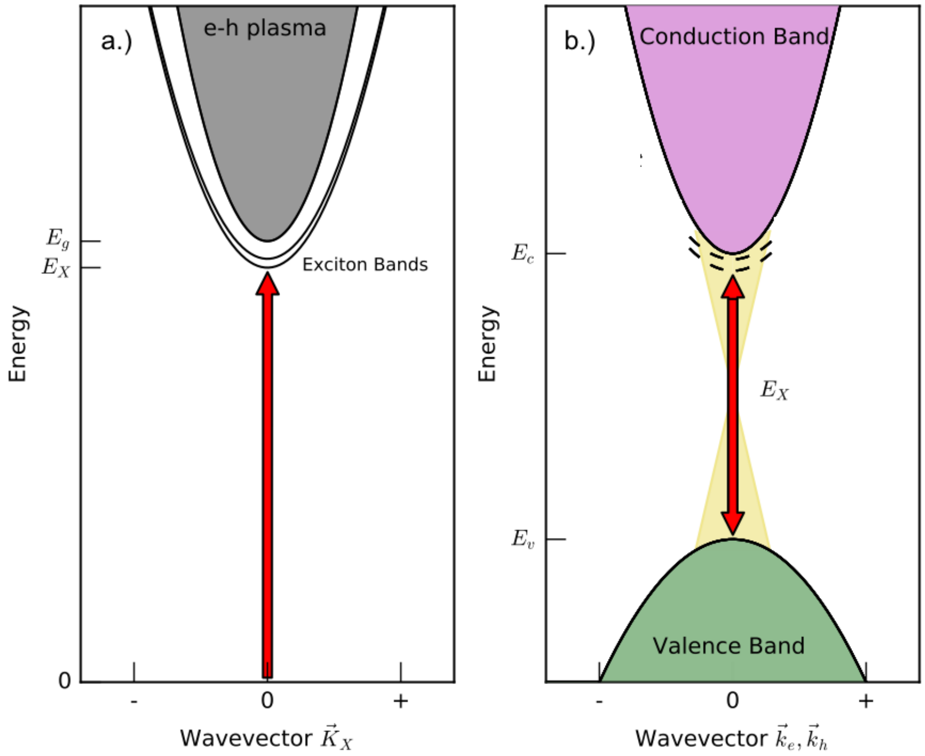

Figure 4.2: a.) Exciton picture of a semiconductor. The exciton exists as a bound state below the electron-hole plasma. Optical excitation must occur at $K_x \sim 0$. b.) Electron-hole picture of a semiconductor. The exciton absorption occurs below the conduction band (dashed energy levels). For an exciton with center of mass wavevector $K_x \sim 0$ there exists a range of electron-holes that contribute to the excitonic wavefunction as indicated by the yellow distribution.

4.2 Perturbative Evaluation of The Effective Exciton Model

In the preceding sections, we established the two-level transitions in a semiconductor as being between the valence and conduction band $k_{e,h}$ states. Unfortunately, in real experiments the Coulomb interaction cannot be turned off and observing the Rabi flopping of a single electron-hole transition is inaccessible, although signatures of inversion have [159] been observed. Part of the issue is that at higher excitation density many-body interactions in the form of Coulomb screening may convert the ensemble back into an e-h plasma, effectively removing the exciton dynamics. As a result, most experiments studying the exciton are conducted in a perturbative optical regime. We therefore attempt to discuss the excitation model in a perturbative regime and learn that while the optical response is perturbative the density matrix elements of the excitation model are highly non-perturbative.

In order to demonstrate this confusing situation we make use of a collective excitonic Bloch vector defined in analogy with the collective Bloch vectors of the Dicke model. The collective Bloch vector can calculate the polarization at any excitation level except in the limit that the pulse area $\theta \to \pi$. In the limit of a rotation that is infinitesimally close to π the rotation operator becomes singular. The collective polarization can be calculated simply by considering the polarization of a single TLS by Eq. 4.2 with $p = \mu_0 \sin\frac{\theta}{2}\cos\frac{\theta}{2}e^{i\phi} = \frac{1}{2}\mu_0 \sin\theta e^{i\phi}$. The polarization of the ensemble can then be calculated by adding each TLS polarization together to form a collective Bloch polarization-vector $\vec{P} = \frac{N}{2}\sin\theta e^{i\phi}$. The polarization vector $\vec{P}$ can be perturbatively expanded about $\theta = 0$, providing a perturbative expansion that scales in odd orders of the pulse area. The polarization scaling with odd orders of the electric field is consistent with the optical susceptibility in centrosymmetric media such as 100 grown GaAs. In this example the polarization transitions from linear to non-linear at a pulse area $\theta \sim .2$ as shown in Fig. 4.3a. The first few expansions are plotted up to third order in Fig. 4.3a. At the same time we make use of the identity $P = \mathrm{tr}(\hat{\mu}\rho)$ to perturbatively expand the polarization from the density matrix elements of Eq. 4.8. From these calculations we are able to correctly calculate the polarization response finding excellent agreement with the expansion of the collective Bloch vector as shown in Fig. 4.3a. Curiously, however, we find that the density matrix elements that calculate the polarization are non-perturbative and are zero for most pulse areas as shown in Fig. 4.3b and are therefore non-perturbative. We also find that this issue becomes even more problematic as, N, the number of states grows.

Essentially we have found that the Taylor expansion gives the right answer for the wrong reasons. This puzzle can be resolved by realizing that the although the perturbative expansion of the first few density matrix results in a dramatic overshoot of lowest-lying den-

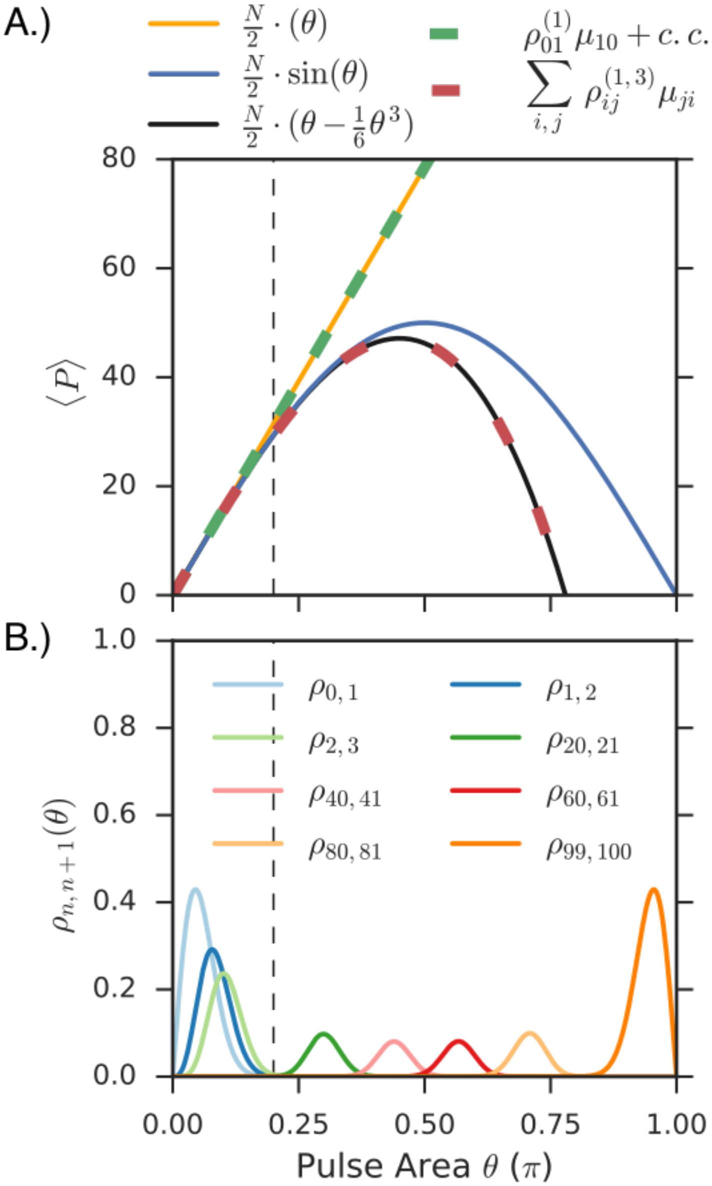

Figure 4.3: A.) Polarization as a function of pulse area for N = 100. Solid curves were calculated using the expansion of $\vec{P} = \frac{N}{2}\sin\theta e^{i\phi}$. Dashed curves represent the polarization calculated using the perturbative expansion of the density matrix. The dashed black line at $\theta \leq .2$ represents approximately where the linear polarization ends and higher order terms are needed. B.) Selected radiating offdiagonal density matrix elements distributed over pulse area θ for $N = 100$. In the linear regime the matrix elements $\rho_{0,1}$ and $\rho_{1,0}$ are non-perturbatively zero.

sity matrix elements, the overshoot is almost perfectly compensated by an equally dramatic undershoot in the perturbative expansion of matrix elements corresponding to higher-lying energies. The polarization resulting from the first few excited states is actually zero even though the response looks linear. This can be resolved by realizing the following. A polynomial with many terms can perfectly describe a line or a simple polynomial with few terms over a finite range. The expansion of the non-zero density matrix elements at a given pulse area results in such a polynomial. Due to the symmetry of the excitation basis, we are able to show that this polynomial must exactly equal both the expansion of the first few terms of the density matrix (that are non-perturbatively zero) and the polarization calculated from the collective Bloch vector. Critically, this result allows us to explain how bosonic models which truncate at the first few excitation levels are able to calculate the qualitative response of the exciton. Importantly, this model may allow the resolution of many-body induced dephasing that has so far been put in by hand. Few-level models are essentially equivalent to truncating the full excitation ladder. This truncation provides no mechanism for power-dependent dephasing after the first pulse in a four-wave mixing experiment. However, such effects have been seen in previous FWM experiments [31]. Fortunately, with an excitation basis that encapsulates all levels this effect is straightforward to understand. The dephasing after the first pulse is caused by dephasing at the nth excitation manifold, varying the power of the first pulse makes the experiment sensitive to dephasing at the $n^{'} \neq n$ manifold. Few level/truncated models completely miss this effect because they incorrectly average the ensemble response and lack the phase space to evaluate the actual statistics of the model of which excitation induced dephasing is dependent.

4.2.1 Mathematics of the Perturbative Expansion of the Density Matrix

In this section we prove the above discussion regarding how to calculate the polarization response and arrive at a our results for the density matrix elements. First we remind the reader of two mathematical theorems that we will refer to.

Theorem 1. ***Uniqueness Theorem for a Taylor Series****: The Taylor series of a func-*

tion $f(x)$ about a point x_0, if it exists, is unique. Therefore, there is only one power series of the form $\sum_{n=0}^{\infty} f_n(x-x_0)^n$ which converges to $f(x)$.

Theorem 2. ***Product of two Convergent Series**: Given two convergent series $\sum_n a_n x^n$ and $\sum_n b_n x^n$ expanded about the same point, the product of these two series is also a convergent series i.e. $\sum_n a_n x^n \cdot \sum_n b_n x^n = \sum_n c_n x^n$*

Definition 4.2.1. ***Density Matrix Expansion*** The general form of the density matrix after a pulse is Eq. 4.8. A convergent series can be written for $\sin(x)^q$ and $\cos(x)^q$ for $q > 0$. We therefore make use of the product-convergent series theorem to write the pulse area expansion for the density matrix elements as:

$$\rho_{n,n'} = \sum_{k=0}^{\infty} c_{n,n',k}\theta^k \tag{4.21}$$

where we are neglecting the terms arising from the azimuthal angle ϕ.

4.2.2 The Perturbative Polarization

This term may be Taylor-Series expanded to find a polarization in powers of the applied pulse area θ. This series expansion has only terms with odd powers in pulse area. We treat this expansion as a sum of terms

$$P = \frac{N}{2}\sum_{k=0}^{\infty} p^{(k)}. \tag{4.22}$$

In spectroscopy n-wave mixing results in the selection of the polarization to the $p^{(n)}$ term.

4.2.2.1 Derivation of $p^{(k)}$

The polarization is

$$P = tr(\hat{\rho}\hat{\mu}) = \sum_{i,j} \rho_{i,j}\mu_{j,i}\delta_{i,j=i\pm 1}. \tag{4.23}$$

Here the δ describes dipole available transitions in the ladder of states. We substitute (Eq. 4.21) into (Eq. 4.23) to find the polarization is

$$P = \sum_{k=0}^{\infty} \theta^k \sum_{i,j} c_{i,j,k}\mu_{j,i}\delta_{i,j=i\pm 1}. \tag{4.24}$$

Using Eq. 4.22 each $p^{(k)}$ term is found to be

$$\frac{N}{2} p^{(k)} = \theta^k \sum_{i,j} c_{i,j,k}\mu_{j,i}. \tag{4.25}$$

4.2.3 The Perturbative Excitation Level

A complete description of of our system should also discuss the excitation level/population. The polarization is but one component of the collective Bloch vector. Consequently, we find there is a similiar issue in calculating the excitation level as for the polarization. Namely, that the excitation level can be calculated from unphysical density matrix elements. From the Bloch sphere, the number of excitations is $\langle \hat{n} \rangle = \frac{N}{2}(1 - \cos\theta)$. This is the projection onto the z-coordinate of the Bloch sphere. We expand this equation to find

$$\langle \hat{n} \rangle = \frac{N}{2} \sum_{k=1}^{\infty} \langle \hat{n} \rangle^k. \tag{4.26}$$

From the density matrix the excitation level is

$$\langle n \rangle = tr(\hat{\rho}\hat{n}) = \sum_{i,j} \rho_{i,j} n_{j,i}\delta_{i,j}. \tag{4.27}$$

The $\delta_{i,j}$ arises because only on-diagonal elements of the density matrix determine the excitation level. We now substitute (Eq. 4.21) into the above equation to find a perturbative expansion of $\langle \hat{n} \rangle$ in powers of pulse area θ

$$\langle n \rangle = \sum_i \sum_k^{\infty} c_{i,i,k} \theta^k n_{i,i}. \tag{4.28}$$

We then reduce this equation and equate it to Eq. 4.26 to find the identity:

$$\frac{N}{2} \langle \hat{n} \rangle^{(k)} = \sum_i c_{i,i,k} \theta^k n_i \tag{4.29}$$

for each $\langle \hat{n} \rangle^{(k)}$.

4.2.4 Two-Wave Mixing

Now that we have the correct expressions to evaluate the wave-mixing process in a collective system, we consider the simplest wave mixing process i.e. two-wave mixing. Experimentally, two-wave mixing corresponds to linear absorption or photoluminescence and is the most straightforward wave mixing process to consider.

4.2.4.1 Collective 2-Wave Mixing: Polarization

The linear polarization response governs the two-wave mixing process that occurs when one driving field excites the sample and a second field is emitted. Using the dipole selection rules $\Delta n = \pm 1$ and (Eq. 4.25) we find the following identity

$$\frac{N}{2} p^{(1)} = \theta \sum_i c_{i,i\pm 1,1} \mu_{i,i\pm 1} \tag{4.30}$$

for the perturbative polarization. The coefficient $c_{i,i\pm 1,1}$ is proportional to $[\cos \frac{\theta}{2}]^{2N-n-n'}$ $[\sin \frac{\theta}{2}]^{n+n'}$ from (Eq. 4.8). The sum over i thus sums n from $n = 0$ to $n = N$ in steps of $\Delta n = 1$. However, the expansion of $c_{i,i\pm 1,1}$ will only have non-zero elements for $c_{0,1}$ and $c_{1,0}$. Simply put, the expansion of $c_{i,i\pm 1,1}$ only provides a linear expansion in θ if $i = n = 0$. From (4.30), the first order polarization is found to be:

$$\frac{N}{2} p^{(1)} = \theta (c_{0,1,1} \mu_{1,0} + c_{1,0,1} \mu_{0,1}). \tag{4.31}$$

The macroscopic first order polarization is calculated by the first term in the perturbative expansion of the first off-diagonal element of the density matrix.

4.2.4.2 2-Wave Mixing: Excitation Level

Additionally, an incoherent two-wave mixing process can be measured when the driving field creates a population in the ensemble. In such experiments the measured signal is then collected either as incoherent photoluminescence or photocurrent etc. We make use of the two relations $\langle\theta,\phi|\hat{n}|\theta,\phi\rangle = \frac{N}{2}(1-\cos\theta)$ and $\frac{N}{2}\langle\hat{n}\rangle^{(k)} = \sum_i c_{i,i,k}\theta^k n_i$ to determine the excitation level. It is evident from the expansion of $\cos\theta$ that only even orders in pulse area will contribute to the population response. The first of these even orders is $k = 2$ which describes two-wave mixing. We therefore calculate the excitation level

$$\frac{N}{2}\langle n\rangle^{(2)} = \theta^2 c_{1,1,2} \tag{4.32}$$

because $n_0 = 0$ and $n_1 = 1$. Thus incoherent two-wave mixing is calculated by the first non-zero term in the pulse area expansion of the first excited state.

4.2.5 Collective Wave Mixing General Discussion

As discussed earlier in this chapter, the first few terms of the density matrix expansion correctly calculate the polarization or excitation level response as we have just shown and as plotted in Fig. 4.3. This result is peculiar as these density matrix elements are identically zero for most pulse-areas for which they are being used to calculate the polarization or excitation level. In the following we consider two cases to understand what elements calculate polarization when these density matrix elements are not zero, and the other case to understand what density matrix elements actually contribute to the polarization for most pulse areas. The first case is that of non-zero density matrix elements at low excitation density. In this case we show that the higher order terms destructively interfere with the each other to make the polarization correctly determined by the first few terms in the density matrix expansion. We then consider the non-intuitive case where these density matrix elements are zero. In this case, we find that the wave-mixing process is well described by a multi-term polynomial that exactly approximates the polarization and excitation components of the Bloch vector.

To resolve the presented paradox we include the higher order terms in the polarization. These are the terms that are typically not included because of the truncation of P or n. The complete expression is

$$\begin{aligned} P^{(n)} = &\sum_{i,j} (\sum_{n=0}^{n} c_{i,j,n}\theta^{n})\mu_{j,i}\delta_{i,j=1\pm 1} + \\ &\sum_{i,j} (\sum_{k>n}^{\infty} c_{i,j,k}\theta^{k})\mu_{j,i}\delta_{i,j=1\pm 1} + \\ &\sum_{i,j} (\sum_{k>n}^{\infty} d_{i,j,k}\theta^{k})\mu_{j,i}\delta_{i,j=1\pm 1}. \end{aligned} \tag{4.33}$$

The above equation is (4.24) broken up into three pieces. The first term consists of density matrix elements with the apparently correct scaling in pulse area $\theta^{0..n}$. The second term consists of the terms typically truncated once the required order in pulse area have been arrived at. So these elements are the higher order $\theta^{n+1,n+1...}$ terms. The final term consists of the density matrix element terms not included in the polarization because $d_{i,j,n}$ is identically zero. These terms are "zero" because no terms exist with the right order in θ. We explicitly consider polarization signals, however we find similar arguments for the excitation level $\langle n \rangle$.

4.2.5.1 Interference of Higher Order Terms at Low Excitation Density

The first case is the case we expect because at low excitation density the first few density matrix elements are non-zero. Therefore these matrix elements contribute to the polarization or excitation level. Furthermore the perturbative expansion including higher order terms still works even if higher lying states are partially occupied. To see this effect we set the perturbative total polarization $P^{(n)}$ equal to the first term in (Eq. 4.33).

$$\begin{gathered}\sum_{i,j}(\sum_{k>n}^{n} c_{i,j,k}\theta^{k})\mu_{j,i}\delta_{i,j=1\pm1} = \\ -\sum_{i,j}(\sum_{k>n}^{n} d_{i,j,k}\theta^{k})\mu_{j,i}\delta_{i,j=1\pm1}\end{gathered} \tag{4.34}$$

Thus the higher order terms $m > n$ of the density matrix elements $c_{i,j,k}$ identically cancel with the higher order terms of $d_{i,j,k}$. This analysis shows that for polarization signals dominated by n-wave mixing the residual higher order $(n+1)$ terms from these first few density matrix elements destructively interfere with the $n+1$ terms from the higher lying density matrix elements. This result is only physical when N is small or when $\theta \to 0$ because the density matrix elements $c_{i,j}$ are non-perturbatively zero for most θ and large N. In the next section we arrive at the case that is physical in most situations.

4.2.5.2 Signal from the Higher Order Terms

The previous section showed that in some very specific situations the polarization calculated from the first few density matrix elements can be "physical" in the sense that these elements are non-zero. For most situations, particularly at large N, these density matrix elements are zero and thus are not actually contributing to the polarization. Therefore the "physics" must be that the polarization arises from non-zero density matrix elements. The sum of these dipole weighted density matrix elements must be adding together to provide a polarization that is *equivalent* to the polarization calculated from the expansion of the first few density matrix elements. We can show that this is true by setting the first two terms of Eq. 4.33 equal to zero since these terms must cancel each other in order for these density matrix elements to be zero.

$$\sum_{i,j}(\sum_{n=0}^{n} c_{i,j,n}\theta^{n})\mu_{j,i}\delta_{i,j=1\pm1} = \sum_{i,j}(\sum_{k>n}^{n} d_{i,j,k}\theta^{k})\mu_{j,i}\delta_{i,j=1\pm1}. \tag{4.35}$$

This description is non-intuitive as the term on the left does not have the same powers of θ as the term on the right. The interpretation is that there exists a valid range of θ for which the higher order terms cancel each other in just the right way to provide a slope that is identical to the terms on the left. For linear polarization, a highly nonlinear function can approximate a linear dependence on θ for an appropriate range of θ as seen in Fig. 4.3. Generalizing to arbitrary polarization order, a highly nonlinear many-term polynomial can approximate a less nonlinear fewer-term polynomial over an appropriate range of pulse area θ. Critically, it is this effect that explains how for a *few level* model can accurately calculate the polarization response of an ensemble with large N acquiring a significant truncation error. In the limit that $N \to \infty$ an infinitesimal pulse area θ will make the density matrix elements non-perturbatively zero rendering this the correct interpretation of the physics of the ensemble.

4.3 Discussion of Model and Numerical Results

In the above sections a statistical model of the exciton was presented in the context of collective coherent states and this model was evaluated in a perturbative regime. We were able to demonstrate that truncation at the first few levels of this model allows for an accurate calculation of the polarization. The truncation process generates what is effectively a few-level model. The physical origin of this was made clear by explaining the interference effect of a many-term polynomial resulting from the pulse-area expansion of the density matrix elements. Thus for systems without many-body interactions and in a large N limit the actual excitation level is unnecessary for calculating the polarization response. However, in the presence of many-body interactions which depend on the actual excitation density, such as EID and EIS, these results become suspect. To evaluate whether the few-level truncation-calculation can still qualitatively agree with the total polarization we numerically evaluate the polarization for $N = 100$ TLS coupled by a two-body many-body interaction as will be discussed in the following.

4.3.1 Numerical Analysis of Many-Body Resonant Energy Shifts

To evaluate the total polarization response in the presence of many-body interactions we implement a numerical simulation. We make the assumption that the largest many-body interaction contributing to the resonant energy shifts is a two-body interaction. The number of possible two-body interactions $k = 2$, where k is the number of many-body interactions, is described by the binomial coefficient from which we can assign an interaction Hamiltonian

$$H_{int} = \frac{1}{N}\binom{n}{k}\hbar\epsilon \sim \frac{1}{N}\hbar\epsilon\hat{n}(\hat{n}-1). \tag{4.36}$$

Here $\hbar\epsilon$ is the interaction energy and $\hat{n}$ are number operators describing the interaction. The factor of $\frac{1}{N}$ is a normalization constant. For this interaction to be perturbative we must satisfy the condition $\hbar\epsilon \ll \hbar\omega_a$ from Eq. 4.9. The simulations numerically solve the Von-Neumann equation in the absence of damping for $N = 100$ TLS as a function of incident pulse area for different interaction energies. We then numerically compute the total polarization immediately after the pulse. In the absence of many-body interactions $\epsilon = 0$ the polarization response is due to phase-space filling, with nonlinearities due to the saturation of the ensemble. The inclusion of many-body interactions allows for the possibility of the polarization to deviate from the phase-space filling only result. Our calculated total polarization does not dramatically deviate from the phase-space dominated polarization in the presence of many-body interactions (Fig. 4.4). This is reassuring as our many-body interaction should be perturbative to the bare Hamiltonian. In a truncated model we expect, although we do not prove, that essentially the same result will be found. Since a truncated system calculates the same polarization as a non-truncated system we expect

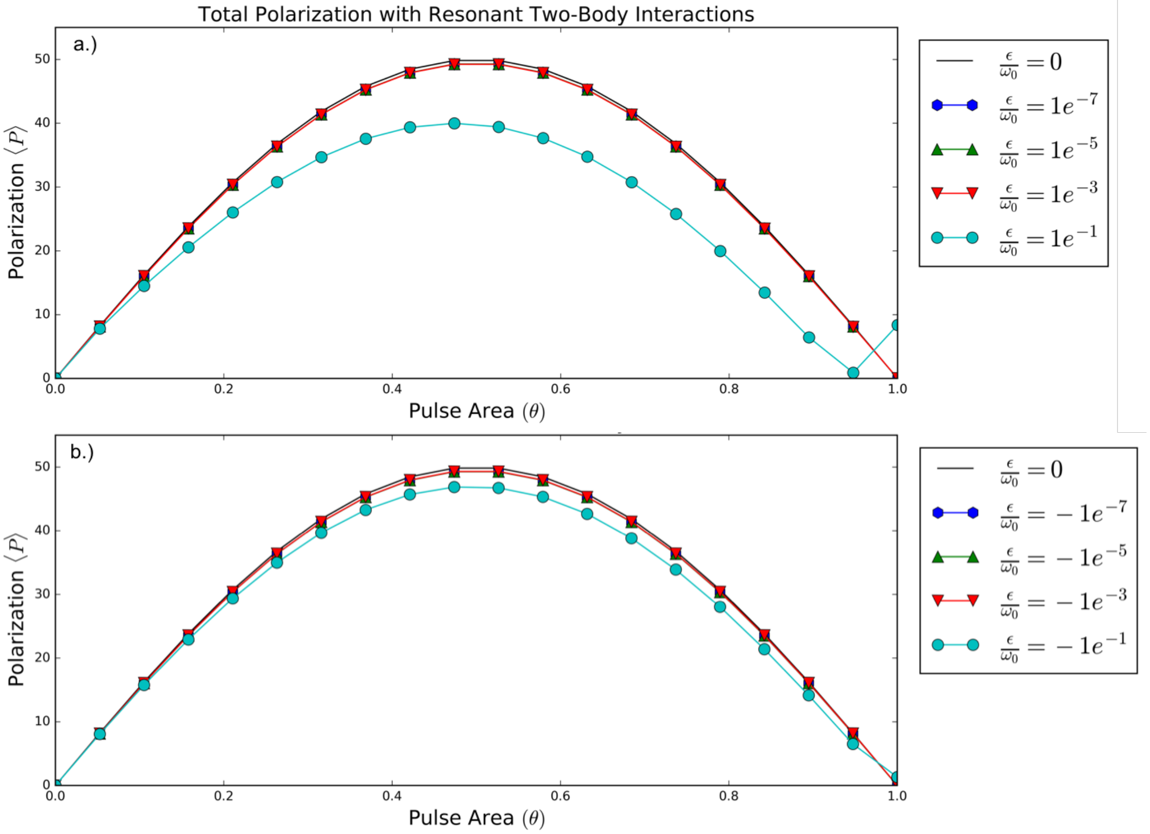

Figure 4.4: Numerical simulations as a function of pulse area θ are presented for $N = 100$ TLS in a collective regime in the absence of damping. Both positive and negative interaction energies reduce the polarization magnitude perturbatively until becoming an appreciable fraction of the transition energy $\hbar\omega_0$. a.) Numerical calculation of the total polarization for positive interaction energies $\hbar\epsilon$. b.) Numerical calculation of the total polarization for negative interaction energies. $\hbar\epsilon$.

that the inclusion of a perturbative many-body parameter is sufficient to capture the many-body induced deviations from phase-space only nonlinear polarization. Thus provided the interaction energies are perturbative, they cause deviations about the interaction free result and therefore may allow for the extraction of an ordered tree of many-body interactions i.e. two-body, three-body etc. We numerically evaluate the model for both positive and negative interaction energy as a function of pulse area θ (Fig. 4.4 a-b) . Both positive and negative interaction energies reduce the total polarization and systematically shift the total polarization to smaller values. Note that the polarization shift to a smaller magnitude is an artifact of our choice of interaction Hamiltonian. The interaction Hamiltonian considers two-body interactions and acts as a resonant energy shift for each rung of the excitation ladder. As a result, the self-resonant interaction energy is not uniform across the unperturbed energy spectrum and grows at higher excitation density to reflect the increased number of bodies available to interact. Thus higher excitation levels are increasingly non-resonant with the driving radiation field and the probability to excite them should decrease. The choice of a different interaction Hamiltonian that can include n-body interactions may correct this effect.

Importantly, effects such as excitation induced dephasing are not captured by this simulation. The effect of many-body interactions on the polarization phase has been previously observed in GaAs quantum wells [41]. These phase effects are critical as they alter the time-dynamics of the polarization as well as the maximum amplitude and are directly related to both resonant energy shifts and additional dephasing. As previously discussed, using a truncated few level model calculates the correct polarization response in the absence of many-body interactions. Fortunately, the inclusion of many-body interactions in a truncated few level model is now more justified since these parameters do not dramatically alter the total polarization response using a non-truncated model.

4.4 Discussion of Model and Relevance to Experiments

As part of our discussion in developing the model and the interference effect of the density matrix elements in calculating the total polarization we realized that there existed a secondary interference effect that would show up in experiments on collective systems. This secondary interference occurs due to experimental methods that involve phase-matching or phase-cycling. As a simple example consider two coincident pulses which excite a spatially extended collective system. The phase across the system will vary as $\phi = (\vec{k_A} - \vec{k_B}) \cdot \vec{x}$ resulting in a non-uniform pulse area across the system. Effectively, the system is experiencing a pulse-area modulation at the spatial difference frequency that leads to a population grating. A grating implies that the signal does not arise from a single distribution of density matrix elements but rather several. In order to quantitatively analyze this effect we consider an analogous system: a spatially localized collective system and use time-dependent pulse-pulse phase cycling in order to evaluate this interference effect quantitatively. Time dependent pulse-pulse phase cycling can be achieved via shifting the carrier frequency of two pulse trains to be slightly different [90–92] resulting in a modulation of the electric field amplitude at a frequency much slower than the optical frequency. This slow modulation process result in a shot-to-shot pulse area modulation that can be quantitatively analyzed. The pulse area in this process for two pulses-coincident in time is:

$$\theta(t) = \theta_0 \cos(\frac{1}{2}(\omega_A - \omega_B) \cdot t). \tag{4.37}$$

where $\omega_{A,B}$ are the shifted carrier frequencies of the two pulse-trains and θ_0 is the amplitude of the electric field when both field A and B constructively interfere. The modulation frequency is $\Delta\omega_{A,B}$. In the case considered here the system decays in the time interval between successive pulses as in Fig. 3.6. The effect of this modulation ensures that successive shots do not excite the collective system with the same amplitude. By detecting at the modulation frequency it is impossible to specify what state or what excitation level the system was excited to since this was varied shot-shot. The effect of detecting at the modulation frequency is to low-pass/integrate the measured signal adding together signals from highly excited density matrix elements and weakly excited density matrix elements measured at different times. Detecting at the modulation frequency results in a signal that cannot demonstrate the same polarization response as Fig. 4.3 or Fig. 4.4a-b because the measurement is not sensitive to the polarization after a single shot of pulses but rather successive unequal amplitude pulses. Perhaps surprisingly, this suggests that coherent spectroscopy techniques as related to collective systems are inappropriate for coherent control as successive shots do not prepare the system in the same state unlike pump-probe techniques.

In order to further evaluate this effect we numerically and analytically evaluate the density matrix with a modulated pulse area. In the limit of infinite N we can solve for $\rho_{n,n}(t)$ and find the following relationships,

$$\rho_{n,n}(t) = \frac{1}{N}\sum_{k=-\infty}^{\infty} F(\frac{n}{N},\theta_0)[\delta(t - t_n \cdot k) + \delta(t + t_n \cdot k)] \tag{4.38}$$

with the function $F(\frac{n}{N},\theta_0)$ given by:

$$F(\frac{n}{N},\theta_0) = \frac{2}{\theta_0 \Delta\omega_{A,B}\sqrt{\frac{n\left(1-\frac{n}{\mathrm{N}}\right)}{\mathrm{N}}}\sqrt{1-\frac{4\sin^{-1}\left(\sqrt{\frac{n}{\mathrm{N}}}\right)^2}{\theta_0^2}}}. \tag{4.39}$$

The peak value of $\rho_{nn}(t)$ is $t_n = \frac{2}{\Delta\omega_{A,B}}\arccos\left(\frac{2}{\theta_0}\arcsin(\sqrt{n})\right)$. The asymptotic limit of $\rho_{n,n}(t)$ is $\frac{1}{N\sqrt{2\pi}}F(\frac{n}{N},\theta_0)$. As the pulse area continuously varies from high to low each density matrix element experiences a burst of probability. Each density matrix element as a sum of time-dependent delta functions effectively becomes a frequency comb with a repetition rate determined by the modulation frequency. Thus each density matrix element acquires phase dependent on the modulation frequency. When filtered to isolate a single frequency component of the pulse train interference occurs between different density matrix elements.

To demonstrate this effect we numerically evaluate an ensemble of $N = 10, 100, 1000$ TLS with a modulated pulse area in order to identify components of the density matrix elements $\rho_{n,n}(\Delta\omega)$ that evolve at the mixing frequency of the two fields $\Delta\omega_{A,B}$ as shown in Fig. 4.5A-C. If the physical signal measured is related to a population or excitation density then the density matrix elements are weighted by the excitation level operator. Surprising features appear in the filtered density matrix elements. The ground state density matrix element remains anti-phased with respect to most higher lying excited states. This effect becomes more pronounced as N grows larger. As can be seen from the figures a complicated interference effect appears where at a given pulse area excited states that are not the ground state become oppositely phased with respect to to higher lying excited states. The highest excited density matrix element can never approach a probability of 1 even for a pulse area of π because this probability becomes distributed amongst different frequency elements. This suggests that phase-matching and phase-cycling schemes may be inappropriate to study collective systems near inversion without first using a pre-pulse. As the number of TLS grows the relative amplitude of the higher excited density matrix elements decreases indicating that the wave mixing process is distributed amongst many more frequencies for higher excited density matrix elements that for lower density matrix elements.

Our analysis of this phenomenon has lead to a secondary interference effect that is primarily related to nonlinear frequency mixing in the highly non-linear density matrix. This frequency mixing provides evidence that experiments that isolate certain wave mixing responses may be inappropriate to study collective systems at higher pulse-induced excitation density.

4.5 Conclusion

We have evaluated wave-mixing processes in collective systems. Our approach utilizes a statistical model to motivate a discussion of the exciton and many-body interactions. We find that there exists significant justification for few level truncated schemes and that the error from these schemes should exist from underestimating the excitation density after the first pulse. We have evaluated the effect of many-body interactions on the polarization response and shown that while they do cause deviations they do not dramatically alter the total polarization. This suggests that truncated few level models that include many-body interactions are appropriate to modeling the deviations from phase-space only effects. Finally, we have also discussed the role of phase-matching and phase-cycling in interpreting wave-mixing experiments in collective systems. We find that standard experimental approaches to wave-mixing are inadequate for studying collective systems near inversion and that even at low excitation density care must be taken when calculating the polarization to make sure it agrees with observables of the experiment. This motivates experiments that use a pre-pulse

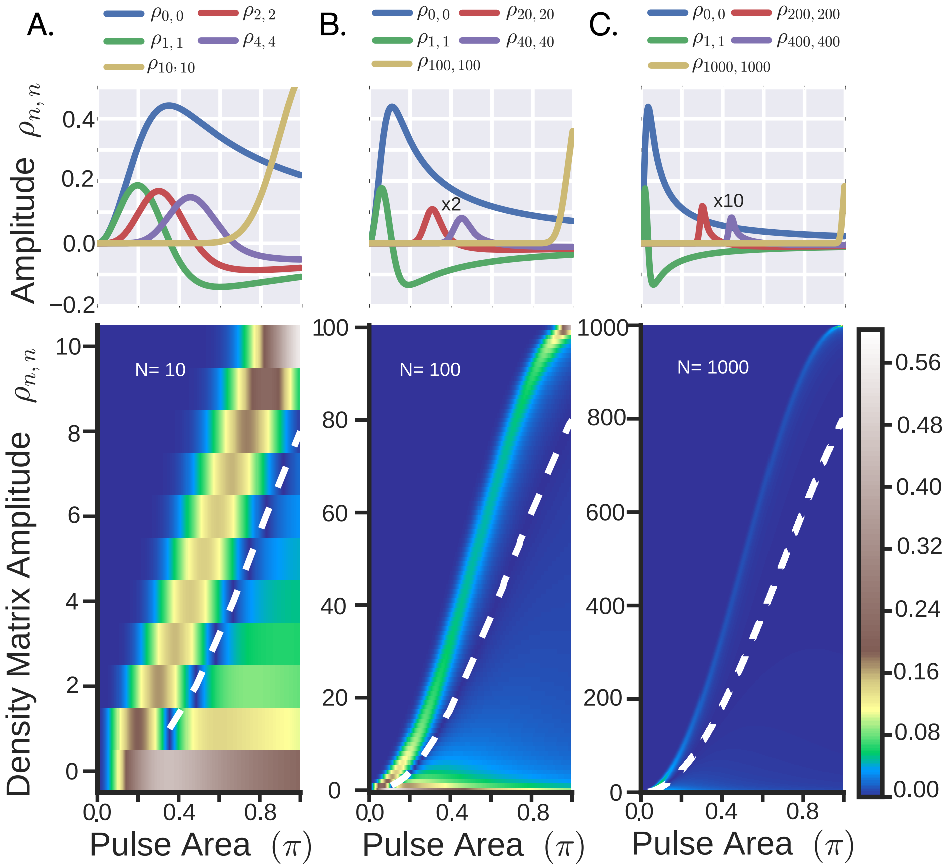

Figure 4.5: Top figures are slices of the probability amplitude $\rho(\Delta\omega_{A,B})$ at time $t = 0$, as a function of pulse area. The bottom figures plot the absolute amplitude of all density matrix elements as a function of pulse area θ_0 at the two-wave mixing frequency. White lines indicate where the modulated density matrix elements develop a π phase shift relative to the pulse area $\theta(t)$. A.) Selected density matrix components at frequency $\Delta\omega_{A,B}$, $\rho(\Delta\omega_{A,B})$ for $N = 10$. B.) Selected density matrix components at frequency $\Delta\omega_{A,B}$, $\rho(\Delta\omega_{A,B})$ for $N = 100$. C.) Selected density matrix components at frequency $\Delta\omega_{A,B}$, $\rho(\Delta\omega_{A,B})$ for $N = 10$.

before probing with coherent based on these modulation schemes spectroscopy. A pre-pulse that is unrelated to the phase matching or phase cycling of coherent spectroscopy will always excite the system in an identical state allowing for a better estimation of the excitation density and many-body parameters.

Chapter 5

Strong Coupling Regime for Two-Level Systems and Collective Ensembles

Light-matter interactions describe the way in which matter absorbs and emits energy to and from driving radiation. Of universal importance is understanding ”what happens” when matter becomes optically excited. Does it disassociate, re-radiate, or transfer the energy to another system? In the modern era of light-matter interactions it has become possible to strongly couple matter to light through the use of high-Q cavities. This regime of strong-coupling is of particular importance because it provides information about absorbing media *and* light itself. The strong-coupling regime is a *coherent* effect in which the quantum states are described by a superposition of photons and matter states. This chapter explores the strong coupling regime for two types of absorbing media, two-level systems and collective systems, with the goal of understanding the characteristic signatures of strong coupling for both systems.

An optically induced matter-coherence represents a superposition of two or more quantum states with a defined relative phase between each other. Dephasing is the process by which information about the phase of this coherence is irreversibly lost. If the dephasing rate is negligible then the coupling strength between light and matter can be recorded as a Rabi frequency. The Rabi frequency describes the cyclical evolution of a driven system of two quantum states. Intuitively, a driving field of longer duration will make it more likely for an initially unexcited system to absorb a photon. Conversely, a driven initially inverted system will be stimulated to re-emit and become de-excited. The Rabi frequency represents the rate at which these processes occur.

For most systems the Rabi frequency is small enough to consider the matter-coherence independently from the quantum states of light. With the advent of strong coherent light sources it became possible to drive the population transfer between two states so strongly that a population-modulation process takes place. The resulting spectrum is the Mollow triplet [160] of resonant fluorescence. This spectrum is characterized by a central emission line and two side-bands with a peak separation corresponding to the Rabi frequency. In the fully quantum picture of this process the two states are interacting with excitation manifolds described by the statistics of the driving radiation. In the limit that the coupling is strong enough the degeneracy of matter states and light states at each excitation manifold is lifted by a Rabi splitting. The resulting allowed-transitions results in the characteristic Mollow triplet spectrum. The key to observing the Rabi splitting is to increase the electromagnetic fields energy density by increasing the driving amplitude while remaining in a regime where dephasing is negligible.

With the advent of high Q cavities it has become possible to dramatically increase the field energy density while remaining in a low excitation regime. This advance has resulted in the observation of vacuum Rabi splittings for both two level systems and collective ensembles. The vacuum Rabi splitting is the characteristic signature of strong coupling. The vacuum Rabi splitting occurs when the energy density of the electromagnetic field is large enough to cause strong coupling at the single photon level. Here we review the strong coupling of both two level systems and collective ensembles strongly coupled to the electromagnetic field with the goal of providing needed background to subsequent chapters exploring the dynamics of strongly coupled collective systems.

5.1 Strong Coupling of the Electromagnetic Field to a Two-Level System

The second quantization Hamiltonian for a two-level system interacting with a monochromatic electromagnetic field is given by the Jaynes-Cummings Hamiltonian (JCH) in the rotating wave approximation [150, 161]:

$$H = \hbar\omega_L(a^\dagger a + \frac{1}{2}) + \hbar\omega_0(\sigma_z) + \hbar g(a^\dagger\sigma^- + \sigma^+ a). \tag{5.1}$$

Here ω_L is the laser frequency, ω_0 is the resonant frequency of the two level system, $a^\dagger(a)$ are the creation(annihilation) operators for the electromagnetic field, σ_z is the Pauli z-matrix, and $\sigma_- = |g\rangle\langle e|$ and $\sigma_+ = |e\rangle\langle g|$ are the lowering-raising operators of the two level system and g is the Rabi frequency. We define a detuning $\delta = \omega_L - \omega_0$ and consider the regime near resonance $|\delta| << \omega_0$. The wavefunctions of this system are described by excitation manifolds in the basis $|i(j), n\rangle$ where $i(j)$ refers to an excited(unexcited) matter state and n refers to the photonic excitation number. The expectation value for the coupling energy is non-constant and changes with respect to excitation manifold n. It's dependence is

$$H_{coupling} = \langle j, n+1|\hbar g(a^\dagger\sigma_- + \sigma^\dagger a)|i, n\rangle = \hbar g\sqrt{n} = \hbar\frac{\Omega}{2}\sqrt{n}. \tag{5.2}$$

In the classical limit of many photons driving a two-level system, the Rabi frequency becomes (Eq. 2.14) and the variation with photon number is unimportant. In the few photon limit this variation has profound consequences on the energy structure as will also be shown.

5.1.1 Classical Limit

A classical laser field can be described quantum mechanically using coherent states $|\alpha\rangle$ in a number basis $|n\rangle$. These states are given by:

$$|\alpha(t)\rangle = e^{-|\alpha|^2/2}e^{-i\omega_L t/2}\sum_{n=0}^{\infty}\frac{\alpha^n e^{-i\omega_L nt}}{\sqrt{n!}}|n\rangle. \tag{5.3}$$

The number of excitations is only defined to within the variance of the coherent state, which scales with the number of excitations in the field. The expectation value and and square of the photon number are

$$\bar{n} = < n > = < a^{\dagger}a > = |\alpha|^2 \tag{5.4}$$

and

$$< n^2 > = < (a^{\dagger}a)^2 > = |\alpha|^2 + |\alpha|^4. \tag{5.5}$$

Using these relations the photon number variance σ_n^2 is

$$(\sigma_n)^2 = < n^2 > - < n >^2 = |\alpha|^2. \tag{5.6}$$

The classical limit occurs when $\sigma_n \gg 1$ but $\bar{n} \gg \sigma_n$. In this limit, the average, coupling taken from Eq. 5.2, is

$$\nu = g\sqrt{\hat{n}}. \tag{5.7}$$

and the deviation in that coupling [162] is given by

$$\Delta\nu \sim \nu \frac{g\sqrt{\sigma_n}}{g\sqrt{\hat{n}}} \tag{5.8}$$

which goes to zero in the classical limit such that ν is a constant. In the classical regime the energy structure produced by the Jaynes-Cummings Hamiltonian at a given manifold ζ is:

$$\mathbf{H}_{\zeta} = \begin{bmatrix} (n+1)\omega_L & g\sqrt{n} \\ g\sqrt{n} & \hbar\omega_0 + n\omega_L \end{bmatrix}. \tag{5.9}$$

The effect of the strong coupling is to mix the field-two state systems eigenvectors and provide new eigenmodes. The eigenmodes are characterized by frequencies:

$$\omega_{n,\pm} = (n-1)\omega_L + \frac{1}{2}(\omega_L + \omega_A) \pm \frac{1}{2}\sqrt{4g^2 n + (\omega_A - \omega_L)^2}. \tag{5.10}$$

In the classical limit the coupling strength constant between manifolds and the energy structure of the system becomes that of Fig. 5.1a. The coupling between the field and the two-level system makes it so that the new eigenfrequencies are split by the factor $\Omega_n = \sqrt{4g^2n + (\omega_A - \omega_L)^2}$ on resonance. This splitting is known as a the Rabi splitting and in the classical limit $\Omega_n \to \bar{\Omega}_{\bar{n}}$ the Rabi frequency at average excitation level $\bar{n}$. At each excitation manifold the two-level system is oscillating between excited and unexcited. The rate of evolution at each manifold is given by the Rabi splitting. At high excitation levels the Rabi frequencies are virtually the same. Subsequently, the two-level system is well approximated as oscillating between excited and unexcited states at the average Rabi frequency.

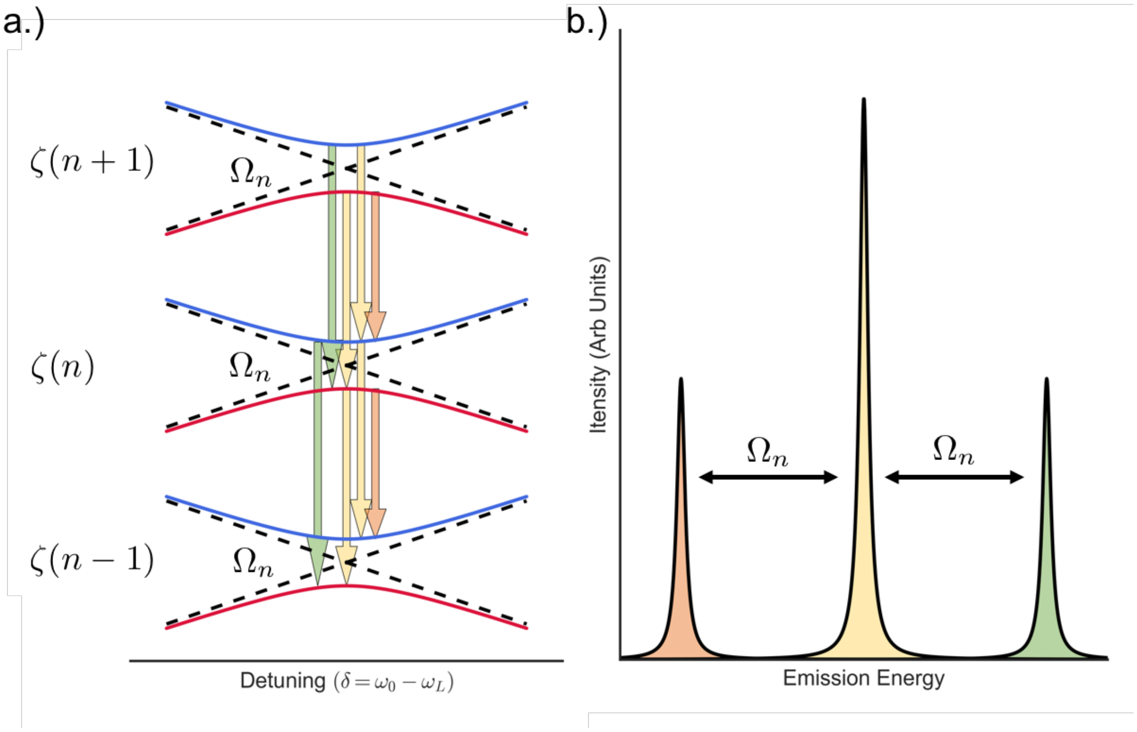

Figure 5.1: The classical regime of the Jaynes-Cummings Hamiltonian. a.) The energy spectrum plotted for $\bar{n} \gg \Delta n$. The uncoupled states are plotted as a function of detuning for the different manifolds ζ. In this regime the Rabi splitting ω_n at each level is constant. The colored arrows indicate the allowed transmission energies. b.) The Mollow triplet spectrum characteristic of the strong electromagnetic driving of a two-level atom with peaks color-coded to match the transitions in a).

The dressed states at a given excitation manifold are found to be

$$|\pm\rangle = \sin(\theta)|0,n\rangle \pm \cos(\theta)|1,n-1\rangle \tag{5.11}$$

such that the system is found to be in a superposition of excited-unexcited atom and photon number state. The ratio of the weighting between the different wavefunction components is [162]

$$\sin 2\theta = \frac{2g\sqrt{n}}{\Omega_n} \tag{5.12}$$

$$\cos 2\theta = \frac{\omega_L - \omega_A}{\Omega_n}. \tag{5.13}$$

For large detuning the energy levels of Fig. 5.1a represent A.C. Stark shifts of the two level system. On resonance $\omega_A = \omega_L$ the state of the system is equally weighted between the field and the two level system. As the detuning is swept from very negative to very positive the state $|+\rangle$ smoothly transitions from $|0,n\rangle \rightarrow |1,n-1\rangle$ passing through an anti-crossing. The state $|-\rangle$ does the converse.

The emission spectrum of this system was first described using a classical single-mode field by Mollow. In this approach essentially each of the manifolds is projected into a single "sum" of all manifolds and an emission spectrum is calculated. That emission spectrum is given by Fig. 5.1b and shows three peaks seperated by the Rabi splitting. As there are two resonant transitions permitted the central peak is larger than the sidebands. Despite being in a classical statistical regime there are a variety of quantum effects provided by the Mollow triplet including radiative cascade and photon antibunching. [160, 162].

5.1.2 Quantum Limit

In the quantum statistical regime the dispersion of photon number for coherent states becomes a significant effect as $< n > \sim \sigma_n \sim 1$. The Poisson distribution defining a coherent state becomes antisymmetric with respect to photon number. The strong coupling regime is characterized by a Rabi-nutation with the collapse and revival of the two-level systems excitation level. At low excitation levels the dispersion in photon number is a significant effect and the Rabi-oscillations from each excitation manifold will beat at incommensurate frequencies. The measurement of the spectrum (Fig. 5.2a), in an atomic system, provided the first *direct* observation of field quantization of the electromagnetic field [20, 163]. As before, the state of the system is a superposition of states

$$|\psi\rangle = c_{g,0}|g,0\rangle + \sum_{n=0}^{\infty}[c_{g,n+1}|g,n+1\rangle + c_{e,n}|e,n\rangle]. \tag{5.14}$$

Plugging this wavefunction into the Schrodinger equation, the dynamics of state $|e,n\rangle$ can be calculated from Eq. A.13. The time evolution for the two-level system to be excited is found to be $P_{e,n} = \sum_{n=0}^{\infty} C_n \cos^2 g\sqrt{n+1}$. The coefficient C_n describes the statistical dispersion of the electromagnetic field, exponential for a thermal field, and Poissonian for a coherent field [163]. The eigenenergies follow from Eq. 5.10 with the exception that the Rabi splitting $\Omega_n = \sqrt{4g^2 n + (\omega_A - \omega_L)^2}$ is no longer quasi-constant. At low excitation levels the discrete nature of this evolution $\sqrt{n+1}$ is observable as the energy spacing in $P_{e,n}$ becomes asymmetric (Fig. 5.2 b,c). The measurement of this scaling with photon number has become a hallmark of strongly-coupled cavity QED systems [20, 163–165]. A current source of fundamental interest is the extension of the strong coupling regime to the ultrastrong coupling regime wherein the Rabi frequencies are a significant fraction of the resonant frequency and the rotating wave approximation breaks down [156, 166].

5.2 Strong Coupling of the Electromagnetic Field to a Collective Ensemble of Two-Level Systems

The problem of extending the strong coupling regime to collective ensembles was studied in detail by Tavis-Cummings [167, 168] where exact solutions were calculated. Since then this problem has been studied to understand the energy spectrum and to include effects like Kerr or Stark shift nonlinearities [121, 135, 169–171]. Renewed interest in this model is driven

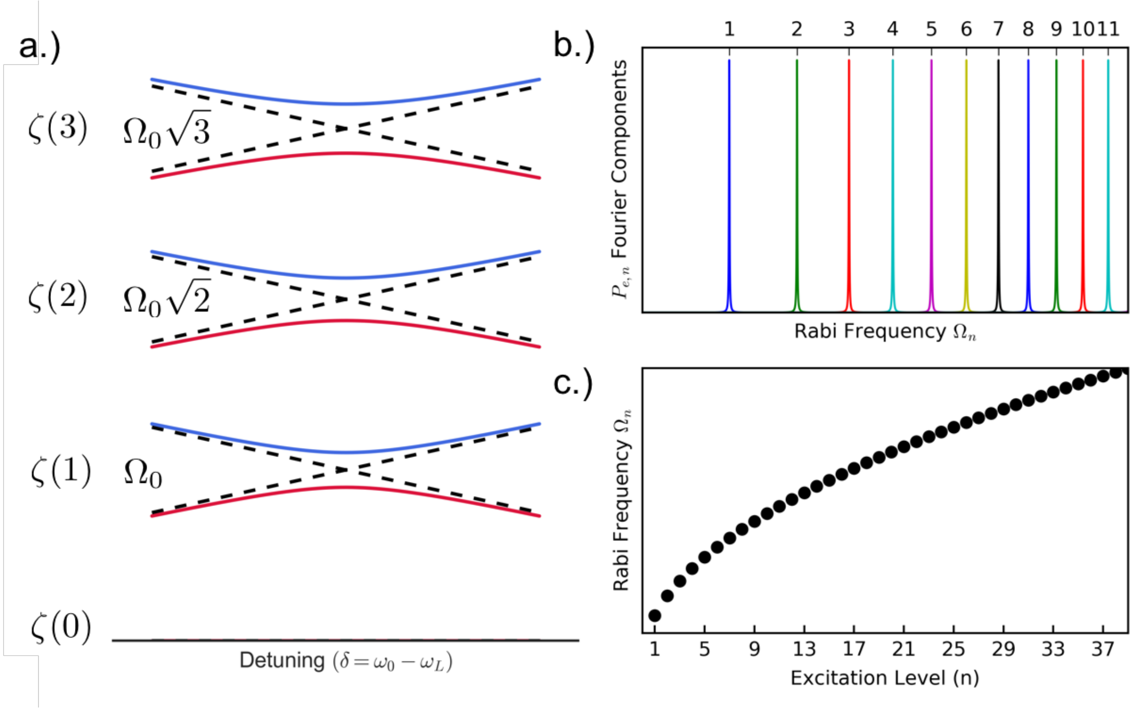

Figure 5.2: The quantum regime of the Jaynes-Cummings Hamiltonian. a.) Representation the few excitation manifolds as a function of detuning. Each manifold ζ consists of two states coupled by manifold dependent Rabi splitting. The uncoupled states are denoted by dashed black lines. b.) The frequency components of the probability amplitude $P_{e,n}$ showing a non-uniform spacing. These Fourier components amplitude depend on the statistical distribution of the photons in the cavity. c.) The Rabi frequency dependence shows curvature for small excitation levels before becoming more linear at higher excitation levels.

by the possibility of including many-body interactions. Many-body interactions may enable the possibility of a photon blockade, using three-dimensional confinement of the electromagnetic field, to create ideal single-photon sources while enjoying the benefits of collective systems such as a larger Rabi frequency [127, 172, 173]. Additionally, the availability of a blockade open the possibility to study single excitation states in both semiconductors and atoms excited by classical light [127, 172, 173].

The Tavis-Cummings Hamiltonian describes a collective ensemble of two-level atoms strongly coupled to the electromagnetic field and in the absence of many-body interactions. In general single-mode descriptions of the exciton strongly interacting with a single mode of the quantized electromagnetic field reduce to dynamics of the Tavis-Cummings type and leads to the concept of the exciton-polariton. However for exciton-polaritons the dynamics are modified by the Coulomb-meditated many-body interactions. These interactions are insufficiently strong to provide the quantum statistical regime that an exciton-blockade could produce while being strong enough to dominate the optical response leading to extensive studies [27, 51, 79, 142, 174–176, 176–191].

In an excitation basis, after reducing the "fermionic" operators to "bosonic" [149, 150, 169] the Tavis-Cummings Hamiltonian is given by [150]:

$$H = \hbar\omega_L a^\dagger a + \hbar\omega_x b^\dagger b + \hbar g\sqrt{N}(a^\dagger b + b^\dagger a) + H_c. \tag{5.15}$$

where ω_x is the exciton transition frequency, ω_L is the laser frequency, N is the number of two-level systems, $g\sqrt{N}$ is a collective Rabi frequency and $a(b)$ represent the photon(exciton) operators. Here H_c represents corrections to the Holstein-Primakoff transformation due to bosonization. The bosonization proceadure is most appropriate in a large N limit where the H_c term is often dropped. Just like for the Jaynes-Cummings picture there exists a coupling at each excitation manifold, and the spectrum of the Tavis-Cummings system is determined by the transitions between these manifolds. In the Tavis-Cummings system the coupling at each excitation manifold changes less dramatically than in the Jaynes-Cummings system. If we denote the exciton excitation level by n_x and the field excitation level by n_c then the coupling at each excitation level is given by:

$$H_{n_x,n_c} = g\sqrt{N - n_x}\sqrt{n_c}\sqrt{n_x}. \tag{5.16}$$

Here the $\sqrt{N-n}$, is due to corrections in the Holstein-Primakoff transformation while the $\sqrt{n_c}\sqrt{n_x}$ is due to the bosonic nature of the ensemble-field operators. The Tavis-Cummings system has a very different energy spectrum than the Jaynes-Cummings system. The Tavis-Cummings system at low excitation levels, for a large number of two-level systems, resembles that of two coupled quantum harmonic oscillators.

5.2.1 Energy Spectrum of Tavis-Cummings Hamiltonian

To determine the dressed states and the spectrum of the Tavis-Cummings Hamiltonian we begin by defining uncoupled product-basis wavefunctions.

$$|\psi_x\rangle = |n_x\rangle|n_c\rangle. \tag{5.17}$$

Here $n_x(n_c)$ is the number of excitations in the ensemble(cavity). The first excitation manifold occurs when $n = n_x + n_c = 1$ and it's Hamiltonian is

$$\mathbf{H}_{\zeta=\mathbf{1}} = \begin{bmatrix} \hbar\omega_x & \hbar g\sqrt{N} \\ \hbar g\sqrt{N} & \hbar\omega_c \end{bmatrix}. \tag{5.18}$$

Diagonalizing this matrix yields new modes of the coupled system

$$\lambda_{n=1} = \frac{(\hbar\omega_x + \hbar\omega_c) \pm \hbar\sqrt{\delta^2 + 4Ng^2}}{2} \tag{5.19}$$

along with their corresponding wave functions at zero-detuning:

$$|+\rangle = \frac{1}{\sqrt{2}}[|1,0\rangle + |0,1\rangle] \tag{5.20}$$

$$|-\rangle = \frac{1}{\sqrt{2}}[|1,0\rangle - |0,1\rangle]. \tag{5.21}$$

As a coupled system it becomes apparent that at zero-detuning the new eigenstates are equally weighted superposition states of ensemble-field just like for the Jaynes-Cummings system previously discussed. At the $n = 2$ level the block-diagonal Hamiltonian is

$$\mathbf{H}_{\zeta=\mathbf{2}} = \begin{bmatrix} \hbar(\omega_c + \omega_x) & \hbar g\sqrt{2}\sqrt{N-1} & \hbar g\sqrt{2}\sqrt{N} \\ \hbar g\sqrt{2}\sqrt{N-1} & 2\hbar\omega_x & 0 \\ \hbar g\sqrt{2}\sqrt{N} & 0 & 2\hbar\omega_c \end{bmatrix}. \tag{5.22}$$

.

In the limit of a very large number of oscillators $\sqrt{N-1}$ reduces to $\sim \sqrt{N}$. Diagonalizing the $n = 2$ matrix, under the assumption that N is large, produces the three new eigenmodes

$$\lambda^{'}_{n=2} = (\hbar\omega_x + \hbar\omega_c) + \hbar\sqrt{\delta^2 + 4Ng^2} \tag{5.23}$$

$$\lambda^{''}_{n=2} = (\hbar\omega_x + \hbar\omega_c) - \hbar\sqrt{\delta^2 + 4Ng^2} \tag{5.24}$$

$$\lambda^{'''}_{n=2} = \hbar(\omega_x + \omega_c). \tag{5.25}$$

It becomes apparent from there energies that one mode has the energy of the cavity-excitation level without any Rabi-splitting, while the other two modes exhibit Rabi splittings comparable to the first excited manifold. The $n = 2$ wave functions at zero-detuning are given by:

$$|++\rangle = \frac{|2,0\rangle + |0,2\rangle + \sqrt{2}|1,1\rangle}{2} \tag{5.26}$$

$$|--\rangle = \frac{|2,0\rangle + |0,2\rangle - \sqrt{2}|1,1\rangle}{2} \tag{5.27}$$

$$|+-\rangle = \frac{|2,0\rangle - |0,2\rangle}{\sqrt{2}}. \tag{5.28}$$

The form of these wavefunction is the combination of states available from the first excitation manifold needed to obtain a wavefunction at twice the energy. Thus the $|{+}{+}\rangle$ state consists of two $|+\rangle$ excitations and the $|{+}{-}\rangle$ state consists of a $|+\rangle$ and a $|-\rangle$ excitation. This immediately motivates an understanding of the spectrum of this Hamitonian. Transitions between excitation manifolds can only occur at the new normal mode frequencies defined by the eigenenergies of the first excitation manifold. In the large N limit there is no appreciable difference in the transition energies even at low excitation density. The energy spectrum and

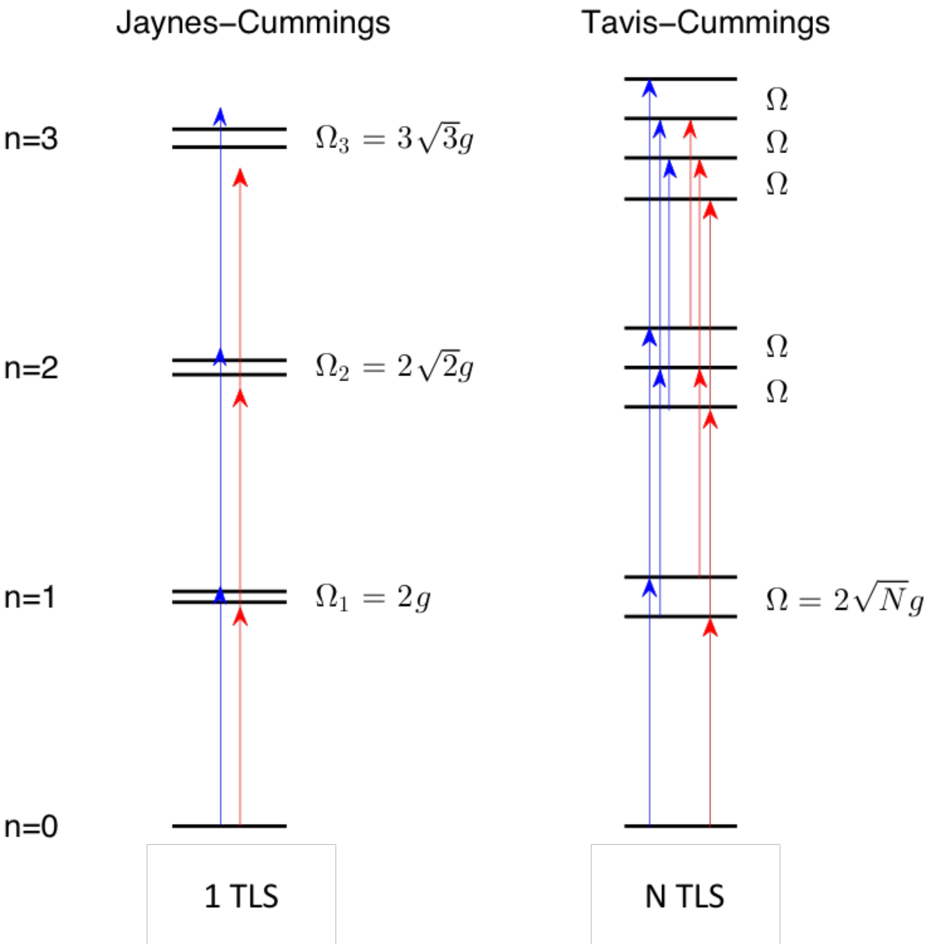

Figure 5.3: The few-excitation regime for both the Tavis and Jaynes Cummings Hamiltonians. a.) Representation the first few excitation manifolds of the Jaynes-Cummings Hamiltonian at zero-detuning. Each manifold ζ consists of two states coupled by a manifold dependent Rabi splitting. The manifold-dependent Rabi splitting leads to unequal transitions energies creating significant nonlinearities at the single-photon level. b.) Representation of the first few excitation manifolds of the Tavis-Cummings Hamiltonian. In the large ensemble at low excitation limit the manifold-dependent Rabi splitting is nearly constant. This leads to approximately equal transition energies which removes the single and few-photon nonlinearity.

transition energies of the first few excited states are illustrated in Fig. 5.3a-b for Jaynes-Cummings systems and for Tavis-Cummings systems in the large N limit.

The Tavis-Cummings system is the collective extension to the Jaynes-Cummings system. For both systems to be in the strong coupling regime the Rabi frequency must be larger than the irreversible decay of the ensemble-cavity system. In the case of Jaynes-Cummings this leads to the strong coupling condition

$$g \gg \gamma_x, \gamma_c \tag{5.29}$$

For the Tavis-Cummings system the strong-coupling condition is [150, 192–194]

$$g\sqrt{N} \gg \gamma_x, \gamma_c. \tag{5.30}$$

This second condition is a much less stringent condition than for a Jaynes-Cummings system and motivates why modern studies of Tavis-Cummings like systems are interested in achieving phenomena like a Rydberg or exciton blockade. A designed system achieves the benefits of a collective coupling strength while leveraging the many-body interactions to alter the large ensemble Tavis-Cummings system to a single-photon nonlinearity regime.

In semiconductor exciton-polaritons it is possible to have multiple quantum wells contribute to the collective strong coupling. For this situation the Rabi splitting is enhanced by a factor $\sqrt{N_{QW}}$ [195]. If a single quantum well has N [156] electrons contributing to the coupling strength then coupling of N_{QW} will have $N * N_{QW}$ electrons contributing to the coupling strength. This scaling is true provided the quantum wells are placed near an antinode of the cavity, placing the well too far away will result in the well not being strongly coupled. [195]. A confusing point in excitonic systems is that changing the spot size does not increase the Rabi splitting. However, this is consistently treated by realizing that the oscillator strength or Rabi frequency of excitonic and atomic systems is always normalized by the mode volume [194, 196–198]. For this reason this $N \cdot N_{QW}$ is often referred to as a density in excitonic systems.

5.2.2 Quantum Limit of the Tavis-Cummings System

Our discussion of Tavis-Cummings has been concerned with large ensembles. With large ensembles the anharmonicity present in the Jaynes-Cummings system is removed. To quantitatively evaluate the degree of remaining anharmonicity we follow the approach of Thompson-Kimble [21] who experimentally and theoretically studied the Tavis-Cummings ladder for $N = 2$ atoms. They introduced a parameter known as the "quantum anharmonicity". The quantum anharmonicity parameter q is the ratio of the second excited state to first excited state splitting and is

$$q_a = \frac{g\sqrt{4N-2}}{2g\sqrt{N}}. \tag{5.31}$$

For $N = 1$ the Tavis-Cummings ladder reduces to that of the Jaynes-Cummings and the anharmonicity parameter $q = .71$, while as $N \to \infty$, $q \to 1$. For $N = 2$ the anharmonicity of the Tavis-Cummings ladder has not been observable. A rough estimate of this anharmonicity for semiconductor exciton-polaritons can be calculated as follows. In a typical semiconductor quantum well the excitonic density is large (Eq. 4.19), if excited by a 50μm spot size $\sim 10^7$ electrons form the excitonic response. This places the exciton-polariton firmly in a large N and near-classical regime. Multiplying the quantum anharmonicity by a transition energy provides a rough estimate of the anharmonicity in units of energy. This energy is on the scale of neV. Many-body interactions in exciton-polaritons which have been reported at the $\sim 10\mu$eV level indicating that these interactions dominate the anharmonic optical response of exciton-polaritons [184, 186, 191].

5.2.3 Saturation of the Tavis-Cummings System

A characteristic of the Tavis-Cummings system is that it saturates with sufficient excitation density. And as it saturates the Rabi splitting decreases until the strong coupling is lost. This has been observed both in atomic and semiconductor systems. The collective dipole scales as $\mu \sim \sqrt{N-n}$ and at high excitation density n becomes appreciable leading to this strong coupling loss. For semiconductors this can be more complicated. The exciton can transition to an electron-hole continuum [158]. Strongly-coupling a semiconductor quantum well to a cavity and screening the oscillator strength has proven to be one of the best methods for measuring the oscillator strength of the quantum well exciton [158, 196, 198]. The saturation of strong coupling is at high excitation density is shown in Fig. 5.4a-b for both atoms and exciton-polaritons.

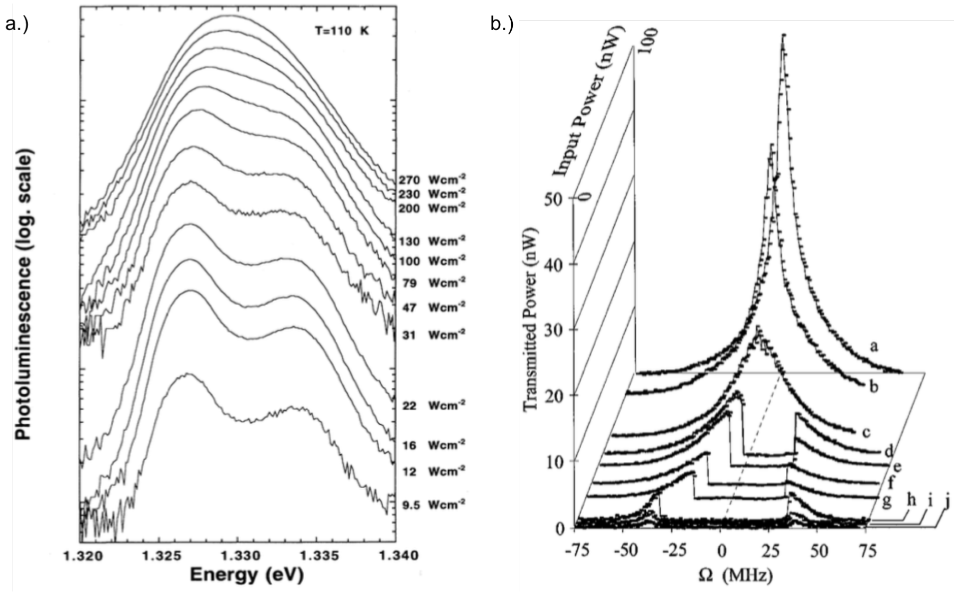

Figure 5.4: The saturation of a strong-coupling in collective systems is shown here for both semiconductor exciton-polaritons and atoms. a.) The saturation of strong-coupling for six InGaAs QW's in a Fabry-Perot(Bragg) cavity. Multiple quantum wells leads to an additional enhancement by $\sqrt{N_{QW}}$ of the transition dipole moment. b.) The saturation of the strong-coupling regime for 220 atoms in a Fabry-Perot cavity. Figures adapted from [158, 199]

5.2.4 Classical Perspective on the Tavis-Cummings System and Strong Coupling

The Tavis-Cummings system is interesting as a model to understand collective strong-coupling. As previously discussed for large ensembles the Tavis-Cummings model exhibits negligible single-photon anharmonicity. This leads to the question of how is the Tavis-Cummings system different from a classical normal-mode system. One main difference appears to be in the ability of the Tavis-Cummings system to saturate and remove the strong coupling, an effect not present in simple classical harmonic oscillators. However, this saturation is the result of the finite number of TLSs and has little to do with the quantum nature of light. A quantum effect only attainable with the Tavis-Cummings system is that of a quantum phase-change for very-strongly coupled systems. This phase-change has been observed in atomic systems [128].

Of significant importance is that no higher lying excited states have been reported for a Tavis-Cummings system. The reason is that for large ensembles the transition energies are largely degenerate, so pump-probe spectroscopy would have to look for very small changes in transition energy in order to observe the quantum nature of light [21]. As pointed out by Carmichael et al.[199], the presence of normal modes between a cavity and absorbing medium as evidenced by a vacuum Rabi splitting is not sufficiently unique to distinguish between a classical or quantum system. The issue being that the first order susceptibility of a semi-classical or fully quantum system is the same as that of a classical harmonic oscillator. A cavity is a reasonable physical approximation of classical harmonic oscillator and thus the coupling of an absorber to a cavity can be understood through simple classical normal-mode coupling. This result is derived in Appendix (B).

5.2.5 Outlook for Spectroscopy and Characterization

Although it may be impossible with current measurement techniques to measure the anharmonicity of the intrinsic Tavis-Cummings system [21], it is possible to consider the role of many-body interactions and optical nonlinearities that are not due to saturation of the oscillators [127, 172, 173]. In the case of very small many-body interactions multi-quantum spectroscopy is an extremely sensitive tool to record deviations from the degeneracy of transitions. Unlike in pump-probe techniques there is no signal without these interactions. The extent of these deviations should characterize if realistic quantum optical behavior can be expected or engineered from a system under study. In this case exciton-polaritons are an ideal candidate. The intrinsic exciton-polariton Hamiltonian reduces to that of the Tavis-Cummings type in the absence of many-body interactions and exists firmly in a large N

limit. Proposals to implement quantum blockades in Tavis-Cummings type systems resort to strong many-body interactions the simplest of which is to create a photonic dot coupled to a semiconductor quantum well [172]. Unfortunately, none of the characteristic strong-coupling studies have been performed on exciton-polaritons due to this issue of transition degeneracy leaving the information about it's strong-coupling structure incomplete.

Chapter 6

Measurement of the Higher-Order Exciton-Polariton Dispersion

In semiconductor cavity electrodynamics the regime of strong-coupling is characterized by a vacuum Rabi-splitting between a semiconductor optical absorber and a light field. The strong-coupling regime for confined excitons in semiconductor quantum wells was first achieved by Weisbuch [19]. The device grown consisted of quantum wells grown at the antinode of a Bragg microcavity. The quantum confined exciton provided sufficient oscillator strength to strongly-couple to the cavity, creating a set of new normal modes known as the exciton-polariton. Unlike exciton-polaritons previously observed in bulk semiconductors, the use of a semiconductor quantum well grown inside a microcavity allowed for the tailoring of the strong coupling. The ability to tailor the strong-coupling regime created a solid-state system capable of exploring quantum electrodynamic effects previously only accessible in atomic systems [192–194, 200–202].

As the experimental conditions for both atomic and solid-state systems improved it became clear through nonlinear experiments that the quantum statistical regime, [163, 200], where the optical properties are changed by the addition of a single photon or oscillator, was not accessible in semiconductor quantum well exciton-polaritons (hereafter exciton-polaritons) [13, 18]. The exciton, as a collective system, is capable of supporting many excitations before saturation. By contrast, all approaches that have achieved the quantum statistical regime rely on a single two level system that saturates with the absorption of a single photon [21, 161, 163, 203, 204]. Since the first observation in atomic systems the quantum statistical regime has been observed in circuit-quantum electrodynamics [20, 164, 166] and signatures of this regime have been observed in quantum-dot microcavity systems [165]. Strongly coupled systems exhibiting nonlinearities at the single-photon level are described by Jaynes-Cummings dynamics [161]. Strong coupling not in a quantum statistical regime is commonly referred to as collective strong coupling or non-perturbative normal mode coupling in an attempt to differentiate it from the quantum statistical strong-coupling regime.

Despite not being able to access the quantum statistical regime exciton-polaritons have demonstrated a variety of quantum effects. These include Bose-Einstein condensation [14, 205] and superfluidity [155, 195]. Of significant interest is the engineering of exciton-polaritons into devices that leverage their collective properties. Such devices include quantum lattice simulators [206] and micropillars where spin-squeezing [207] has been observed. An unrealized, but novel approach to a non-classical light source proposes leveraging the many-body interactions and the collective strong coupling of exciton-polaritons to achieve an excitation blockade at the single-photon level [172].

Before engineering a quantum optical application based on exciton-polaritons it is vital to understand the bare system. A common measurement, for strongly coupled systems in the quantum statistical regime, is to record an avoided crossing at different excitation manifolds or to observe beating between different excitation probabilities at several manifolds (Ch.5.1.2). These measurements then map the strong coupling as a function of statistical dispersion in excitation level. Analogous measurements for the exciton-polariton have proven difficult. Unlike in systems described by Jaynes-Cummings dynamics, the Rabi splitting in exciton-polaritons is nearly constant at low excitation density making it extremely difficult to resolve beating between different excitation manifold probabilities. Nonlinear pump-probe style experiments are also insensitive because the Rabi frequency is nearly constant at low excitation density and because exciton-polaritons have no change in absorption at the single photon level. Additionally, most characterization of exciton-polaritons have been done at relatively high excitation density while most quantum statistical effects occur in the few quanta regime.

Here we have implemented a novel measurement scheme to characterize the strong coupling for *differential* excitation manifolds. We use multidimensional coherent photocurrent spectroscopy to measure excitation manifolds $\Delta n = 1, 2, 3$, where Δn is the difference between excitation manifolds, as a function of exciton-cavity detuning in the weak excitation regime. From these spectra we are able to measure higher-order dispersion relations that characterize the strong coupling at each Δn manifold. Our measurements show that exciton-polaritons, at low excitation density, are nearly harmonic quantum oscillators. These results provide qualitative information about the system characteristics needed to engineer quantum optical effects.

6.1 Background

The statistical variance(dispersion) of excitations for a collective ensemble strongly coupled to the electromagnetic field was first theoretically considered by Tavis and Cummings [167, 168, 170]. This analysis provided evidence for both a quantum and classical statistical regime. The quantum regime is most evident for a single-two level system where the Tavis-Cummings Hamiltonian reduces to that of the Jaynes-Cummings Hamiltonian. Although technically the quantum regime is still applicable for $N > 1$, exhaustive studies, in ideal systems, have shown that even at $N = 2$ no quantum statistical effects can be observed [21]. The classical regime occurs in the limit that the number of collective oscillators N becomes large or in the regime that the number of photons becomes large. The classical regime is characterized by the statistical dispersion of either the oscillators or the photons such that the system is well described by an average coupling.

Exciton-polaritons do not represent an ideal system described by the Tavis-Cummings Hamiltonian. The Tavis-Cummings model, in the classical limit, only captures the Rabi-splitting and eigenmodes of the exciton-polariton system. The model incorrectly describes the optical response predominately because exciton-polaritons have been known to exhibit strong optical nonlinearities due to exciton-exciton interactions. And unlike ideal systems, as the exciton density bleaches the system converts into an electron-hole plasma [13, 158]. This process changes the nature of the optical absorber from consisting of discrete levels to a continuum. Additionally, semiconductor quantum wells are known to experience spatial disorder that can decrease the collective properties of the exciton. In the highly disordered limit the excitons become localized "quantum dots", a two-level system [67, 82, 208]. The single-mode exciton-polariton Hamiltonian describing the eigenmodes and capturing the many-body interactions is [12, 153]:

$$H = \hbar\omega_X b^\dagger b^\dagger + \hbar\omega_\gamma a^\dagger a^\dagger + \hbar g_0(a^\dagger b + b^\dagger a) + \frac{1}{2}V_{XX} b^\dagger b^\dagger bb + V_{sat}(a^\dagger b^\dagger bb + h.c.). \tag{6.1}$$

Here $a^\dagger(a)$ are the bosonic photon creation(annihalation) operators, $b^\dagger(b)$ are the bosonic exciton creation(annihalation) operators, $2g_0$ is the collective vacuum Rabi frequency, V_{XX} is the exciton-exciton interaction energy and V_{sat} is the exciton saturation energy given by $\frac{\hbar g_0}{n_{sat}A}$ where n_{sat} is the exciton saturation density and A is the area of the quantization. In the low density limit of a perfectly ordered quantum well, the many-body interactions break the symmetry in the excitation ladder allowing for non-destructive interference of the multi-quantum pathways measured here. In semiconductor quantum wells, the excitonic dispersion is effectively flat, $\omega_x(k) = \omega_x$. The cavity modes vary with in-plane wavevector (Eq. 1.21) resulting in a cavity dispersion that is parabolic in incident excitation angle, $\omega_c(k) \sim \theta^2$ near normal incidence. The exciton-cavity photon interaction results in an avoided crossing when the exciton and cavity-photon resonances intersect at the zero-detuning excitation angle θ_0 as shown in Fig. 6.1. Since the exciton-exciton interactions are perturbative, these dispersion curves are dominated by the eigenmodes of the exciton-cavity coupling. For exciton-polaritons, all of the transitions in the expected ladder of states are degenerate doublets. The higher rungs in the expected ladder of states is expected to demonstrate multiple avoided crossings between the bare exciton-cavity modes at zero-detuning.

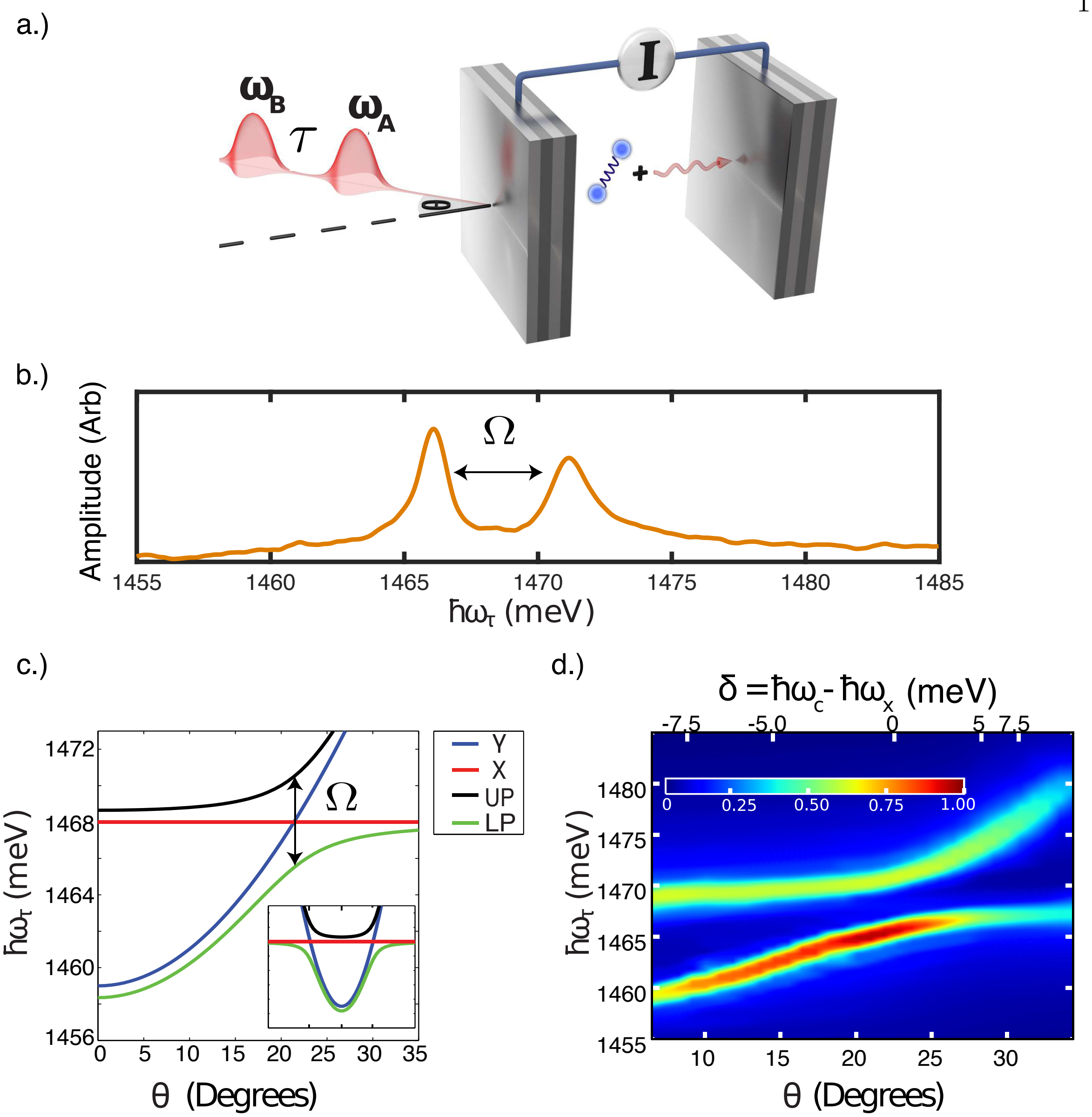

Figure 6.1: a.) Two-pulse excitation scheme to study exciton-polaritons via photocurrent Fourier transform spectroscopy. The signal is recorded as a function of inter-pulse delay τ. b.) Linear absorption spectra are generated by Fourier transforming the time-domain signal with respect to τ. The spectrum shown here was taken at zero detuning and shows a Rabi splitting of $\sim$ 5meV between the upper and lower polaritons. c.) Calculated dispersion curves for exciton X, cavity γ and the strongly coupled normal modes UP and LP. d.) Contour map of the linear absorption spectra as a function of detuning (top) and excitation angle (bottom) axis. Spectra are normalized to the peak amplitude on a scale of $0 \rightarrow 1$.

In general, the collective coupling strength is determined by g_0 where $2g_0$ is the collective Rabi frequency, Ω. In semiconductor quantum wells, the addition of N quantum wells enhances the collective coupling [195, 197] providing a system-dependent coupling strength. The collective strong coupling condition is fulfilled when the photon-exciton coupling g satisfies the condition $2g\sqrt{N_{QW}} \gg \gamma_x, \gamma_c$ where γ_x, γ_c are the excitonic dephasing rate and cavity decay rate [192, 194].

6.2 Sample Structure

Our sample is a device built by our collaborators to demonstrate optical bistability and an electrically injected exciton-polariton LED [209, 210]. The sample consists of a microcavity with doped mirrors grown by molecular beam epitaxy on a n-doped GaAs substrate (Fig. 6.2a). The mirrors are made by alternated $Ga_{0.9}Al_{0.1}As/Ga_{0.1}Al_{0.9}$ layers. The bottom mirrors contains 24 pairs and is n-doped using silicon, the top mirror contains 20 pairs and is p-doped using carbon. The p-doped Bragg mirror is completed by a highly-doped p++ GaAs thin top contact layer. Aluminium graded concentrations at each interface in the Bragg mirrors are introduced to optimize mirror resistance. The GaAs cavity contains three $In_{0.05}Ga_{0.95}As$ quantum wells at the antinode of the field. The cavity layer is undoped to maintain the excitonic character of the quantum well excitations. The thickness of the cavity layer smoothly varies across the sample in order to tune the cavity mode with the exciton resonance.

Square mesas of 300 μm lateral size were etched down to the GaAs substrate using e-beam lithography followed by wet chemical etching. The mesas were defined at different positions of the wafer, thus obtaining different detunings between the cavity mode and the excitonic transition energy. Annular contacts were defined by e-beam lithography and Ti-Au evaporation (220 nm in thickness) on the top of the sample (Fig. 6.2b). In order to obtain a spatially homogeneous current flow, the internal part of the contacts is completed with a semitransparent (transmission $\sim$ 40 %) 13 nm Ti-Au layer. A uniform AuGeNi contact was evaporated and alloyed on the backside of the wafer [210].

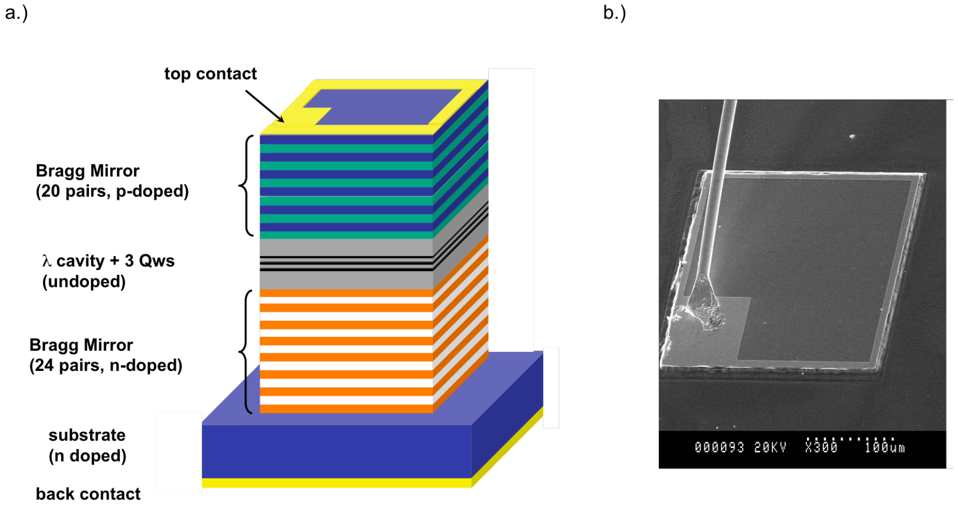

Figure 6.2: a.) Sample structure used for exciton-polariton experiments. The top mirror is a p-doped Bragg stack. The bottom mirror is a n-doped Bragg stack. The diode is etched into a mesa with top and bottom electrical contacts. b.) SEM picture of a wire-bonded exciton-polariton mesa.

6.3 Experimental Setup

In order to record MDCS spectra as a function of exciton-cavity detuning we built additional apparatus after our final beamsplitter. Exciton-polaritons are tuned by use of the wedged cavity thickness [19] or by varying the incident excitation wavevector [197]. Both approaches rely on changing the optical path length in the cavity. The wedged cavity method is a poor choice for photocurrent spectroscopy as contacts on a large lateral surface lead to poor device physics. We make use of the dispersion properties of the cavity to vary the exciton-cavity detuning. The cavity energy varies with the in-plane wavevector $k_{||}$ of the incident light (Eq. 1.21). The in-plane wavevector can be tuned by the angle of the incident angle of light from the relation [14]

$$k_{||} = n_c \frac{2\pi}{\lambda} \tan\left[\sin^{-1}\left(\frac{\sin(\theta)}{n_c}\right)\right] \sim \frac{2\pi}{\lambda}\theta. \tag{6.2}$$

To vary the incident excitation angle we position a translation stage before a two-inch diameter, 5cm focal length aspheric lens. We then translate the position of the beam across the lens to vary the excitation angle. This lens choice provides ~ 27° of range (Fig. 6.3). We also rotate the sample by ~ 7° in order to provide scanning range after the exciton-cavity avoided crossing that occurs at ~ 23°.

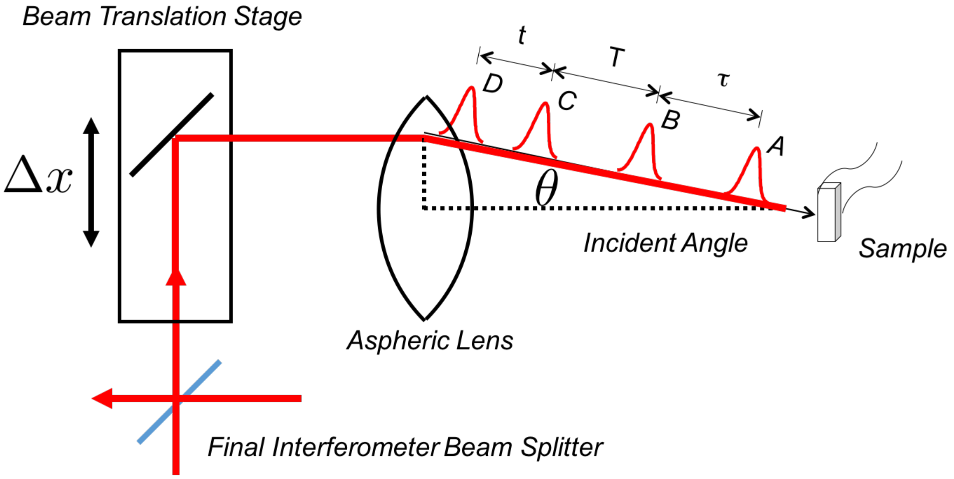

Figure 6.3: Experimental configuration for scanning the exciton-cavity detuning. The final beamsplitter combines all four pulses from the MDCS experiment. They are then spatially translated across the 5cm aspheric lens using a translation stage. The sample is rotated by ~ 7°.

6.4 Linear Characterization of Exciton-Polaritons

To characterize the exciton-polariton Rabi splitting we use a simplified two-pulse experiment to record linear absorption spectrum as a function of excitation angle(detuning) $\theta(\delta)$ (Fig. 6.1a). At zero-detuning $\delta = \hbar\omega_c - \hbar\omega_x = 0$ the linear absorption spectra exhibits two peaks split by a Rabi frequency $\Omega \sim 5$meV. These two peaks in Fig. 6.1b are the high energy and low energy normal modes of the strongly coupled system and are referred to as the upper polariton (UP) and lower polariton (LP). At zero-detuning the upper and lower polaritons are equally weighted superpositions of exciton and cavity. As the excitation angle is varied the absorption spectrum should exhibit an avoided crossing between the exciton (X) and cavity (γ) dispersion as calculated in (Fig. 6.1c). As the excitation angle decreases from zero detuning, the relative weighting of exciton to cavity of the upper polariton wavefunction should asymptote to favor excitonic character. In contrast the lower polariton should asymptote to more cavity character. At larger excitation angle, above zero detuning, the opposite behavior should be observed where the upper polariton becomes cavity-like and the lower polariton becomes exciton-like. For detunings $|\delta| \gg \hbar\Omega$ the more excitonic mode is the AC Stark shift of the bare exciton. By measuring the linear absorption as a function of excitation angle we are able to verify that our calculations from Eq. 6.1 agrees with our measurement (Fig. 6.1d).

Our measurements are insensitive to definite excitation numbers because our modulation scheme integrates over a range of excitation manifolds. The optically active transitions between excitation manifolds require transitions that satisfy $\Delta n = 1$. Therefore our spectrum is sensitive to the relative difference in excitation manifolds $\Delta n = 1$ across a range of excitation manifolds that goes from $n = 0 \rightarrow n \sim \frac{\epsilon\beta E^2}{2\hbar\omega_L}$. In this excitation density, ϵ is the dielectric constant, ω_L is the center laser frequency and β is the external field-cavity coupling fraction. Our nonlinear measurements are sensitive to the relative $\Delta n = 2, 3$ difference in excitation manifold depending on the pulse sequence used. However these are non-radiative, and our observation of them is only made possible through MDCS where the coherences between these higher order excitation manifolds are mapped onto radiative transitions.

6.5 MDCS of Exciton-Polaritons

Our characterization measurements presented linear spectra recorded by two incident pulses and Fourier-transformed with respect to the interpulse delay τ. A unique advantage of our approach is that conventional optical nonlinear spectroscopy relies on wavevector selection to isolate nonlinear signals. In polaritonic systems, non-collinear methods imply a mixing of different polariton wavevectors [174, 182, 187, 188]. Our collinear apparatus, which isolates non-linear signals in the radio frequency domain [49, 91, 92] circumvents this issue allowing us to study wavemixing within a single k mode of the exciton-polariton system. To perform multi-quantum MDCS experiments we use all four pulses prepared by our nested interferometers (Fig. 3.3) and depicted in Fig. 6.4a. In a two-quantum coherence ($\Delta n = 2$) experiment [42, 47, 145, 147, 188] a sequence of pulses excites the sample. The first pulse (A) creates a one-quantum coherence between the nth excitation manifold and the $(n+1)$ manifold. This coherence is subsequently converted by pulse (B) into a two-quantum coherence between the $(n+2)$ manifold and the (n)th manifold during time T. The third excitation pulse (C) converts this two-quantum coherence into a one-quantum coherence between the $(n+2)$ manifold and the $(n \pm 1)$th manifold. In this experiment, a fourth pulse converts this coherence into a population state where it is read out as photocurrent. The population produces a photocurrent because a small forward bias of 1.4V provides a field that separates the charges that make up the polaritons.

The experiment [92] uses four co-circularly polarized 100 fs pulses (Fig. 6.4), that have been radio-frequency shifted relative to each other. Third and fifth order nonlinear signals are collected as a modulated photocurrent. The fifth order signal can be measured by considering higher order wave-mixing signals and synthesizing an appropriate reference. The signal is recorded as a function of angle and the inter-pulse time delays T and t with $\tau = 0$. The signal $\mathrm{S}(\theta, T, t)$ is Fourier-transformed with respect to T, t to provide $\mathrm{S}(\theta, \hbar\omega_T, \hbar\omega_t)$. The multi-quantum coherence evolves during the time delay T and is sensitive to $\Delta n > 1$ coherences. In Fig. 6.4b we plot the absolute value of two-quantum ($\Delta n = 2$) MDCS spectra recorded at zero-detuning $\delta = 0$. The MDCS spectra reveals four peaks split by the Rabi frequency Ω. The two diagonal peaks correspond to the lower and upper polariton modes. The two off-diagonal peaks represent a state that is a mixture of the lower and upper polariton modes. This state has two quantum pathways, it can radiate at either the upper polariton energy or the lower polariton energy. The projection onto the $\hbar\omega_\tau$ axis shows the spectrum that conventional spectroscopy techniques are sensitive to; the two mode frequencies UP and LP corresponding to $\Delta n = 1$ coherences. The projection onto $\hbar\omega_{tau}$ shows that the spectrum that two-quantum coherences are sensitive to; the frequencies corresponding to $\Delta n = 2$ coherences. The real part of the MDCS spectrum is shown in Fig. 6.4c. All four peaks are

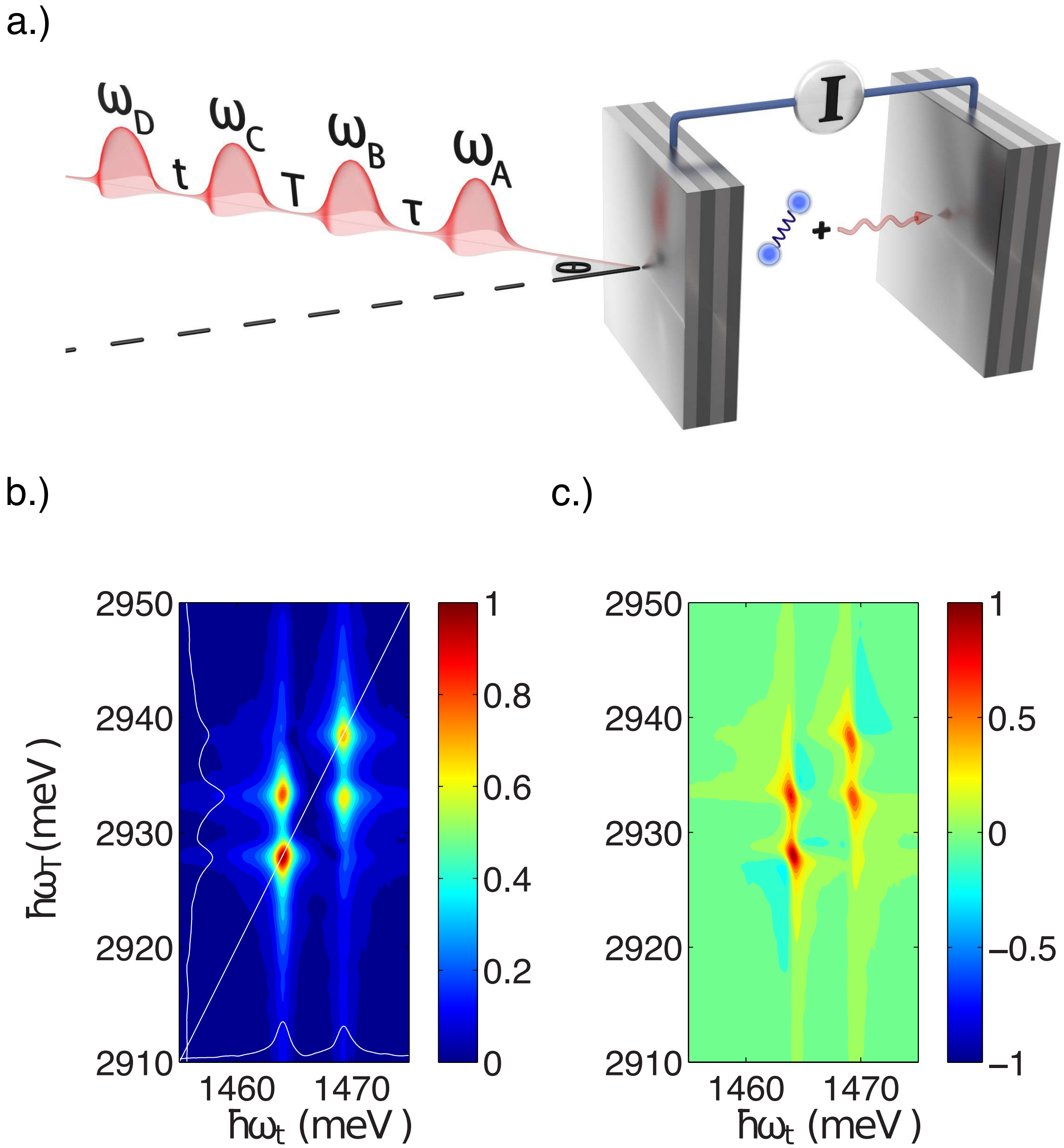

Figure 6.4: a.) Four pulse excitation scheme to study exciton-polaritons via photocurrent Fourier transform spectroscopy. The signal is recorded as a function of inter-pulse delays t and T with $\tau = 0$. b.) Absolute two-quantum MDCS spectrum generated by Fourier transforming the time-domain signal with respect to t and T. This plot reveals two diagonal peaks and two off-diagonal peaks. c.) The real part of the MDCS spectrum reveals that absorptive peaks. Absorptive peaks are an indication of excitation induced dephasing or Pauli blocking.

dominantly absorptive Ch.2 as indicated by their positive phase indicating that excitation induced dephasing or Pauli blocking is the primary many-body interaction responsible for breaking the symmetry in the quantum pathways at zero detuning.

We calculate and plot Fig. 6.5a-b, for low excitation density where the quantum well exciton is not screened by electron-holes pairs [158], the bare and coupled $\Delta n = 2$ cavity-exciton modes from Eq. 6.1 as a function of excitation angle θ. The bare modes intersect at the zero-detuning angle, where the coupled modes demonstrate a double avoided crossing. Each of the avoided crossings is predicted to have a Rabi splitting Ω of 5meV. In order to isolate and measure these avoided crossings using multi-quantum spectroscopy we record MDCS spectra as a function of excitation angle θ. We then integrate the measured signal along $\hbar\omega_t$ and plot the frequency integrated FWM spectrum as a function of excitation angle (Fig. 6.5c). Our measurement matches our calculations exhibiting two avoided crossings at zero-detuning $\sim 23°$. The observed spectrum corresponds to pairs of polaritons labeled $U2P$ for two upper polaritons, $L2P$ for two lower polaritons and $M2P$ for a mixture of upper and lower polariton. Within the resolution of the experiment, the Rabi splittings in the two-quantum spectrum match those in the linear spectrum. In other words the $L2P$ peak is observed at twice the lower polariton energy, the $U2P$ peak is observed at twice the upper polariton energy and the $M2P$ peak is observed at the sum of the upper and lower polariton energies. This result is only expected if our measurement occurs at sufficiently low excitation density so as not to screen the excitons. We also calculate the expected dispersion for $\Delta n = 3$ coherences (not shown) and find that we expect six peaks in the absolute MDCS spectrum. Two of the six peaks are expected to be along the diagonal and four off the diagonal. The four off-diagonal peaks, like the off-diagonal peaks of the two-quantum coherence, represent mixed states with two quantum pathways capable of radiating into either an upper or lower polariton. We performed a higher order three-quantum coherence measurement and plot the frequency integrated six-wave mixing as a function of excitation angle in Fig. 6.5d. The measurement agrees with our calculation showing a triply avoided crossing between four modes each with a Rabi splitting of 5meV. We discuss the power dependence of this data in Section(6.6). The spectra at different powers exhibits no deviation from that presented here.

The series of spectra recorded $\Delta n = 1, 2, 3$ has the eigenstructure expected for two coupled quantum harmonic oscillators. However, coupled quantum harmonic oscillators are not expected to produce nonlinear wave mixing signals due to destructive interference of quantum pathways [211, 212]. Excitons are composite bosons at low excitation density; corrections to the bosonic approximation take the form of many-body interactions that break the symmetry in the quantum pathways and enable the observation of these multi-quantum coherences. The analogous strongly coupled atomic system would require significant atomic collisions or dipole interactions [127, 173, 213, 214] to produce sufficient nonlinearity to break the symmetry observed here [215].

Since the many-body interactions are perturbative we are able to consider the dressed states involved in the transitions. In the exciton-polariton eigenbasis the nth manifold has an excitation level

$$n = n_{UP} + n_{LP}. \tag{6.3}$$

The wavefunctions at the nth manifold are combinations of UP and LP with wavefunctions $|n_{UP}, n_{LP}\rangle = |n_{UP}\rangle \otimes |n_{LP}\rangle$. The radiative transitions occur between $\Delta n = 1$ of each excitation manifold. Thus the coherences that contributed to the linear absorption spectra are between states with the difference of a single polariton such as $\rho_{n,m} = |n_{UP}, 0\rangle\langle m_{UP}, 0\rangle \delta_{n,m=n\pm1}$ where $\rho_{n,m}$ is a density matrix element and n and m are two different excitation manifolds each separately subscripted by Eq. 6.3. The single polariton wavefunctions can be solved from Eq. 6.1. In an exciton-cavity $|n_x, n_c\rangle$ basis at zero-detuning they are the equally weighted superpositions

$$|UP\rangle = \frac{|1,0\rangle + |0,1\rangle}{\sqrt{2}} \tag{6.4}$$

$$|LP\rangle = \frac{|1,0\rangle - |0,1\rangle}{\sqrt{2}}. \tag{6.5}$$

In the MDCS spectrum the peaks along the diagonal correspond to coherences between states of only a single type of polariton either LP or UP. The off-diagonal peaks correspond to mixtures of both UP and LP. During time t the coherences recorded are between states with the difference of a single polariton. During time T higher order non-radiative coherences such as $\rho_{n,m} = |n_{UP}, 0\rangle\langle m_{UP}, 0\rangle\delta_{n,m=n\pm 2(3)}$ exist for the two(three) quantum coherence. These coherences evolve with the energy difference of two(three) polaritons. The two polariton wavefunctions can also be solved from Eq. 6.1. In an exciton-cavity $|n_x, n_c\rangle$ basis at zero-detuning they are

$$|U2P\rangle = \frac{|2,0\rangle + |0,2\rangle + \sqrt{2}|1,1\rangle}{2} \tag{6.6}$$

$$|L2P\rangle = \frac{|2,0\rangle + |0,2\rangle - \sqrt{2}|1,1\rangle}{2} \tag{6.7}$$

$$|M2P\rangle = \frac{|2,0\rangle - |0,2\rangle}{\sqrt{2}}. \tag{6.8}$$

Of potential interest to engineering quantum optical devices is accessing the $|M2P\rangle$ states deterministically. This state represents a $NOON$ state with $N = 2$. NOON states are of interest for accessing macroscopically entangled “Schrodinger cat states” that evolve with a phase that is N times faster than classical states. These states are of fundamental interest to studying decoherence on many-particle entanglement as well as enhanced measurement sensitivity [216–219]. We expect there is series of such high-NOON states at n = even excitation manifolds as our Hamiltonian is closely analogous to a quantum beamsplitter [220] as discussed in Appendix(C).

Because of our detection scheme our measurement is not sensitive to specific coherences; we are not able to deterministically achieve a quantum optical-few quanta limit.

However, our modulation scheme samples all excitation manifolds integrating together the multi-quantum coherences of *many* different excitation densities. Since the coherences from different excitation densities sum together to provide our spectrum we expect that the ladder we have observed is symmetric all the way down to the few quantum regime. Varying the peak excitation power provides no observable deviation in the recorded spectra. The lowest peak excitation density for which we recorded two-quantum spectra is estimated as $\sim 3 \cdot 10^{8}\text{cm}^{-2}$ (all four pulses coincident), more than two orders of magnitude below the exciton-polariton saturation density [158].

6.6 Power Dependence Measurements

In order to characterize our measurement and the nonlinear regime for exciton-polaritons we varied the peak excitation density and recorded a power dependence. The e^{-2} beam waist is $\sim 45\mu$m, the laser has a repetition rate of 76MHz and we calculated the cavity-external field coupling to be 17%. The peak signal strength is recorded as a function of *external* excitation power and plot the nonlinear regime in Fig. 6.6. In MDCS a four-wave mixing signal (FWM) is recorded. In our detection scheme the FWM scheme should have a fourth order power dependence. For reference this slop is plotted in Fig. 6.6.

The data recorded in Fig. 6.5 at zero-detuning was recorded at 6.4μW. The power was slightly varied across different detunings in order to keep the linear absorption (measured simultaneously) constant. Additional spectra was recorded at lower and higher excitation density and exhibit no difference. The six wave dispersion curve of (Fig. 6.5d) was recorded at a constant power of 85μW.

6.7 Conclusion

Our measurements explore the exciton-polariton ladder of states in the weak excitation regime providing qualitative information about the energy structure of this system. This structure is characteristic spectrum of two coupled quantum harmonic oscillators with perturbative nonlinearities due to Coulomb mediated many-body effects. While we are not able to excite the system deterministically with few quanta, our spectrum is the integrated sum of many excitation densities providing evidence for this structure over a large range of excitation densities. Varying the peak excitation density provides no observable change in the spectrum or Rabi splitting of the avoided crossings. Our measurement is made possible by our use of multi quantum coherent spectroscopy and a novel approach that allows us to excite exciton-polaritons in a single mode. In the context of quantum optics our results explore the statistical dispersion of exciton-polaritons providing the energy eigenstructure and dressed states. As an analogue to measurements performed in the quantum optical statistical regime our results present a new approach to characterizing the excitation statistics of strongly coupled systems. This approach may be well suited to characterizing quantum systems that are naturally in the quantum statistical regime.

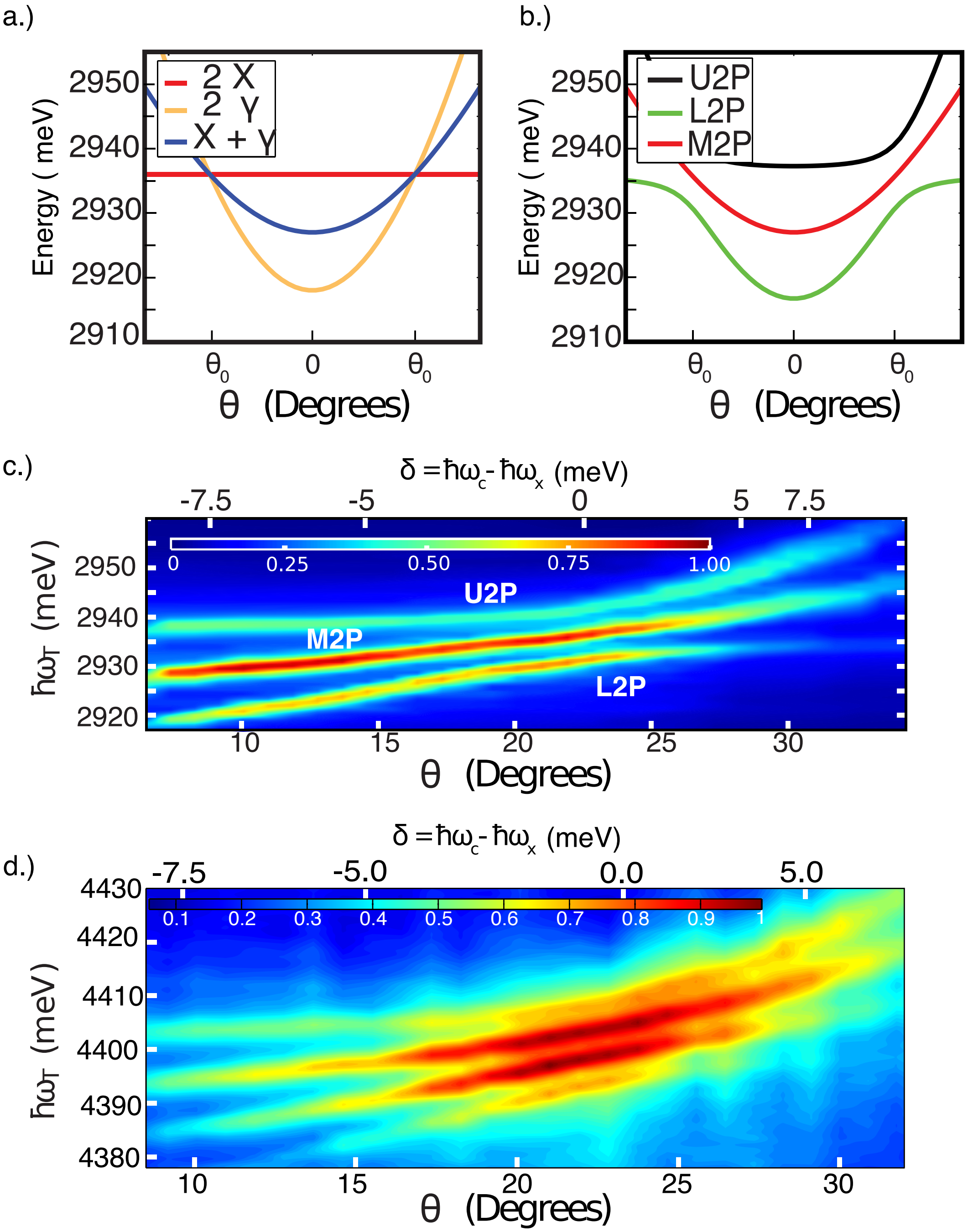

Figure 6.5: a.) Dispersion of uncoupled doubly excited exciton ($2X$) and doubly excited cavity (2γ) pairs as a function of excitation angle. A dispersion curve of an exciton and a cavity $X + \gamma$ is included. At the avoided crossing angle θ_0 all three energies are degenerate. b.) Dispersion of strongly coupled exciton and cavity pairs as a function of excitation angle. At θ_0 a double avoided crossing is calculated. The new modes are pairs of upper polariton (U2P), middle polariton (M2P) and lower polariton (L2P). The three new modes are split with an energy of $\sim$ 5meV. c.) Frequency integrated four-wave-mixing plotted as a function of excitation angle-detuning. The data exhibits three modes split by 5meV exhibiting a doubly avoided crossing. d.) Frequency integrated six-wave-mixing plotted as a function of excitation angle-detuning. The data exhibits four modes split by 5meV exhibiting a triply avoided crossing.

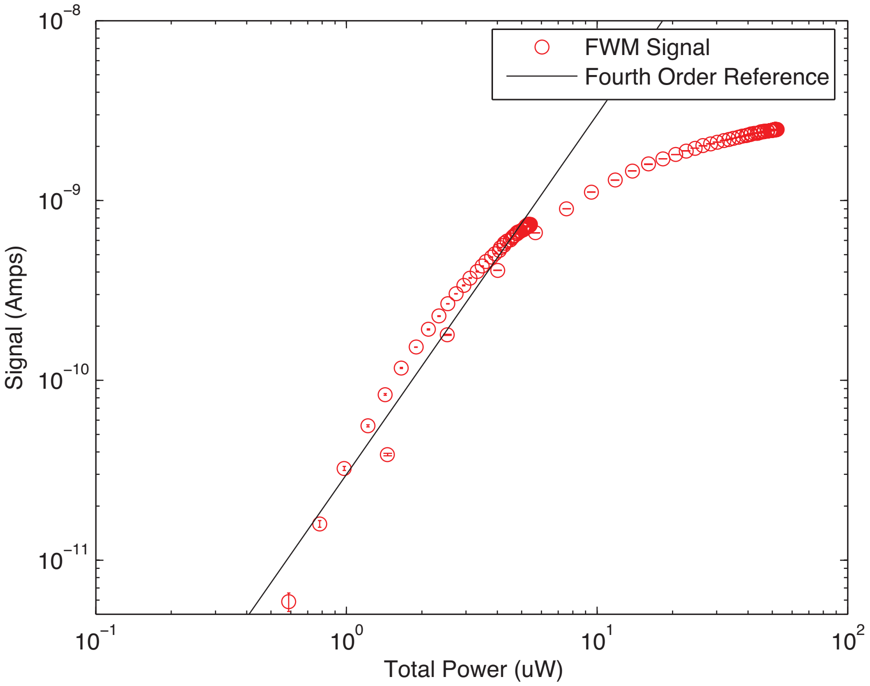

Figure 6.6: Power dependence of the FWM signal as a function of total power. The signal is in the fourth order regime from the lowest powers to about 8μW. The excitation density at the lowest power is $7.5 \cdot 10^{7}\text{cm}^{-2}$

Chapter 7

Measurement of Polariton-Polariton Interactions

The optical response of semiconductor quantum wells is altered by many-body interactions and exciton-exciton scattering. These interactions are polarization dependent and lead to states such as the biexciton and the dropleton. A theoretical description of the biexciton [47, 221–226] or dropleton [227] requires higher order many-body correlations, which are not captured in a model that treats the polarization as arising from $\sigma^+(\sigma^-)$ populations of excitons [30, 228]. These higher body correlations are exemplified by the biexciton, which is a four-particle state, whose binding energy is an appreciable fraction of the exciton binding energy in GaAs. Historically, the difficulty of understanding the role of the biexciton led to a rich exploration of many-body physics in semiconductors [30, 42, 47, 143, 221–226, 229–231]. In quantum wells, the co-polarized exciton has a significantly smaller interaction energy that leads to four particle states that are correlated but not bound. Despite being smaller, it is these interactions that have the most dramatic effect on excitons in the strong coupling regime.

The interesting properties of exciton polaritons historically arose from co-polarized interactions. In particular, superfluidity does not exist in bosonic systems without interparticle interactions [232–234] and these interactions are responsible for the blueshift and optical nonlinearities in both polariton lasers and parametric amplifiers [174, 178, 183, 235]. The effect of these interactions on the optical response of exciton-polaritons is a difficult topic due to the large effect of the cavity coupling. Since the cavity-exciton coupling creates new normal modes this effect must be considered first. However, transforming into a polariton basis leads to truncated excitonic interactions providing only an effective polariton many-body interaction potential. The role of higher order correlations, such as the one that provides the biexciton, are even murkier. For instance, it is unclear if these correlations create a biexciton that is decoupled from the cavity or if the biexciton is strongly coupled to the cavity forming a biexciton-polariton or if two polaritons bind to form a bipolariton. This problem is particularly difficult in GaAs-systems as the biexciton binding energy of ~ 1.5meV is comparable to the Rabi energy of 5meV [177, 188, 191, 236–239].

Despite their importance, understanding of these interaction potentials remains poor. As a result, recently there has been an improved effort to characterize these many-body interactions [184, 186–189, 191, 240, 241]. Unfortunately, the experiments typically used are not ideal to studying exciton-polariton interactions due to their reliance on wave-vector matching or single-pulse differential transmission. The mixing of wave-vectors is a particular problem since it requires a multi k-mode analysis of the polariton effectively mixing the interaction potentials of a single mode with that of two-or more modes. Conversely, our approach allows us to excite polaritons in a single mode providing a clear picture of polariton-polariton interactions.

We have performed experiments on exciton-polaritons in both cocircular and crosscircular regimes. In this chapter we review progress in these experiments. The first section is concerned with experiments on cross-polarized exciton-polaritons where we attempt to understand the role of the biexciton(or bipolariton). We find that neither a bipolariton nor a biexciton is present for cross circularly polarized exciton polaritons. Therefore, our results directly contrast with claims to observe these states [177, 237–239] . Interestingly, we observe a change in the phase of our MDCS spectrum that is consist with the Feshbach resonance reported by for high excitation density[191]. Additionally, we observe the same behavior with a mixed upper and lower polariton state. Therefore, our results suggest a three state interaction beyond the simple Feshbach resonance presented by [191]. Our ability to disentangle this interaction is limited by our understanding of the scattering process of the polaritons. We excite these states at relatively high dispersion from which they can relax to lower energy polaritons. In the second section we attempt to quantitatively measure the cocircular polariton interaction constants. We devise a scheme to remove the effect of phase space filling from the many-body interactions effect and fit our theory to the data.

7.1 Background on Many-Body Interactions

7.1.1 Exciton-Exciton Interactions in Quantum Wells

In semiconductors the exciton is a two-body low excitation density hydrogenic eigenstate of the crystal. In the Heitler-London picture where the hole is treated as much heavier than the electron, it is the electron-electron scattering that determines the exciton-exciton scattering process. This scattering process leads to both repulsive and attractive interactions depending on the spin of the electrons. The two scattering electrons can form either symmetric (triplet) or antisymmetric (singlet) spin states. The triplet configuration is characterized by an antisymmetric spatial wavefunction, which has an anti-node between relative excitons leading to a repulsive interaction. In contrast, the singlet has a symmetric spatial wavefunction that increases the electron density between the two excitons. In the singlet configuration the interaction potential has a local minimum which can bind the two excitons into a molecular state known as the biexciton. The depth of this local minimum is large in GaAs quantum wells giving a biexciton binding energy of ~ 1.5 meV, an appreciable fraction of the exciton binding energy ~ 9 meV. This biexciton represents a four-particle correlated state because it involves two holes and two electrons.

To optically excite these singlet or triplet configurations requires consideration of the optical polarization. Optical excitation with a single circular polarization can only lead to the formation of the triplet state for which the dominant exciton-exciton interaction is repulsive. Biexcitons form when semiconductors are excited with both left and right optical polarizations because then singlet states can form.

A more complete picture of the biexciton must take into account all electron-hole spin configurations. For excitation that excites heavy-hole excitons, the electron-hole "soup" after both left and right optical excitation contains both $J_z = \pm\frac{3}{2}$ holes and $J_z = \pm\frac{1}{2}$ electrons. This soup has the ingredients for optically inactive "dark" (due to $\Delta J = 1$ transition rules) excitons which play a critical role in the biexciton formation [242].

Understanding the role of these interactions and their effect on the optical response is difficult to disentangle. In order to achieve an appreciable degree of exciton-exciton scattering it is tempting to increase the exciton density. However larger excitation density makes the residual Coulomb and phase space filling effects more important and can lead to a transition from excitons to an electron-hole continuum. Studies of exciton-exciton interactions are therefore best done in a perturbative regime at the lowest power possible.

7.1.2 Exciton-Polaritons

In the previous discussion exciton-exciton interactions were reviewed with the intent to explain the rich many-body physics that arises from them. This section is concerned with discussing how these interactions manifest for exciton-polaritons. For cocircularly polarized excitation these theories expect a repulsive polariton-polariton interaction [12]. For cross-polarized excitation there is no consensus as to how the interactions manifest. Can the biexciton strongly couple to the electromagnetic field [191] creating a biexciton-polariton [237]? Is the biexciton in the weak coupling regime even when the exciton is strongly coupled[177, 238, 239]? Do the polaritons interact to form bipolaritons? Recently, it has been suggested that the cross-polarized polaritons can scatter against an inaccessible bound biexciton state leading to a Feshbach resonance [191].

The manifestations of polariton interactions are not well understood. It is only recently, twenty-five years after the first polariton samples, that it became apparent that lower and upper polaritons interact with each other [188, 240]. Most experiments and theories have focused on the lower polariton, where for cocircularly polarized interactions there is typically a blue shift due to repulsive polariton-polariton interactions. However, both the cross-polarized interactions and the interactions between upper and lower polaritons are poorly understood. The goal of our experiments is to understand and quantitatively measure these interactions.

7.2 Cross Polarized Excitation of Exciton-Polaritons

In this section, we discuss our measurements attempting to study the cross-polarized properties of exciton-polaritons. Our measurements are the same as Fig. 6.3 except we use the exciton-cavity detuning to vary the polariton-polariton interactions. We attempt to access the bipolariton (or biexciton) using different cross polarized light pulses. The polarization sequence of most interest is $\sigma^-\sigma^+\sigma^+\sigma^-$ (Fig. 7.1a) because in a third order regime this pulse sequence does not have a quantum pathway that provides a population. Note we are not strictly in a third-order regime, as we were attempting to access the higher excitation density regime of the reported Feschbach resonance [191]. However we estimate our excitation density is $\sim 1.2 \cdot 10^{10}$ cm^{-2} about fives times lower than their recorded result. We use MDCS to isolate the different interactions (Table 7.1). The different coherences induced by the four pulses are illustrated in Fig. 7.1b. In exciton-polaritons there is a two-mode degeneracy in polarization, however our pulse sequence spectrally separates the different cross-circular interactions. In a model in which there is no biexciton, we expect there should be four peaks corresponding to the higher-order coherences of the doubly excited states. During time T these doubly excited states will have contributions only from cross-circular interactions Table(7.1). After the third pulse each singly-excited state $|LP(UP)\rangle^{\pm}$ contributes to two coherences (Fig. 7.1b).(Note: The doubly excited states in this basis are separable product states). For non-zero interaction energies, and no bipolaritons, we expect to see the spectrum of Fig. 7.1c with peaks corresponding to the color-coded Feynman diagrams of Fig. 7.1d.

Table 7.1: Interactions Δ Probed by $\sigma^-\sigma^+\sigma^+\sigma^-$ Polarized Pulses.

$\boldsymbol{\rho_{ij}}$	**Cross-Circular Interactions**
$\|UP\rangle^-\|UP\rangle^{++}\langle g\|$	$\Delta_{UP-,UP+}$
$\|LP\rangle^-\|LP\rangle^{++}\langle g\|$	$\Delta_{LP-,LP+}$
$\|UP\rangle^-\|LP\rangle^{++}\langle g\|$	$\Delta_{UP-,LP+}$
$\|LP\rangle^-\|UP\rangle^{++}\langle g\|$	$\Delta_{LP-,UP+}$

In this pulse sequence the interactions probed during time T are the cross-polarized interactions. These will give rise to four distinct peaks in the multi-quantum spectrum. It is possible to identify four distinct interactions.

Most studies of biexciton dynamics in exciton-polaritons have focused on the lower polariton branch. This is because, in a two-mode or mean field picture of polaritons it is difficult to imagine a situation where the upper polariton can contribute biexcitonic effects. The upper polariton is always higher energy than the exciton and thus can not approach the biexciton energy as a function of exciton-cavity detuning. In contrast the lower polariton can be tuned to near-resonance with the expected biexciton binding energies. Here we show that the mixed mode of an upper and lower polariton can intersect with the expected biexciton energy. This pulse sequence accesses the doubly excited manifold where the biexciton can be directly observed [42]. If the cross-mode interactions $\Delta_{LP-,UP+}, \Delta_{UP-,LP+}$ are non-zero then these states can be tuned into resonance with the biexciton. We measure both the higher order (Fig. 7.2a) and first order dispersion of the cross-polarized polaritons in Fig. 7.2b. In our measurements only cross-polarized doubly excited polaritons, and no biexcitons, are observed in direct contrast to previous claims [237–239]. Because we do not see a biexcitonic resonance we plot both the expected doubly excited exciton energy (black line) and the biexciton energy (1.5meV binding energy) (green line) in Fig. 7.2a. The biexciton energy never overlaps with the doubly excited upper polaritons, however it does intersect both the mixed mode of upper and lower polariton (middle dispersion) and the doubly excited lower polaritons. In our measurements, the biexciton intersects the mixed-state dispersion near the doubly avoided crossing. At the doubly avoided crossing we expect biexcitonic interactions, leading to bound states, to be a smaller effect because the polariton wave functions are an equal superposition of cavity-exciton. At larger detuning $\delta \sim 5$meV the doubly excited lower polariton intersects the biexciton energy. At these detunings the lower-polariton has an increasing excitonic fraction making biexcitonic effects more likely.

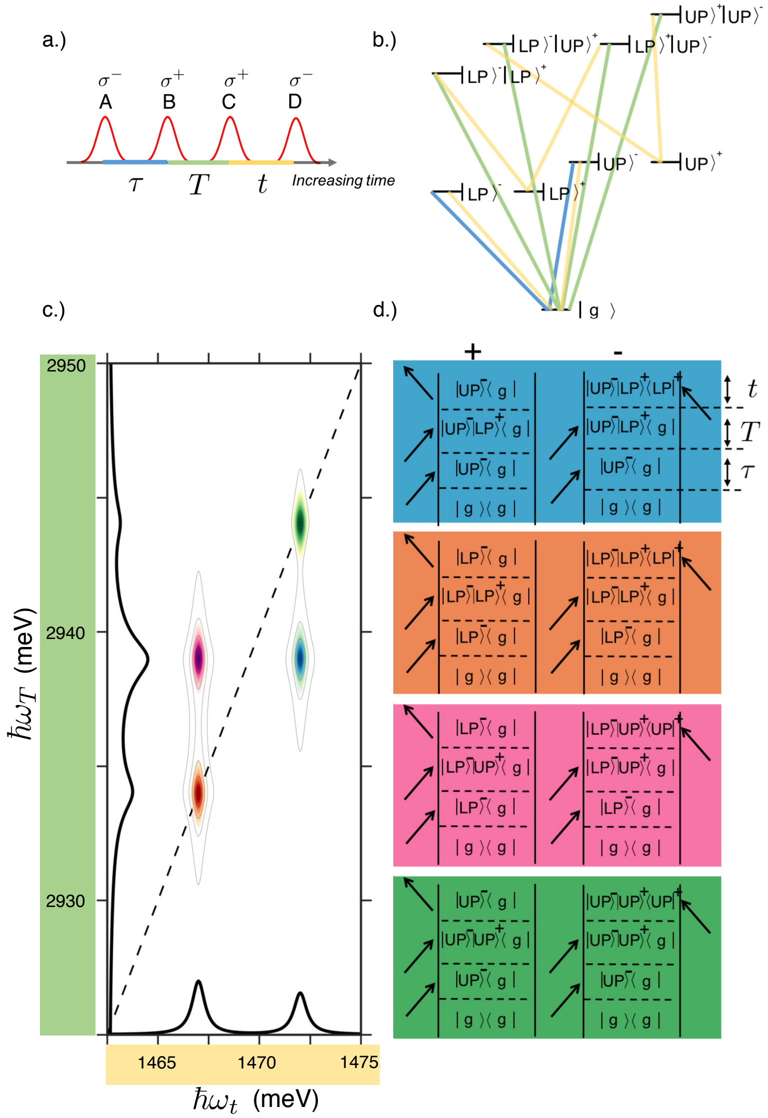

Figure 7.1: a.) Excitation pulse sequence for exciton-polaritons excited by $\sigma^-\sigma^+\sigma^+\sigma^-$ polarized pulses. b.) Effective energy diagram showing the coherences during times τ (light blue), T (light green) and t (yellow). c.) Expected two-quantum MDCS spectrum in the presence of cross-polarized many-body interactions. The peaks are color coded according to their quantum pathways. d.) The Feynman diagrams for this polarization including only the first three pulses. The final σ^+ pulse reads out the states effectively multiplying the number of diagrams by a factor of two. The rephasing diagrams lack a population term. Each peak in a MDCS spectrum corresponds to two diagrams.

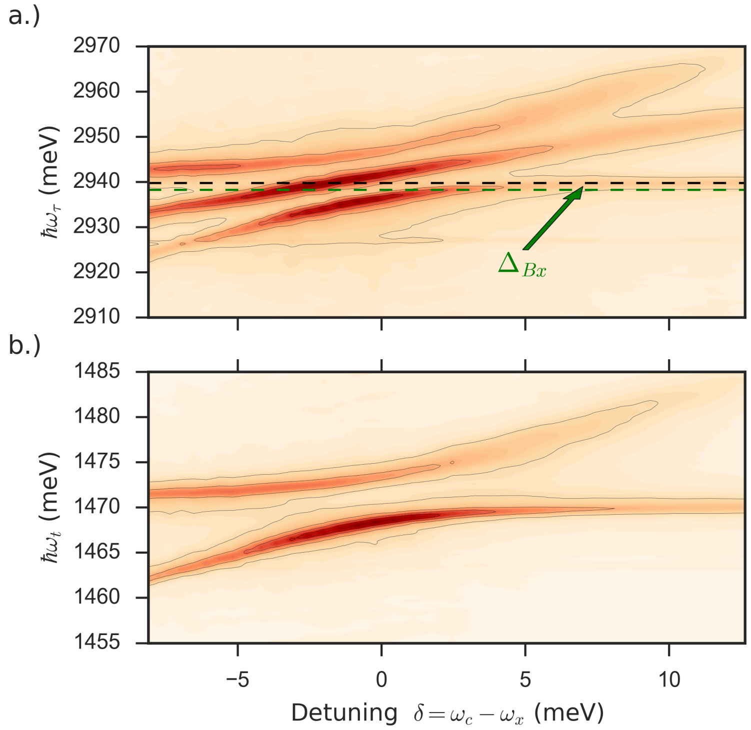

Figure 7.2: Measured dispersion curves for polaritons excited by cross-polarized light. a.) Frequency integrated two-quantum spectra as a function of exciton-cavity detuning. The dispersion curves reveal no biexciton which would have a flat dispersion curve (green line). Plotted for references is the doubly excited exciton dispersion (black line). At large detuning the lower-polariton wavefunction asymptotes to the doubly excited exciton. b.) The frequency integrated one-quantum spectra plotted as a function of exciton-cavity detuning.

In the work of Takemura et al. [191] an exciton-polariton Feshbach resonance was reported when the lower polariton mode intersected the biexciton energy. A Feshbach resonance describes the scattering of a continuum off of an inaccessible bound state [243]. This phenomena is characterized by a scattering length and a collisional loss (Fig. 7.3). In the context of semiconductor physics the scattering length is related to the self-resonant energy shifts (EIS) and the collisional loss is related to the scattering-induced dephasing (EID). Takemura proposed the scattering of an oppositely polarized continuum of two-lower polaritons scattering off of the bound biexciton state. The evidence for this was the dispersive energy shift as a function of exciton-cavity detuning of the lower-polariton branch.

Using MDCS, we observe a similar change in the self-resonant energy as a function

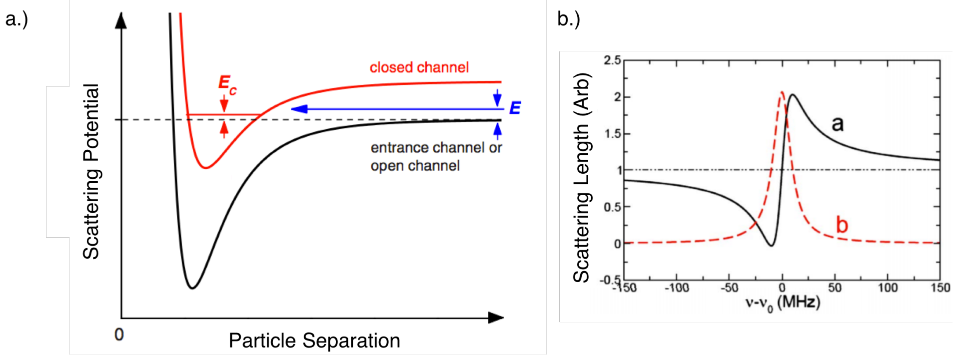

Figure 7.3: a.) Scattering potentials for the continuum and bound channels. The bound channel is inaccessible to the continuum but when the continuum comes into resonance with a state in the bound channel the polaritons exhibit enhanced scattering. b.) Characteristic scattering of a Feshbach resonance as a function of detuning. The scattering length between two states becomes very large (a) as the continuum is tuned onto resonance with the bound state providing a dispersive shape. The collisional loss (b) exhibits a resonant character. Figures adapted from [243].

of exciton-cavity detuning. We plot the real part of the MDCS spectra as a function of detuning in Fig. 7.4. Near the biexciton resonance, the doubly excited states $|LP\rangle^{-}|LP\rangle^{+}\langle 0|$ and $|LP\rangle^{-}|UP\rangle^{+}\langle 0|$ experience a dramatic change in their phase. This phase change is indicated in the real part of an MDCS spectrum by a transition from dispersive with positive EIS, to *emissive* indicating excitation induced *narrowing* and then to dispersive indicating negative EIS. This dramatic shift in the real part essentially confirms the measured result of [191]. However the $|LP\rangle^{-}|UP\rangle^{+}\langle 0|$ state indicates that the right polarized upper polariton plays a critical role in the scattering process. It is possible that there are two Feshbach resonances, a closed channel for both the doubly excited lower polaritons and for the mixed states. However, the $|UP\rangle^{-}|LP\rangle^{+}\langle 0|$ state does not exhibit the same dispersive change in its interaction energy. This fact suggests that the observed dispersive change in the interaction energy is the result of a three state scattering process between the $|LP\rangle^{-}$,$|LP\rangle^{+}$, and $|UP\rangle^{+}$ states. We are currently theoretically investigating this phenomenon.

Note that in further studies of we observe similar physics in resphasing data with $\sigma^{-}\sigma^{+}\sigma^{-}\sigma^{+}$ polarization (not shown). However we do not observe this behavior for $\sigma^{-}\sigma^{-}\sigma^{+}\sigma^{+}$

polarization. To make this change in interaction energy clear we plot diagonal slices (Fig 7.5) of the left-two peaks in the MDCS spectra of Fig. 7.4. A clear transition of the lineshape from positive interaction energy at lower detuning (red curves) to negative interaction energy at larger detuning (blue curves) is observed. In between the MDCS spectra becomes *emissive* indicating that instead of excitation induced dephasing there is an excitation induced *narrowing.*

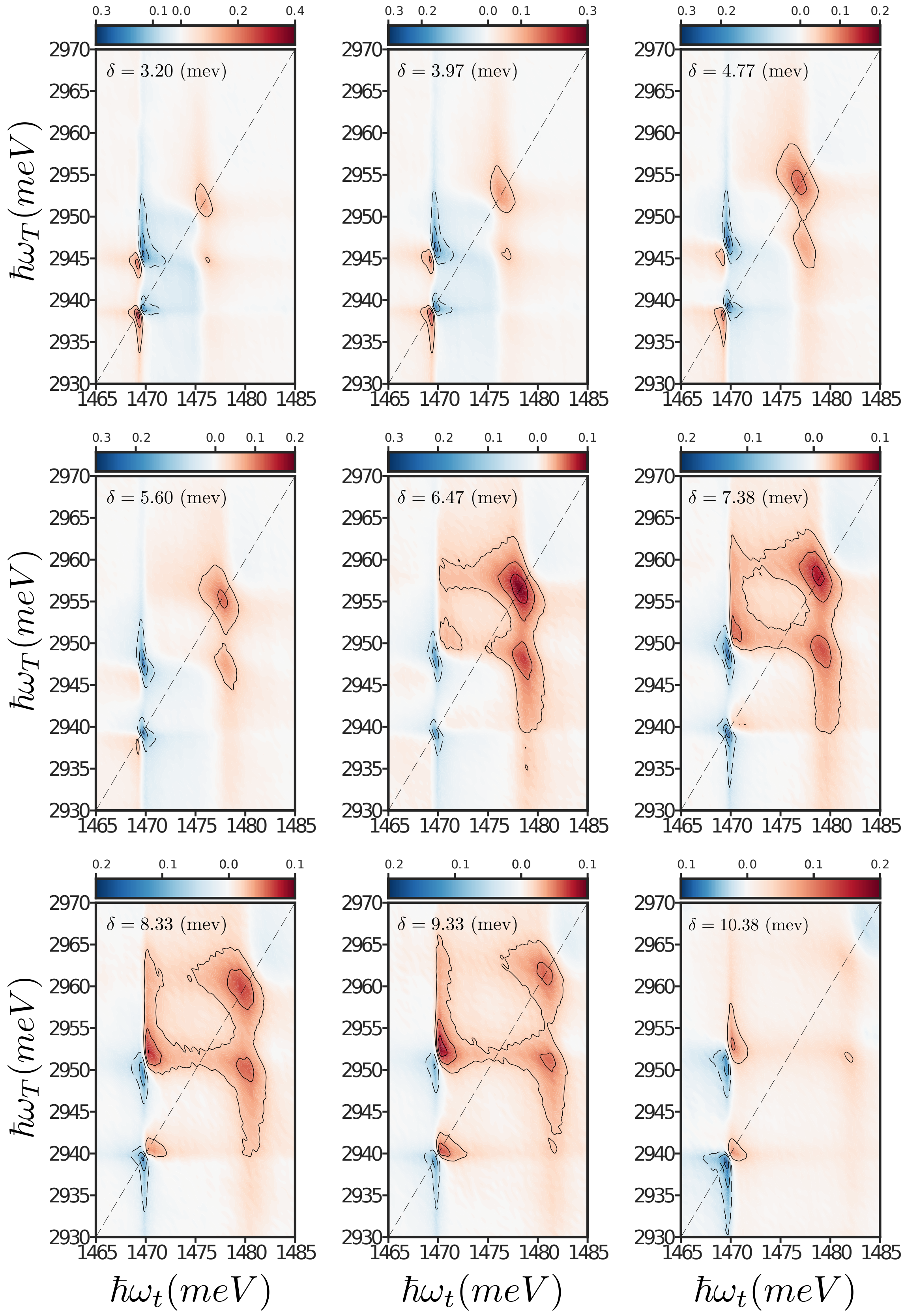

Figure 7.4: Real Part of MDCS spectra as a function of exciton-cavity detuning δ measured for $\sigma^-\sigma^+\sigma^+\sigma^-$ polarized excitation pulses. The states $|LP\rangle^-|LP\rangle^+\langle 0|$ and $|LP\rangle^-|UP\rangle^+\langle 0|$ experience a phase roll when near-resonance with the biexciton.

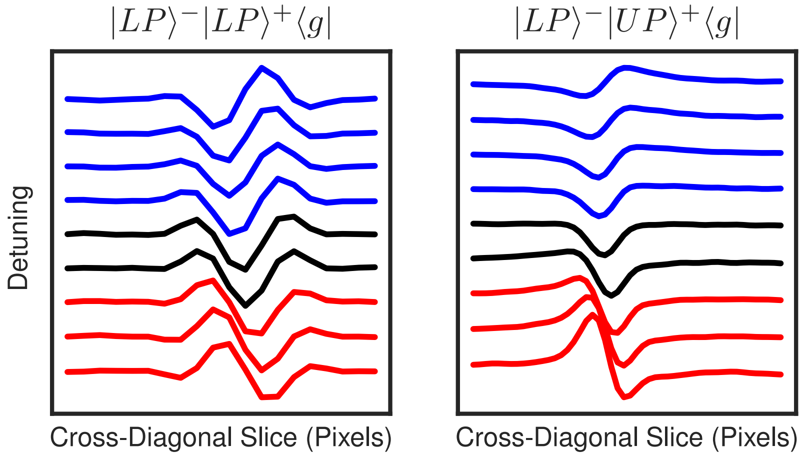

Figure 7.5: Diagonal slices of MDCS spectra as a function of increasing detuning. Red curves correspond to smaller detuning and positive interaction energy, (black) curves for an emissive lineshape and (blue) curves for negative interaction energy. The left panel shows slices of $|LP\rangle^{-}|LP\rangle^{+}\langle 0|$ and the right panel shows slices of $|LP\rangle^{-}|UP\rangle^{+}\langle 0|$.

Our measurements indicate a new type of polariton scattering exists for cross-polarized polaritons due to the biexciton resonance. In particular we expect that the $|LP\rangle^{-}$ state is involved in three-state collisions with both the $|LP\rangle^{+}$ and $|UP\rangle^{+}$ states at the biexciton resonance. This mapping is unavailable to the other mixed mode peak in the MDCS spectrum for unknown reasons for which we are trying to understand.

7.3 The Co-Circular Interaction in Exciton-Polaritons

In the previous section we considered the role of the biexciton in polariton-polariton scattering. In this section we consider a simpler subset of polariton-polariton scattering due to co-circular interactions. In these experiments we excited the polaritons with only σ^{-} polarization using the multi-quantum coherences as a direct probe of these interaction energies. Our analysis is motivated by a desire to quantify these interactions as they are responsible for effects such as superfluidity and play a role in Bose-Einstein condensation. Despite their importance, the exact role of these interactions is poorly understood and controversial in no small part because they are poorly measured [184, 244].

Quantitatively, measuring interaction energies in semiconductors is a convoluted problem, the transition dipole moments change with excitation density due to Pauli screening, there can be self-resonant interactions and inter-resonant interactions. It has been argued that Pauli exclusion between the excitons fermionic components is the most important interaction for excitons, so that Coulomb mediated many-body interactions only provide corrections [244–248]. Additionally, for exciton-polaritons there is a photon-assisted exchange interaction independent of the Coulomb interaction [244]. Unfortunately, experiment cannot distinguish between these mechanisms directly.

Pump-probe techniques project inter- and intra-resonant interactions onto the same peak where they become inseparable. For this reason MDCS is a preferred technique because it can in principle isolate the inter- and intra-mode interactions. In a few-level model, that effectively truncates the excitation ladder, it is often a reasonable approximation that the dipole moments of the different transitions are the same. In this case the many-body interactions can be read out from the real part of the MDCS spectrum. This picture essentially neglects the phase-space filling of the ensemble, providing only the phase space filling of the two-levels. The phase-space filling of the ensemble manifests as a reduced dipole moment between different excitation manifolds and can be included in truncated models (Ch.4). The problem with this assumption is, that if it is wrong, the interfering quantum pathways in an MDCS spectrum have both different phases (due to many-body interactions) *and* different amplitudes due to the changing dipole moment. At this point, a fit to a measurement will be hopeless for extracting physical many-body parameters. The problem of fitting many resonances that are nearly degenerate with each other is famously poorly behaved [249, 250] and the inclusion of these resonances having different amplitudes is then nearly hopeless. A separate issue in MDCS spectroscopy is the error-bars that are typically reported. Often an experiment is done, the data without errorbars is fitted and then this process is repeated. Reported error-bars are then given as the deviation in the unweighted fitted results [68, 69, 231, 251]. Such a fit is unreliable as it does not find the most likely model parameter, which requires a weighted fit, (although with very high signal-to-noise it might be close) and it is improbable that the error estimate is correct. Analysis should rather involve *weighted* fits of experimental data where a single best-fit is recorded and error-bars are provided by the quality of the fit (for instance the probability density of the fit parameters).

To address these issues, we have spent some time developing both a simplified lineshape to fit in order to extract many-body interactions and in removing the effect of phase-space filling from the fits by using additional measurements. While still in development, we discuss our progress towards these goals using the weighted fit approach to quantify polariton-polariton interaction energies using MDCS spectroscopy.

7.3.1 The Problem of Extracting Many-Body Parameters

The problem of extracting many-body parameters is that one must deal with the limitations of fitting analysis and with the limitations of the experiment. The problem of fitting a sum of decaying exponentials is famously difficult [249, 250]. The situation where data is fit to a function of the form

$$y = ae^{\alpha t} + be^{\beta t} \tag{7.1}$$

and all four parameters must be inferred usually leads to an *extremely* ill conditioned fit, with many combinations of these parameters that will fit a given curve. This is the exact form of the functions from a Feynman pathway analysis except that the constants α and β are complex, with two parameters each describing the resonant frequency and the dephasing. In the case of a simple two-level system the functional form can be reduced since $\alpha = \beta$ and $a = b$ in the Feynman diagrams. With the addition of many-body interactions in a few-level scheme the fits become much more difficult and there is a need to reduce the complexity of the fit.

Here we discuss a few-level diagram such as a diamond structure mapped into an effective three-level energy structure. In this scheme, we are implicitly working in a truncated collective model that can correctly calculate the polarization response as discussed in Ch.4. In a collective scheme the dipole between manifolds changes by $\sqrt{N-n}$ to reflect the role of phase-space filling. For a three-level system, there are three Feynman diagrams for a rephasing pulse sequence corresponding to a positive S_+ and negative S_- amplitude quantum pathways. Given a dipole moment, μ_0, the sum of these signal pathways results in

$$S = S_+ + S_- = \mu_0^4 N[2-(N-1)e^{i\phi_{int}}]e^{-i\omega_\tau \tau + i\omega_t t - \gamma_\tau \tau - \gamma_t t}E^*EE^*E. \tag{7.2}$$

Here N is the number of electrons participating in the radiative dipole transition, ω_{tau} and ω_t are the radiative frequencies during time periods t and τ, and $\phi_{int} = \Delta_{int}t$ represents the complex time-dependent phase associated with many-body interactions and is typically of the form $\phi_{int} = i(EIS + iEID)t$. Since EIS(EID) are self-resonant interactions and self-resonant dephasing we use them explicitly as a frequency and an additional linewidth. As the sum of the Feynman diagrams it is S that should be fit to. In the limit of large N it might be possible to reduce this function by factoring out N from the brackets and ignoring the $\frac{1}{N}$ terms. However this only reduces the complexity of the amplitude. This equation is still problematic from a fitting perspective as during time t there are two nearly identical frequencies (split by the interaction energy) and two dephasing rates (split by the interaction mediated dephasing).

To reduce the number and complexity of approximations it is better to use a different pulse sequence that is more sensitive to many-body interactions, for example the two-quantum coherence. One advantage of this pulse sequence is that all two-quantum coherence pathways have the same phase-space filling factor. The sum of the signal pathways results in

$$S = S_+ + S_- = \mu_0^4 N(N-1)[1-e^{i\phi_{int}}]e^{-i\omega_T T + i\omega_t t - \gamma_T T - \gamma_t t}E^*EE^*E. \tag{7.3}$$

In contrast to the rephasing pulse sequence, the amplitude has only a single phase-space filling term $N(N-1)$ and the amplitude goes to zero for $\phi_{int}=0$. This is still a poorly conditioned fit since it is still looking for small frequency and linewidth shifts in the ω_t direction but the amplitude requires no simplifications. Following the conventions of [252] and taking a Fourier transform of this function results in the fitting model

$$S(\omega)=\frac{-2\cdot\mu^4}{16\hbar^4}(P(\omega_{t,int})-P(\omega_{t,0}))\cdot P(\omega_{T,int})e^{i\Omega_\tau\tau}e^{i\Omega_{t^*}t^*}E^*EE^*E. \tag{7.4}$$

Here $\Omega_{ij}=\omega_{ij}-i\gamma_{ij}$ is the complex resonance frequency between transitions i,j and $P(\omega)=\frac{i}{\omega-\Omega_{ij}}$. The subscript *int* indicates whether the frequency Ω_{ij} should include many-body interactions during time t. This fitting model can be simplified if we define the variables $A=\omega-(\omega_t+i\cdot\gamma_t)$ and $B=EIS+iEID$. The functional form of Eq. 7.4 is

$$S(\omega)=\frac{-2\mu_0^4}{16\hbar^4}\cdot i(\frac{-B}{(1+\frac{B}{A})\cdot A^2})\cdot P(\omega_{T,int})e^{i\Omega_\tau\tau}e^{i\Omega_{t^*}t^*}E^*EE^*E. \tag{7.5}$$

In the limit that the many-body interactions are perturbative $\frac{B}{A}\ll 1$ this equation reduces to

$$S(\omega)=\frac{-2N(N-1)(iEIS-EID)\cdot\mu^4}{16\hbar^4}P(\omega_{t,0})^2\cdot P(\omega_T)e^{I\Omega_\tau\tau}e^{I\Omega_{t^*}t^*}E^*EE^*E. \tag{7.6}$$

The functional form of this equation is much simpler to fit to because there is only a single set of frequencies and linewidths to extract. Rather it is the overall phase and amplitude that determines the value of the many-body interactions. However, at this level the model is still not able to extract the many-body interactions. The fit will return one power-dependent complex amplitude. By recording MDCS spectra at a specific power and fitting it to Eq. 7.6 the amplitude product $\frac{-2N(N-1)(iEIS-EID)\cdot\mu^4}{16\hbar^4}E^*EE^*E$ can be extracted. This can be further reduced by taking data as a function of excitation power and fitting it to find $\frac{-2N(N-1)(iEIS-EID)\cdot\mu^4}{16\hbar^4}$. At this level an additional measurement must be made to remove the phase-space filling $\mu_0^4 N(N-1)$ contribution to the amplitude. The separate measurement consists of linear absorption spectra recorded as a function of power.

The linear spectra at a given power will have a model lineshape (including higher order corrections)

$$S_{linear}(\omega) = 2(\frac{N\mu_0^2}{4\hbar^2}P(\omega)E^*E - \frac{N(N-1)\mu_0^4}{16\hbar^4}P(\omega)E^*EE^*E. \tag{7.7}$$

By fitting this expression to data recorded as a function of power, the amplitude product $\frac{\mu^2}{4\hbar^2}NE^*E$ can be extracted and fit to a power dependence to find $\beta^2 = (\frac{\mu^2}{4\hbar^2})N$.

The final step in the procedure is to divide $\frac{-2N(N-1)(iEIS-EID)\cdot\mu^4}{16\hbar^4}$ by β^4 providing the result

$$\frac{\text{Amplitude}}{\beta^4} = -1(1-\frac{1}{N})(iEIS - EID) = \frac{A_{real} + i\cdot A_{imag}}{\beta^4} \tag{7.8}$$

where $A_{real,imag}$ is the real and imaginary component of the extracted data. The procedure calls for four fitting steps before the many-body interactions can be extracted reliably. This procedure requires that a great deal of care be taken in propagating the errors and ensuring that high-quality fits are achieved.

In a simple exciton-cavity coupling picture the polaritons are expected to be homogeneously broadened. However, upper polaritons are known to exhibit long energy tails on the high energy side due to interaction of the light with continuum states and interbranch scattering [253, 254]. Both the upper and lower polariton are expected to have subaverage broadening with their linewidth below that of a Voigt profile [254]. However, what has not yet been discussed but is clearly seen in these papers is that the lower polariton clearly also has an asymmetric *low* energy tail [254]. To capture these asymmetries and provide a better fit and estimate of the amplitude of the linear absorption spectra we introduce an asymmetry parameter α following the method of [255]. They proposed using a frequency dependent linewidth that can vary across the Lorentzian to capture asymmetries. The functional form of the proposed linewidth has an asymmetry parameter α that on resonance becomes the usual homogeneous linewidth of a Lorentzian. This linewidth can get larger/smaller in the wings of the Lorentzian.

$$\gamma(\omega) = \frac{2\gamma_0}{1 + e^{\alpha(\omega-\omega_0)}} \tag{7.9}$$

When using this functional form our reduced χ improved by about ~ 10 for both the upper and lower polariton fits. The fits using the asymmetry parameter showed a clear blueshift of the upper and lower polariton energies with increasing power; this effect was not observable with the simple Lorentzians.

7.3.2 Preliminary Fitting Results

In this section we discuss our preliminary fitting results. The fit parameters of the absorption at different power are shown for lower polaritons in Fig. 7.7 and for upper polaritons in Fig. 7.8. Both peaks show a nonlinear scaling with excitation power as expected since the data is recorded over three orders of excitation power and our model is designed to fit this including higher order corrections (Top Left Panels). At lower excitation power the lower polariton linewidth (Fig. 7.7) is constant before increasing at higher excitation density. As the excitation power increases the lower polariton blueshifts. The upper polariton linewidth (Fig. 7.7) top right appears constant before decreasing. We attribute this to a fit that is insensitive to the linewidth rather than a physical result (possibly due to low signal-noise). The upper polariton center frequency clearly blue shifts to higher energy as the excitation power increases.

In order to find the errors on these fits we make use of a Markov Chain Monte-Carlo Ensemble Sampler (The MCMC Hammer) [256] to sample the posterior probability distribution of the fit. The posterior probability distribution provides a statistical estimate of the quality of the fit and the confidence interval of the fitted parameters; details can be found in

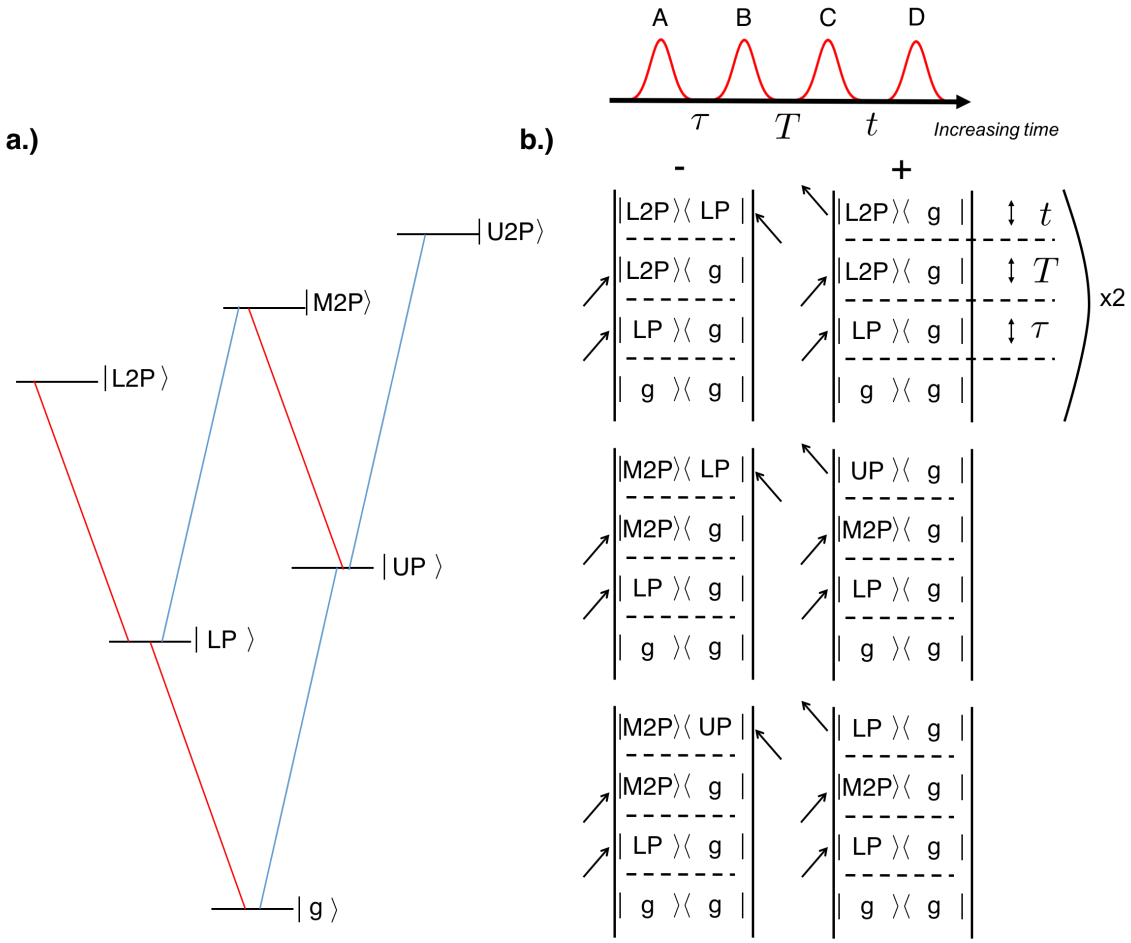

Figure 7.6: a.) Effective energy level diagram for exciton-polaritons probed by cocircular light. Shown are the upper and lower polaritons as well as their doubly excited states including a mixed $M2P$ state. b.) Feynman diagrams showing the different quantum pathways accessible in a two-quantum coherence. (Top) Four pulses used to excite the sample. Shown here are Feynman diagrams for two-quantum coherences with only the first three pulses represented. The final pulse converts the coherent state into a population state effectively multiplying the number of diagrams by two. The measurement is insensitive to the readout state, only the states that evolve during time τ, T and t. Not shown are the pathways that access the $U2P$ state, these are indicated by the x2 in the diagram because they are identical to the pathways that excite the $L2P$ state.

[250]. The projections of this distribution for both upper and lower polaritons are plotted in (Appendix D) with the mean fit value and the one sigma values indicated in the integrated fit projections by dashed lines.

Using the fitting errors from this process we fit the amplitudes of the upper and lower polariton absorption peaks (Fig. 7.9) to find the parameter $N\beta^2$. For the lower polariton we find $N\beta^2_{LP} = .205 \pm .005$ and for the upper polariton we find $N\beta^2_{UP} = .406 \pm .012$. The residual variance of these fits was ~ 2 providing a high quality measurement of this dipole factor.

For nonlinear MDCS measurements data was recorded as a function of excitation density and exciton-cavity detuning. These measurements explored the effective energy diagram and the quantum pathways of (Fig. 7.6). The data to the fits of these curves are not included here due to their poor preliminary quality. An issue with the measurement is that the blue-shift of the peaks is observable even for relatively low excitation powers. This complicates our analysis where we assume the resonant frequency remains essentially constant and resonant interaction energies provide a change in the phase of the MDCS spectrum. We hope to resolve these issues in the near future.

7.3.3 Conclusion

We have performed measurements on polaritons excited by both co circular and cross circular excitation. Our results confirm the phase roll reported as a Feshbach resonance, but indicate that there is an asymmetric scattering channel that involves an upper polariton. We do not observe a biexciton, or a bipolariton. For our cocircular results we have performed extensive measurements and the data is collected. Concurrently, we developed an analysis method capable of measuring many-body interactions quantitatively. This method allows for a quantitative measurement of the many-body interactions as predicted by few-level models of the exciton-polariton nonlinear optical response. We have successfully measured the phase space filling factor $N\beta^2$ within the context of our experiment and we hope to use this parameter to quantitatively measure the self-resonant interaction energies EIS and EID accurately. Our analysis is ongoing.

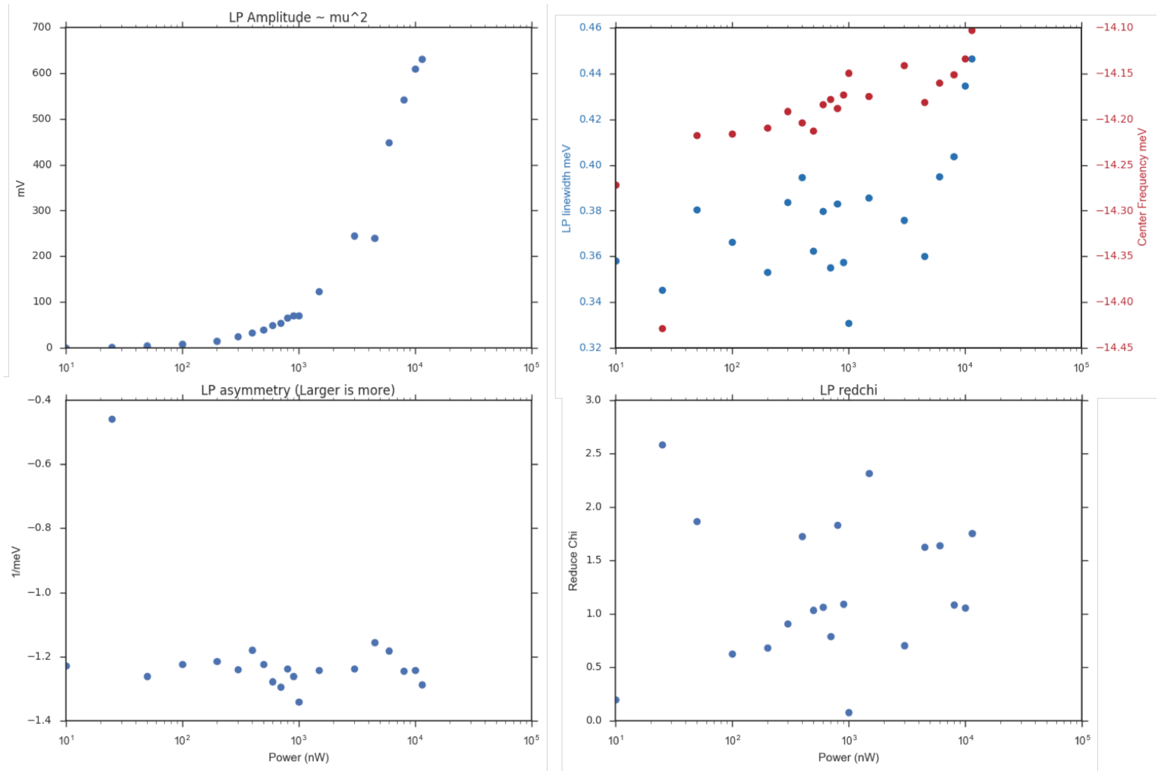

Figure 7.7: Fitting curves for two-pulse absorption data. Fitted results for the lower-polariton with the fitted parameters found as function of power. The amplitude (top left panel) clearly scales nonlinearly with increasing excitation power. The linewidth varies across the excitation power range but the peak is clearly blue-shifting to higher energy as the excitation density increases (top right panel). The asymmetry parameter is found to be ~ -1.2 meV^{-1} (bottom left panel). The lower right panel shows the reduced χ for each fit at each power.

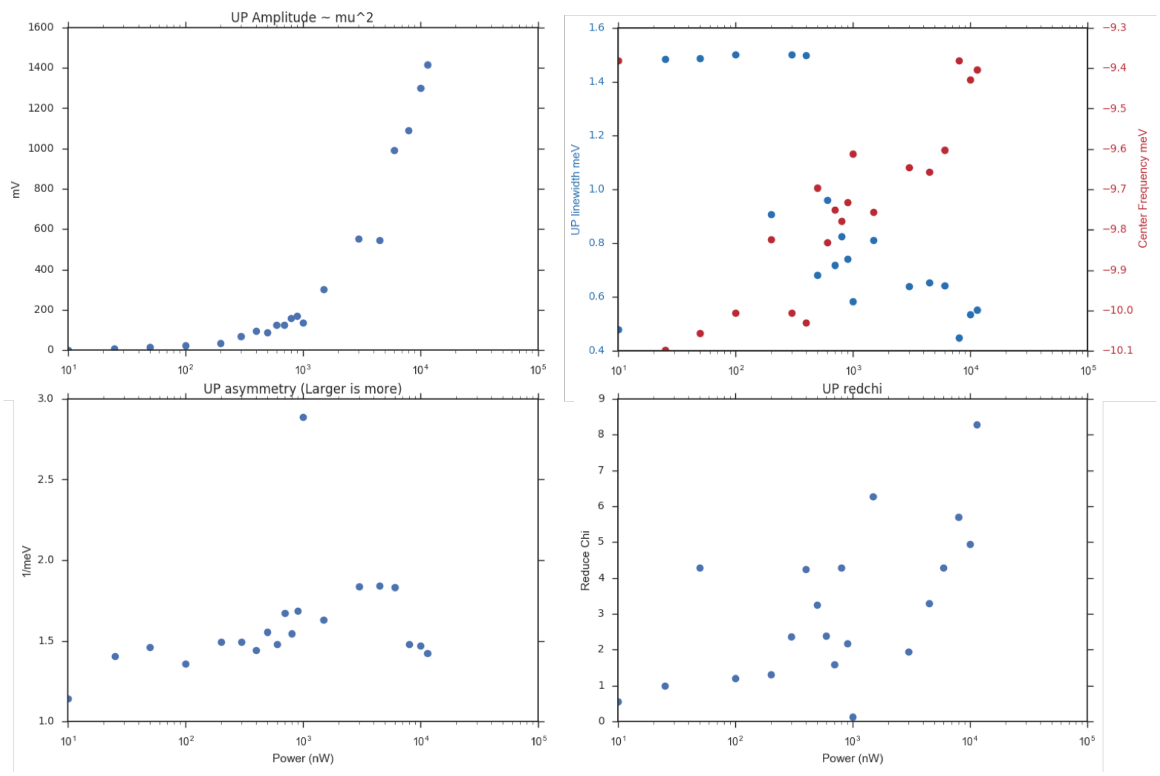

Figure 7.8: Fitting curves for two-pulse absorption data. Fitted results for the upper-polariton with the fitted parameters found as function of power. The amplitude (top left panel) clearly scales nonlinearly with increasing excitation power. The linewidth varies across the excitation power range but the peak is clearly blue-shifting to higher energy as the excitation density increases (top right panel). The asymmetry parameter is found to be ~ 1.5 meV^{-1} (bottom left panel). The lower right panel shows the reduced χ for each fit at each power.

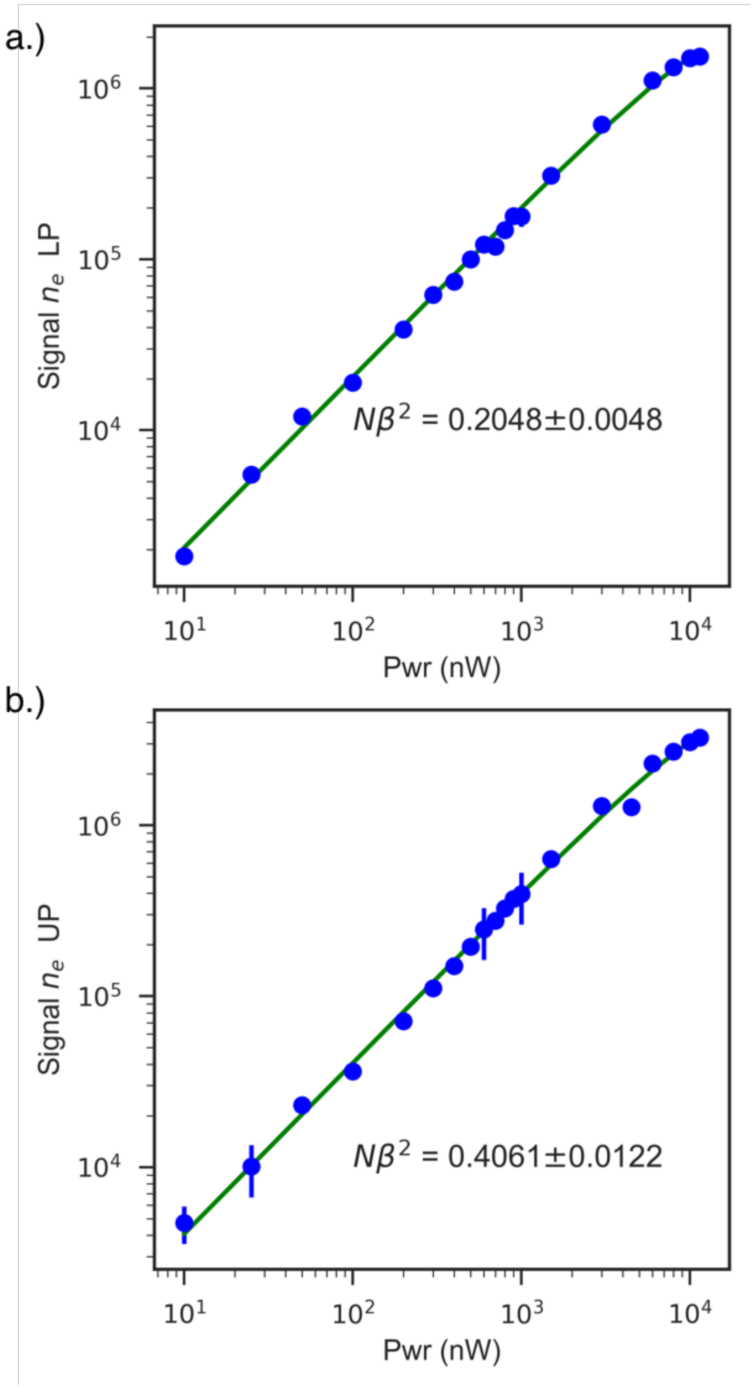

Figure 7.9: Fitted curves to the amplitude of the Upper and Lower polaritons on a log-log scale. Amplitude error-bars are included in both plots. a.) The lower-polariton fit to extract the parameter $N\beta^2$ for which we find a value of $N\beta^2 = .2048$. The amplitude of this plot is in number of electrons n_e. b.) The upper-polariton fit to extract the parameter $N\beta^2$ for which we find a value of $N\beta^2 = .4061$.

Chapter 8

Conclusion

In this thesis I have explored some of the work that I have led the progress on. My work with Gaël Nardin on developing a new method to perform MDCS spectroscopy was extensively discussed. Our technique relies on dynamic phase cycling to select a nonlinear process of interest. Because our dynamic phase cycling results in a signal at a particular radio frequency; we are able to use an external reference laser to monitor interferometer fluctuations and correct them in a demodulated signal. The use of the external reference laser puts our measurement into a rotating frame allowing the system to physically under sample the optical frequencies. An innovation of our approach is that our signal is collected as a photocurrent. This approach make MDCS appropriate for exploring device coupled nanophotonic systems.

The process of collective wave mixing in an effective model for quantum well excitons was developed based on a statistical approach. This model reduced to a Dicke model when considering excitons at $K_x = 0$. This model demonstrates that a system with a large number of energy levels can have a perturbative polarization response while some of it's density matrix elements remain in a non-perturbative regime. In this model we explored the role of level truncation and how this model relates to few-level models that are currently ubiquitous. We then considered the role of many-body interactions (specifically a two-body interaction) and discussed how it would modify the total polarization of the ensemble. This model provides a link between the fermionic models of excitons and the bosonic models of excitons.

We reviewed strong coupling and cavity quantum electrodynamics for both single-two level systems and collective ensembles. This provided motivation for our measurements of the higher order dispersion curves of exciton-polaritons. The excitation ladder for collective ensembles, and exciton-polaritons in particular, measured by higher order avoided crossings had not been explored. Our work attempted to address this issue and provide information about the exciton-polariton ladder of states. While not able to deterministically access particular states, a wealth of new information is revealed from our measurements. First our measurements reveal that at low excitation density the exciton-polariton eigenstates match that of two coupled quantum harmonic oscillators. Secondly, our measurements indicate that the many-body interactions are perturbative to the optical response of the exciton-polaritons. Thirdly, there appears to be a series of cavity-exciton NooN states in the excitation ladder of exciton-polaritons. While we were not able to deterministically access these states they may be of interest to future quantum devices.

We have reviewed our progress to date on measuring the exciton-polariton interaction constants. For cross-circular excitation our results confirm the phase roll that was reported as a Feshbach resonance. However, the asymmetry in the mixed state polaritons indicates that this scattering is more complicated and involves the upper polariton. The co-circular excitation measurements are incomplete. We have recorded the required data however our fits are preliminary. Our analysis was developed to reduce the complexity of the fitting algorithms.

8.1 Outlook

The ongoing projects from this work include:

- The use of an field programmable gate array (FPGA) as opposed to a digital signal processor to mix our reference signals for the demodulated nonlinear signal. The use of a higher speed will allow the experiment to move to MHz beat notes. In this regime the noise of our detection electronics should improve as well as the phase noise associated with long term interferometer drift.

- Not discussed in this thesis, but a project I started, was to use a nano-probe to perform single molecule MDCS. I demonstrated the first FWM off of a grating-etched into an atomic force microscope. While we were not able to time resolve the dynamics (due to our pulse duration) this measurement provided crucial proof of principle for Chris Smallwood and others to follow. He is currently in the process of expanding upon the setup and attempting to reduce the required measurement time as this becomes a four-dimensional scan in order to perform MDCS in a nanoprobe configuration with spatial resolution.

- The collective wave mixing of excitons is an interesting topic that has not been extensively explored through a Dicke model. The role of the biexciton and dark exciton (by selection rules) states needs to be considered in this model. It may be possible to consider the subradiant states in the Dicke model as a treatment of the dark excitons. It is also unclear how to incorporate exciton-exciton scattering that moves excitons out of the light cone.

- The strong-coupling regime of exciton-polaritons remains a rich area to be explored. In particular, devising a scheme to deterministically access the polaritonic noon states, that our results indicate exists, is of significant interest. There is also significant interest in characterizing the higher order dispersion in photonic quantum dot cavities where the light is confined in three dimensions.

- Our measurements of the reported Feshbach resonance need to be explored theoretically. While we are able to confirm the reported phase change (as evidenced by the real part of the MDCS spectra) we do not understand the asymmetry in the mixed exciton-polariton states. We are collaborating with Shaul Mukamel (UC Davis) to develop a theoretical understanding of this phenomena.

- Our measurement of the co-circular interaction energy are a work in progress. We have been successful in reducing the complexity of our model but so far the results have been inconclusive. We expect that further fine-tuning of the model parameters will help us record high-quality fits. An issue with the measurement is that the blue-shift of the peaks is observable even for relatively low excitation powers. This complicates our analysis where we assume the resonant frequency remains essentially constant and resonant interaction energies provide a change in the phase of the MDCS spectrum. We hope to resolve these issues in the near future.

Bibliography

[1] R. J. Elliott, "Intensity of Optical Absorption by Excitons," Physical Review, vol. 108, pp. 1384–1389, Dec. 1957.

[2] N. W. Ashcroft and N. D. Mermin, Solid State Physics. New York: Rinehart and Winston, 1976.

[3] J. Singh, Electronic and Optoelectronic Properties of Semiconductor Structures. Cambridge University Press, 2003.

[4] S. T. Cundiff, "Optical two-dimensional Fourier transform spectroscopy of semiconductor nanostructures [Invited]," Journal of the Optical Society of America B, vol. 29, p. A69, Feb. 2012.

[5] C. Kittel, Introduction to Solid State Physics. Wiley, Nov. 2004. Google-Books-ID: kym4QgAACAAJ.

[6] E. Hanamura and H. Haug, "Condensation effects of excitons," Physics Reports, vol. 33, pp. 209–284, Oct. 1977.

[7] G. H. Wannier, "The Structure of Electronic Excitation Levels in Insulating Crystals," Physical Review, vol. 52, pp. 191–197, Aug. 1937.

[8] T. Kazimierczuk, D. Fröhlich, S. Scheel, H. Stolz, and M. Bayer, "Giant Rydberg excitons in the copper oxide Cu2o," Nature, vol. 514, pp. 343–347, Oct. 2014.

[9] S. B. Nam, D. C. Reynolds, C. W. Litton, R. J. Almassy, T. C. Collins, and C. M. Wolfe, "Free-exciton energy spectrum in GaAs," Physical Review B, vol. 13, pp. 761–767, Jan. 1976.

[10] T. Zang, Optical Two-Dimensional Fourier Transform Spectroscopy of Semiconductors, vol. PhD thesis. Boulder, Co: University of Colorado Boulder, 2008.

[11] J. J. Hopfield, "Theory of the Contribution of Excitons to the Complex Dielectric Constant of Crystals," Physical Review, vol. 112, pp. 1555–1567, Dec. 1958.

[12] C. Ciuti, P. Schwendimann, B. Deveaud, and A. Quattropani, "Theory of the angle-resonant polariton amplifier," Physical Review B, vol. 62, pp. R4825–R4828, Aug. 2000.

[13] G. Khitrova, H. M. Gibbs, F. Jahnke, M. Kira, and S. W. Koch, "Nonlinear optics of normal-mode-coupling semiconductor microcavities," Reviews of Modern Physics, vol. 71, pp. 1591–1639, Oct. 1999.

[14] H. Deng, H. Haug, and Y. Yamamoto, "Exciton-polariton Bose-Einstein condensation," Reviews of Modern Physics, vol. 82, pp. 1489–1537, May 2010.

[15] J.-Y. Marzin, M. N. Charasse, and B. Sermage, "Optical investigation of a new type of valence-band configuration in $\mathrm{In_xGa_{1x}As}$-GaAs strained superlattices," Physical Review B, vol. 31, pp. 8298–8301, June 1985.

[16] M. Moran, P. Dawson, and K. J. Moore, "The nature of the light hole potential profile in GaAsInGaAs double quantum well structures," Solid State Communications, vol. 107, pp. 119–123, May 1998.

[17] L. C. Andreani and A. Pasquarello, "Accurate theory of excitons in GaAs-$\mathrm{Ga_{1\text{-}x}Al_x}$ quantum wells," Physical Review B, vol. 42, pp. 8928–8938, Nov. 1990.

[18] G. Khitrova, H. M. Gibbs, M. Kira, S. W. Koch, and A. Scherer, "Vacuum Rabi splitting in semiconductors," Nature Physics, vol. 2, pp. 81–90, Feb. 2006.

[19] C. Weisbuch, M. Nishioka, A. Ishikawa, and Y. Arakawa, "Observation of the coupled exciton-photon mode splitting in a semiconductor quantum microcavity," Physical Review Letters, vol. 69, pp. 3314–3317, Dec. 1992.

[20] J. M. Fink, M. Göppl, M. Baur, R. Bianchetti, P. J. Leek, A. Blais, and A. Wallraff, "Climbing the Jaynes–Cummings ladder and observing its nonlinearity in a cavity QED system," Nature, vol. 454, pp. 315–318, July 2008.

[21] R. J. Thompson, Q. A. Turchette, O. Carnal, and H. J. Kimble, "Nonlinear spectroscopy in the strong-coupling regime of cavity QED," Physical Review A, vol. 57, pp. 3084–3104, Apr. 1998.

[22] J. H. Hodak, I. Martini, and G. V. Hartland, "Spectroscopy and Dynamics of Nanometer-Sized Noble Metal Particles," The Journal of Physical Chemistry B, vol. 102, pp. 6958–6967, Sept. 1998.

[23] C.-K. Sun, F. Vallée, L. H. Acioli, E. P. Ippen, and J. G. Fujimoto, "Femtosecond-tunable measurement of electron thermalization in gold," Physical Review B, vol. 50, pp. 15337–15348, Nov. 1994.

[24] K. Müller, A. Bechtold, C. Ruppert, M. Zecherle, G. Reithmaier, M. Bichler, H. J. Krenner, G. Abstreiter, A. W. Holleitner, J. M. Villas-Boas, M. Betz, and J. J. Finley, "Electrical Control of Interdot Electron Tunneling in a Double InGaAs Quantum-Dot Nanostructure," Physical Review Letters, vol. 108, p. 197402, May 2012.

[25] F. Eickemeyer, K. Reimann, M. Woerner, T. Elsaesser, S. Barbieri, C. Sirtori, G. Strasser, T. Müller, R. Bratschitsch, and K. Unterrainer, "Ultrafast Coherent Electron Transport in Semiconductor Quantum Cascade Structures," Physical Review Letters, vol. 89, p. 047402, July 2002.

[26] K. L. Hall, G. Lenz, E. P. Ippen, and G. Raybon, "Heterodyne pump-probe technique for time-domain studies of optical nonlinearities in waveguides," Optics Letters, vol. 17, pp. 874–876, June 1992.

[27] A. Hayat, C. Lange, L. A. Rozema, A. Darabi, H. M. van Driel, A. M. Steinberg, B. Nelsen, D. W. Snoke, L. N. Pfeiffer, and K. W. West, "Dynamic Stark Effect in Strongly Coupled Microcavity Exciton Polaritons," Physical Review Letters, vol. 109, p. 033605, July 2012.

[28] F. Quochi, G. Bongiovanni, A. Mura, J. L. Staehli, B. Deveaud, R. P. Stanley, U. Oesterle, and R. Houdré, "Strongly Driven Semiconductor Microcavities: From the Polariton Doublet to an ac Stark Triplet," Physical Review Letters, vol. 80, pp. 4733–4736, May 1998.

[29] J. M. Shacklette and S. T. Cundiff, "Role of excitation-induced shift in the coherent optical response of semiconductors," Physical Review B, vol. 66, p. 045309, July 2002.

[30] K. Bott, O. Heller, D. Bennhardt, S. T. Cundiff, P. Thomas, E. J. Mayer, G. O. Smith, R. Eccleston, J. Kuhl, and K. Ploog, "Influence of exciton-exciton interactions on the coherent optical response in GaAs quantum wells," Physical Review B, vol. 48, pp. 17418–17426, Dec. 1993.

[31] H. Wang, K. B. Ferrio, D. G. Steel, P. R. Berman, Y. Z. Hu, R. Binder, and S. W. Koch, "Transient four-wave-mixing line shapes: Effects of excitation-induced dephasing," Physical Review A, vol. 49, pp. R1551–R1554, Mar. 1994.

[32] W. P. Aue, E. Bartholdi, and R. R. Ernst, "Twodimensional spectroscopy. Application to nuclear magnetic resonance," The Journal of Chemical Physics, vol. 64, pp. 2229–2246, Mar. 1976.

[33] G. Bodenhausen, R. Freeman, G. A. Morris, and D. L. Turner, "NMR spectra of some simple spin systems studied by two-dimensional fourier transformation of spin echoes," Journal of Magnetic Resonance (1969), vol. 31, pp. 75–95, July 1978.

[34] B. Vogelsanger and A. Bauder, "Twodimensional microwave Fourier transform spectroscopy," The Journal of Chemical Physics, vol. 92, pp. 4101–4114, Apr. 1990.

[35] I. Noda, "Two-dimensional infrared spectroscopy," Journal of the American Chemical Society, vol. 111, pp. 8116–8118, Oct. 1989.

[36] D. Suter, H. Klepel, and J. Mlynek, "Time-resolved two-dimensional spectroscopy of optically driven atomic sublevel coherences," Physical Review Letters, vol. 67, pp. 2001–2004, Oct. 1991.

[37] P. Hamm, M. Lim, and R. M. Hochstrasser, "Structure of the Amide I Band of Peptides Measured by Femtosecond Nonlinear-Infrared Spectroscopy," The Journal of Physical Chemistry B, vol. 102, pp. 6123–6138, July 1998.

[38] O. Golonzka, M. Khalil, N. Demirdöven, and A. Tokmakoff, "Vibrational Anharmonicities Revealed by Coherent Two-Dimensional Infrared Spectroscopy," Physical Review Letters, vol. 86, pp. 2154–2157, Mar. 2001.

[39] N. Demirdöven, M. Khalil, and A. Tokmakoff, "Correlated Vibrational Dynamics Revealed by Two-Dimensional Infrared Spectroscopy," Physical Review Letters, vol. 89, p. 237401, Nov. 2002.

[40] J. D. Hybl, A. W. Albrecht, S. M. Gallagher Faeder, and D. M. Jonas, "Two-dimensional electronic spectroscopy," Chemical Physics Letters, vol. 297, pp. 307–313, Nov. 1998.

[41] X. Li, T. Zhang, C. N. Borca, and S. T. Cundiff, "Many-Body Interactions in Semiconductors Probed by Optical Two-Dimensional Fourier Transform Spectroscopy," Physical Review Letters, vol. 96, p. 057406, Feb. 2006.

[42] K. W. Stone, K. Gundogdu, D. B. Turner, X. Li, S. T. Cundiff, and K. A. Nelson, "Two-Quantum 2d FT Electronic Spectroscopy of Biexcitons in GaAs Quantum Wells," Science, vol. 324, pp. 1169–1173, May 2009.

[43] C. Li, W. Wagner, M. Ciocca, and W. S. Warren, "Multiphoton femtosecond phase-coherent two-dimensional electronic spectroscopy," The Journal of Chemical Physics, vol. 126, pp. 164307–164307–6, Apr. 2007.

[44] W. Langbein and B. Patton, "Heterodyne spectral interferometry for multidimensional nonlinear spectroscopy of individual quantum systems," Optics Letters, vol. 31, pp. 1151–1153, Apr. 2006.

[45] F. Albert, K. Sivalertporn, J. Kasprzak, M. Strauß, C. Schneider, S. Höfling, M. Kamp, A. Forchel, S. Reitzenstein, E. A. Muljarov, and W. Langbein, "Microcavity controlled coupling of excitonic qubits," Nature Communications, vol. 4, p. 1747, Apr. 2013.

[46] X. Dai, M. Richter, H. Li, A. D. Bristow, C. Falvo, S. Mukamel, and S. T. Cundiff, "Two-Dimensional Double-Quantum Spectra Reveal Collective Resonances in an Atomic Vapor," Physical Review Letters, vol. 108, p. 193201, May 2012.

[47] D. Karaiskaj, A. D. Bristow, L. Yang, X. Dai, R. P. Mirin, S. Mukamel, and S. T. Cundiff, "Two-Quantum Many-Body Coherences in Two-Dimensional Fourier-Transform Spectra of Exciton Resonances in Semiconductor Quantum Wells," Physical Review Letters, vol. 104, p. 117401, Mar. 2010.

[48] M. Aeschlimann, T. Brixner, A. Fischer, C. Kramer, P. Melchior, W. Pfeiffer, C. Schneider, C. Strüber, P. Tuchscherer, and D. V. Voronine, "Coherent Two-Dimensional Nanoscopy," Science, vol. 333, pp. 1723–1726, Sept. 2011.

[49] K. J. Karki, J. R. Widom, J. Seibt, I. Moody, M. C. Lonergan, T. Pullerits, and A. H. Marcus, “Coherent two-dimensional photocurrent spectroscopy in a PbS quantum dot photocell,” Nature Communications, vol. 5, Dec. 2014.

[50] M. Woerner, W. Kuehn, P. Bowlan, K. Reimann, and T. Elsaesser, “Ultrafast two-dimensional terahertz spectroscopy of elementary excitations in solids,” New Journal of Physics, vol. 15, p. 025039, Feb. 2013.

[51] T. Maag, A. Bayer, S. Baierl, M. Hohenleutner, T. Korn, C. Schüller, D. Schuh, D. Bougeard, C. Lange, R. Huber, M. Mootz, J. E. Sipe, S. W. Koch, and M. Kira, “Coherent cyclotron motion beyond Kohn/’s theorem,” Nature Physics, vol. 12, pp. 119–123, Feb. 2016.

[52] N. F. Ramsey, “Experiments with separated oscillatory fields and hydrogen masers,” Reviews of Modern Physics, vol. 62, pp. 541–552, July 1990.

[53] M. Frimmer and L. Novotny, “The classical Bloch equations,” American Journal of Physics, vol. 82, pp. 947–954, Oct. 2014.

[54] N. V. Vitanov, T. F. Gloger, P. Kaufmann, D. Kaufmann, T. Collath, M. Tanveer Baig, M. Johanning, and C. Wunderlich, “Fault-tolerant Hahn-Ramsey interferometry with pulse sequences of alternating detuning,” Physical Review A, vol. 91, p. 033406, Mar. 2015.

[55] D. J. Wineland, J. J. Bollinger, W. M. Itano, F. L. Moore, and D. J. Heinzen, “Spin squeezing and reduced quantum noise in spectroscopy,” Physical Review A, vol. 46, pp. R6797–R6800, Dec. 1992.

[56] D. J. Wineland, J. J. Bollinger, W. M. Itano, and D. J. Heinzen, “Squeezed atomic states and projection noise in spectroscopy,” Physical Review A, vol. 50, pp. 67–88, July 1994.

[57] N. Huntemann, B. Lipphardt, M. Okhapkin, C. Tamm, E. Peik, A. V. Taichenachev, and V. I. Yudin, “Generalized Ramsey Excitation Scheme with Suppressed Light Shift,” Physical Review Letters, vol. 109, p. 213002, Nov. 2012.

[58] N. Timoney, I. Baumgart, M. Johanning, A. F. Varón, M. B. Plenio, A. Retzker, and C. Wunderlich, “Quantum gates and memory using microwave-dressed states,” Nature, vol. 476, pp. 185–188, Aug. 2011.

[59] C. Piltz, B. Scharfenberger, A. Khromova, A. F. Varón, and C. Wunderlich, “Protecting Conditional Quantum Gates by Robust Dynamical Decoupling,” Physical Review Letters, vol. 110, p. 200501, May 2013.

[60] S. C. Webster, S. Weidt, K. Lake, J. J. McLoughlin, and W. K. Hensinger, “Simple Manipulation of a Microwave Dressed-State Ion Qubit,” Physical Review Letters, vol. 111, p. 140501, Oct. 2013.

[61] E. L. Hahn, “Spin Echoes,” Physical Review, vol. 80, pp. 580–594, Nov. 1950.

[62] I. D. Abella, N. A. Kurnit, and S. R. Hartmann, “Photon Echoes,” Physical Review, vol. 141, pp. 391–406, Jan. 1966.

[63] T. Zhang, I. Kuznetsova, T. Meier, X. Li, R. P. Mirin, P. Thomas, and S. T. Cundiff, “Polarization-dependent optical 2d Fourier transform spectroscopy of semiconductors,” Proceedings of the National Academy of Sciences, vol. 104, pp. 14227–14232, Sept. 2007.

[64] M. E. Siemens, G. Moody, H. Li, A. D. Bristow, and S. T. Cundiff, “Resonance lineshapes in two-dimensional?Fourier transform spectroscopy,” Optics Express, vol. 18, pp. 17699–17708, Aug. 2010.

[65] A. D. Bristow, T. Zhang, M. E. Siemens, S. T. Cundiff, and R. P. Mirin, “Separating Homogeneous and Inhomogeneous Line Widths of Heavy- and Light-Hole Excitons in Weakly Disordered Semiconductor Quantum Wells,” The Journal of Physical Chemistry B, vol. 115, pp. 5365–5371, May 2011.

[66] J. D. Bell, R. Conrad, and M. E. Siemens, “Analytical calculation of two-dimensional spectra,” Optics Letters, vol. 40, p. 1157, Apr. 2015.

[67] G. Moody, M. E. Siemens, A. D. Bristow, X. Dai, D. Karaiskaj, A. S. Bracker, D. Gammon, and S. T. Cundiff, “Exciton-exciton and exciton-phonon interactions in an interfacial GaAs quantum dot ensemble,” Physical Review B, vol. 83, p. 115324, Mar. 2011.

[68] R. Singh, T. M. Autry, G. Nardin, G. Moody, H. Li, K. Pierz, M. Bieler, and S. T. Cundiff, “Anisotropic homogeneous linewidth of the heavy-hole exciton in (110)-oriented GaAs quantum wells,” Physical Review B, vol. 88, p. 045304, July 2013.

[69] G. Moody, C. Kavir Dass, K. Hao, C.-H. Chen, L.-J. Li, A. Singh, K. Tran, G. Clark, X. Xu, G. Berghäuser, E. Malic, A. Knorr, and X. Li, “Intrinsic homogeneous linewidth and broadening mechanisms of excitons in monolayer transition metal dichalcogenides,” Nature Communications, vol. 6, p. 8315, Sept. 2015.

[70] T. Suzuki, R. Singh, M. Bayer, A. Ludwig, A. D. Wieck, and S. T. Cundiff, “Coherent Control of the Exciton-Biexciton System in an InAs Self-Assembled Quantum Dot Ensemble,” Physical Review Letters, vol. 117, no. 15, p. 157402, 2016.

[71] S. M. Gallagher Faeder and D. M. Jonas, “Two-Dimensional Electronic Correlation and Relaxation Spectra: Theory and Model Calculations,” The Journal of Physical Chemistry A, vol. 103, pp. 10489–10505, Dec. 1999.

[72] Y.-C. Cheng and G. R. Fleming, “Coherence Quantum Beats in Two-Dimensional Electronic Spectroscopy,” The Journal of Physical Chemistry A, vol. 112, pp. 4254–4260, May 2008.

[73] V. Butkus, D. Zigmantas, L. Valkunas, and D. Abramavicius, “Vibrational vs. electronic coherences in 2d spectrum of molecular systems,” Chemical Physics Letters, vol. 545, pp. 40–43, Aug. 2012.

[74] T. Brixner, J. Stenger, H. M. Vaswani, M. Cho, R. E. Blankenship, and G. R. Fleming, “Two-dimensional spectroscopy of electronic couplings in photosynthesis,” Nature, vol. 434, pp. 625–628, Mar. 2005.

[75] G. S. Engel, T. R. Calhoun, E. L. Read, T.-K. Ahn, T. Mančal, Y.-C. Cheng, R. E. Blankenship, and G. R. Fleming, “Evidence for wavelike energy transfer through quantum coherence in photosynthetic systems,” Nature, vol. 446, pp. 782–786, Apr. 2007.

[76] H. Lee, Y.-C. Cheng, and G. R. Fleming, “Coherence Dynamics in Photosynthesis: Protein Protection of Excitonic Coherence,” Science, vol. 316, pp. 1462–1465, June 2007.

[77] K. J. Karki, L. Kringle, A. H. Marcus, and T. Pullerits, “Phase-synchronous detection of coherent and incoherent nonlinear signals,” Journal of Optics, vol. 18, no. 1, p. 015504, 2016.

[78] H. Wang, J. Shah, T. C. Damen, W. Y. Jan, J. E. Cunningham, M. Hong, and J. P. Mannaerts, “Coherent oscillations in semiconductor microcavities,” Physical Review B, vol. 51, pp. 14713–14716, May 1995.

[79] Y. P. Svirko, M. Shirane, H. Suzuura, and M. Kuwata-Gonokami, “Four-Wave Mixing Theory at the Excitonic Resonance: Weakly Interacting Boson Model,” Journal of the Physical Society of Japan, vol. 68, pp. 674–682, Feb. 1999.

[80] W. Langbein and B. Patton, “Microscopic Measurement of Photon Echo Formation in Groups of Individual Excitonic Transitions,” Physical Review Letters, vol. 95, p. 017403, June 2005.

[81] R. R. Ernst, G. Bodenhausen, and A. Wokaun, Principles of Nuclear Magnetic Resonance in One and Two Dimensions. Clarendon Press, Sept. 1990.

[82] J. Kasprzak, B. Patton, V. Savona, and W. Langbein, “Coherent coupling between distant excitons revealed by two-dimensional nonlinear hyperspectral imaging,” Nature Photonics, vol. 5, pp. 57–63, Jan. 2011.

[83] A. D. Bristow, D. Karaiskaj, X. Dai, T. Zhang, C. Carlsson, K. R. Hagen, R. Jimenez, and S. T. Cundiff, “A versatile ultrastable platform for optical multidimensional Fourier-transform spectroscopy,” Review of Scientific Instruments, vol. 80, pp. 073108–073108–8, July 2009.

[84] E. M. Grumstrup, S.-H. Shim, M. A. Montgomery, N. H. Damrauer, and M. T. Zanni, “Facile collection of two-dimensional electronic spectra using femtosecond pulse-shaping Technology,” Optics Express, vol. 15, pp. 16681–16689, Dec. 2007.

[85] D. R. Skoff, J. E. Laaser, S. S. Mukherjee, C. T. Middleton, and M. T. Zanni, "Simplified and economical 2d IR spectrometer design using a dual acousto-optic modulator," Chemical Physics, vol. 422, pp. 8–15, Aug. 2013.

[86] T. Zhang, C. Borca, X. Li, and S. Cundiff, "Optical two-dimensional Fourier transform spectroscopy with active interferometric stabilization," Optics Express, vol. 13, pp. 7432–7441, Sept. 2005.

[87] E. Harel, A. F. Fidler, and G. S. Engel, "Real-time mapping of electronic structure with single-shot two-dimensional electronic spectroscopy," Proceedings of the National Academy of Sciences, vol. 107, pp. 16444–16447, Sept. 2010.

[88] A. D. Bristow, D. Karaiskaj, X. Dai, and S. T. Cundiff, "All-optical retrieval of the global phase for two-dimensional Fourier-transform spectroscopy," Optics Express, vol. 16, pp. 18017–18027, Oct. 2008.

[89] P. Tian, D. Keusters, Y. Suzaki, and W. S. Warren, "Femtosecond Phase-Coherent Two-Dimensional Spectroscopy," Science, vol. 300, pp. 1553–1555, June 2003.

[90] P. F. Tekavec, T. R. Dyke, and A. H. Marcus, "Wave packet interferometry and quantum state reconstruction by acousto-optic phase modulation," The Journal of Chemical Physics, vol. 125, pp. 194303–194303–19, Nov. 2006.

[91] P. F. Tekavec, G. A. Lott, and A. H. Marcus, "Fluorescence-detected two-dimensional electronic coherence spectroscopy by acousto-optic phase modulation," The Journal of Chemical Physics, vol. 127, pp. 214307–214307–21, Dec. 2007.

[92] G. Nardin, T. M. Autry, K. L. Silverman, and S. T. Cundiff, "Multidimensional coherent photocurrent spectroscopy of a semiconductor nanostructure," Optics Express, vol. 21, pp. 28617–28627, Nov. 2013.

[93] Y. Abe, Y. Tokuda, K. Kanamoto, and N. Tsukada, "Optical nonlinear responses of a quantum well photodiode with a nonohmic contact," Applied Physics Letters, vol. 60, pp. 1664–1666, Apr. 1992.

[94] R. T. Collins, K. v. Klitzing, and K. Ploog, "Photocurrent spectroscopy of GaAs/Al_{x}Ga_{1-x}As quantum wells in an electric field," Physical Review B, vol. 33, pp. 4378–4381, Mar. 1986.

[95] F. Findeis, M. Baier, E. Beham, A. Zrenner, and G. Abstreiter, "Photocurrent and photoluminescence of a single self-assembled quantum dot in electric fields," Applied Physics Letters, vol. 78, p. 2958, May 2001.

[96] H. Pettersson, L. Baath, N. Carlsson, W. Seifert, and L. Samuelson, "Case study of an InAs quantum dot memory: Optical storing and deletion of charge," Applied Physics Letters, vol. 79, pp. 78–80, July 2001.

[97] A. Zrenner, E. Beham, S. Stufler, F. Findeis, M. Bichler, and G. Abstreiter, "Coherent properties of a two-level system based on a quantum-dot photodiode," Nature, vol. 418, pp. 612–614, Aug. 2002.

[98] E. Beham, A. Zrenner, S. Stufler, F. Findeis, M. Bichler, and G. Abstreiter, "Coherent and incoherent properties of single quantum dot photodiodes," Physica E: Low-dimensional Systems and Nanostructures, vol. 16, pp. 59–67, Jan. 2003.

[99] S. Chanyawadee, R. T. Harley, M. Henini, D. V. Talapin, and P. G. Lagoudakis, "Photocurrent Enhancement in Hybrid Nanocrystal Quantum-Dot p-i-n Photovoltaic Devices," Physical Review Letters, vol. 102, p. 077402, Feb. 2009.

[100] M. Zecherle, C. Ruppert, E. C. Clark, G. Abstreiter, J. J. Finley, and M. Betz, "Ultrafast few-fermion optoelectronics in a single self-assembled InGaAs/GaAs quantum dot," Physical Review B, vol. 82, p. 125314, Sept. 2010.

[101] J. D. Mar, X. L. Xu, J. J. Baumberg, A. C. Irvine, C. Stanley, and D. A. Williams, "Voltage-controlled electron tunneling from a single self-assembled quantum dot embedded in a two-dimensional-electron-gas-based photovoltaic cell," Journal of Applied Physics, vol. 110, p. 053110, Sept. 2011.

[102] B. N. Pal, I. Robel, A. Mohite, R. Laocharoensuk, D. J. Werder, and V. I. Klimov, "High-Sensitivity p–n Junction Photodiodes Based on PbS Nanocrystal Quantum Dots," Advanced Functional Materials, vol. 22, no. 8, pp. 1741–1748, 2012.

[103] J. H. Quilter, R. J. Coles, A. J. Ramsay, A. M. Fox, and M. S. Skolnick, "Enhanced photocurrent readout for a quantum dot qubit by bias modulation," Applied Physics Letters, vol. 102, pp. 181108–181108–4, May 2013.

[104] H. J. Krenner, M. Sabathil, E. C. Clark, A. Kress, D. Schuh, M. Bichler, G. Abstreiter, and J. J. Finley, "Direct Observation of Controlled Coupling in an Individual Quantum Dot Molecule," Physical Review Letters, vol. 94, p. 057402, Feb. 2005.

[105] K. Müller, G. Reithmaier, E. C. Clark, V. Jovanov, M. Bichler, H. J. Krenner, M. Betz, G. Abstreiter, and J. J. Finley, "Excited state quantum couplings and optical switching of an artificial molecule," Physical Review B, vol. 84, p. 081302, Aug. 2011.

[106] N. M. Gabor, Z. Zhong, K. Bosnick, and P. L. McEuen, "Ultrafast Photocurrent Measurement of the Escape Time of Electrons and Holes from Carbon Nanotube p-i-n Photodiodes," Physical Review Letters, vol. 108, p. 087404, Feb. 2012.

[107] D. Keusters, H.-S. Tan, and Warren, "Role of Pulse Phase and Direction in Two-Dimensional Optical Spectroscopy," The Journal of Physical Chemistry A, vol. 103, pp. 10369–10380, Dec. 1999.

[108] S. T. Cundiff and J. Ye, "\textit{Colloquium} : Femtosecond optical frequency combs," Reviews of Modern Physics, vol. 75, pp. 325–342, Mar. 2003.

[109] D. Brida, C. Manzoni, and G. Cerullo, “Phase-locked pulses for two-dimensional spectroscopy by a birefringent delay line,” Optics Letters, vol. 37, pp. 3027–3029, Aug. 2012.

[110] P. Borri, W. Langbein, S. Schneider, U. Woggon, R. L. Sellin, D. Ouyang, and D. Bimberg, “Ultralong Dephasing Time in InGaAs Quantum Dots,” Physical Review Letters, vol. 87, p. 157401, Sept. 2001.

[111] D. Birkedal, K. Leosson, and J. M. Hvam, “Long Lived Coherence in Self-Assembled Quantum Dots,” Physical Review Letters, vol. 87, p. 227401, Nov. 2001.

[112] P. C. D. Hobbs, Building Electro-Optical Systems: Making It all Work. Hoboken, N.J: Wiley, 2 edition ed., Aug. 2009.

[113] K. Hayashi, K. Saitoh, Y. Shibayama, and K. Shirahama, “A current to voltage converter for cryogenics using a CMOS operational amplifier,” Journal of Physics: Conference Series, vol. 150, p. 012016, Feb. 2009.

[114] A. Pullia and F. Zocca, “Low-noise current preamplifier for photodiodes with DC-current rejector and precise intensity meter suited for optical light spectroscopy,” in 2010 IEEE Nuclear Science Symposium Conference Record (NSS/MIC), pp. 1343–1345, 2010.

[115] T.-Y. Lin, R. J. Green, and P. B. O’Connor, “A gain and bandwidth enhanced transimpedance preamplifier for Fourier-transform ion cyclotron resonance mass spectrometry,” The Review of Scientific Instruments, vol. 82, Dec. 2011.

[116] E. D. Buchanan, D. J. Benford, J. B. Forgione, S. Harvey Moseley, and E. J. Wollack, “Cryogenic applications of commercial electronic components,” Cryogenics, vol. 52, pp. 550–556, Oct. 2012.

[117] G. Bulgarini, M. E. Reimer, M. Hocevar, E. P. A. M. Bakkers, L. P. Kouwenhoven, and V. Zwiller, “Avalanche amplification of a single exciton in a semiconductor nanowire,” Nature Photonics, vol. 6, no. 7, pp. 455–458, 2012.

[118] J. Graeme, Photodiode Amplifiers: OP AMP Solutions. Boston, Mass: McGraw-Hill Education, 1 edition ed., Dec. 1995.

[119] L. Technology, “Apllication Note for LTC6244,” March 2017.

[120] R. H. Dicke, “Coherence in Spontaneous Radiation Processes,” Physical Review, vol. 93, pp. 99–110, Jan. 1954.

[121] L. M. Narducci, M. Orszag, and R. A. Tuft, “Energy Spectrum of the Dicke Hamiltonian,” Physical Review A, vol. 8, pp. 1892–1906, Oct. 1973.

[122] A. V. Andreev, V. I. Emel’yanov, and Y. A. Il’inskiĭ, “Collective spontaneous emission (Dicke superradiance),” Soviet Physics Uspekhi, vol. 23, p. 493, Aug. 1980.

[123] M. Gross and S. Haroche, "Superradiance: An essay on the theory of collective spontaneous emission," Physics Reports, vol. 93, pp. 301–396, Dec. 1982.

[124] S M Chumakov and M Kozierowski, "Dicke model: quantum nonlinear dynamics and collective phenomena," Quantum and Semiclassical Optics: Journal of the European Optical Society Part B, vol. 8, no. 4, p. 775, 1996.

[125] R. K. Bullough, "Photon, quantum and collective, effects from rydberg atoms in cavities," Hyperfine Interactions, vol. 37, pp. 71–108, Dec. 1987.

[126] A. Gaëtan, Y. Miroshnychenko, T. Wilk, A. Chotia, M. Viteau, D. Comparat, P. Pillet, A. Browaeys, and P. Grangier, "Observation of collective excitation of two individual atoms in the Rydberg blockade regime," Nature Physics, vol. 5, pp. 115–118, Feb. 2009.

[127] C. Guerlin, E. Brion, T. Esslinger, and K. Mølmer, "Cavity quantum electrodynamics with a Rydberg-blocked atomic ensemble," Physical Review A, vol. 82, p. 053832, Nov. 2010.

[128] K. Baumann, C. Guerlin, F. Brennecke, and T. Esslinger, "Dicke quantum phase transition with a superfluid gas in an optical cavity," Nature, vol. 464, pp. 1301–1306, Apr. 2010.

[129] J. Feldmann, G. Peter, E. O. Göbel, P. Dawson, K. Moore, C. Foxon, and R. J. Elliott, "Linewidth dependence of radiative exciton lifetimes in quantum wells," Physical Review Letters, vol. 59, pp. 2337–2340, Nov. 1987.

[130] E. Hanamura, "Rapid radiative decay and enhanced optical nonlinearity of excitons in a quantum well," Physical Review B, vol. 38, pp. 1228–1234, July 1988.

[131] B. Deveaud, F. Clérot, N. Roy, K. Satzke, B. Sermage, and D. S. Katzer, "Enhanced radiative recombination of free excitons in GaAs quantum wells," Physical Review Letters, vol. 67, pp. 2355–2358, Oct. 1991.

[132] L. C. Andreani, F. Tassone, and F. Bassani, "Radiative lifetime of free excitons in quantum wells," Solid State Communications, vol. 77, pp. 641–645, Mar. 1991.

[133] J. A. Schreier, A. A. Houck, J. Koch, D. I. Schuster, B. R. Johnson, J. M. Chow, J. M. Gambetta, J. Majer, L. Frunzio, M. H. Devoret, S. M. Girvin, and R. J. Schoelkopf, "Suppressing charge noise decoherence in superconducting charge qubits," Physical Review B, vol. 77, p. 180502, May 2008.

[134] M. H. Volkmann, A. Sahu, C. J. Fourie, and O. A. Mukhanov, "Implementation of energy efficient single flux quantum digital circuits with sub-aJ/bit operation," Superconductor Science and Technology, vol. 26, no. 1, p. 015002, 2013.

[135] J. M. Fink, R. Bianchetti, M. Baur, M. Göppl, L. Steffen, S. Filipp, P. J. Leek, A. Blais, and A. Wallraff, "Dressed Collective Qubit States and the Tavis-Cummings Model in Circuit QED," Physical Review Letters, vol. 103, p. 083601, Aug. 2009.

[136] P. A. Volkov and M. V. Fistul, “Collective quantum coherent oscillations in a globally coupled array of superconducting qubits,” Physical Review B, vol. 89, p. 054507, Feb. 2014.

[137] F. T. Arecchi, E. Courtens, R. Gilmore, and H. Thomas, “Atomic Coherent States in Quantum Optics,” Physical Review A, vol. 6, pp. 2211–2237, Dec. 1972.

[138] C. R. Stroud, J. H. Eberly, W. L. Lama, and L. Mandel, “Superradiant Effects in Systems of Two-Level Atoms,” Physical Review A, vol. 5, pp. 1094–1104, Mar. 1972.

[139] S. Schmitt-Rink and D. S. Chemla, “Collective Excitations and the Dynamical Stark Effect in a Coherently Driven Exciton System,” Physical Review Letters, vol. 57, pp. 2752–2755, Nov. 1986.

[140] M. Lindberg and S. W. Koch, “Effective Bloch equations for semiconductors,” Physical Review B, vol. 38, pp. 3342–3350, Aug. 1988.

[141] M. Lindberg, R. Binder, and S. W. Koch, “Theory of the semiconductor photon echo,” Physical Review A, vol. 45, pp. 1865–1875, Feb. 1992.

[142] M. Shirane, C. Ramkumar, Y. P. Svirko, H. Suzuura, S. Inouye, R. Shimano, T. Someya, H. Sakaki, and M. Kuwata-Gonokami, “Degenerate four-wave mixing measurements on an exciton-photon coupled system in a semiconductor microcavity,” Physical Review B, vol. 58, pp. 7978–7985, Sept. 1998.

[143] M. Kuwata-Gonokami, T. Aoki, C. Ramkumar, R. Shimano, and Y. Svirko, “Role of exciton–exciton interaction on resonant third-order nonlinear optical responses,” Journal of Luminescence, vol. 87–89, pp. 162–167, May 2000.

[144] L. Yang, I. V. Schweigert, S. T. Cundiff, and S. Mukamel, “Two-dimensional optical spectroscopy of excitons in semiconductor quantum wells: Liouville-space pathway analysis,” Physical Review B, vol. 75, p. 125302, Mar. 2007.

[145] L. Yang and S. Mukamel, “Revealing exciton-exciton couplings in semiconductors using multidimensional four-wave mixing signals,” Physical Review B, vol. 77, p. 075335, Feb. 2008.

[146] G. Moody, I. Akimov, H. Li, R. Singh, D. Yakovlev, G. Karczewski, M. Wiater, T. Wojtowicz, M. Bayer, and S. Cundiff, “Coherent Coupling of Excitons and Trions in a Photoexcited CdTe/CdMgTe Quantum Well,” Physical Review Letters, vol. 112, p. 097401, Mar. 2014.

[147] G. Nardin, G. Moody, R. Singh, T. M. Autry, H. Li, F. Morier-Genoud, and S. T. Cundiff, “Coherent Excitonic Coupling in an Asymmetric Double InGaAs Quantum Well Arises from Many-Body Effects,” Physical Review Letters, vol. 112, p. 046402, Jan. 2014.

[148] A. Singh, G. Moody, S. Wu, Y. Wu, N. J. Ghimire, J. Yan, D. G. Mandrus, X. Xu, and X. Li, “Coherent Electronic Coupling in Atomically Thin ${\mathrm{MoSe}}_{2}$,” Physical Review Letters, vol. 112, p. 216804, May 2014.

[149] T. Holstein and H. Primakoff, “Field Dependence of the Intrinsic Domain Magnetization of a Ferromagnet,” Physical Review, vol. 58, pp. 1098–1113, Dec. 1940.

[150] B. M. Garraway, “The Dicke model in quantum optics: Dicke model revisited,” Philosophical Transactions of the Royal Society A: Mathematical, Physical and Engineering Sciences, vol. 369, pp. 1137–1155, Mar. 2011.

[151] T. Usui, “Excitations in a High Density Electron Gas. I,” Progress of Theoretical Physics, vol. 23, pp. 787–798, May 1960.

[152] V. M. Agranovich and B. S. Toshich, “Collective Properties of Frenkel Excitons,” Soviet Journal of Experimental and Theoretical Physics, vol. 26, p. 104, Jan. 1968.

[153] G. Rochat, C. Ciuti, V. Savona, C. Piermarocchi, A. Quattropani, and P. Schwendimann, “Excitonic Bloch equations for a two-dimensional system of interacting excitons,” Physical Review B, vol. 61, pp. 13856–13862, May 2000.

[154] F. Brennecke, T. Donner, S. Ritter, T. Bourdel, M. Köhl, and T. Esslinger, “Cavity QED with a Bose–Einstein condensate,” Nature, vol. 450, pp. 268–271, Nov. 2007.

[155] A. Amo, D. Sanvitto, F. P. Laussy, D. Ballarini, E. d. Valle, M. D. Martin, A. Lemaître, J. Bloch, D. N. Krizhanovskii, M. S. Skolnick, C. Tejedor, and L. Viña, “Collective fluid dynamics of a polariton condensate in a semiconductor microcavity,” Nature, vol. 457, pp. 291–295, Jan. 2009.

[156] G. Günter, A. A. Anappara, J. Hees, A. Sell, G. Biasiol, L. Sorba, S. De Liberato, C. Ciuti, A. Tredicucci, A. Leitenstorfer, and R. Huber, “Sub-cycle switch-on of ultrastrong light–matter interaction,” Nature, vol. 458, pp. 178–181, Mar. 2009.

[157] Y. O. Dudin, L. Li, F. Bariani, and A. Kuzmich, “Observation of coherent many-body Rabi oscillations,” Nature Physics, vol. 8, pp. 790–794, Nov. 2012.

[158] R. Houdré, J. L. Gibernon, P. Pellandini, R. P. Stanley, U. Oesterle, C. Weisbuch, J. O’Gorman, B. Roycroft, and M. Ilegems, “Saturation of the strong-coupling regime in a semiconductor microcavity: Free-carrier bleaching of cavity polaritons,” Physical Review B, vol. 52, pp. 7810–7813, Sept. 1995.

[159] S. T. Cundiff, A. Knorr, J. Feldmann, S. W. Koch, E. O. Göbel, and H. Nickel, “Rabi Flopping in Semiconductors,” Physical Review Letters, vol. 73, pp. 1178–1181, Aug. 1994.

[160] B. R. Mollow, “Power Spectrum of Light Scattered by Two-Level Systems,” Physical Review, vol. 188, pp. 1969–1975, Dec. 1969.

[161] E. T. Jaynes and F. W. Cummings, "Comparison of quantum and semiclassical radiation theories with application to the beam maser," Proceedings of the IEEE, vol. 51, pp. 89–109, Jan. 1963.

[162] C. Cohen-Tannoudji, J. Dupont-Roc, and G. Grynberg, Atom-Photon Interactions: Basic Processes and Applications.

[163] M. Brune, F. Schmidt-Kaler, A. Maali, J. Dreyer, E. Hagley, J. M. Raimond, and S. Haroche, "Quantum Rabi Oscillation: A Direct Test of Field Quantization in a Cavity," Physical Review Letters, vol. 76, pp. 1800–1803, Mar. 1996.

[164] L. S. Bishop, J. M. Chow, J. Koch, A. A. Houck, M. H. Devoret, E. Thuneberg, S. M. Girvin, and R. J. Schoelkopf, "Nonlinear response of the vacuum Rabi resonance," Nature Physics, vol. 5, pp. 105–109, Feb. 2009.

[165] J. Kasprzak, S. Reitzenstein, E. A. Muljarov, C. Kistner, C. Schneider, M. Strauss, S. Höfling, A. Forchel, and W. Langbein, "Up on the Jaynes-Cummings ladder of a quantum-dot/microcavity system," Nature Materials, vol. 9, pp. 304–308, Apr. 2010.

[166] T. Niemczyk, F. Deppe, H. Huebl, E. P. Menzel, F. Hocke, M. J. Schwarz, J. J. Garcia-Ripoll, D. Zueco, T. Hümmer, E. Solano, A. Marx, and R. Gross, "Circuit quantum electrodynamics in the ultrastrong-coupling regime," Nature Physics, vol. 6, pp. 772–776, Oct. 2010.

[167] M. Tavis and F. W. Cummings, "Exact Solution for an N-Molecule—Radiation-Field Hamiltonian," Physical Review, vol. 170, pp. 379–384, June 1968.

[168] M. TAVIS and F. W. CUMMINGS, "Approximate Solutions for an N-Molecule-Radiation-Field Hamiltonian," Physical Review, vol. 188, pp. 692–695, Dec. 1969.

[169] M. S. Abdalla, S. S. Hassan, and A. S. F. Obada, "Multiphoton transition in the Tavis-Cummings model," Physical Review A, vol. 34, pp. 4869–4874, Dec. 1986.

[170] N. M. Bogoliubov, R. K. Bullough, and J. Timonen, "Exact solution of generalized Tavis - Cummings models in quantum optics," Journal of Physics A: Mathematical and General, vol. 29, p. 6305, Oct. 1996.

[171] A. Retzker, E. Solano, and B. Reznik, "Tavis-Cummings model and collective multiqubit entanglement in trapped ions," Physical Review A, vol. 75, p. 022312, Feb. 2007.

[172] A. Verger, C. Ciuti, and I. Carusotto, "Polariton quantum blockade in a photonic dot," Physical Review B, vol. 73, p. 193306, May 2006.

[173] I. I. Beterov, T. Andrijauskas, D. B. Tretyakov, V. M. Entin, E. A. Yakshina, I. I. Ryabtsev, and S. Bergamini, "Jaynes-Cummings dynamics in mesoscopic ensembles of Rydberg-blockaded atoms," Physical Review A, vol. 90, Oct. 2014. arXiv: 1404.1437.

[174] M. Kuwata-Gonokami, S. Inouye, H. Suzuura, M. Shirane, R. Shimano, T. Someya, and H. Sakaki, “Parametric Scattering of Cavity Polaritons,” Physical Review Letters, vol. 79, pp. 1341–1344, Aug. 1997.

[175] Y. P. S. a. M. S. a. H. S. a. M. Kuwata-Gonokami, “Four-Wave Mixing Theory at the Excitonic Resonance,” Journal of the Physical Society of Japan, vol. 68, no. 2, pp. 674–682, 1999.

[176] T. Baars, M. Bayer, A. Forchel, F. Schäfer, and J. P. Reithmaier, “Polariton-polariton scattering in semiconductor microcavities: Experimental observation of thresholdlike density dependence,” Physical Review B, vol. 61, pp. R2409–R2412, Jan. 2000.

[177] T. Baars, G. Dasbach, M. Bayer, and A. Forchel, “Biexciton states in semiconductor microcavities,” Physical Review B, vol. 63, p. 165311, Apr. 2001.

[178] S. Savasta, O. Di Stefano, and R. Girlanda, “Many-Body and Correlation Effects on Parametric Polariton Amplification in Semiconductor Microcavities,” Physical Review Letters, vol. 90, p. 096403, Mar. 2003.

[179] K. V. Kavokin, I. A. Shelykh, A. V. Kavokin, G. Malpuech, and P. Bigenwald, “Quantum Theory of Spin Dynamics of Exciton-Polaritons in Microcavities,” Physical Review Letters, vol. 92, p. 017401, Jan. 2004.

[180] S. Savasta, O. D. Stefano, V. Savona, and W. Langbein, “Quantum Complementarity of Microcavity Polaritons,” Physical Review Letters, vol. 94, p. 246401, June 2005.

[181] M. J. Hartmann, F. G. S. L. Brandão, and M. B. Plenio, “Strongly interacting polaritons in coupled arrays of cavities,” Nature Physics, vol. 2, pp. 849–855, Dec. 2006.

[182] M. Romanelli, C. Leyder, J. P. Karr, E. Giacobino, and A. Bramati, “Four Wave Mixing Oscillation in a Semiconductor Microcavity: Generation of Two Correlated Polariton Populations,” Physical Review Letters, vol. 98, p. 106401, Mar. 2007.

[183] M. Wouters, “Resonant polariton-polariton scattering in semiconductor microcavities,” Physical Review B, vol. 76, p. 045319, July 2007.

[184] M. Vladimirova, S. Cronenberger, D. Scalbert, M. Nawrocki, A. V. Kavokin, A. Miard, A. Lemaître, and J. Bloch, “Polarization controlled nonlinear transmission of light through semiconductor microcavities,” Physical Review B, vol. 79, p. 115325, Mar. 2009.

[185] I. Carusotto, T. Volz, and A. Imamoğlu, “Feshbach blockade: Single-photon nonlinear optics using resonantly enhanced cavity polariton scattering from biexciton states,” EPL (Europhysics Letters), vol. 90, p. 37001, May 2010.

[186] M. Vladimirova, S. Cronenberger, D. Scalbert, K. V. Kavokin, A. Miard, A. Lemaître, J. Bloch, D. Solnyshkov, G. Malpuech, and A. V. Kavokin, “Polariton-polariton interaction constants in microcavities,” Physical Review B, vol. 82, p. 075301, Aug. 2010.

[187] V. Kohnle, Y. Léger, M. Wouters, M. Richard, M. T. Portella-Oberli, and B. Deveaud, "Four-wave mixing excitations in a dissipative polariton quantum fluid," Physical Review B, vol. 86, p. 064508, Aug. 2012.

[188] P. Wen, G. Christmann, J. J. Baumberg, and K. A. Nelson, "Influence of multi-exciton correlations on nonlinear polariton dynamics in semiconductor microcavities," New Journal of Physics, vol. 15, p. 025005, Feb. 2013.

[189] T. Lecomte, D. Taj, A. Lemaitre, J. Bloch, C. Delalande, J. Tignon, and P. Roussignol, "Polariton-polariton interaction potentials determination by pump-probe degenerate scattering in a multiple microcavity," Physical Review B, vol. 89, p. 155308, Apr. 2014.

[190] F. Marchetti and J. Keeling, "Collective Pairing of Resonantly Coupled Microcavity Polaritons," Physical Review Letters, vol. 113, p. 216405, Nov. 2014.

[191] N. Takemura, S. Trebaol, M. Wouters, M. T. Portella-Oberli, and B. Deveaud, "Polaritonic Feshbach resonance," Nature Physics, vol. 10, pp. 500–504, July 2014.

[192] Y. Kaluzny, P. Goy, M. Gross, J. M. Raimond, and S. Haroche, "Observation of Self-Induced Rabi Oscillations in Two-Level Atoms Excited Inside a Resonant Cavity: The Ringing Regime of Superradiance," Physical Review Letters, vol. 51, pp. 1175–1178, Sept. 1983.

[193] M. G. Raizen, L. A. Orozco, M. Xiao, T. L. Boyd, and H. J. Kimble, "Squeezed-state generation by the normal modes of a coupled system," Physical Review Letters, vol. 59, pp. 198–201, July 1987.

[194] M. G. Raizen, R. J. Thompson, R. J. Brecha, H. J. Kimble, and H. J. Carmichael, "Normal-mode splitting and linewidth averaging for two-state atoms in an optical cavity," Physical Review Letters, vol. 63, pp. 240–243, July 1989.

[195] I. Carusotto and C. Ciuti, "Quantum fluids of light," Rev. Mod. Phys., vol. 85, pp. 299–366, Feb. 2013.

[196] R. Houdré, R. P. Stanley, U. Oesterle, M. Ilegems, and C. Weisbuch, "Room-temperature cavity polaritons in a semiconductor microcavity," Physical Review B, vol. 49, pp. 16761–16764, June 1994.

[197] R. Houdré, C. Weisbuch, R. P. Stanley, U. Oesterle, P. Pellandini, and M. Ilegems, "Measurement of Cavity-Polariton Dispersion Curve from Angle-Resolved Photoluminescence Experiments," Physical Review Letters, vol. 73, pp. 2043–2046, Oct. 1994.

[198] R. Houdré, R. P. Stanley, and M. Ilegems, "Vacuum-field Rabi splitting in the presence of inhomogeneous broadening: Resolution of a homogeneous linewidth in an inhomogeneously broadened system," Physical Review A, vol. 53, pp. 2711–2715, Apr. 1996.

[199] J. Gripp, S. L. Mielke, L. A. Orozco, and H. J. Carmichael, "Anharmonicity of the vacuum Rabi peaks in a many-atom system," Physical Review A, vol. 54, pp. R3746–R3749, Nov. 1996.

[200] R. E. Slusher, L. W. Hollberg, B. Yurke, J. C. Mertz, and J. F. Valley, "Observation of Squeezed States Generated by Four-Wave Mixing in an Optical Cavity," Physical Review Letters, vol. 55, pp. 2409–2412, Nov. 1985.

[201] Y. Zhu, D. J. Gauthier, S. E. Morin, Q. Wu, H. J. Carmichael, and T. W. Mossberg, "Vacuum Rabi splitting as a feature of linear-dispersion theory: Analysis and experimental observations," Physical Review Letters, vol. 64, pp. 2499–2502, May 1990.

[202] J. P. Karr, A. Baas, R. Houdré, and E. Giacobino, "Squeezing in semiconductor microcavities in the strong-coupling regime," Physical Review A, vol. 69, p. 031802, Mar. 2004.

[203] R. J. Thompson, G. Rempe, and H. J. Kimble, "Observation of normal-mode splitting for an atom in an optical cavity," Physical Review Letters, vol. 68, pp. 1132–1135, Feb. 1992.

[204] A. Boca, R. Miller, K. M. Birnbaum, A. D. Boozer, J. McKeever, and H. J. Kimble, "Observation of the Vacuum Rabi Spectrum for One Trapped Atom," Physical Review Letters, vol. 93, p. 233603, Dec. 2004.

[205] J. Kasprzak, M. Richard, S. Kundermann, A. Baas, P. Jeambrun, J. M. J. Keeling, F. M. Marchetti, M. H. Szymańska, R. André, J. L. Staehli, V. Savona, P. B. Littlewood, B. Deveaud, and L. S. Dang, "Bose–Einstein condensation of exciton polaritons," Nature, vol. 443, pp. 409–414, Sept. 2006.

[206] T. Jacqmin, I. Carusotto, I. Sagnes, M. Abbarchi, D. Solnyshkov, G. Malpuech, E. Galopin, A. Lemaître, J. Bloch, and A. Amo, "Direct Observation of Dirac Cones and a Flatband in a Honeycomb Lattice for Polaritons," Physical Review Letters, vol. 112, p. 116402, Mar. 2014.

[207] T. Boulier, M. Bamba, A. Amo, C. Adrados, A. Lemaitre, E. Galopin, I. Sagnes, J. Bloch, C. Ciuti, E. Giacobino, and A. Bramati, "Polariton-generated intensity squeezing in semiconductor micropillars," Nature Communications, vol. 5, p. 3260, Feb. 2014.

[208] K. Leosson, J. R. Jensen, W. Langbein, and J. M. Hvam, "Exciton localization and interface roughness in growth-interrupted GaAs/AlAs quantum wells," Physical Review B, vol. 61, pp. 10322–10329, Apr. 2000.

[209] D. Bajoni, E. Semenova, A. Lemaître, S. Bouchoule, E. Wertz, P. Senellart, S. Barbay, R. Kuszelewicz, and J. Bloch, "Optical Bistability in a GaAs-Based Polariton Diode," Physical Review Letters, vol. 101, p. 266402, Dec. 2008.

[210] D. Bajoni, E. Semenova, A. Lemaître, S. Bouchoule, E. Wertz, P. Senellart, and J. Bloch, "Polariton light-emitting diode in a GaAs-based microcavity," Physical Review B, vol. 77, p. 113303, Mar. 2008.

[211] G. V. Varada, M. S. Kumar, and G. S. Agarwal, “Quantum effects of the atom-cavity interaction on four-wave mixing,” Optics Communications, vol. 62, pp. 328–332, June 1987.

[212] R. R. Puri and A. Ray, “Quantum effects in four-wave mixing in a cavity,” Physical Review A, vol. 57, pp. 4061–4064, May 1998.

[213] B. Coffey and R. Friedberg, “Effect of short-range Coulomb interaction on cooperative spontaneous emission,” Physical Review A, vol. 17, pp. 1033–1048, Mar. 1978.

[214] A. Joshi and S. V. Lawande, “Effect of Dipole Interaction on the Vacuum Field Rabi Oscillations of Two-level Atoms in an Ideal Cavity,” Journal of Modern Optics, vol. 40, pp. 1035–1042, June 1993.

[215] R. R. Puri and A. Ray, “Collision-induced quantum effects in four-wave mixing in a high-Q cavity,” Journal of the Optical Society of America B, vol. 14, pp. 1289–1294, June 1997.

[216] B. L. Higgins, D. W. Berry, S. D. Bartlett, H. M. Wiseman, and G. J. Pryde, “Entanglement-free Heisenberg-limited phase estimation,” Nature, vol. 450, pp. 393–396, Nov. 2007.

[217] I. Afek, O. Ambar, and Y. Silberberg, “High-NOON States by Mixing Quantum and Classical Light,” Science, vol. 328, pp. 879–881, May 2010.

[218] Y.-A. Chen, X.-H. Bao, Z.-S. Yuan, S. Chen, B. Zhao, and J.-W. Pan, “Heralded Generation of an Atomic NOON State,” Physical Review Letters, vol. 104, p. 043601, Jan. 2010.

[219] Y. Israel, S. Rosen, and Y. Silberberg, “Supersensitive Polarization Microscopy Using NOON States of Light,” Physical Review Letters, vol. 112, p. 103604, Mar. 2014.

[220] P. Kok, W. J. Munro, K. Nemoto, T. C. Ralph, J. P. Dowling, and G. J. Milburn, “Linear optical quantum computing with photonic qubits,” Reviews of Modern Physics, vol. 79, pp. 135–174, Jan. 2007.

[221] S. Adachi, T. Miyashita, S. Takeyama, Y. Takagi, A. Tackeuchi, and M. Nakayama, “Polarization choices in exciton-biexciton system of GaAs quantum wells,” Physical Review B, vol. 55, pp. 1654–1660, Jan. 1997.

[222] T. F. Albrecht, K. Bott, T. Meier, A. Schulze, M. Koch, S. T. Cundiff, J. Feldmann, W. Stolz, P. Thomas, S. W. Koch, and E. O. Göbel, “Disorder mediated biexcitonic beats in semiconductor quantum wells,” Physical Review B, vol. 54, pp. 4436–4439, Aug. 1996.

[223] A. D. Bristow, D. Karaiskaj, X. Dai, R. P. Mirin, and S. T. Cundiff, “Polarization dependence of semiconductor exciton and biexciton contributions to phase-resolved optical two-dimensional Fourier-transform spectra,” Physical Review B, vol. 79, p. 161305, Apr. 2009.

[224] R. Cingolani, Y. Chen, and K. Ploog, "Biexciton formation in GaAs-$\mathrm{Al_xGa_{1-x}As}$ multiple quantum wells: an optical investigation," Physical Review B, vol. 38, pp. 13478–13481, Dec. 1988.

[225] A. L. Ivanov and H. Haug, "Self-consistent theory of the biexciton optical nonlinearity," Physical Review B, vol. 48, pp. 1490–1504, July 1993.

[226] D. J. Lovering, R. T. Phillips, G. J. Denton, and G. W. Smith, "Resonant generation of biexcitons in a GaAs quantum well," Physical Review Letters, vol. 68, pp. 1880–1883, Mar. 1992.

[227] A. E. Almand-Hunter, H. Li, S. T. Cundiff, M. Mootz, M. Kira, and S. W. Koch, "Quantum droplets of electrons and holes," Nature, vol. 506, pp. 471–475, Feb. 2014.

[228] D. Bennhardt, P. Thomas, R. Eccleston, E. J. Mayer, and J. Kuhl, "Polarization dependence of four-wave-mixing signals in quantum wells," Physical Review B, vol. 47, pp. 13485–13490, May 1993.

[229] R. T. Phillips, D. J. Lovering, G. J. Denton, and G. W. Smith, "Biexciton creation and recombination in a GaAs quantum well," Physical Review B, vol. 45, pp. 4308–4311, Feb. 1992.

[230] S. Weiser, T. Meier, J. Möbius, A. Euteneuer, E. J. Mayer, W. Stolz, M. Hofmann, W. W. Rühle, P. Thomas, and S. W. Koch, "Disorder-induced dephasing in semiconductors," Physical Review B, vol. 61, pp. 13088–13098, May 2000.

[231] R. Singh, T. Suzuki, T. M. Autry, G. Moody, M. E. Siemens, and S. T. Cundiff, "Polarization-dependent exciton linewidth in semiconductor quantum wells: A consequence of bosonic nature of excitons," Physical Review B, vol. 94, p. 081304, Aug. 2016.

[232] Y. G. Rubo, A. V. Kavokin, and I. A. Shelykh, "Suppression of superfluidity of exciton-polaritons by magnetic field," Physics Letters A, vol. 358, pp. 227–230, Oct. 2006.

[233] J. Keeling, F. M. Marchetti, M. H. Szymańska, and P. B. Littlewood, "Collective coherence in planar semiconductor microcavities," Semiconductor Science and Technology, vol. 22, no. 5, p. R1, 2007.

[234] A. Amo, T. C. H. Liew, C. Adrados, R. Houdré, E. Giacobino, A. V. Kavokin, and A. Bramati, "Exciton–polariton spin switches," Nature Photonics, vol. 4, pp. 361–366, June 2010.

[235] P. G. Savvidis, J. J. Baumberg, R. M. Stevenson, M. S. Skolnick, D. M. Whittaker, and J. S. Roberts, "Angle-Resonant Stimulated Polariton Amplifier," Physical Review Letters, vol. 84, pp. 1547–1550, Feb. 2000.

[236] X. Fan, H. Wang, H. Q. Hou, and B. E. Hammons, "Biexcitonic effects in the non-perturbative regime of semiconductor microcavities," Physical Review B, vol. 57, pp. R9451–R9454, Apr. 1998.

[237] M. Saba, F. Quochi, C. Ciuti, U. Oesterle, J. L. Staehli, B. Deveaud, G. Bongiovanni, and A. Mura, "Crossover from Exciton to Biexciton Polaritons in Semiconductor Microcavities," Physical Review Letters, vol. 85, pp. 385–388, July 2000.

[238] P. Borri, W. Langbein, U. Woggon, J. R. Jensen, and J. M. Hvam, "Biexcitons or bipolaritons in a semiconductor microcavity," Physical Review B, vol. 62, pp. R7763–R7766, Sept. 2000.

[239] P. Borri, W. Langbein, U. Woggon, A. Esser, J. R. Jensen, and J. M. Hvam, "Biexcitons in semiconductor microcavities," Semiconductor Science and Technology, vol. 18, p. S351, Oct. 2003.

[240] N. Takemura, S. Trebaol, M. D. Anderson, V. Kohnle, Y. Léger, D. Y. Oberli, M. T. Portella-Oberli, and B. Deveaud, "Two-dimensional Fourier transform spectroscopy of exciton-polaritons and their interactions," Physical Review B, vol. 92, p. 125415, Sept. 2015.

[241] N. Takemura, M. D. Anderson, S. Biswas, M. Navadeh-Toupchi, D. Y. Oberli, M. T. Portella-Oberli, and B. Deveaud, "Coherent and incoherent aspects of polariton dynamics in semiconductor microcavities," Physical Review B, vol. 94, p. 195301, Nov. 2016.

[242] J.-i. Inoue, T. Brandes, and A. Shimizu, "Renormalized bosonic interaction of excitons," Physical Review B, vol. 61, pp. 2863–2873, Jan. 2000.

[243] C. Chin, R. Grimm, P. Julienne, and E. Tiesinga, "Feshbach resonances in ultracold gases," Reviews of Modern Physics, vol. 82, pp. 1225–1286, Apr. 2010.

[244] M. Combescot, O. Betbeder-Matibet, and R. Combescot, "Bose-Einstein Condensation in Semiconductors: The Key Role of Dark Excitons," Physical Review Letters, vol. 99, p. 176403, Oct. 2007.

[245] M. Combescot and O. Betbeder-Matibet, "Faraday rotation in photoexcited semiconductors: A composite-exciton many-body effect," Physical Review B, vol. 74, p. 125316, Sept. 2006.

[246] M. Combescot, O. Betbeder-Matibet, K. Cho, and H. Ajiki, "Novel approach to nonlinear susceptibility in semiconductors," EPL (Europhysics Letters), vol. 72, p. 618, Oct. 2005.

[247] M. Combescot, M. A. Dupertuis, and O. Betbeder-Matibet, "Polariton-polariton scattering: Exact results through a novel approach," EPL (Europhysics Letters), vol. 79, no. 1, p. 17001, 2007.

[248] M. Combescot and O. Betbeder-Matibet, "Theory of spin precession monitored by laser pulse," Solid State Communications, vol. 132, pp. 129–134, Oct. 2004.

[249] F. S. Acton, Numerical Methods that Work. Washington, D.C: The Mathematical Association of America, 1st edition edition ed., Dec. 1990.

[250] D. Sivia and J. Skilling, Data Analysis: A Bayesian Tutorial. Oxford; New York: Oxford University Press, 2 edition ed., July 2006.

[251] G. Moody, R. Singh, H. Li, I. A. Akimov, M. Bayer, D. Reuter, A. D. Wieck, and S. T. Cundiff, “Correlation and dephasing effects on the non-radiative coherence between bright excitons in an InAs QD ensemble measured with 2d spectroscopy,” Solid State Communications, vol. 163, pp. 65–69, June 2013.

[252] C. L. Smallwood, T. M. Autry, and S. T. Cundiff, “Analytical solutions to the finite-pulse Bloch model for multidimensional coherent spectroscopy,” JOSA B, vol. 34, pp. 419–429, Feb. 2017.

[253] G. Bongiovanni, A. Mura, F. Quochi, S. Gürtler, J. L. Staehli, F. Tassone, R. P. Stanley, U. Oesterle, and R. Houdré, “Coherent exciton-photon dynamics in semiconductor microcavities:The influence of inhomogeneous broadening,” Physical Review B, vol. 55, pp. 7084–7090, Mar. 1997.

[254] V. Savona, C. Piermarocchi, A. Quattropani, F. Tassone, and P. Schwendimann, “Microscopic Theory of Motional Narrowing of Microcavity Polaritons in a Disordered Potential,” Physical Review Letters, vol. 78, pp. 4470–4473, June 1997.

[255] A. L. Stancik and E. B. Brauns, “A simple asymmetric lineshape for fitting infrared absorption spectra,” Vibrational Spectroscopy, vol. 47, pp. 66–69, May 2008.

[256] D. Foreman-Mackey, D. W. Hogg, D. Lang, and J. Goodman, “emcee: The MCMC Hammer,” Publications of the Astronomical Society of the Pacific, vol. 125, p. 306, Mar. 2013.

[257] R. W. Boyd, “Chapter 3 - Quantum-Mechanical Theory of the Nonlinear Optical Susceptibility,” in Nonlinear Optics (Third Edition), pp. 135–206, Burlington: Academic Press, 2008.

Appendix A

Jaynes-Cummings Dynamics

Solving the dynamics of the Jaynes-Cummings model is useful in that it provides an immediate recognition of the observable quantum phenomena present in such a system such as single-photon nonlinear optics and field-quantization. To solve these dynamics we make use of the time-dependent Schrodinger equation:

$$i\hbar\partial_t|\psi\rangle = H|\psi\rangle \tag{A.1}$$

with the general initial wavefunction

$$\frac{\partial}{\partial t}\begin{pmatrix} c_{e,n} \\ c_{g,n+1} \end{pmatrix} = \begin{pmatrix} -i(\omega_0 + n\omega_L) & -i\sqrt{n+1}g \\ -i\sqrt{n+1}g & -i(n+1)\omega_L \end{pmatrix}\begin{pmatrix} c_{e,n} \\ c_{g,n+1} \end{pmatrix} \tag{A.2}$$

which can be solved with the ansantz $c_i = A_i e^{i\lambda\cdot t}$, $\dot{A} = 0$ which removes the sums

$$\begin{pmatrix} \dot{A}_{e,n} \\ \dot{A}_{g,n+1} \end{pmatrix} e^{i\lambda\cdot t} + \begin{pmatrix} A_{e,n} \\ A_{g,n+1} \end{pmatrix} i\lambda\cdot e^{i\lambda\cdot t} = \begin{pmatrix} -i(\omega_0 + n\omega_L) & -i\sqrt{n+1}g \\ -i\sqrt{n+1}g & -i(n+1)\omega_L \end{pmatrix}\begin{pmatrix} A_{e,n} \\ A_{g,n+1} \end{pmatrix} e^{i\lambda\cdot t} \tag{A.3}$$

Solving for the values λ using $M - I_{2,2}\lambda = 0$ we find

$$\begin{pmatrix} -i(\omega_0 + n\omega_L) - i\lambda & -i\sqrt{n+1}g \\ -i\sqrt{n+1}g & -i(n+1)\omega_L - i\lambda \end{pmatrix}\begin{pmatrix} A_{e,n} \\ A_{g,n+1} \end{pmatrix} e^{i\lambda\cdot t} == 0 \tag{A.4}$$

$$\lambda_{\pm} = n\omega_L + \frac{1}{2}(\omega_0 + \omega_L \pm \sqrt{4g^2(n+1) + (\omega_0 - \omega_L)^2}) \tag{A.5}$$

Solving for the eigenfunctions with $A^2_{g,n+1} + A^2_{e,n} = 1$ yields two conditions for $A_{g,n+1}$

$$A_{g,n+1,\lambda_-} = -\frac{\omega_0 + n\omega_L - \lambda_-}{g\sqrt{n+1}} A_{e,n} \tag{A.6}$$

$$A_{g,n+1,\lambda_+} = -\frac{\omega_0 + n\omega_L - \lambda_+}{g\sqrt{n+1}} A_{e,n} \tag{A.7}$$

for λ_- on resonance $A_{g,n+1,\lambda_-} = -A_{e,n}$ while for λ_+ on resonance $A_{g,n+1,\lambda_+} = A_{e,n}$. This provides two symmetric wavefunctions on resonance

$$|+\rangle = \frac{1}{2}[|e,n\rangle + |g,n+1\rangle] \tag{A.8}$$

$$|-\rangle = \frac{1}{2}[|e,n\rangle - |g,n+1\rangle] \tag{A.9}$$

$$\tag{A.10}$$

re-writing $|e,n\rangle$ in the new basis and solving for $P_{e,n} = |\langle e,n|e^{\frac{iH\cdot t}{\hbar}}|e,n\rangle|^2$ yields

$$P_{e,n} = |\frac{1}{\sqrt{2}}(\langle +| + \langle -|)\frac{1}{\sqrt{2}}(e^{i\lambda_+ t}|+\rangle + e^{i\lambda_- t}|-\rangle)|^2 \tag{A.11}$$

$$P_{e,n} = \frac{1}{4}[2 + 2\cos\frac{(\lambda_+ - \lambda_-)t}{2}] = \cos^2(g\sqrt{n+1}) \tag{A.12}$$

Thus the evolution of any prepared state $|e,n\rangle$ oscillates at a rate given by the Rabi frequency at the level n. For a general state generally written with Eq.

$$P_{e,n} = \sum_{n=0}^{\infty} C_n \cos^2(g\sqrt{n+1}). \tag{A.13}$$

In general C_n represents the statistical dispersion of photon numbers. For thermal fields it is exponential, while for coherent fields it is Poissonian [163].

Appendix B

Semi-Classical vs Tavis-Cummings Linear Susceptibility

In this appendix I derive the semi-classical linear susceptibility for both a semi-classical ensemble of two-level systems (TLS) and for the Tavis-Cummings system. In both cases the linear susceptibility for both a collective and non-collective ensemble of two-level systems is found to be the same. Since only a linear susceptibility is required to establish a regime of strong-coupling the observation of a vacuum Rabi splitting is not sufficient to establish a regime of quantum coupling. The derivation of macroscopic polarization follows the approach of Boyd [257]. In general in quantum mechanics a wave-equation must be solved to find the emitted field. This wave equation depends on the polarization induced by incident light. The general form of this equation is given by:

$$\nabla^2 E - \frac{1}{c^2}\frac{\partial^2 E}{\partial t^2} = \frac{1}{\epsilon_0 c^2}\frac{\partial^2 P}{\partial t^2}. \tag{B.1}$$

The physics of spectroscopy is described by trying to understand the nature of P the polarization. The polarization for a classical harmonic oscillator excited by a driving laser at frequency ω_L is given by:

$$P = \frac{N}{V\epsilon_0\hbar}\frac{\mu_{01}^2 E_0 e^{i\omega_L t}}{(\omega_{01}-\omega_L) - i\gamma_{01}} \tag{B.2}$$

where N is the number of oscillators and V is the volume of the oscillators. As we will see the first order polarization of an ensemble of TLS is the same as that of a classical harmonic oscillator.

B.0.1 Calculation of the Linear Susceptibility using a Non-Collective Ensemble of TLS

In order to derive this polarization we start with a semi-classical, non-collective ensemble. The density matrix of a TLS can be calculated from Boyd Equation 3.5.1 − 3.5.5 and is given by

$$\rho_{nm}^{(1)} = e^{-(i\omega_{nm}+\gamma_{nm})t}\int_{-\infty}^{t} dt' \frac{-i}{\hbar}[V(t'),\rho^{(0)}]_{nm} e^{(i\omega_{nm}+\gamma_{nm})t}. \tag{B.3}$$

Where the interaction Hamiltonian $V(t')$ is given by:

$$V(t') = -\mu \cdot E(t') \tag{B.4}$$

$$E(t) = E_0 e^{-i\omega_L t} \tag{B.5}$$

$$[V(t'),\rho^{(0)}]_{nm} = -(\rho_{mm}^{(0)} - \rho_{nn}^{(0)})\mu_{nm} \cdot E(t) \tag{B.6}$$

Solving the differential equation we find:

$$\rho_{nm}^{(1)} = \frac{(\rho_{mm}^{(0)} - \rho_{nn}^{(0)})}{\hbar} \frac{\mu_{nm} E_0 e^{-i\omega_L t}}{(\omega_{nm} - \omega_L) - i\gamma_{nm}} \tag{B.7}$$

$$< \mu >= tr(\rho^{(1)}\hat{\mu} >= \sum_{nm} \rho_{nm}^{(1)}\mu_{mn} = \sum_{nm} \frac{(\rho_{mm}^{(0)} - \rho_{nn}^{(0)})}{\hbar} \frac{\mu_{mn}\mu_{nm} E_0 e^{-i\omega_L t}}{(\omega_{nm} - \omega_L) - i\gamma_{nm}} \tag{B.8}$$

This equation can now be averaged over all TLS excited in the same way.

$$P = \frac{N}{V} \sum_{nm} \frac{(\rho_{mm}^{(0)} - \rho_{nn}^{(0)})}{\hbar} \frac{\mu_{mn}\mu_{nm} E_0 e^{-i\omega_L t}}{(\omega_{nm} - \omega_L) - i\gamma_{nm}} \tag{B.9}$$

For a two level system this equation can be reduced so that only two terms exist.

$$P \sim \frac{N}{V}\sum_{nm}(\rho_{mm}^{(0)} - \rho_{nn}^{(0)}) =$$

$$\sum_{n}[(\rho_{11}^{(0)} - \rho_{nn}^{(0)}) + (\rho_{00}^{(0)} - \rho_{nn}^{(0)})] =$$

$$[(\rho_{11}^{(0)} - \rho_{11}^{(0)}) + (\rho_{00}^{(0)} - \rho_{11}^{(0)}) + (\rho_{11}^{(0)} - \rho_{00}^{(0)}) + (\rho_{00}^{(0)} - \rho_{00}^{(0)})]$$

$$P \sim \frac{N}{V}[(\rho_{00}^{(0)} - \rho_{11}^{(0)}) + (\rho_{11}^{(0)} - \rho_{00}^{(0)})] \tag{B.10}$$

$$P = \frac{N}{V}[\frac{(\rho_{00}^{(0)} - \rho_{11}^{(0)})}{\hbar}\frac{\mu_{10}\mu_{01}E_0 e^{-i\omega_L t}}{(\omega_{10} - \omega_L) - i\gamma_{10}} + \frac{(\rho_{11}^{(0)} - \rho_{00}^{(0)})}{\hbar}\frac{\mu_{01}\mu_{10}E_0 e^{-i\omega_L t}}{(\omega_{01} - \omega_L) - i\gamma_{01}}] \tag{B.11}$$

Let $\rho_{00} = 1$ and $\rho_{11} = 0$.

$$P = \frac{N}{V}[\frac{\rho_{00}^{(0)}}{\hbar}\frac{\mu_{10}\mu_{01}E_0 e^{-i\omega_L t}}{(\omega_{10} - \omega_L) - i\gamma_{10}} - \frac{\rho_{00}^{(0)}}{\hbar}\frac{\mu_{01}\mu_{10}E_0 e^{-i\omega_L t}}{(\omega_{01} - \omega_L) - i\gamma_{01}}] \tag{B.12}$$

and $\omega_{10} = -\omega_{01}$ and $\gamma_{10} = \gamma_{01}$

$$P = \frac{N}{V}[\frac{\rho_{00}^{(0)}}{\hbar}\frac{\mu_{10}\mu_{01}E_0 e^{-i\omega_L t}}{(\omega_{10} - \omega_L) - i\gamma_{10}} + \frac{\rho_{00}^{(0)}}{\hbar}\frac{\mu_{01}\mu_{10}E_0 e^{-i\omega_L t}}{(\omega_{01} + \omega_L) + i\gamma_{01}}] \tag{B.13}$$

The term on the right is the non resonant term. Thus

$$P = \frac{N}{V}[\frac{\rho_{00}^{(0)}}{\hbar}\frac{\mu_{10}\mu_{01}E_0 e^{-i\omega_L t}}{(\omega_{10} - \omega_L) - i\gamma_{10}}] \tag{B.14}$$

B.0.2 Calculation of the Linear Susceptibility using a Collective Dipole

The calculation of the linear susceptibility for a collective ensemble is primarily concerned with making use of the collective dipole moment of the ensemble. Thus we can start by directly analyzing Eq.(B.8) for the Tavis-Cummings model. Since we know that for the first dipole transition moment is given by $\langle|0|\mu|1\rangle = -\mu_0\sqrt{N}$. We find that

$$< \mu >= tr(\rho^{(1)}\hat{\mu} >= \sum_{nm} \rho^{(1)}_{nm}\mu_{mn} = \sum_{nm} \frac{(\rho^{(0)}_{mm} - \rho^{(0)}_{nn})}{\hbar} \frac{\mu_0^2 N E_0 e^{-i\omega_L t}}{(\omega_{nm} - \omega_L) - i\gamma_{nm}} \tag{B.15}$$

The polarization is defined as the number of dipoles per unit volume. The above dipole already represents the number of dipoles. Therefore all that remains is to normalize by the volume.

$$P = \frac{< \mu >}{V} = \frac{tr(\rho^{(1)}\hat{\mu} >}{V} = \sum_{nm} \frac{\rho^{(1)}_{nm}\mu_{mn}}{V} = \frac{N}{V} \sum_{nm} \frac{(\rho^{(0)}_{mm} - \rho^{(0)}_{nn})}{\hbar} \frac{\mu_0^2 E_0 e^{-i\omega_L t}}{(\omega_{nm} - \omega_L) - i\gamma_{nm}} \tag{B.16}$$

The equivalence between the first order polarization of classical ensemble of TLS and a collective ensemble of TLS indicates that linear spectroscopy is unsuitable for distinguishing between the two. Additionally, since the first order polarization of both systems is equivalent to the linear polarization of a classical system, the observation of strong-coupling between a cavity and an optical absorber is not sufficient to establish a quantum statistical regime [201]. Nonlinear corrections to the polarization will alter the polarization providing information about the saturation and optical response of a quantum absorber [13, 18], while a classical oscillator will exhibit no saturation. Thus only through nonlinear measurements can information about quantum statistics be learned [20, 21, 45, 163–166, 200, 203, 204].

Appendix C

Understanding the Eigenstates of Exciton-Polaritons Through a Quantum Beamsplitter

In the limit that the exciton-polariton is unsaturated the eigenstates of the exciton-polariton can be understood through a close analogy with a quantum beamsplitter. The beamsplitter Hamiltonian couples two photonic modes at the two input ports of the beamsplitter. These photonic modes are bosonic providing a direct analogy with the exciton-polariton system where the exciton is bosonic. The exciton-polariton Hamiltonian of Eq.(6.1) performs a basis transformation between exciton-cavity and upper-lower polariton in exactly the same fashion as the quantum beamsplitter. Instead of two photon input ports there is an upper and lower polariton input port and a photon and exciton output port. The quantum beamsplitter Hamiltonian at zero-detuning between inputs is [220]:

$$H = \theta(e^{i\phi}a_1^\dagger a_2 + e^{-i\phi}a_2^\dagger a_1) \tag{C.1}$$

Here θ is the coupling constant and ϕ is a relative phase with $a_{1,2}^\dagger(a_{1,2})$ representing the input port creation(annihilation) operators. For an optical beamsplitter the reflection coefficient $R = \sin^2(\theta)$. The formulation of the beamsplitter Hamiltonian allows for a unitary operator $S = e^{iH}$ to be written which transforms the initial state to it's final state.

$$|out\rangle = Sa_1^\dagger|0_1, 0_2\rangle = Sa_1^\dagger S^\dagger S|0_1, 0_2\rangle \tag{C.2}$$

$$= \cos\theta|1_3, 0_4\rangle + ie^{-i\phi}\sin\theta|0_3, 1_4\rangle \tag{C.3}$$

Where the subscripts indicate the two entrance $(1-2)$ and output $(3-4)$ ports. The relative phase can be set $(\phi = \frac{\pi}{2})$ making the wave function identical to that of the UP-LP state. This clear analogy leads to the middle eigenstate consisting of both UP and LP states inputs having the form of a NOON state. This leads to the M2P state $|\psi\rangle = \frac{1}{\sqrt{2}}(|2,0\rangle - |0,2\rangle)$. This state has the form.

$$
\begin{aligned}
|out\rangle &= S a_1^\dagger a_2^\dagger |0_1, 0_2\rangle = S a_1^\dagger S^\dagger S a_2^\dagger S^\dagger S |0_1, 0_2\rangle && \text{(C.4)} \\
&= \cos 2\theta |1_3, 1_4\rangle + \frac{\sin 2\theta}{\sqrt{2}} (e^{i(\frac{pi}{2}+\phi)} |0_3, 2_4\rangle + e^{-i(\frac{pi}{2}-\phi)} |2_3, 0_4\rangle) && \text{(C.5)}
\end{aligned}
$$

The difference is that instead of being composed of two two photons in one or the other output of the beam splitter the polariton state is composed of either two-excitons or two-photons. The coupling angle θ of the quantum beamsplitter is then analogous to the coupling constant g. The other $n = 2$ states fall directly out of this by inputing in either two UP or two LP into the quantum beamsplitter. The beamsplitter Hamiltonian provides a convenient method to calculating the exciton-polariton wavefunctions at low saturation density. The quantum beamsplitter can support many $NOON$ states and we expect that these states should naturally exist in exciton-polariton systems. Deterministically accessing these states is a challenging proposition.

Appendix D

Supplemental Fitting Plots

In this section we include some fitting results from our analysis. In particular the posterior probability projections from the linear absorption fits are included here. The variables are as follows w1 is the resonant frequency, gt is the linewidth (half width at half max),A is the amplitude, sigma is the asymmetry parameter, phase is to deal with interference terms and background is a constant background term.

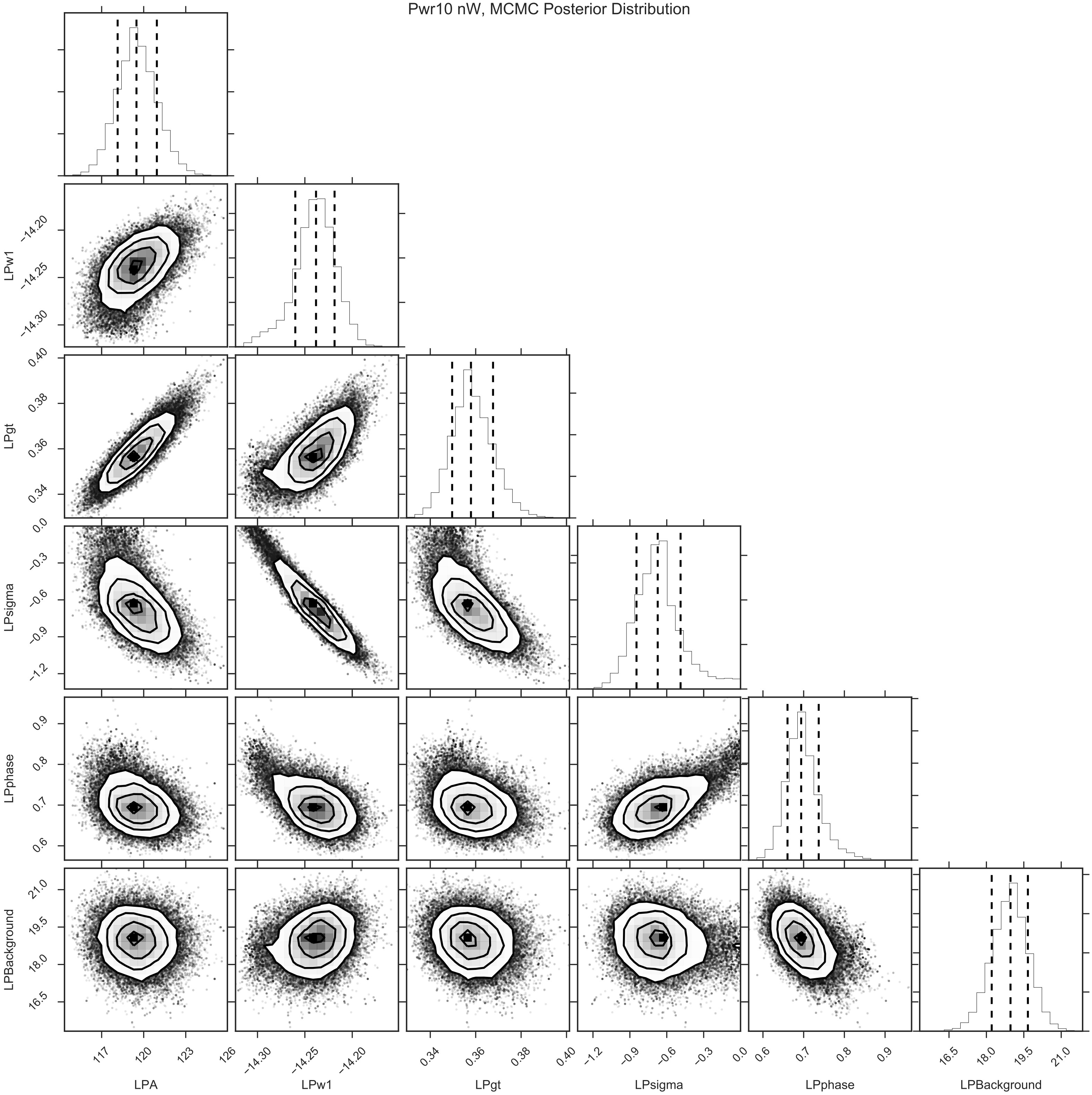
Pwr10 nW, MCMC Posterior Distribution

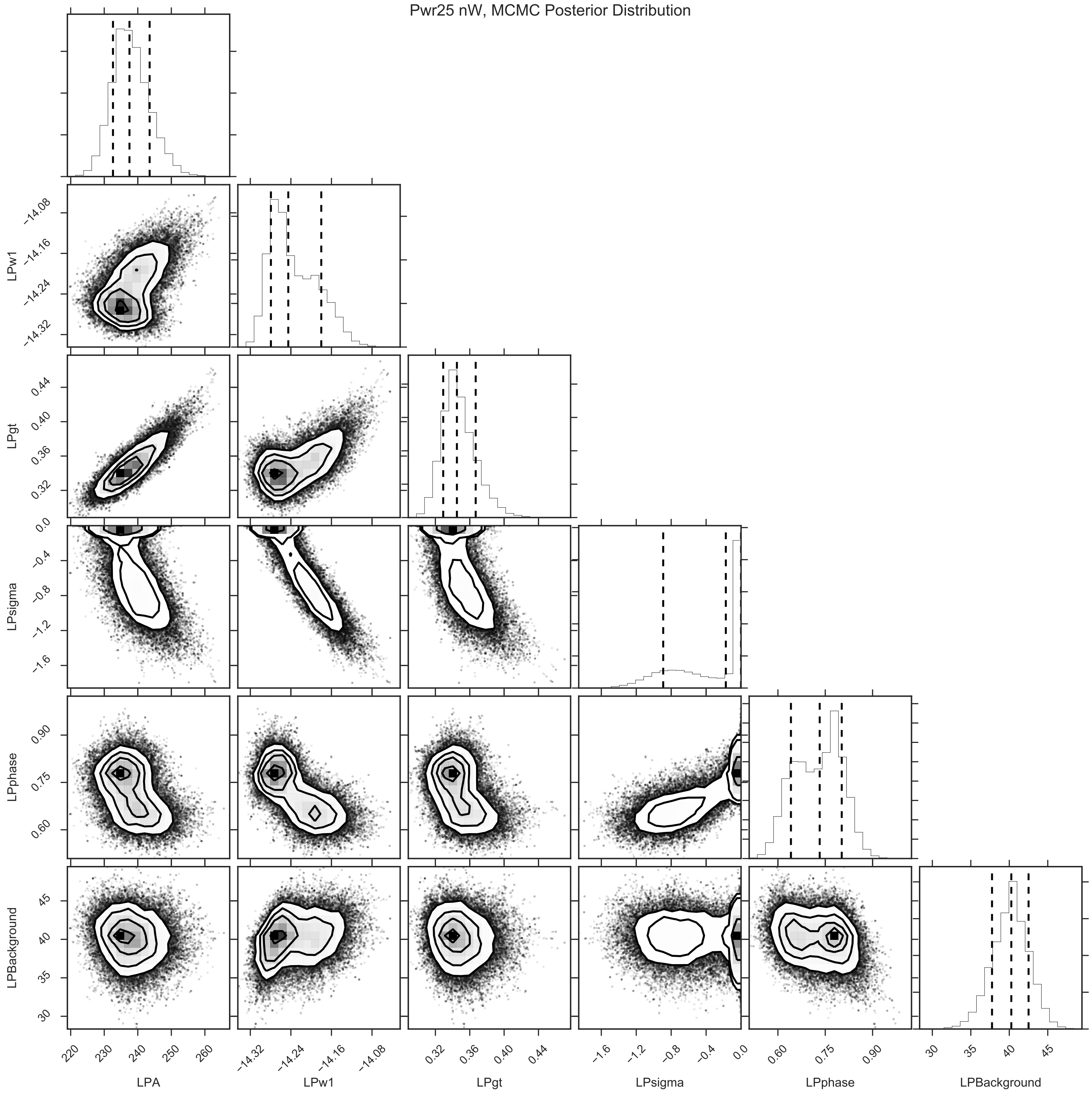

Pwr25 nW, MCMC Posterior Distribution

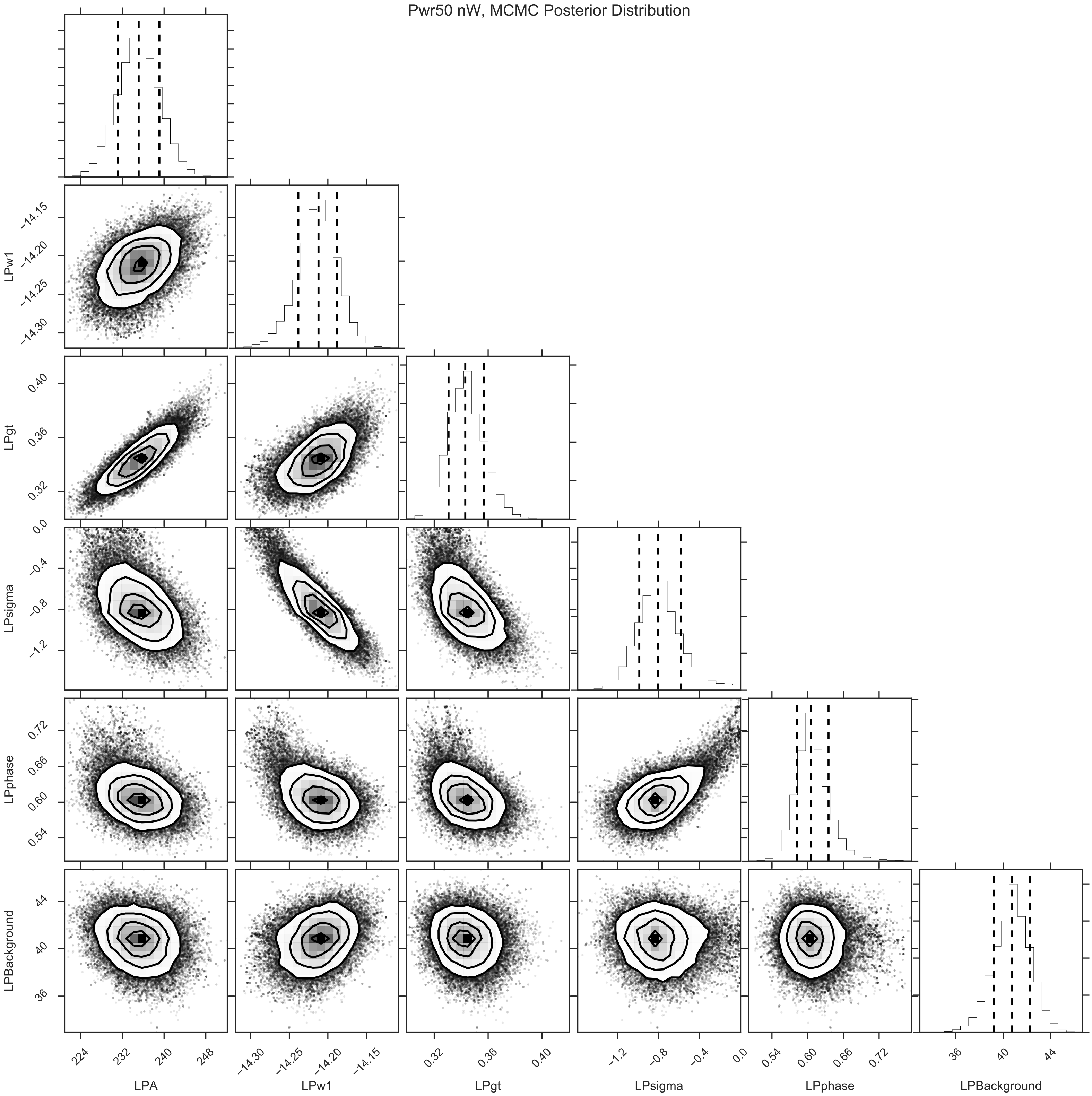

Pwr50 nW, MCMC Posterior Distribution

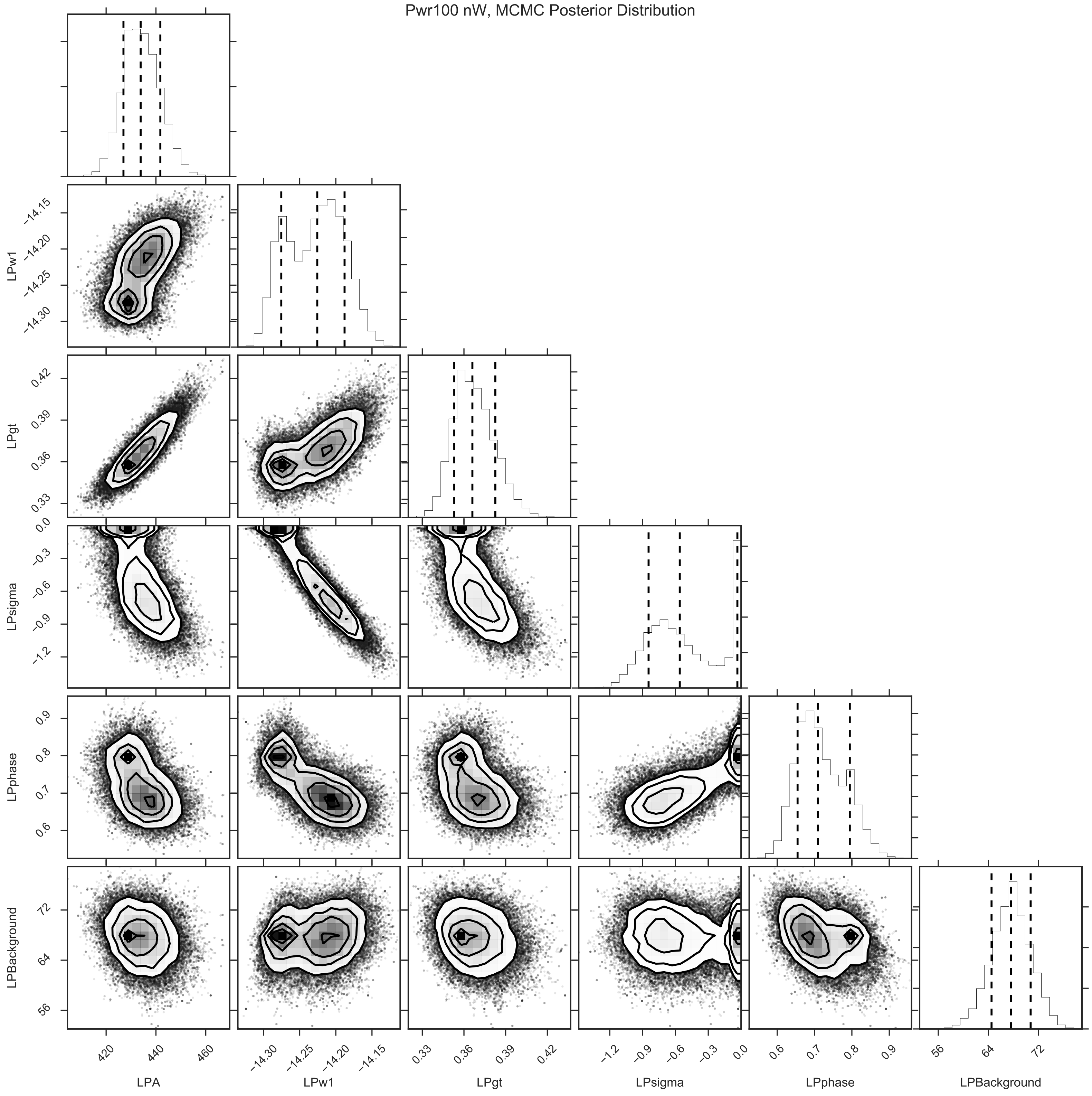
Pwr100 nW, MCMC Posterior Distribution

Pwr200 nW, MCMC Posterior Distribution

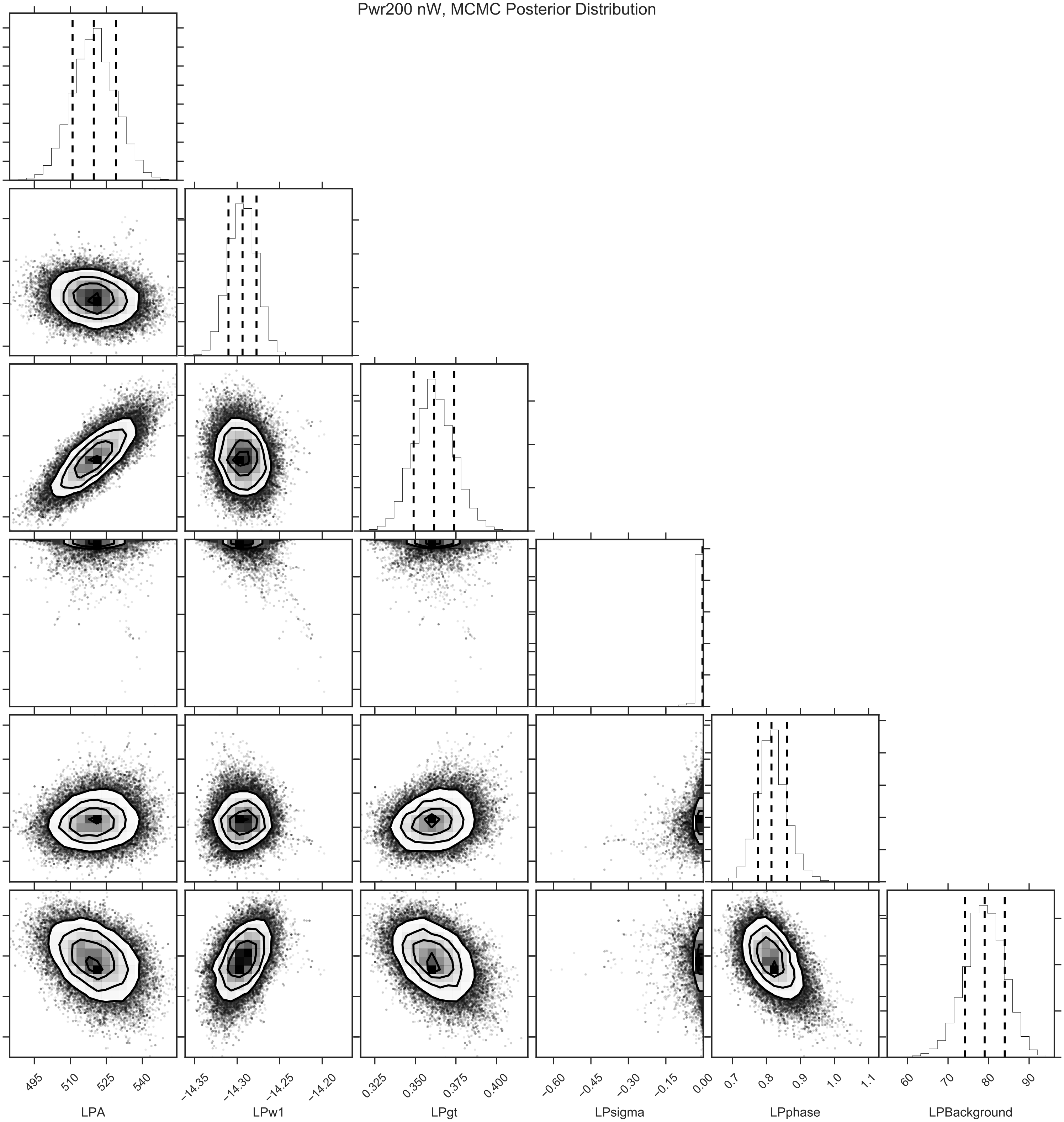

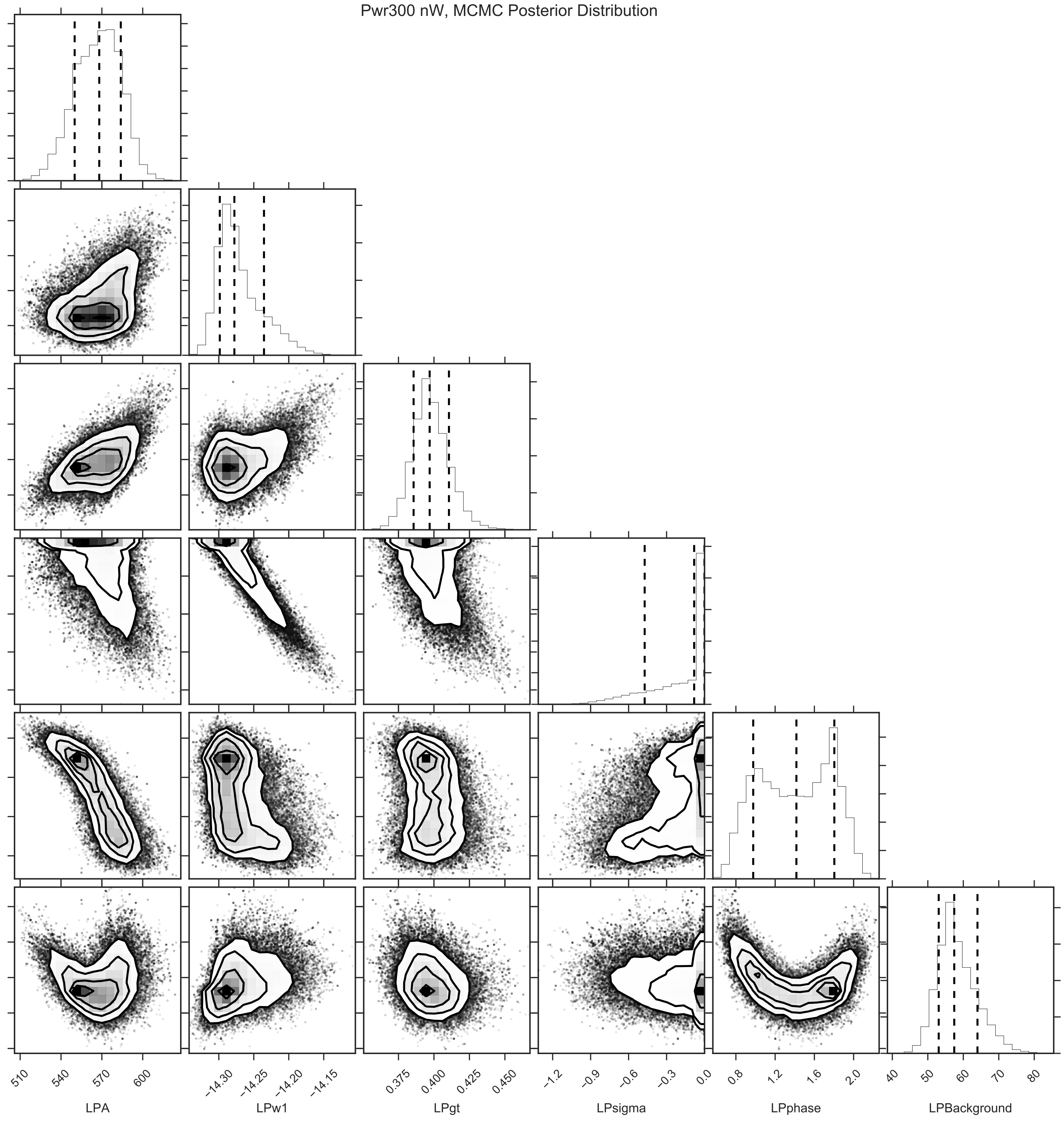
Pwr300 nW, MCMC Posterior Distribution
LPw1
−14.15
−14.20
−14.25
−14.30
LPgt
0.450
0.425
0.400
0.375
LPsigma
0.0
−0.3
−0.6
−0.9
−1.2
LPphase
2.0
1.6
1.2
0.8
LPBackground
80
70
60
50
40
510
540
570
600
LPA
−14.30
−14.25
−14.20
−14.15
LPw1
0.375
0.400
0.425
0.450
LPgt
−1.2
−0.9
−0.6
−0.3
0.0
LPsigma
0.8
1.2
1.6
2.0
LPphase
40
50
60
70
80
LPBackground

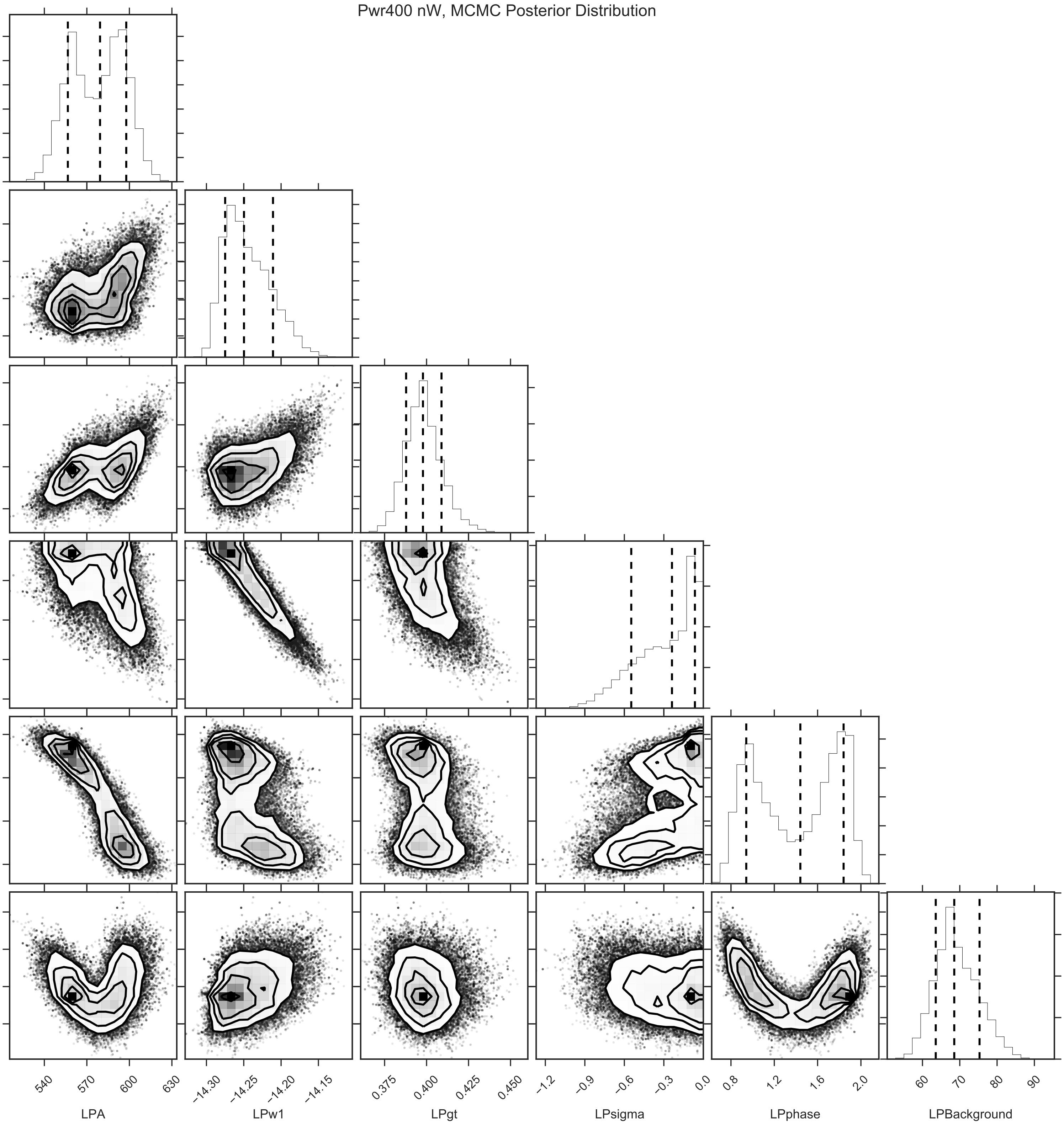
Pwr400 nW, MCMC Posterior Distribution
LPw1
−14.15
−14.20
−14.25
−14.30
LPgt
0.450
0.425
0.400
0.375
LPsigma
0.0
−0.3
−0.6
−0.9
−1.2
LPphase
2.0
1.6
1.2
0.8
LPBackground
90
80
70
60
540
570
600
630
LPA
−14.30
−14.25
−14.20
−14.15
LPw1
0.375
0.400
0.425
0.450
LPgt
−1.2
−0.9
−0.6
−0.3
0.0
LPsigma
0.8
1.2
1.6
2.0
LPphase
60
70
80
90
LPBackground

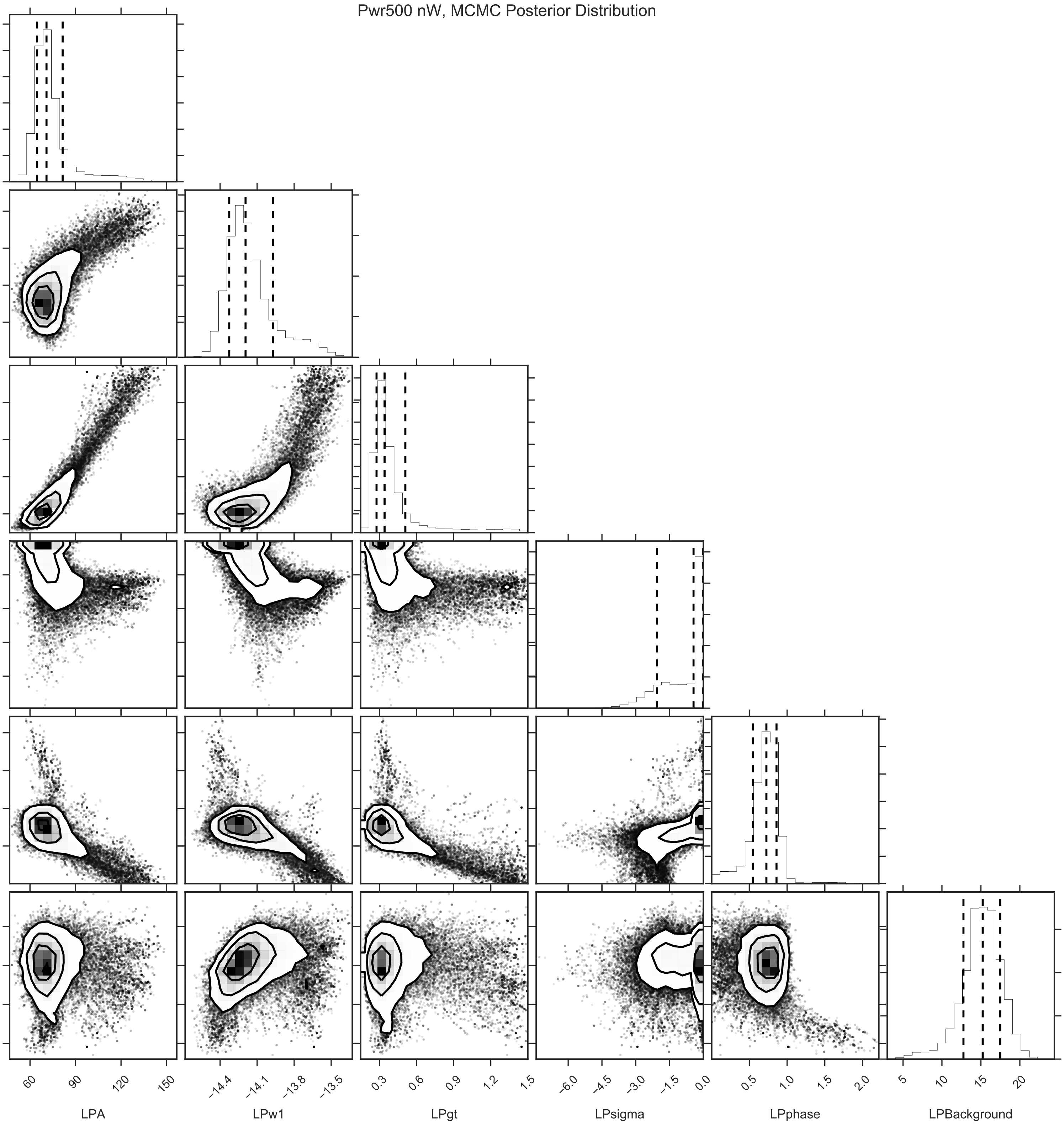
Pwr500 nW, MCMC Posterior Distribution
LPw1
−13.5
−13.8
−14.1
−14.4
LPgt
1.5
1.2
0.9
0.6
0.3
LPsigma
0.0
−1.5
−3.0
−4.5
−6.0
LPphase
2.0
1.5
1.0
0.5
LPBackground
20
15
10
5
60
90
120
150
LPA
−14.4
−14.1
−13.8
−13.5
LPw1
0.3
0.6
0.9
1.2
1.5
LPgt
−6.0
−4.5
−3.0
−1.5
0.0
LPsigma
0.5
1.0
1.5
2.0
LPphase
5
10
15
20
LPBackground

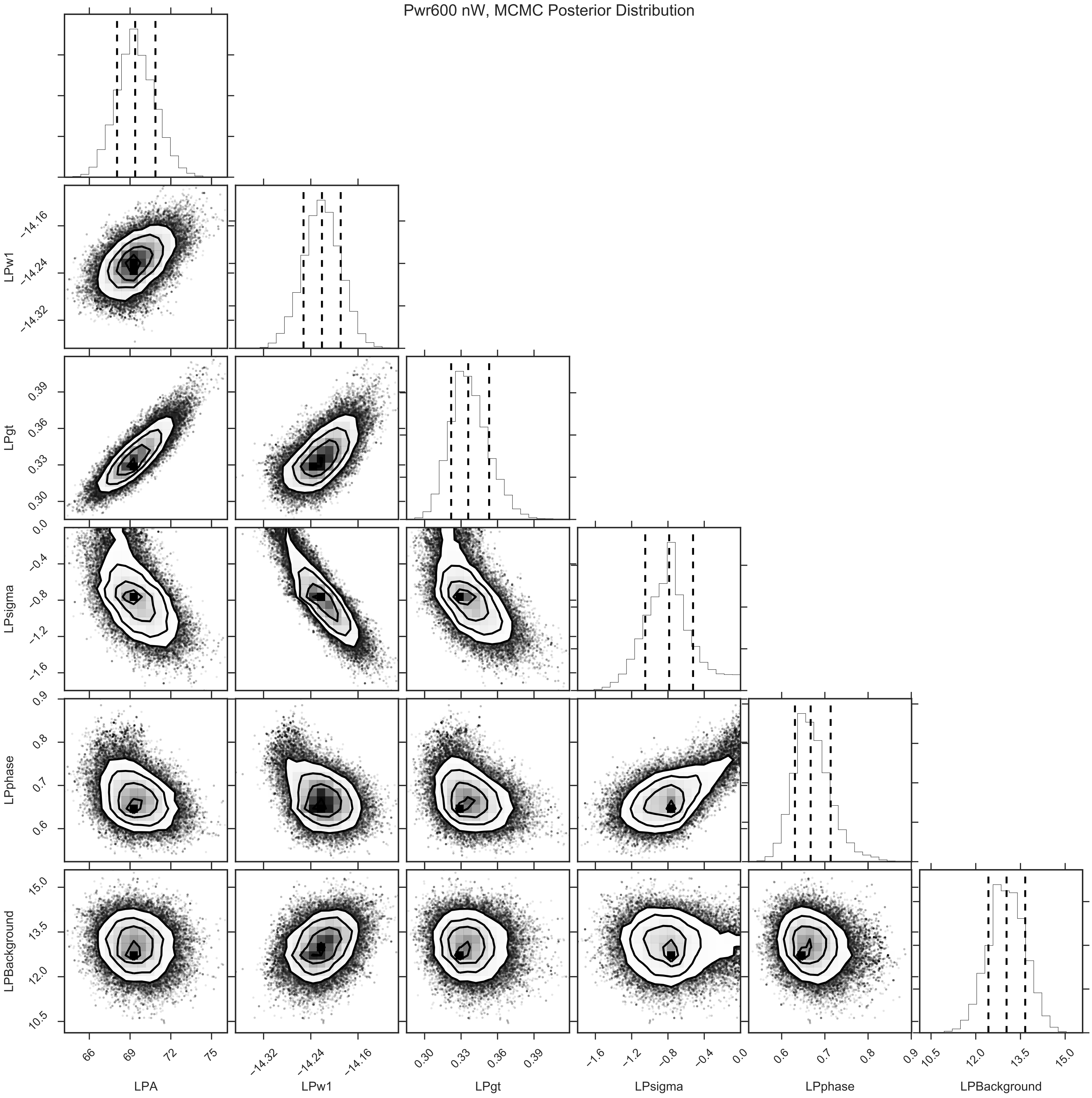

Pwr600 nW, MCMC Posterior Distribution

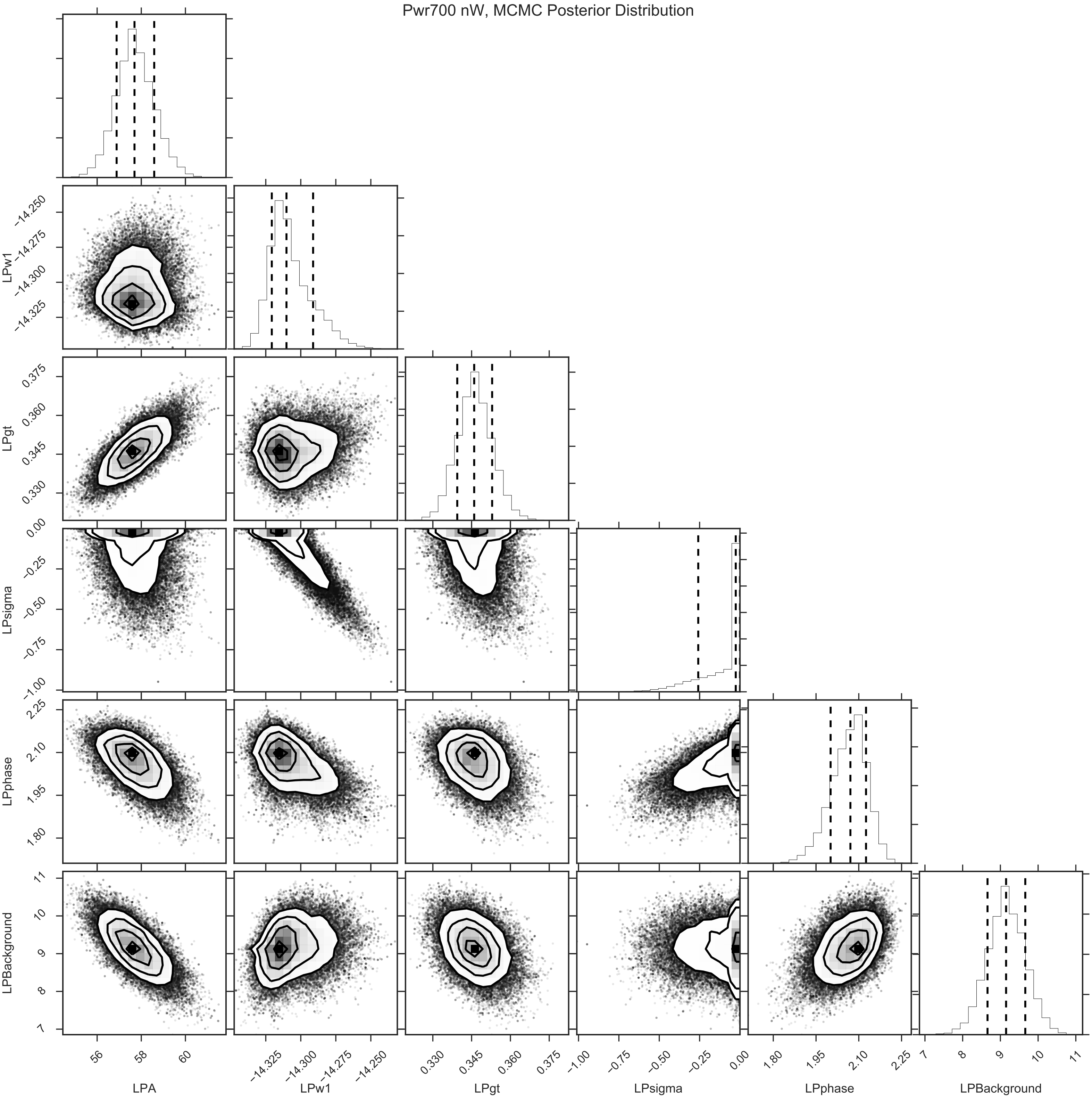
Pwr700 nW, MCMC Posterior Distribution
LPw1
−14.250
−14.275
−14.300
−14.325
LPgt
0.375
0.360
0.345
0.330
LPsigma
0.00
−0.25
−0.50
−0.75
−1.00
LPphase
2.25
2.10
1.95
1.80
LPBackground
11
10
9
8
7
56
58
60
LPA
−14.325
−14.300
−14.275
−14.250
LPw1
0.330
0.345
0.360
0.375
LPgt
−1.00
−0.75
−0.50
−0.25
0.00
LPsigma
1.80
1.95
2.10
2.25
LPphase
7
8
9
10
11
LPBackground

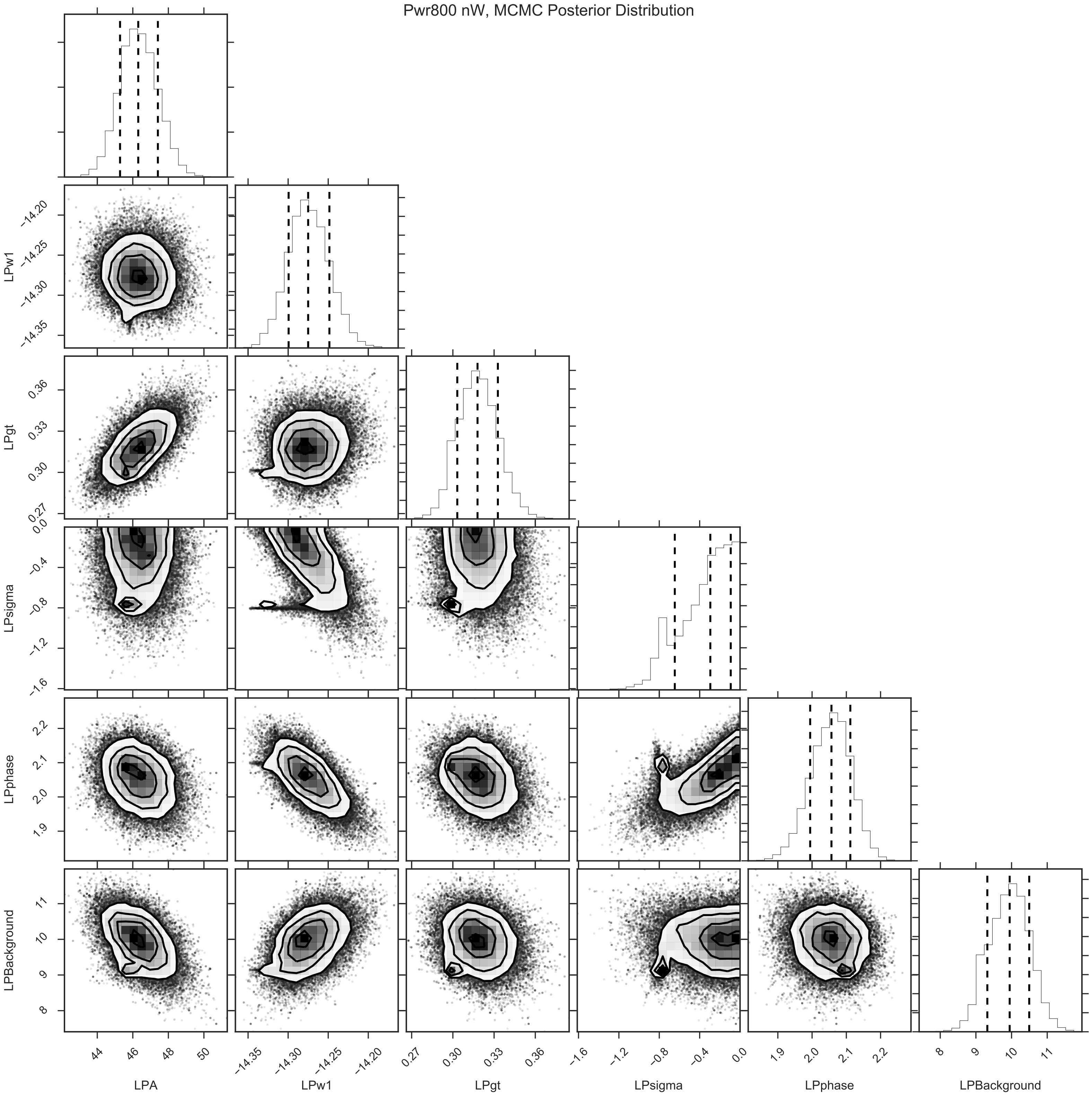
Pwr800 nW, MCMC Posterior Distribution

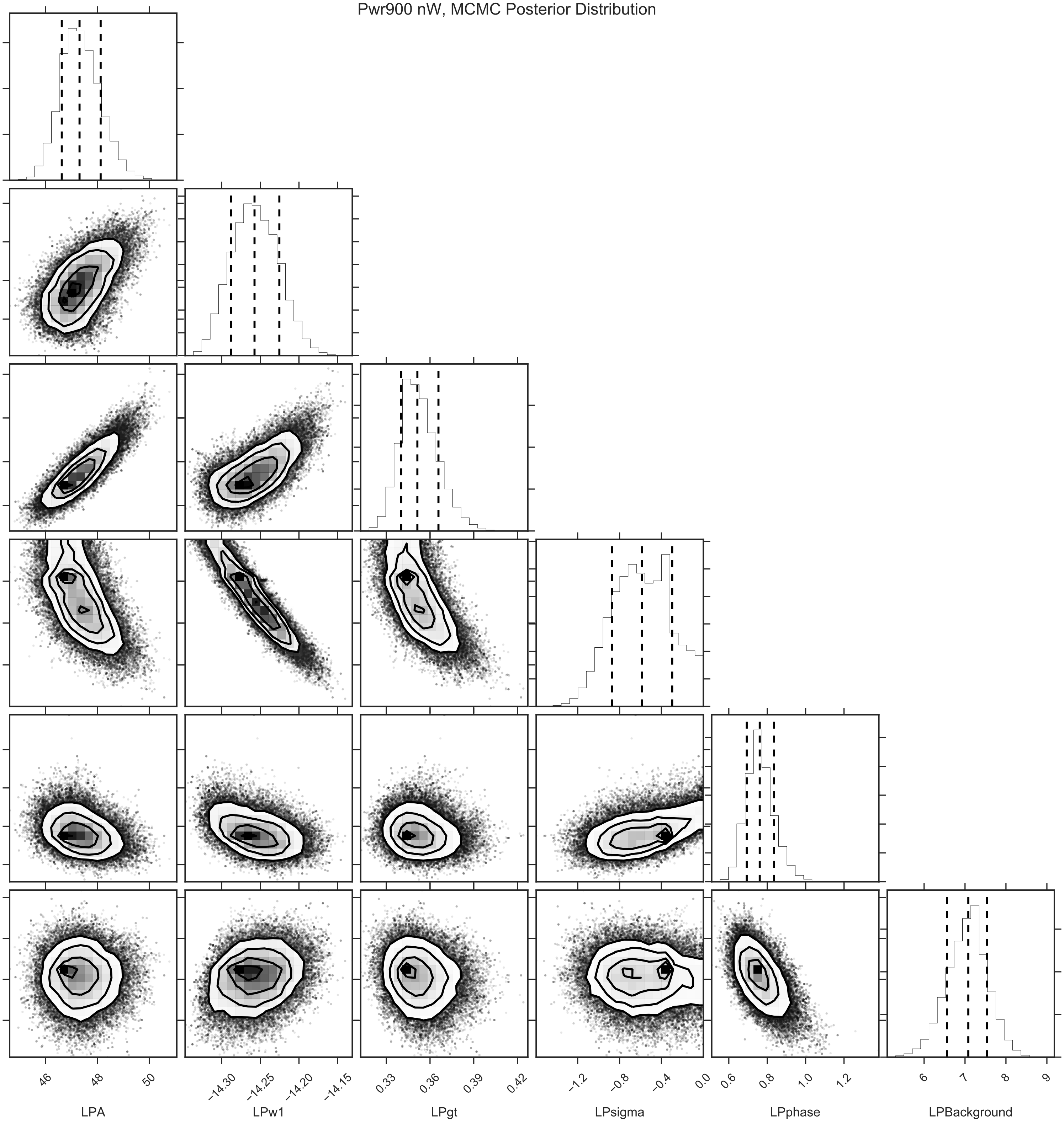
Pwr900 nW, MCMC Posterior Distribution
LPw1
−14.15
−14.20
−14.25
−14.30
LPgt
0.42
0.39
0.36
0.33
LPsigma
0.0
−0.4
−0.8
−1.2
LPphase
1.2
1.0
0.8
0.6
LPBackground
9
8
7
6
46
48
50
LPA
−14.30
−14.25
−14.20
−14.15
LPw1
0.33
0.36
0.39
0.42
LPgt
−1.2
−0.8
−0.4
0.0
LPsigma
0.6
0.8
1.0
1.2
LPphase
6
7
8
9
LPBackground

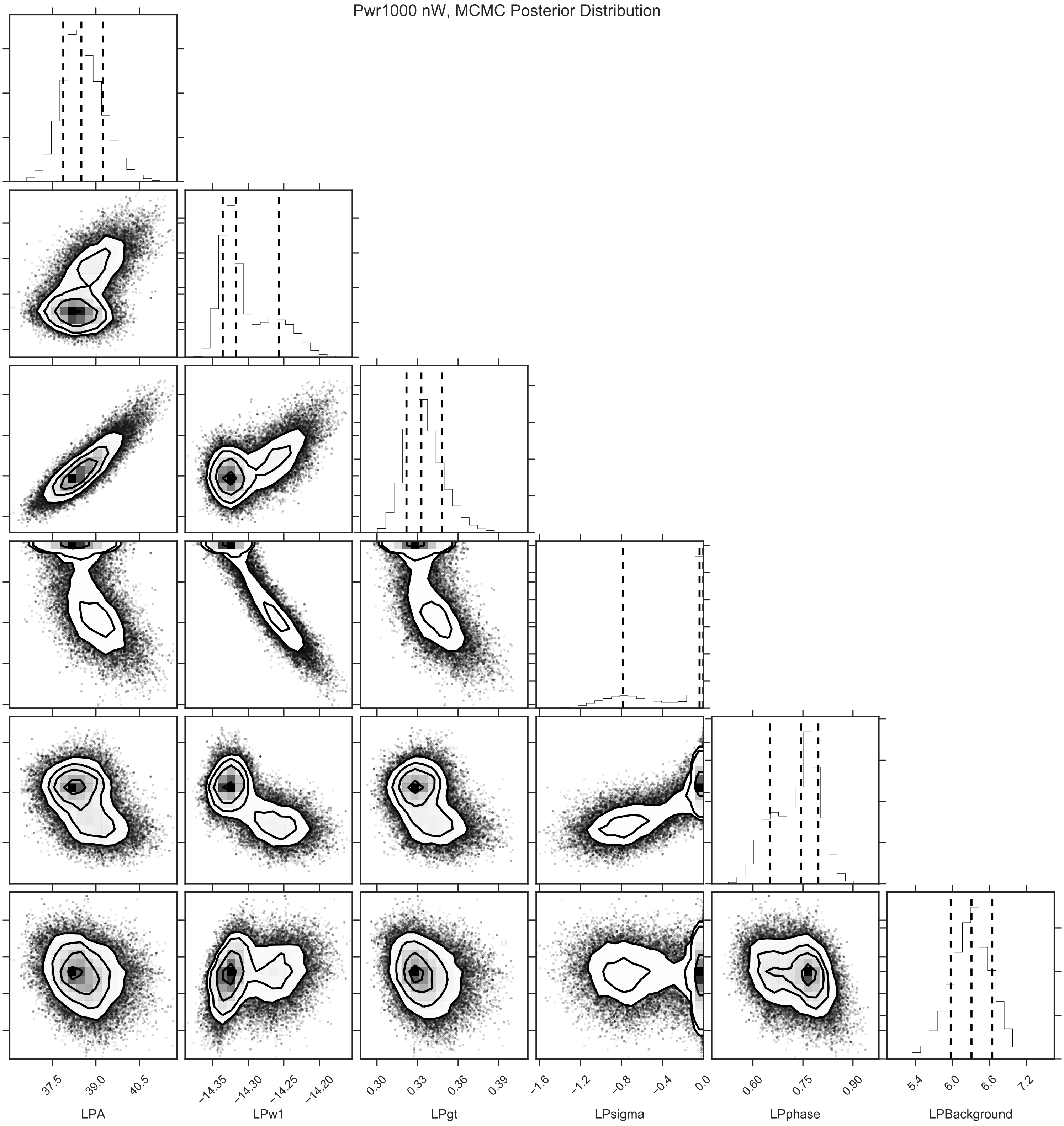
Pwr1000 nW, MCMC Posterior Distribution

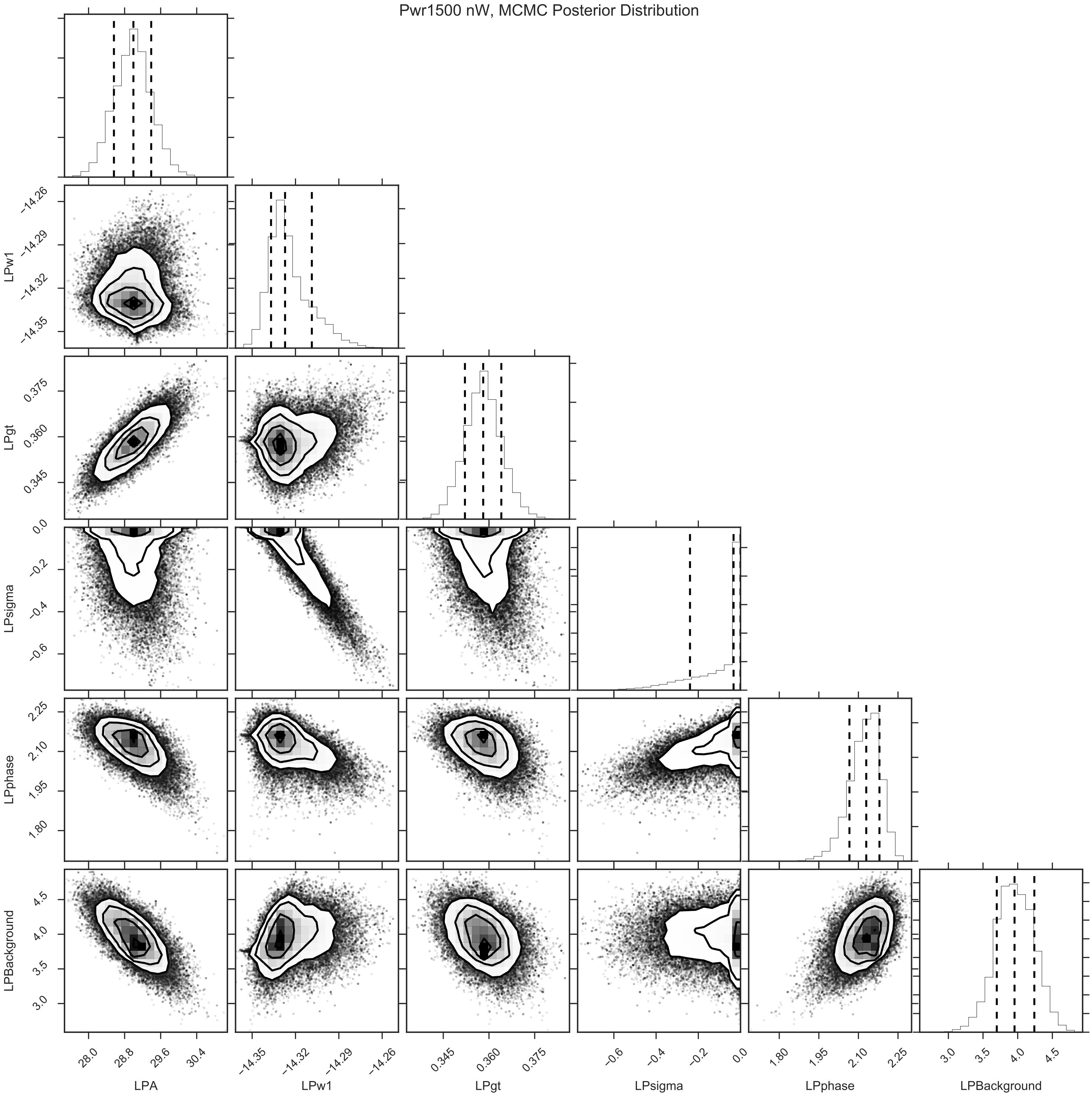
Pwr1500 nW, MCMC Posterior Distribution
LPw1
−14.26
−14.29
−14.32
−14.35
LPgt
0.375
0.360
0.345
LPsigma
0.0
−0.2
−0.4
−0.6
LPphase
2.25
2.10
1.95
1.80
LPBackground
4.5
4.0
3.5
3.0
28.0
28.8
29.6
30.4
LPA
−14.35
−14.32
−14.29
−14.26
LPw1
0.345
0.360
0.375
LPgt
−0.6
−0.4
−0.2
0.0
LPsigma
1.80
1.95
2.10
2.25
LPphase
3.0
3.5
4.0
4.5
LPBackground

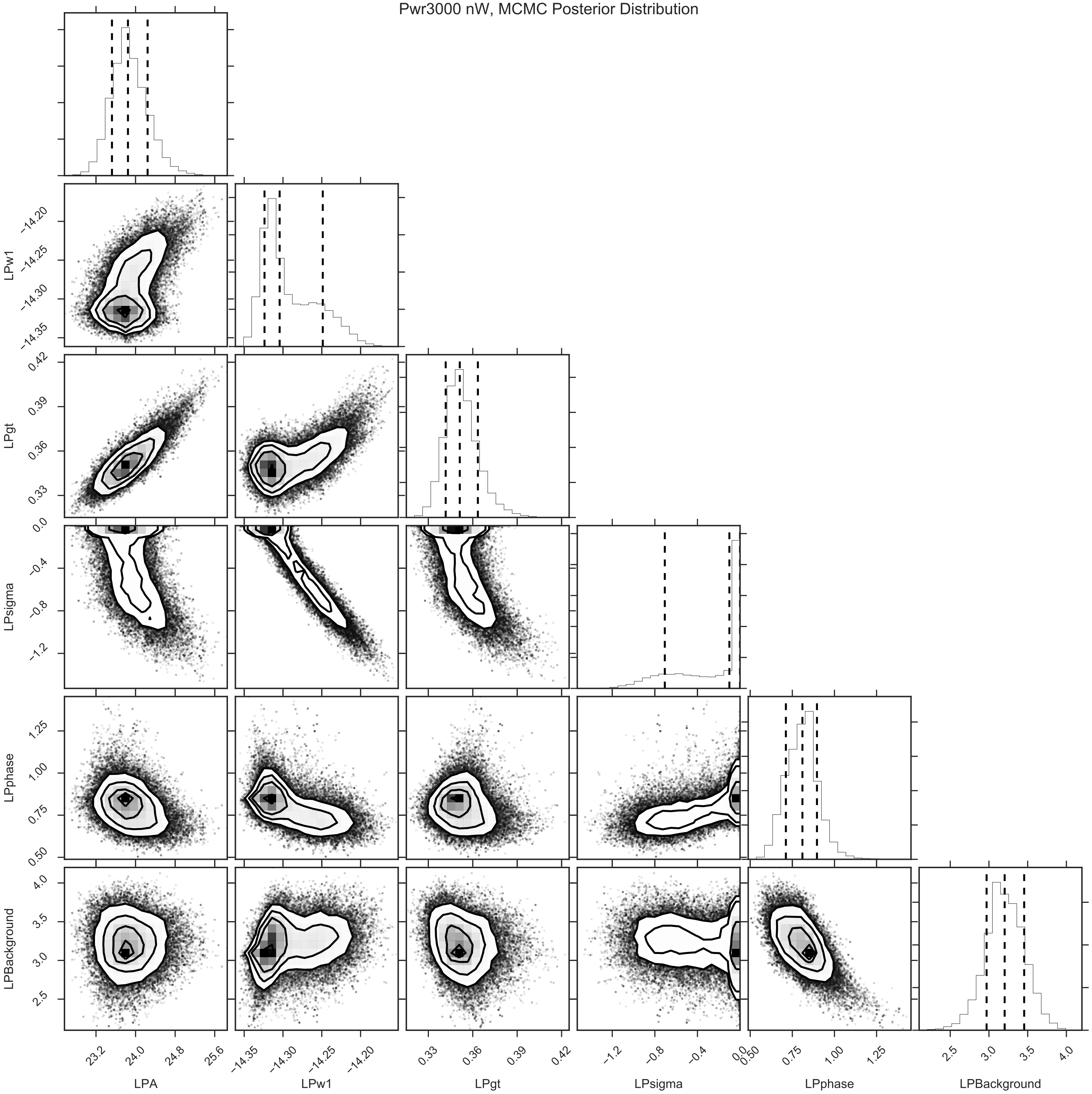

Pwr3000 nW, MCMC Posterior Distribution

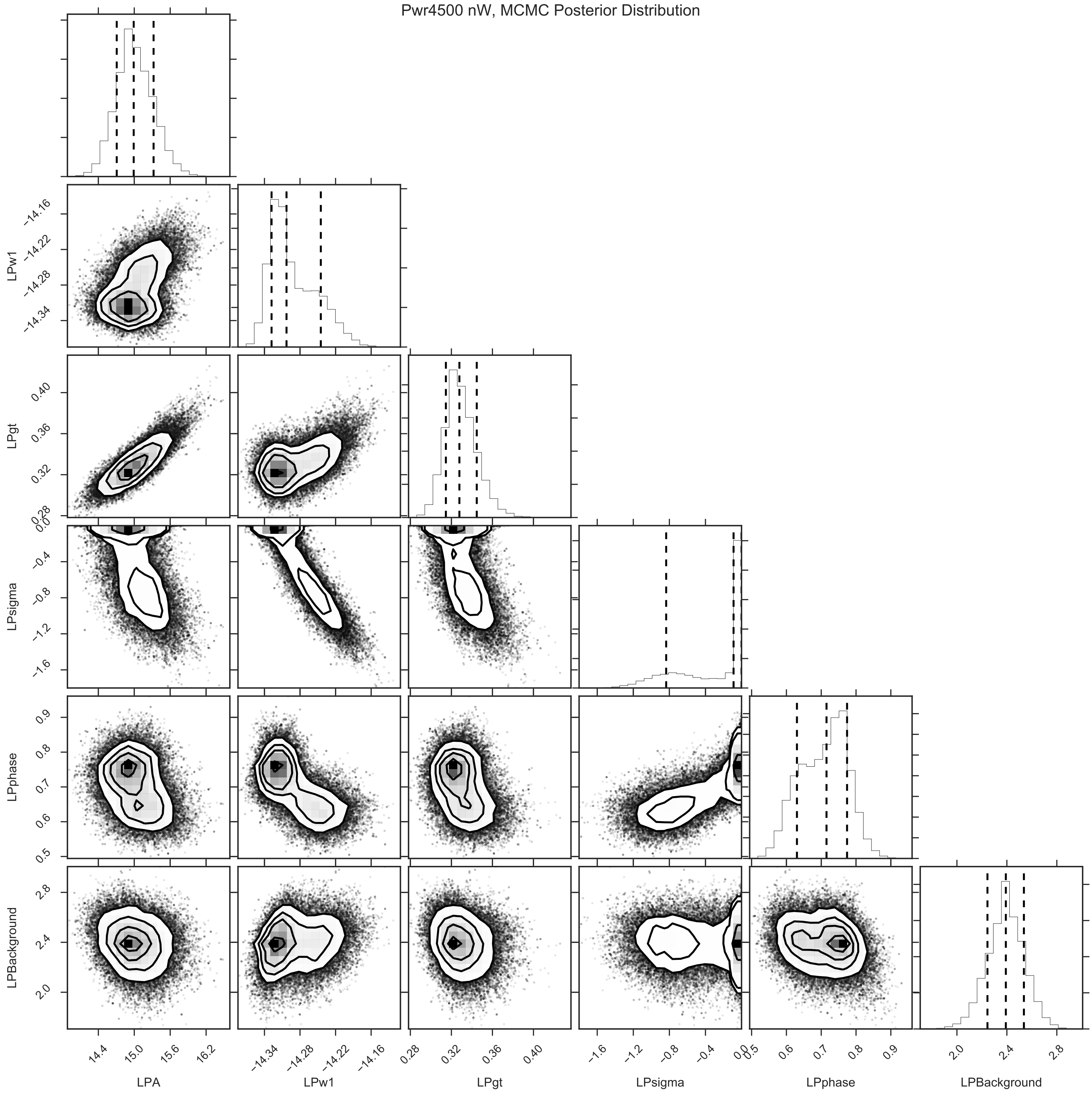
Pwr4500 nW, MCMC Posterior Distribution

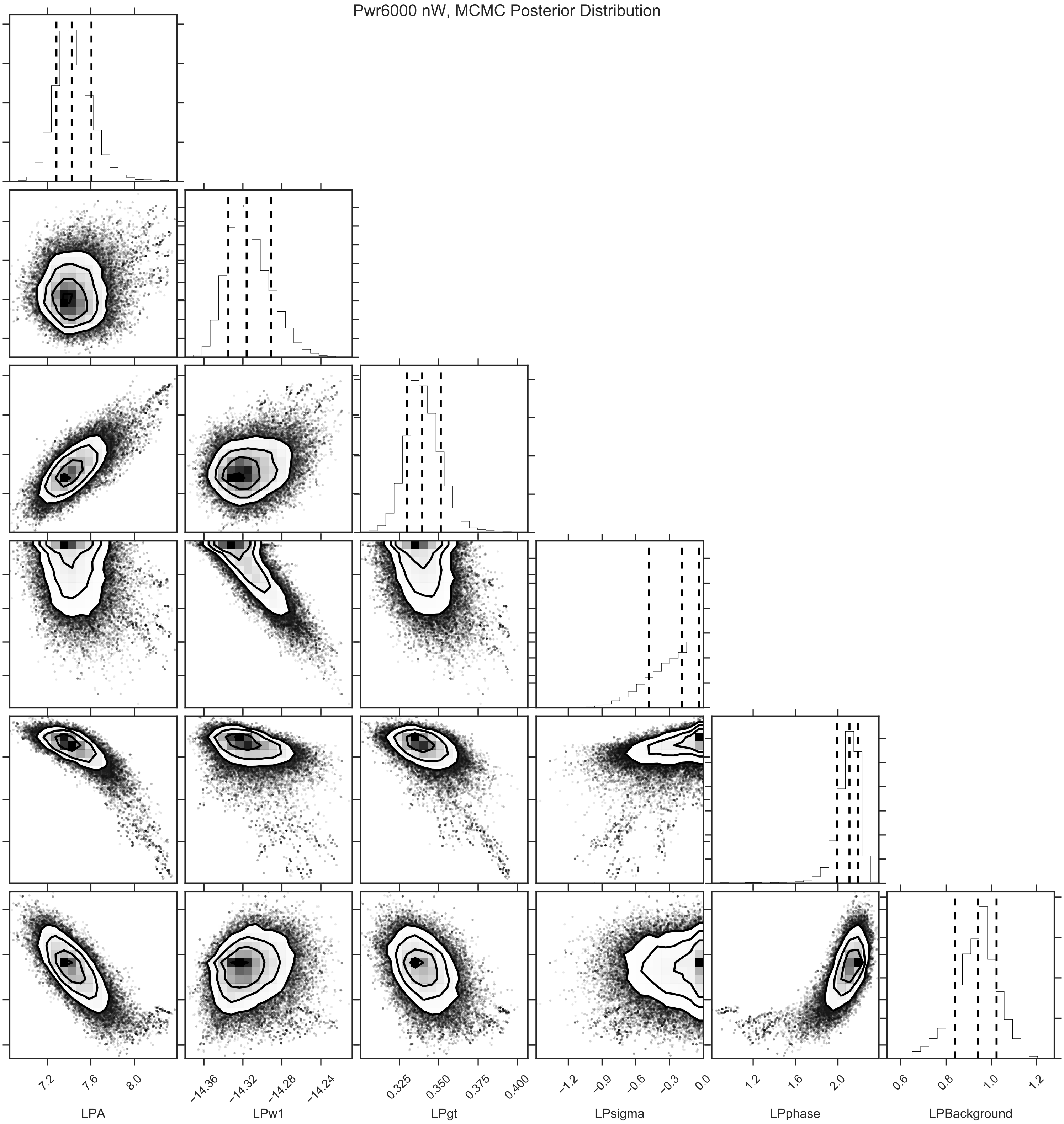
Pwr6000 nW, MCMC Posterior Distribution
LPw1
−14.24
−14.28
−14.32
−14.36
LPgt
0.400
0.375
0.350
0.325
LPsigma
0.0
−0.3
−0.6
−0.9
−1.2
LPphase
2.0
1.6
1.2
LPBackground
1.2
1.0
0.8
0.6
7.2
7.6
8.0
LPA
−14.36
−14.32
−14.28
−14.24
LPw1
0.325
0.350
0.375
0.400
LPgt
−1.2
−0.9
−0.6
−0.3
0.0
LPsigma
1.2
1.6
2.0
LPphase
0.6
0.8
1.0
1.2
LPBackground

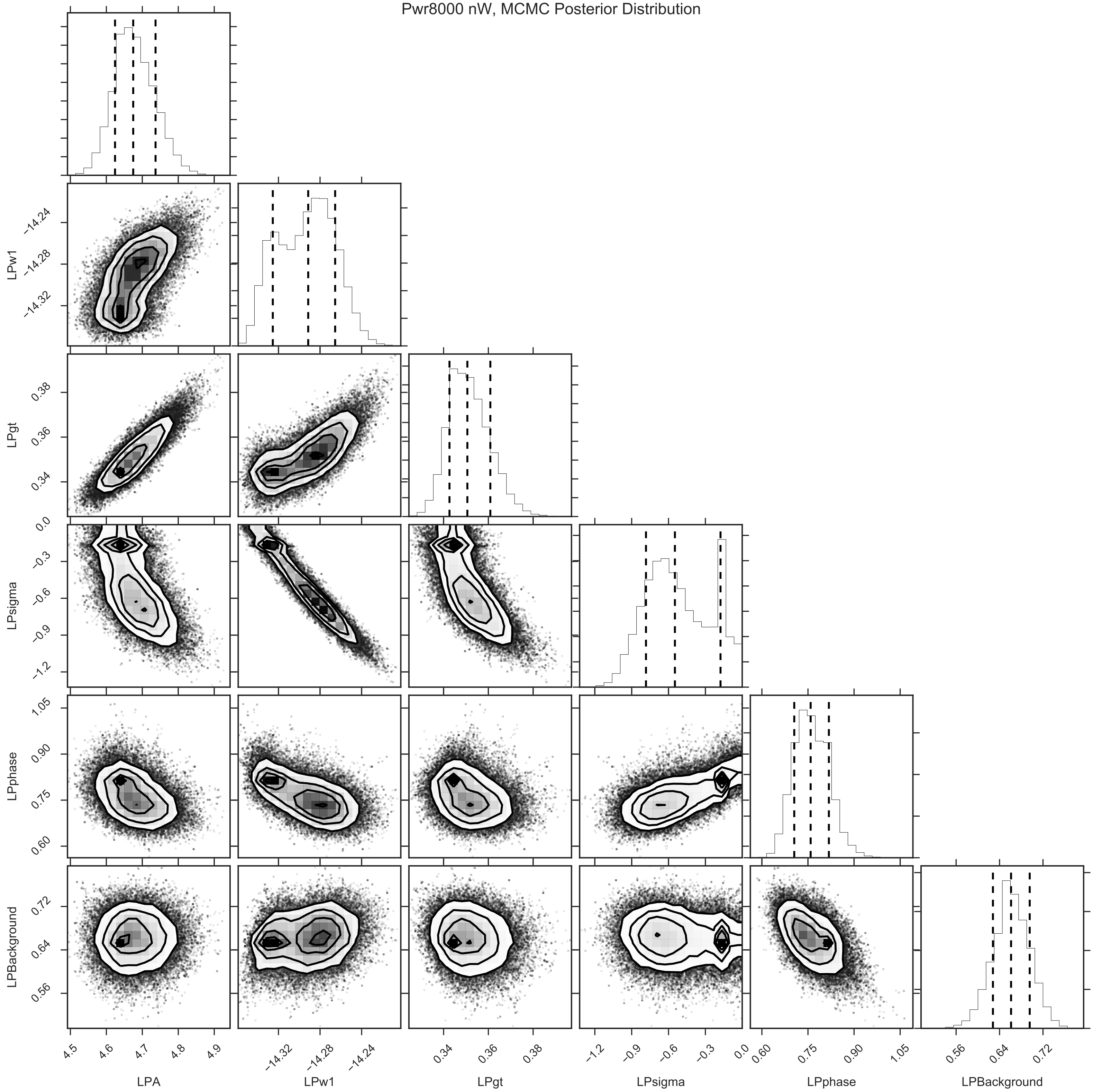
Pwr8000 nW, MCMC Posterior Distribution
LPw1
−14.24
−14.28
−14.32
LPgt
0.38
0.36
0.34
LPsigma
0.0
−0.3
−0.6
−0.9
−1.2
LPphase
1.05
0.90
0.75
0.60
LPBackground
0.72
0.64
0.56
4.5
4.6
4.7
4.8
4.9
LPA
−14.32
−14.28
−14.24
LPw1
0.34
0.36
0.38
LPgt
−1.2
−0.9
−0.6
−0.3
0.0
LPsigma
0.60
0.75
0.90
1.05
LPphase
0.56
0.64
0.72
LPBackground

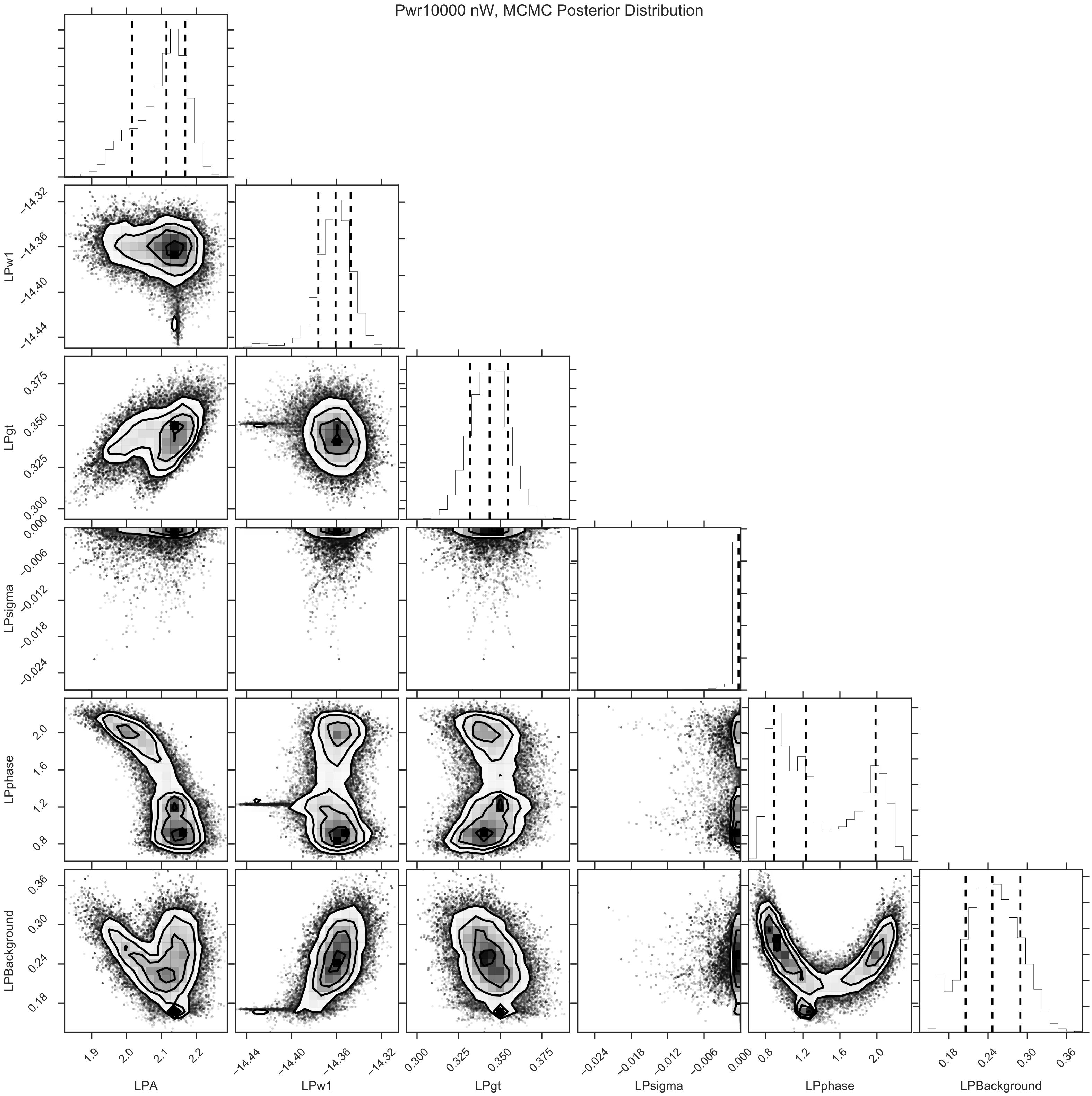
Pwr10000 nW, MCMC Posterior Distribution

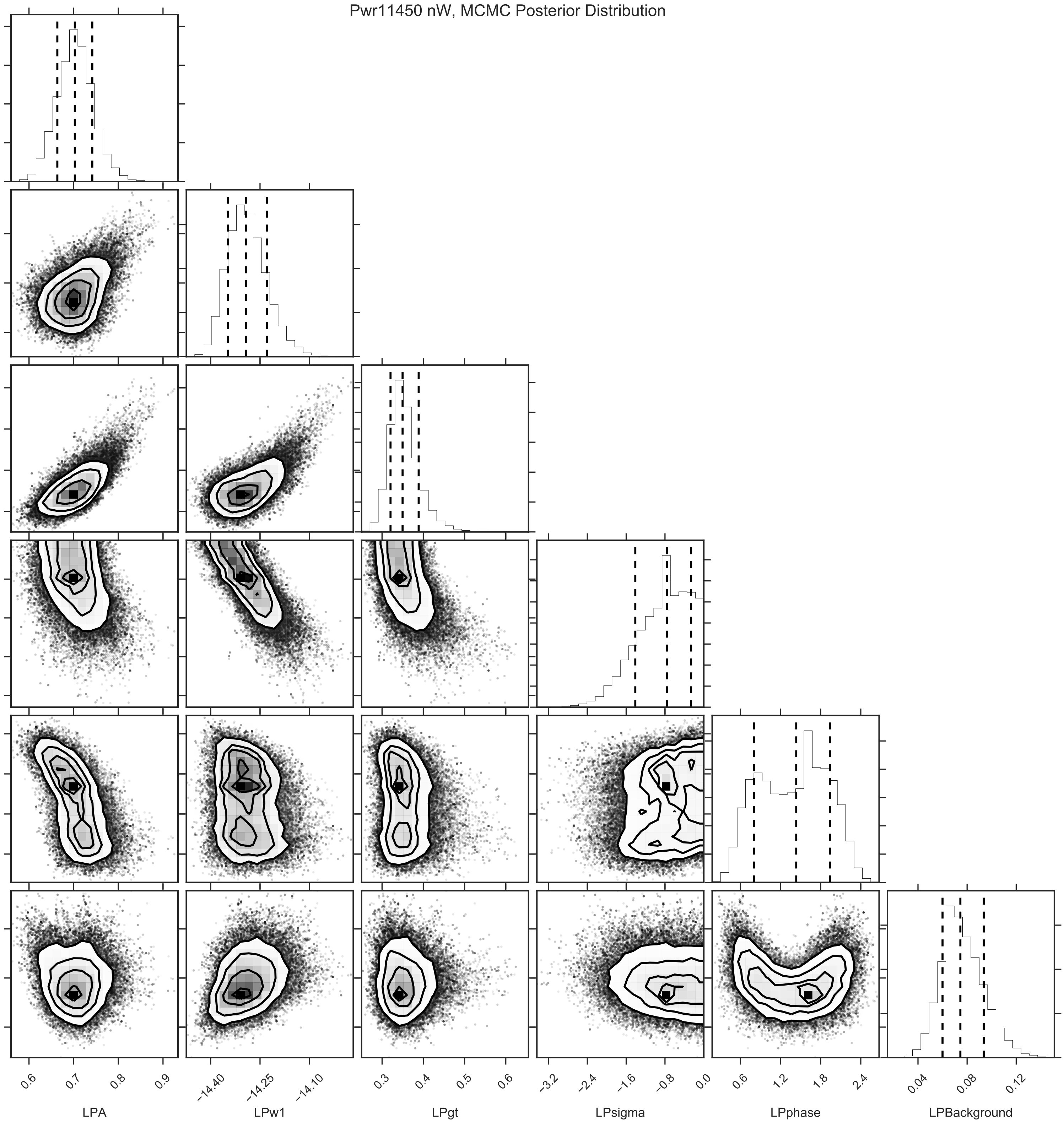
Pwr11450 nW, MCMC Posterior Distribution

Pwr10 nW, MCMC Posterior Distribution

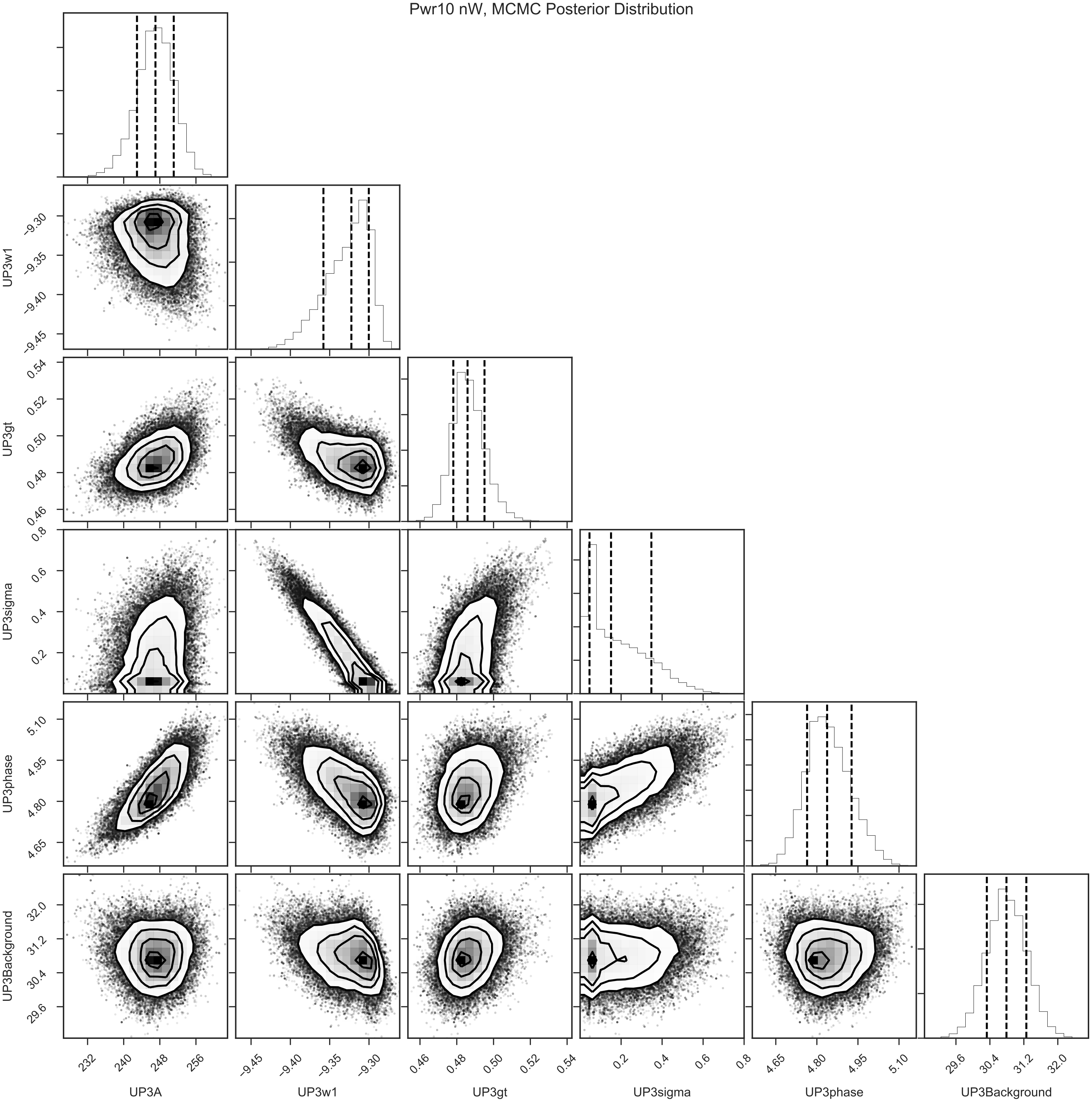

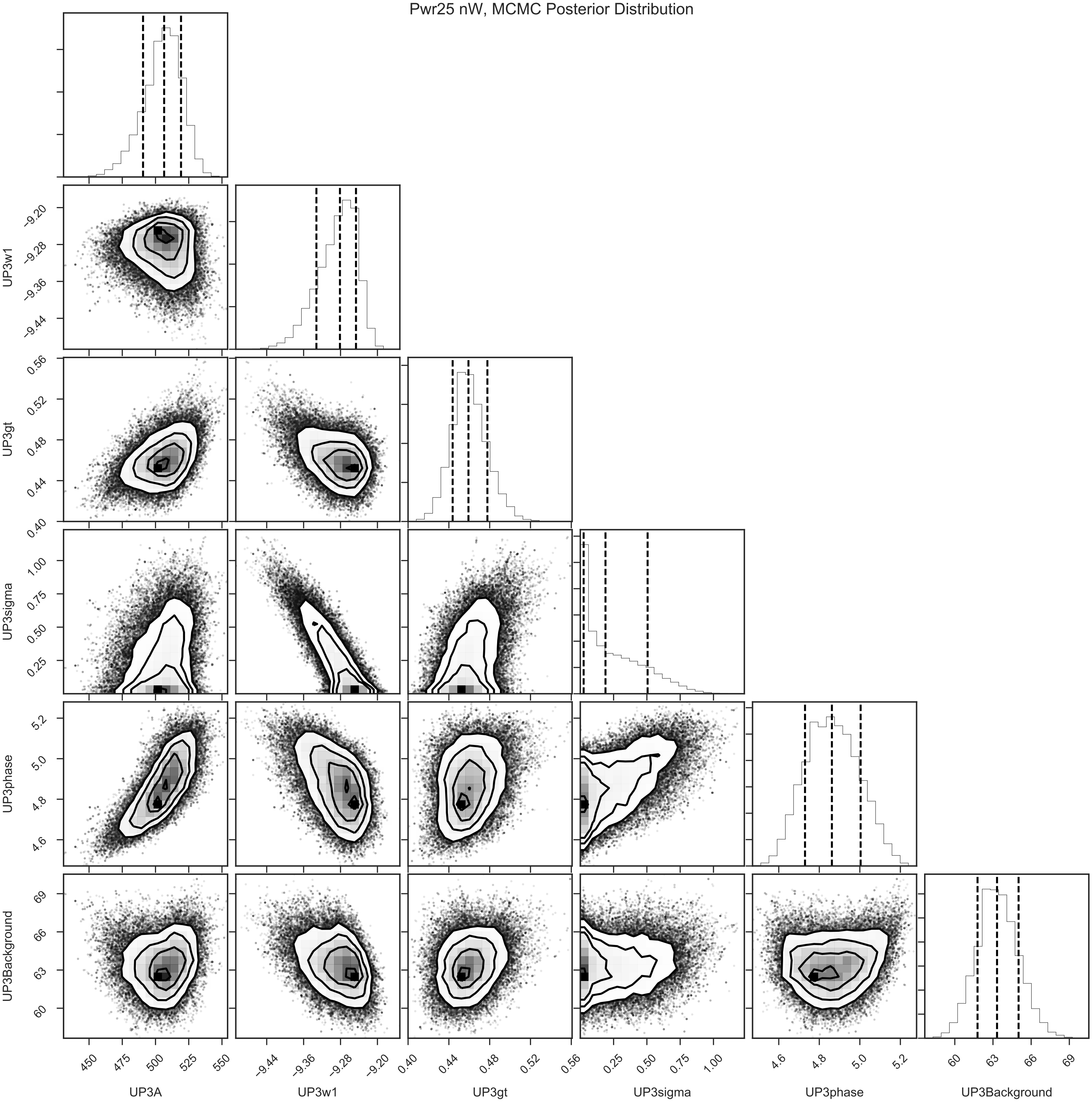
Pwr25 nW, MCMC Posterior Distribution
UP3w1
−9.20
−9.28
−9.36
−9.44
UP3gt
0.56
0.52
0.48
0.44
0.40
UP3sigma
1.00
0.75
0.50
0.25
UP3phase
5.2
5.0
4.8
4.6
UP3Background
69
66
63
60
450
475
500
525
550
UP3A
−9.44
−9.36
−9.28
−9.20
UP3w1
0.40
0.44
0.48
0.52
0.56
UP3gt
0.25
0.50
0.75
1.00
UP3sigma
4.6
4.8
5.0
5.2
UP3phase
60
63
66
69
UP3Background

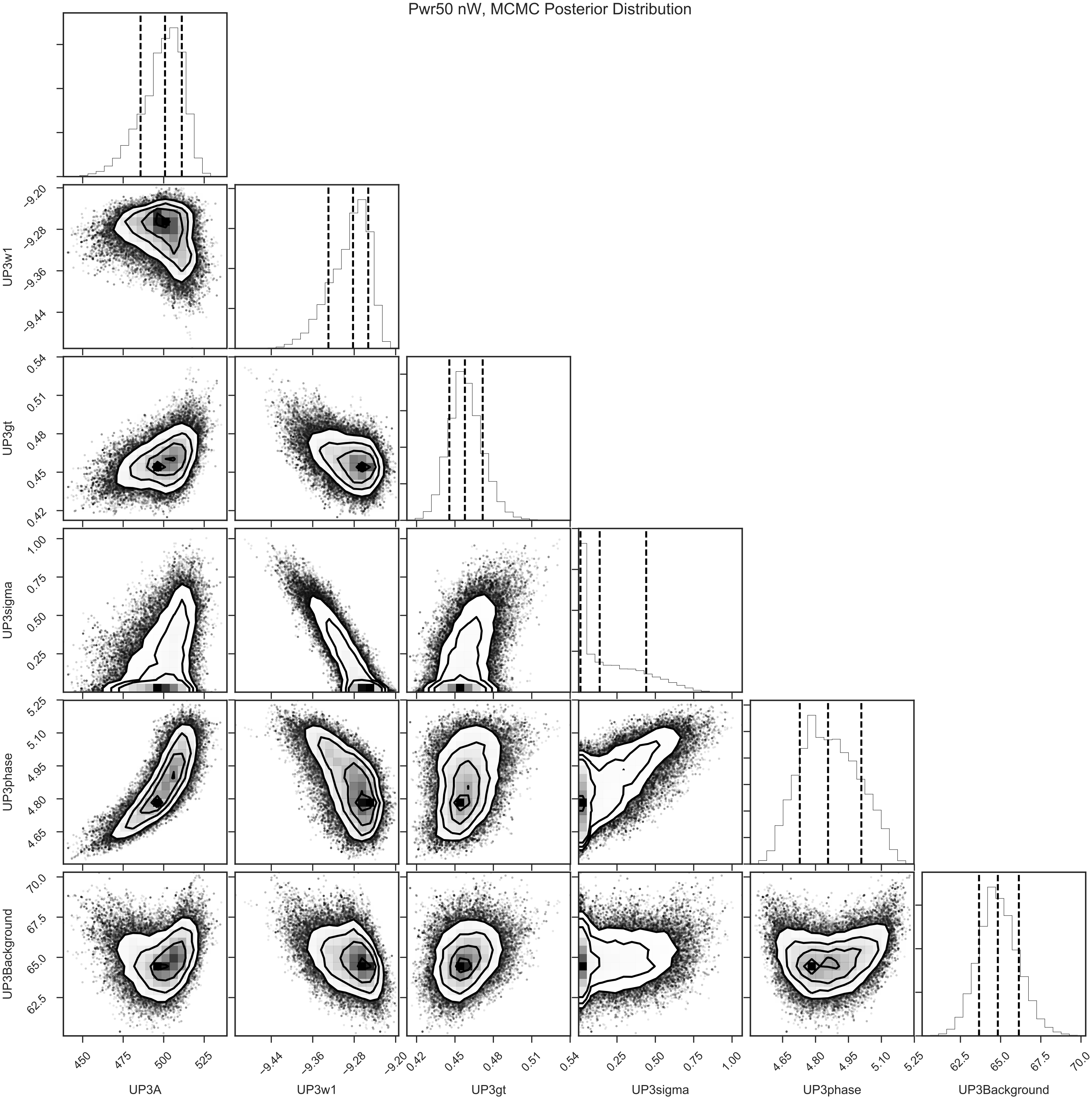

Pwr50 nW, MCMC Posterior Distribution

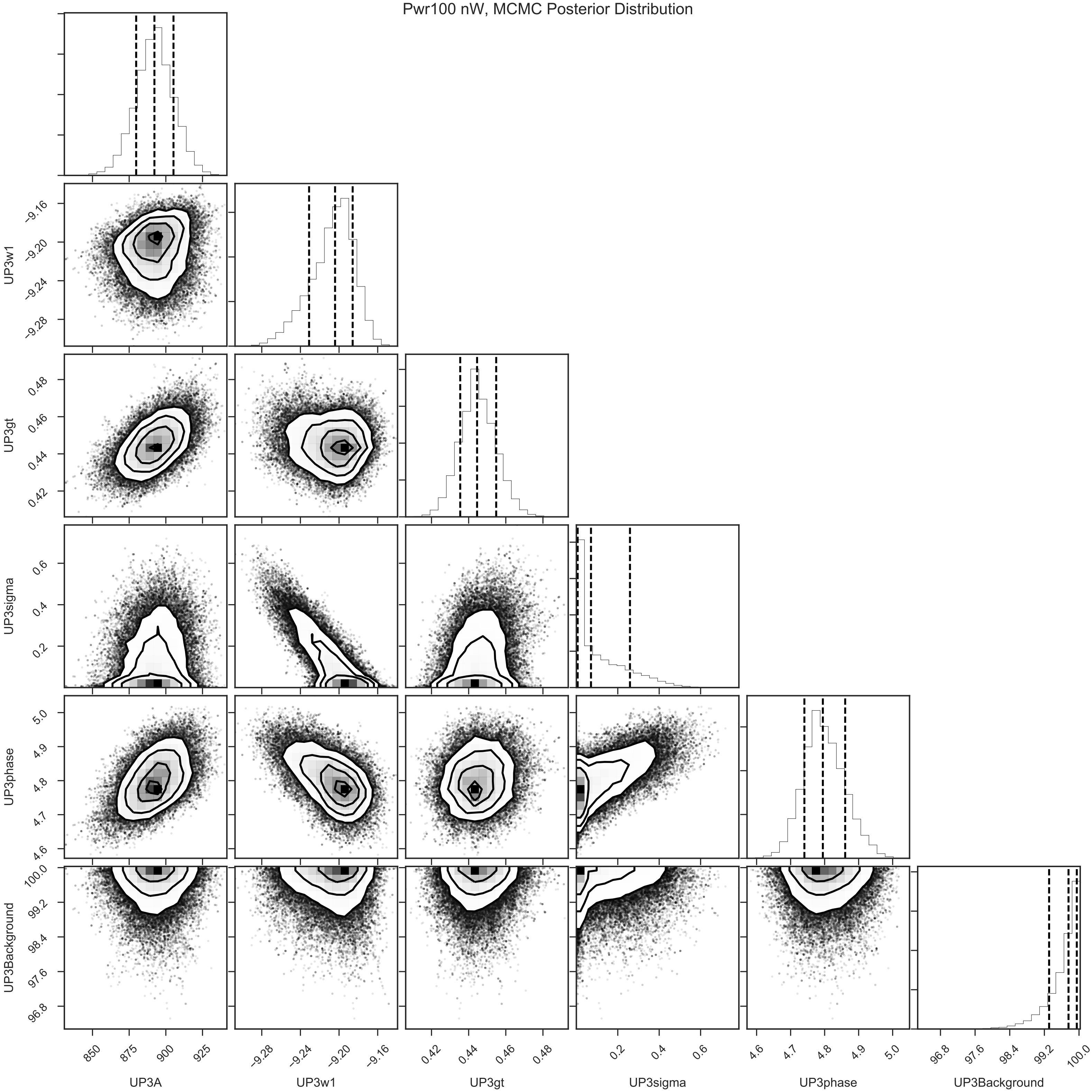
Pwr100 nW, MCMC Posterior Distribution

Pwr200 nW, MCMC Posterior Distribution

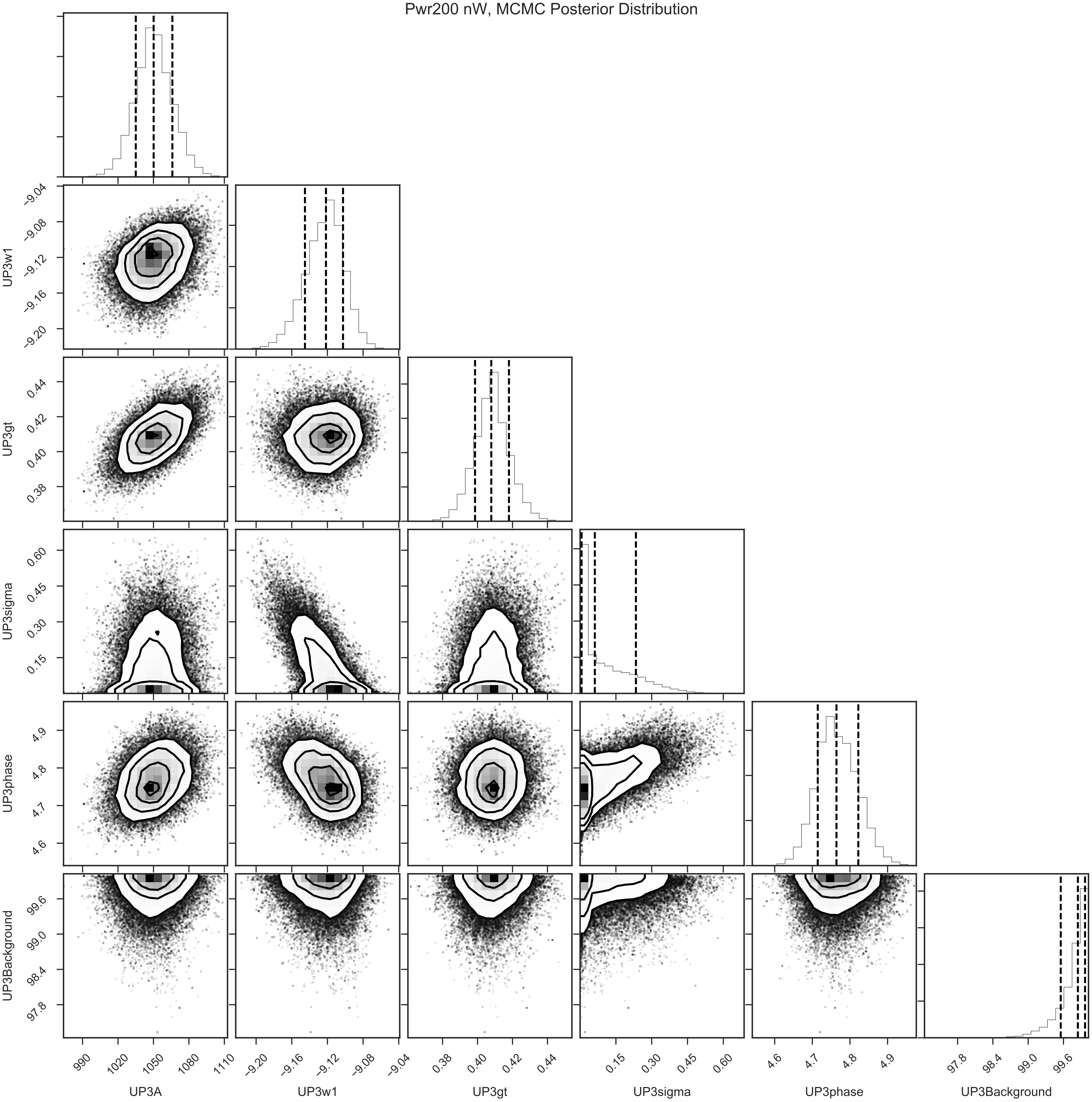

Pwr300 nW, MCMC Posterior Distribution

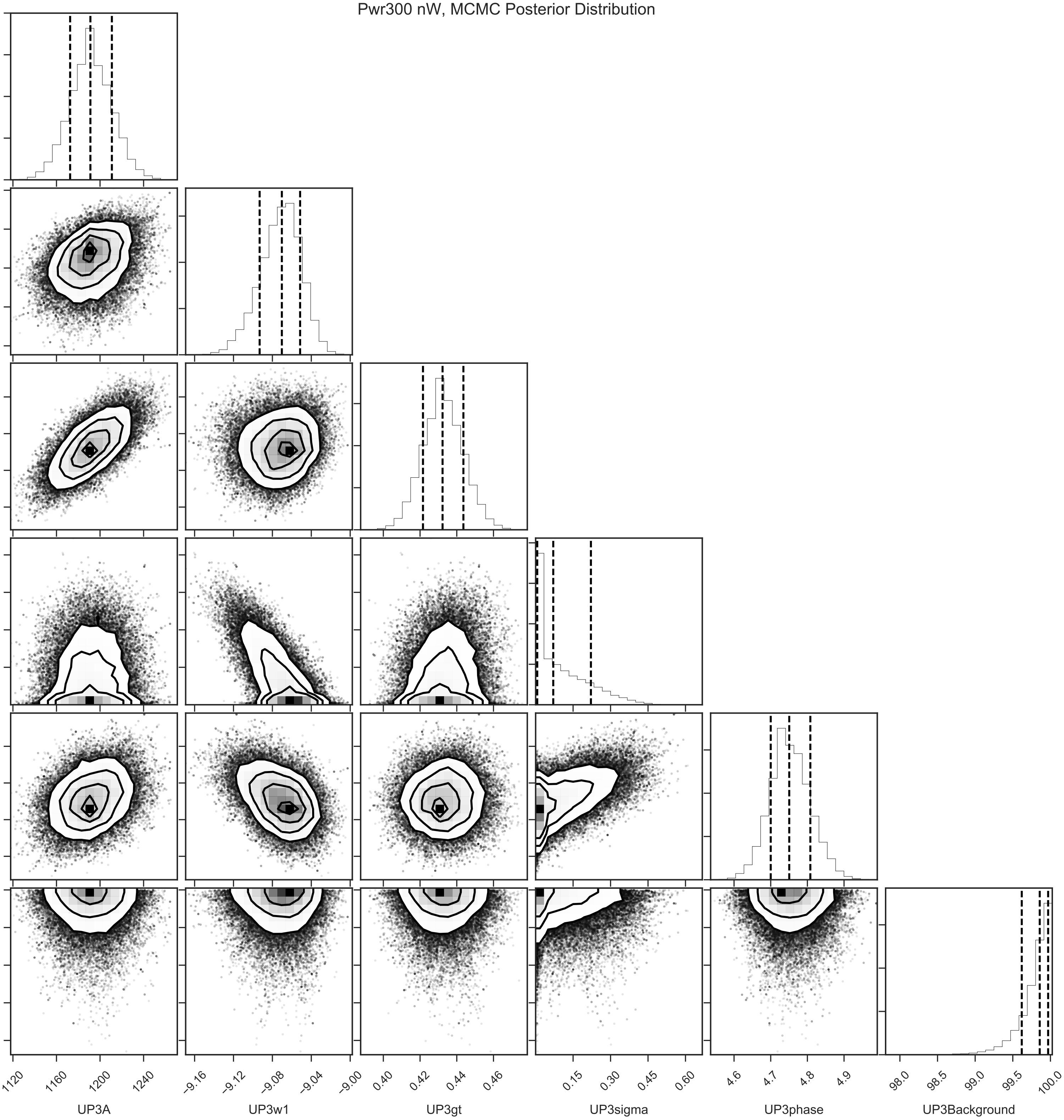

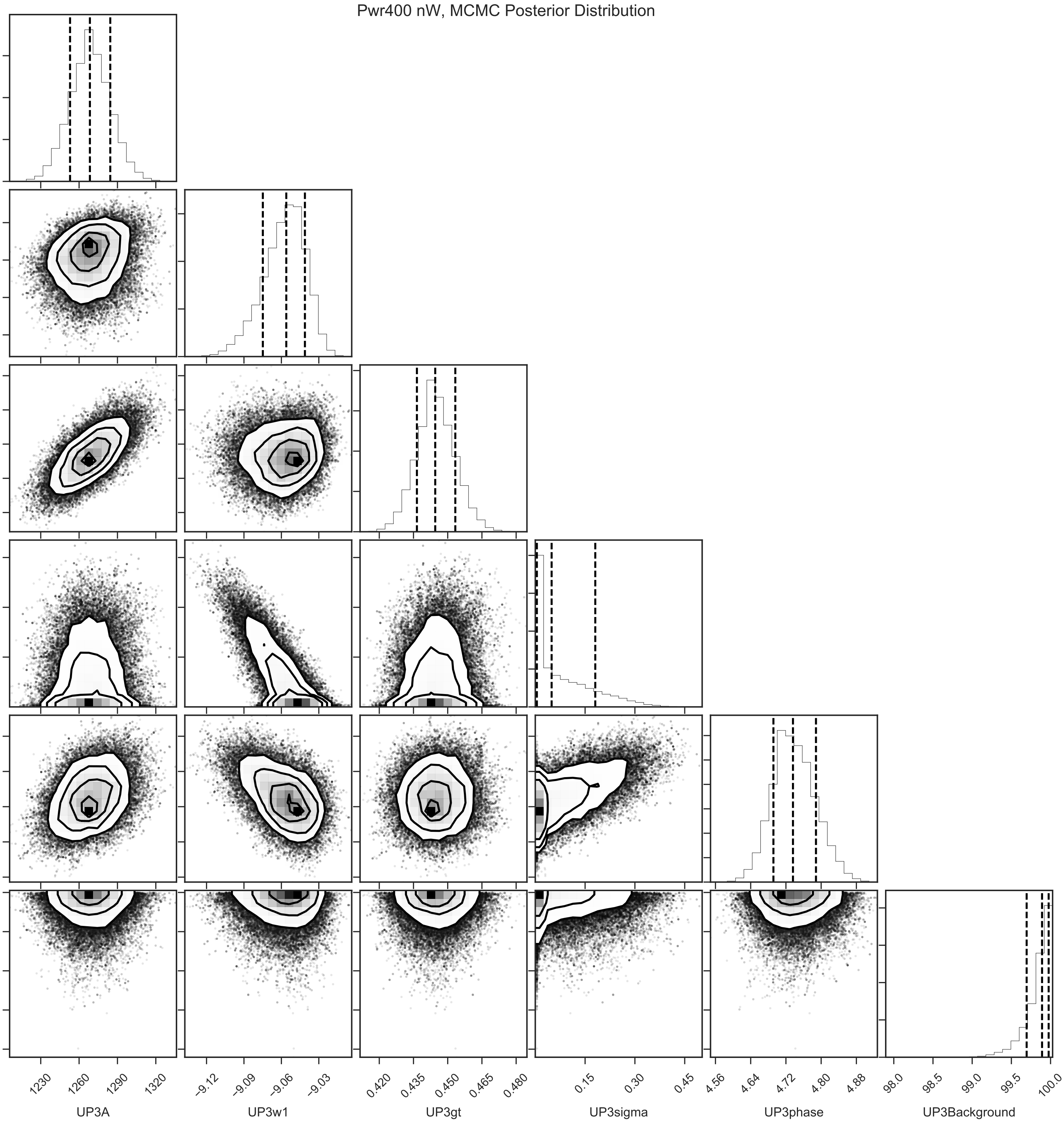
Pwr400 nW, MCMC Posterior Distribution
UP3w1
−9.03
−9.06
−9.09
−9.12
UP3gt
0.480
0.465
0.450
0.435
0.420
UP3sigma
0.45
0.30
0.15
UP3phase
4.88
4.80
4.72
4.64
4.56
UP3Background
100.0
99.5
99.0
98.5
98.0
1230
1260
1290
1320
UP3A
−9.12
−9.09
−9.06
−9.03
UP3w1
0.420
0.435
0.450
0.465
0.480
UP3gt
0.15
0.30
0.45
UP3sigma
4.56
4.64
4.72
4.80
4.88
UP3phase
98.0
98.5
99.0
99.5
100.0
UP3Background

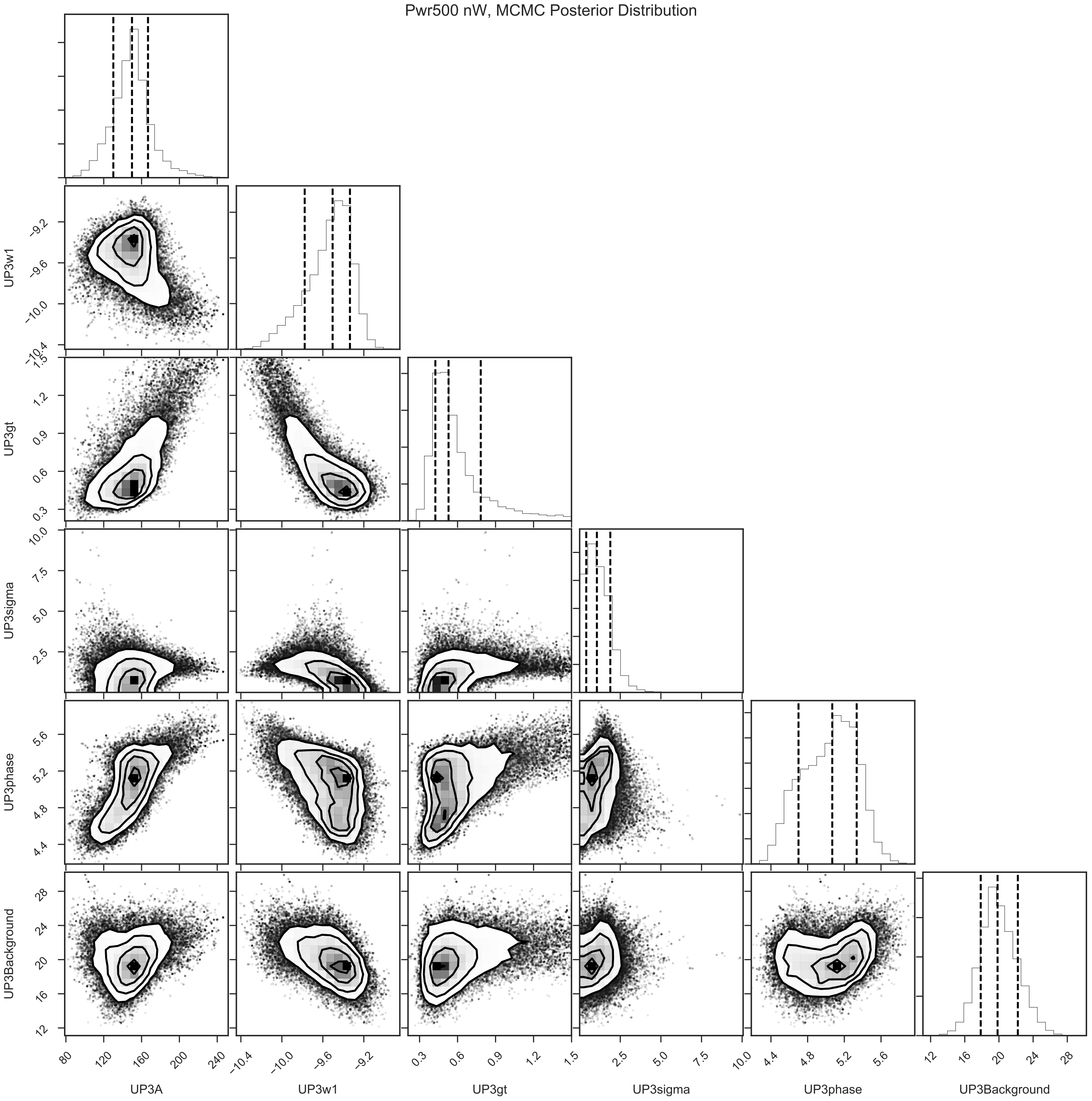

Pwr500 nW, MCMC Posterior Distribution

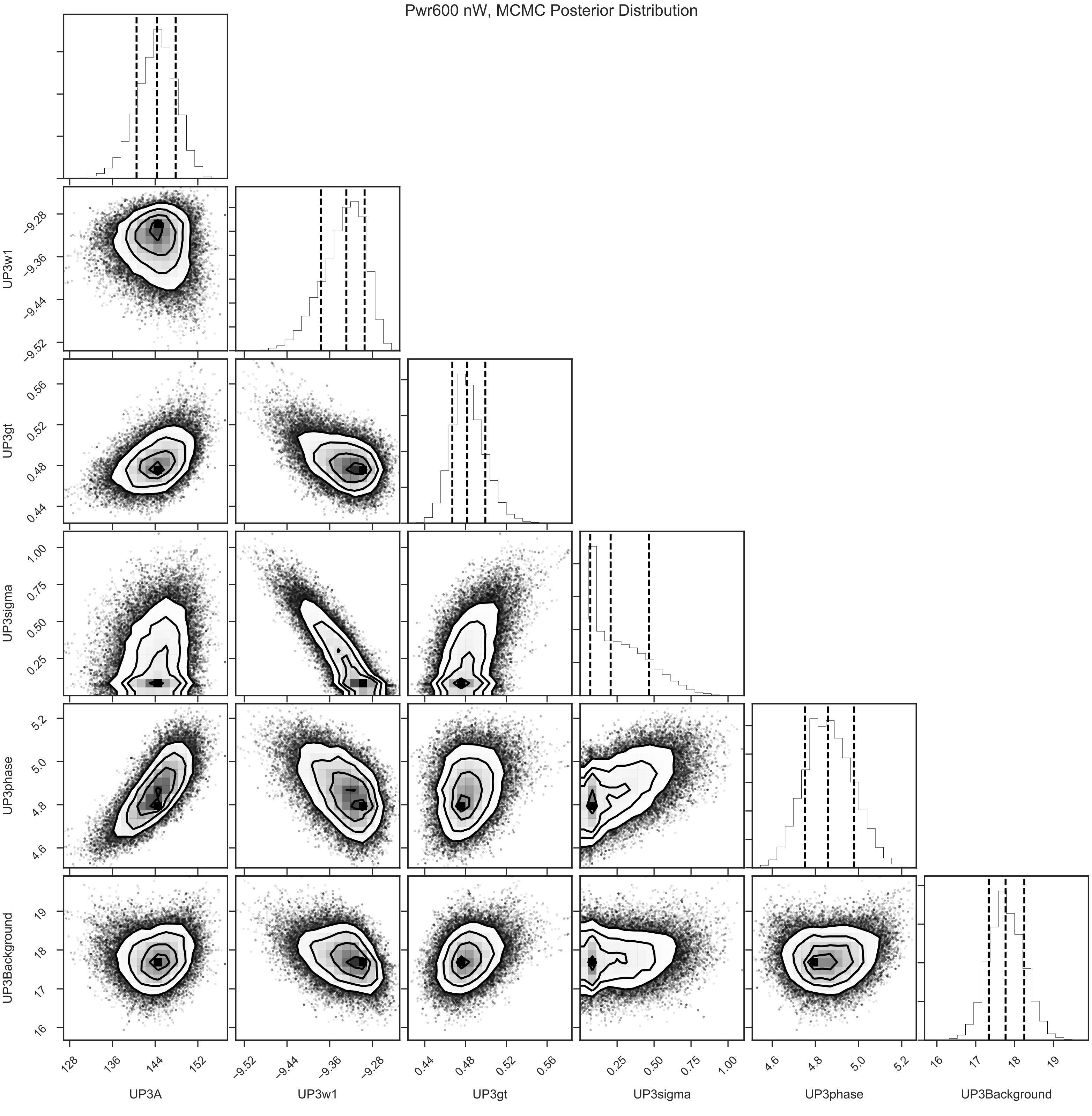
Pwr600 nW, MCMC Posterior Distribution
UP3w1
−9.28
−9.36
−9.44
−9.52
UP3gt
0.56
0.52
0.48
0.44
UP3sigma
1.00
0.75
0.50
0.25
UP3phase
5.2
5.0
4.8
4.6
UP3Background
19
18
17
16
128
136
144
152
UP3A
−9.52
−9.44
−9.36
−9.28
UP3w1
0.44
0.48
0.52
0.56
UP3gt
0.25
0.50
0.75
1.00
UP3sigma
4.6
4.8
5.0
5.2
UP3phase
16
17
18
19
UP3Background

Pwr700 nW, MCMC Posterior Distribution

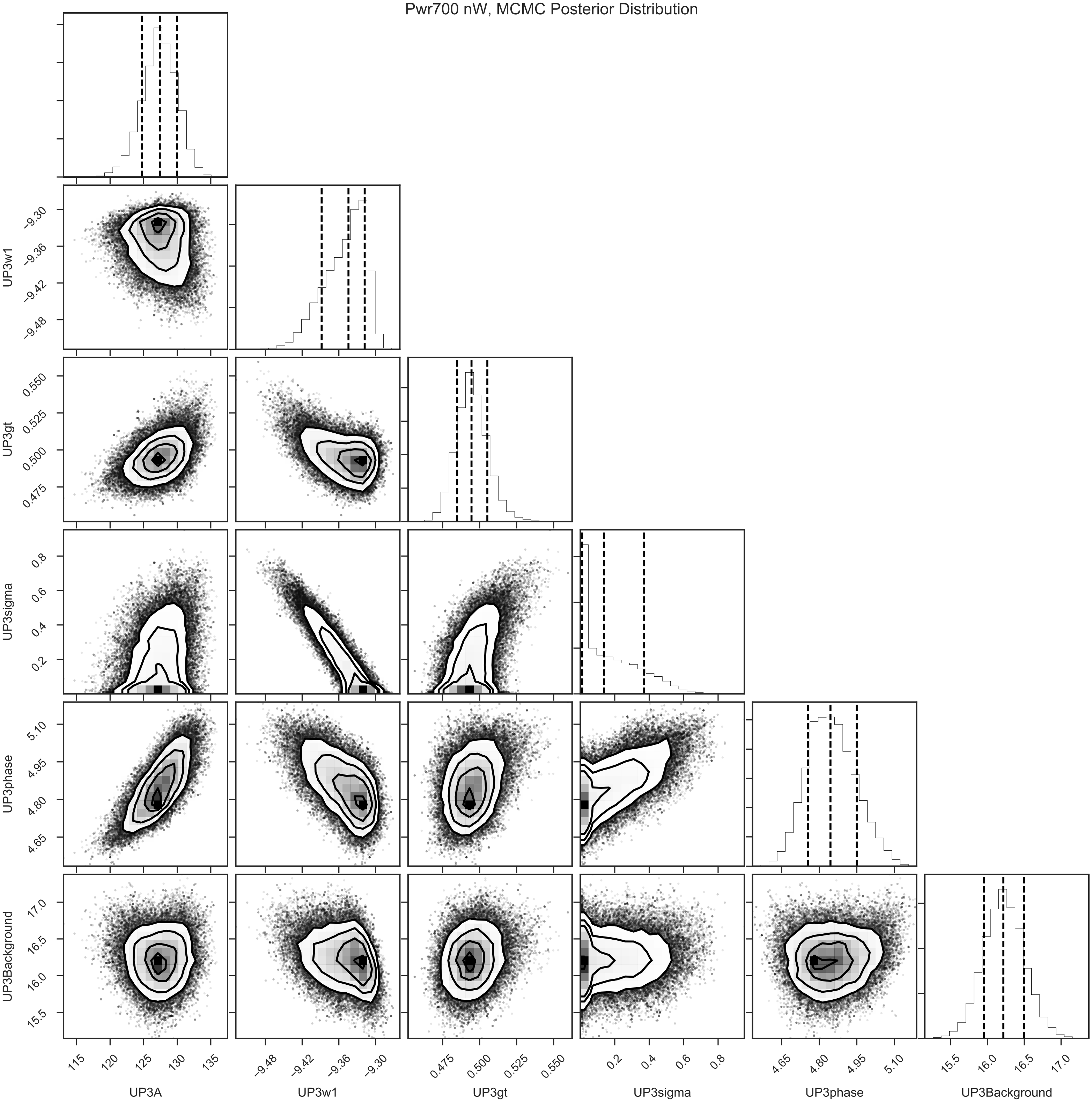

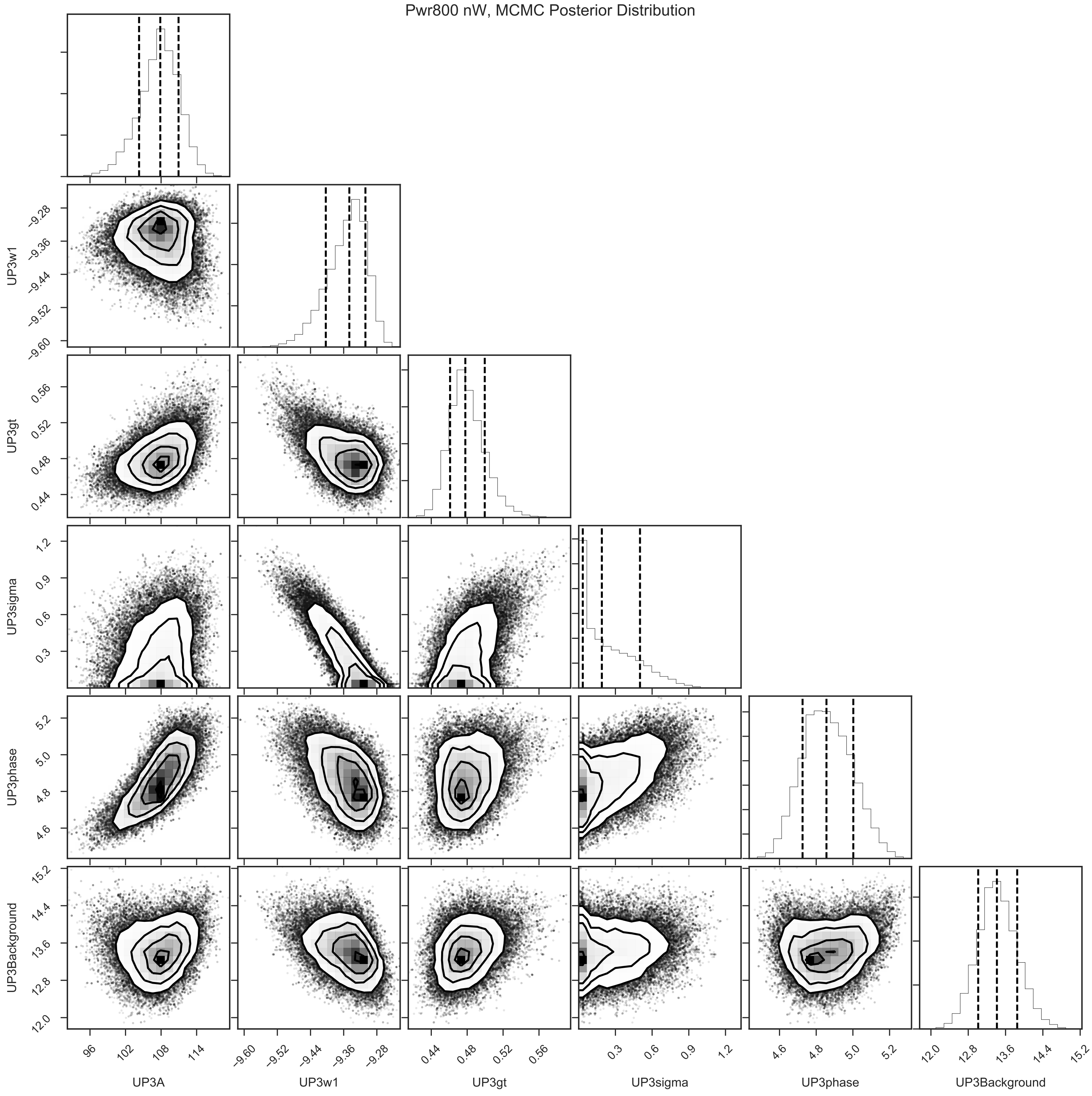
Pwr800 nW, MCMC Posterior Distribution
UP3w1
-9.28
-9.36
-9.44
-9.52
-9.60
UP3gt
0.56
0.52
0.48
0.44
UP3sigma
1.2
0.9
0.6
0.3
UP3phase
5.2
5.0
4.8
4.6
UP3Background
15.2
14.4
13.6
12.8
12.0
96
102
108
114
UP3A
-9.60
-9.52
-9.44
-9.36
-9.28
UP3w1
0.44
0.48
0.52
0.56
UP3gt
0.3
0.6
0.9
1.2
UP3sigma
4.6
4.8
5.0
5.2
UP3phase
12.0
12.8
13.6
14.4
15.2
UP3Background

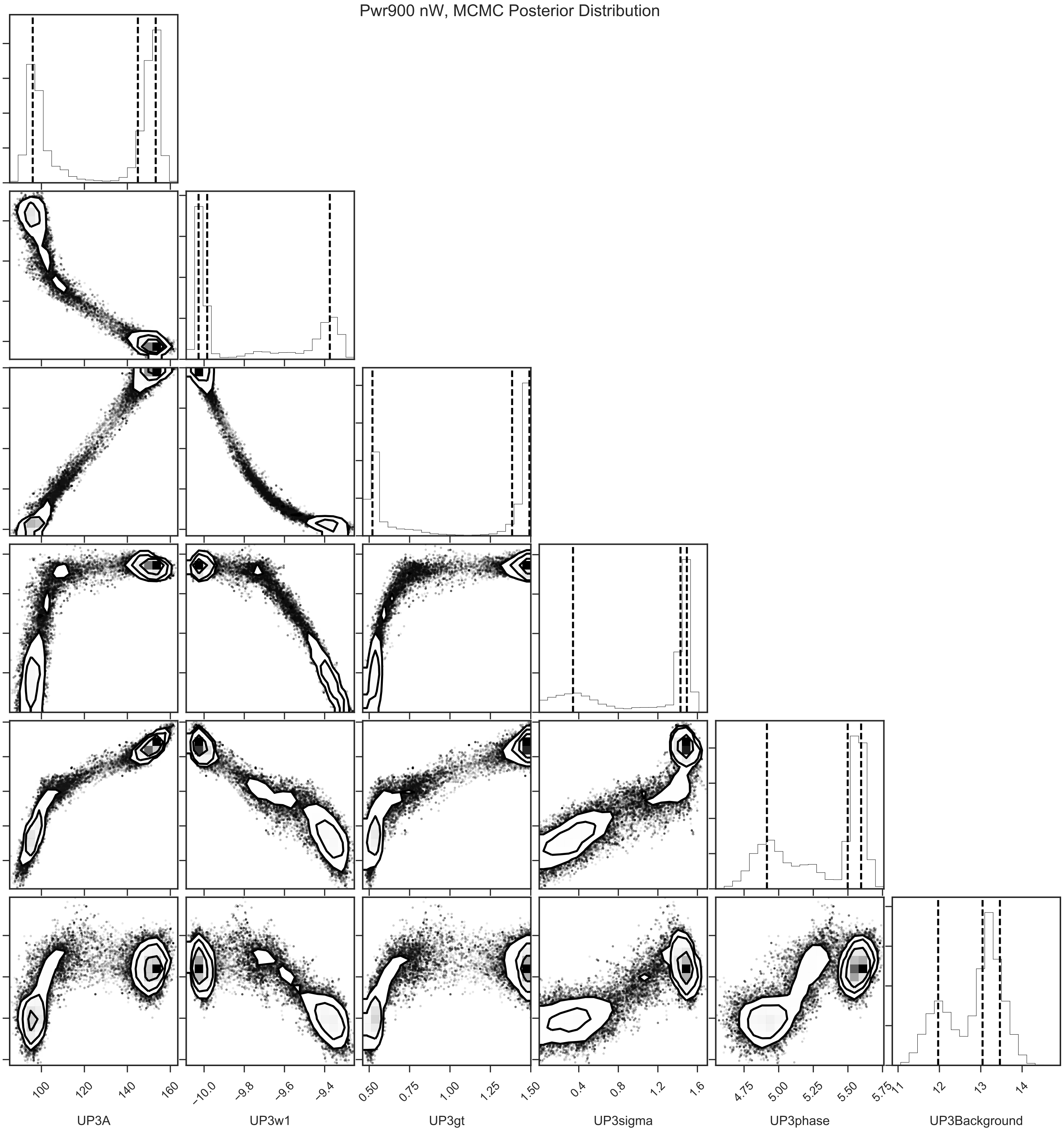
Pwr900 nW, MCMC Posterior Distribution
UP3w1
UP3gt
UP3sigma
UP3phase
UP3Background
UP3A
UP3w1
UP3gt
UP3sigma
UP3phase
UP3Background
−9.4
−9.6
−9.8
−10.0
1.50
1.25
1.00
0.75
0.50
1.6
1.2
0.8
0.4
5.75
5.50
5.25
5.00
4.75
14
13
12
11
100
120
140
160
−10.0
−9.8
−9.6
−9.4
0.50
0.75
1.00
1.25
1.50
0.4
0.8
1.2
1.6
4.75
5.00
5.25
5.50
5.75
11
12
13
14

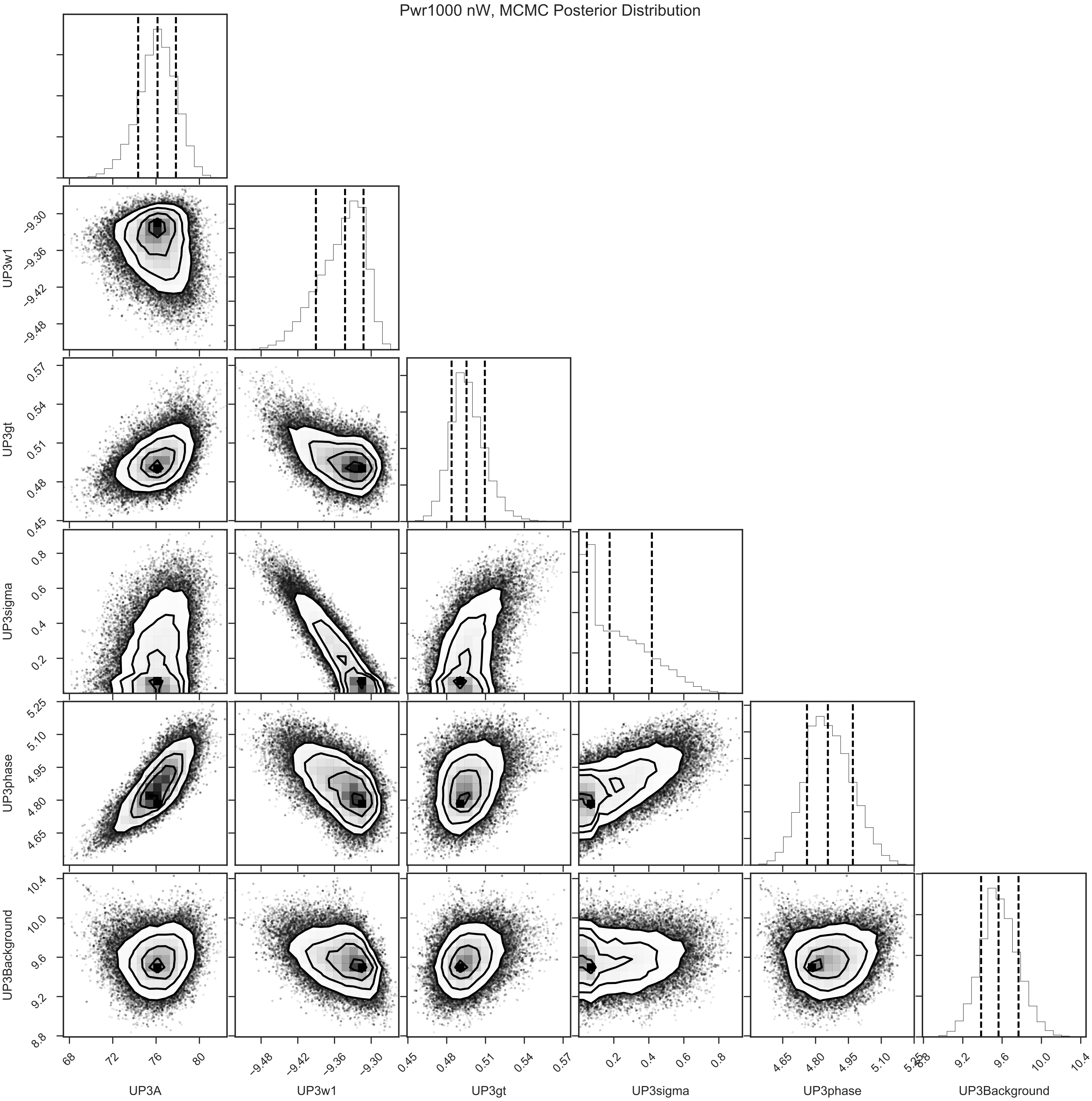
Pwr1000 nW, MCMC Posterior Distribution
UP3w1
−9.30
−9.36
−9.42
−9.48
UP3gt
0.57
0.54
0.51
0.48
0.45
UP3sigma
0.8
0.6
0.4
0.2
UP3phase
5.25
5.10
4.95
4.80
4.65
UP3Background
10.4
10.0
9.6
9.2
8.8
68
72
76
80
UP3A
−9.48
−9.42
−9.36
−9.30
UP3w1
0.45
0.48
0.51
0.54
0.57
UP3gt
0.2
0.4
0.6
0.8
UP3sigma
4.65
4.80
4.95
5.10
5.25
UP3phase
8.8
9.2
9.6
10.0
10.4
UP3Background

Pwr1500 nW, MCMC Posterior Distribution

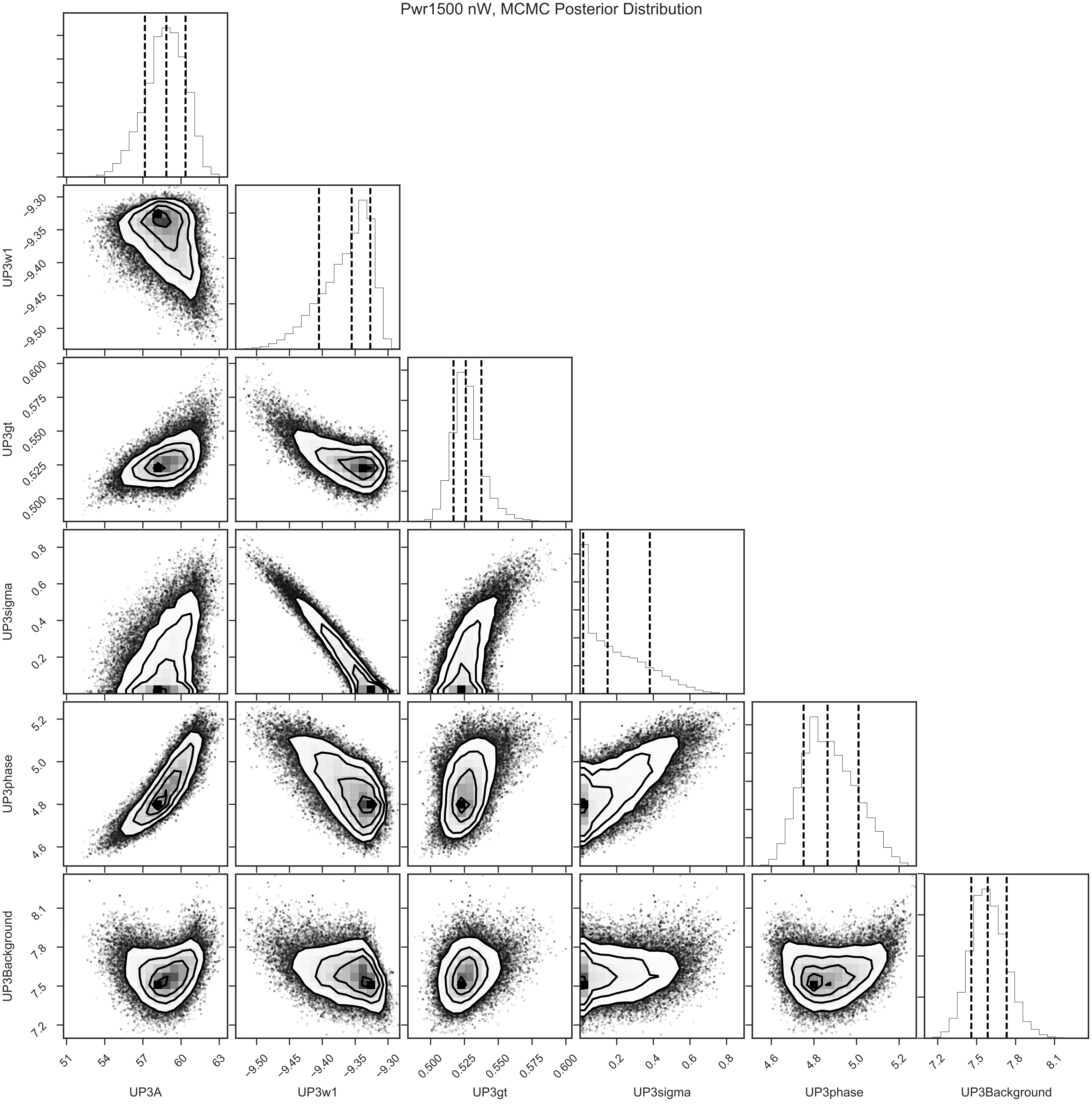

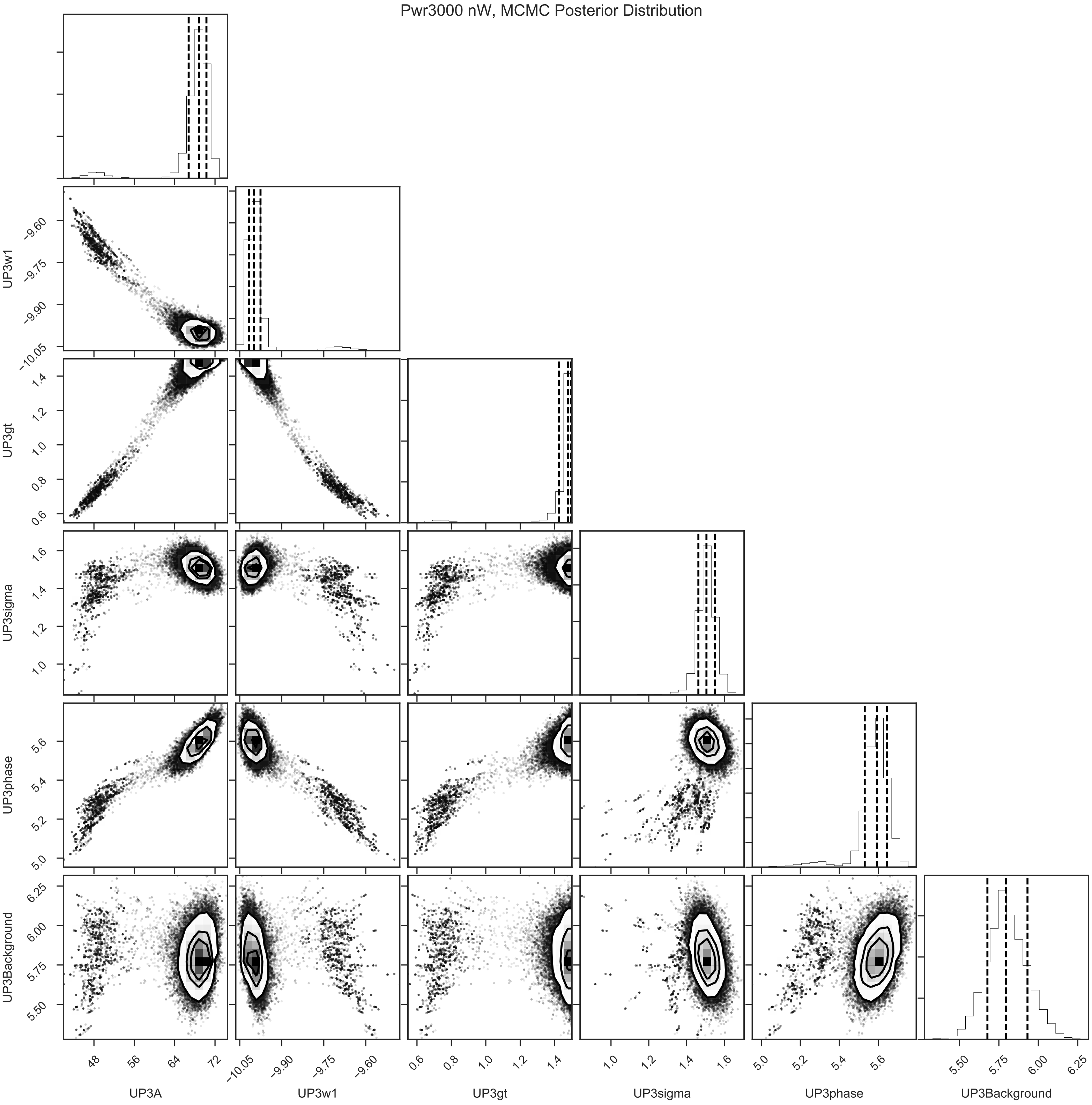
Pwr3000 nW, MCMC Posterior Distribution
UP3w1
−9.60
−9.75
−9.90
−10.05
UP3gt
1.4
1.2
1.0
0.8
0.6
UP3sigma
1.6
1.4
1.2
1.0
UP3phase
5.6
5.4
5.2
5.0
UP3Background
6.25
6.00
5.75
5.50
48
56
64
72
UP3A
−10.05
−9.90
−9.75
−9.60
UP3w1
0.6
0.8
1.0
1.2
1.4
UP3gt
1.0
1.2
1.4
1.6
UP3sigma
5.0
5.2
5.4
5.6
UP3phase
5.50
5.75
6.00
6.25
UP3Background

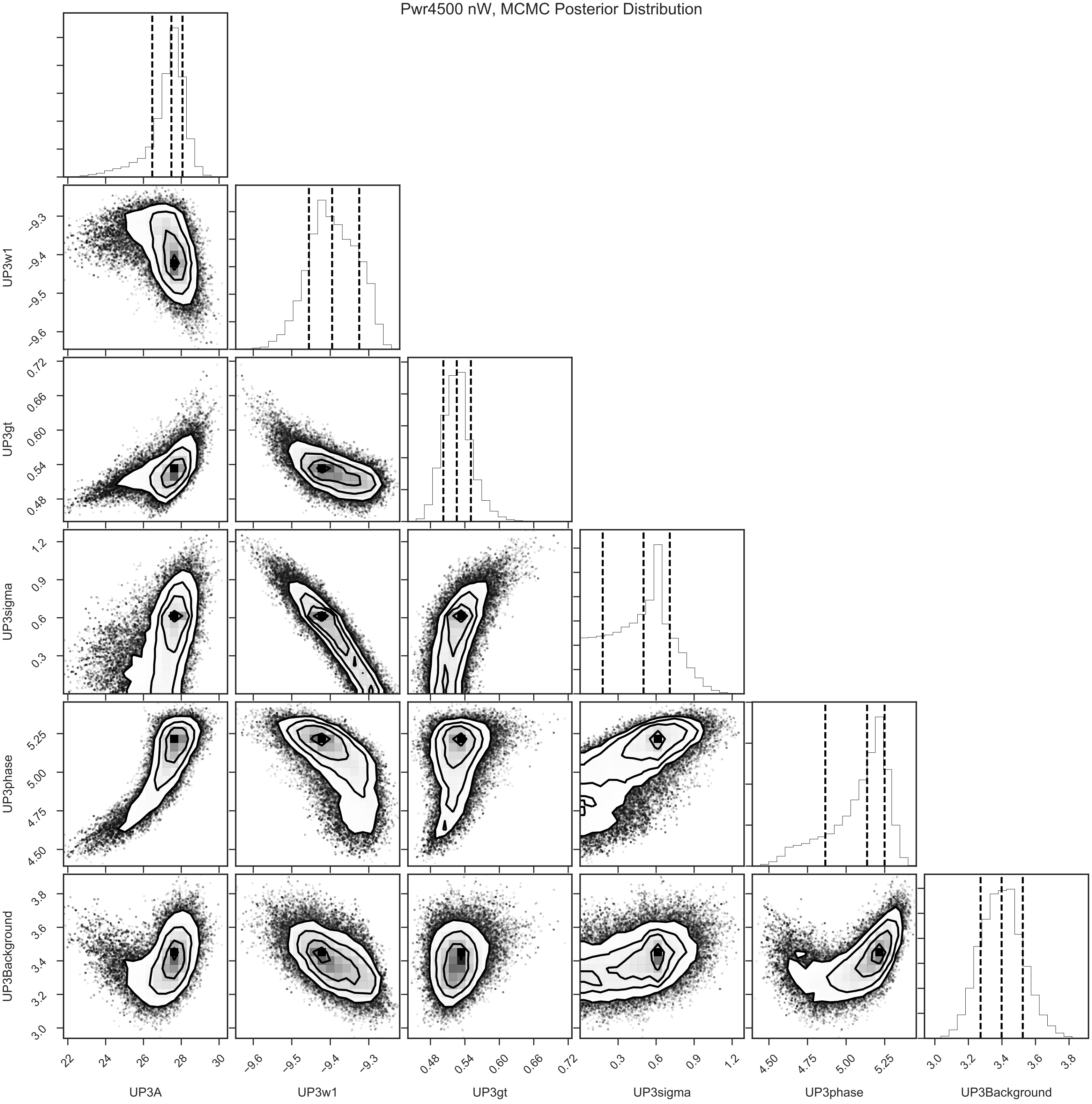
Pwr4500 nW, MCMC Posterior Distribution
UP3w1
UP3gt
UP3sigma
UP3phase
UP3Background
UP3A
UP3w1
UP3gt
UP3sigma
UP3phase
UP3Background
22
24
26
28
30
−9.6
−9.5
−9.4
−9.3
0.48
0.54
0.60
0.66
0.72
0.3
0.6
0.9
1.2
4.50
4.75
5.00
5.25
3.0
3.2
3.4
3.6
3.8

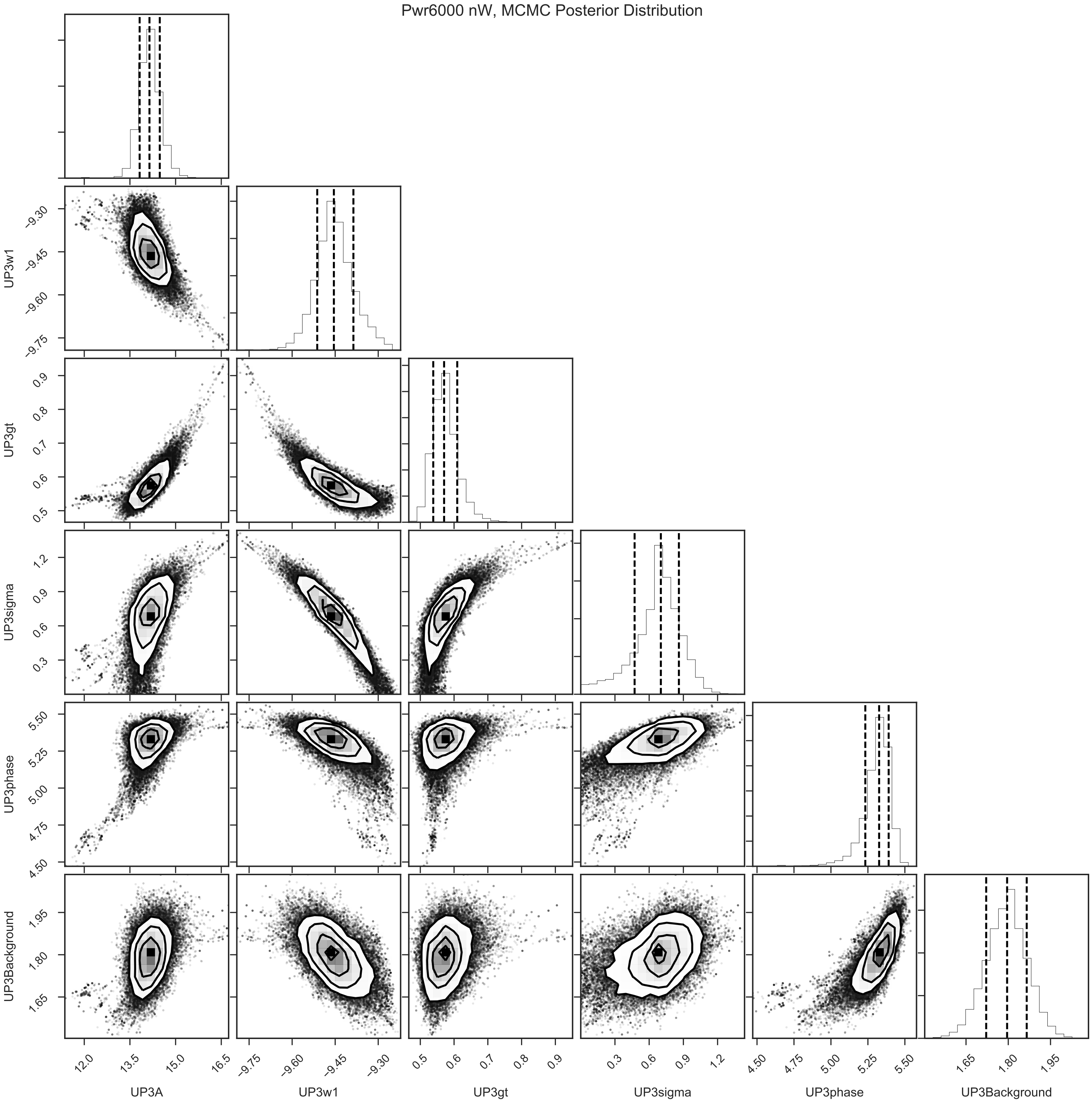
Pwr6000 nW, MCMC Posterior Distribution
UP3w1
−9.30
−9.45
−9.60
−9.75
UP3gt
0.9
0.8
0.7
0.6
0.5
UP3sigma
1.2
0.9
0.6
0.3
UP3phase
5.50
5.25
5.00
4.75
4.50
UP3Background
1.95
1.80
1.65
12.0
13.5
15.0
16.5
UP3A
−9.75
−9.60
−9.45
−9.30
UP3w1
0.5
0.6
0.7
0.8
0.9
UP3gt
0.3
0.6
0.9
1.2
UP3sigma
4.50
4.75
5.00
5.25
5.50
UP3phase
1.65
1.80
1.95
UP3Background

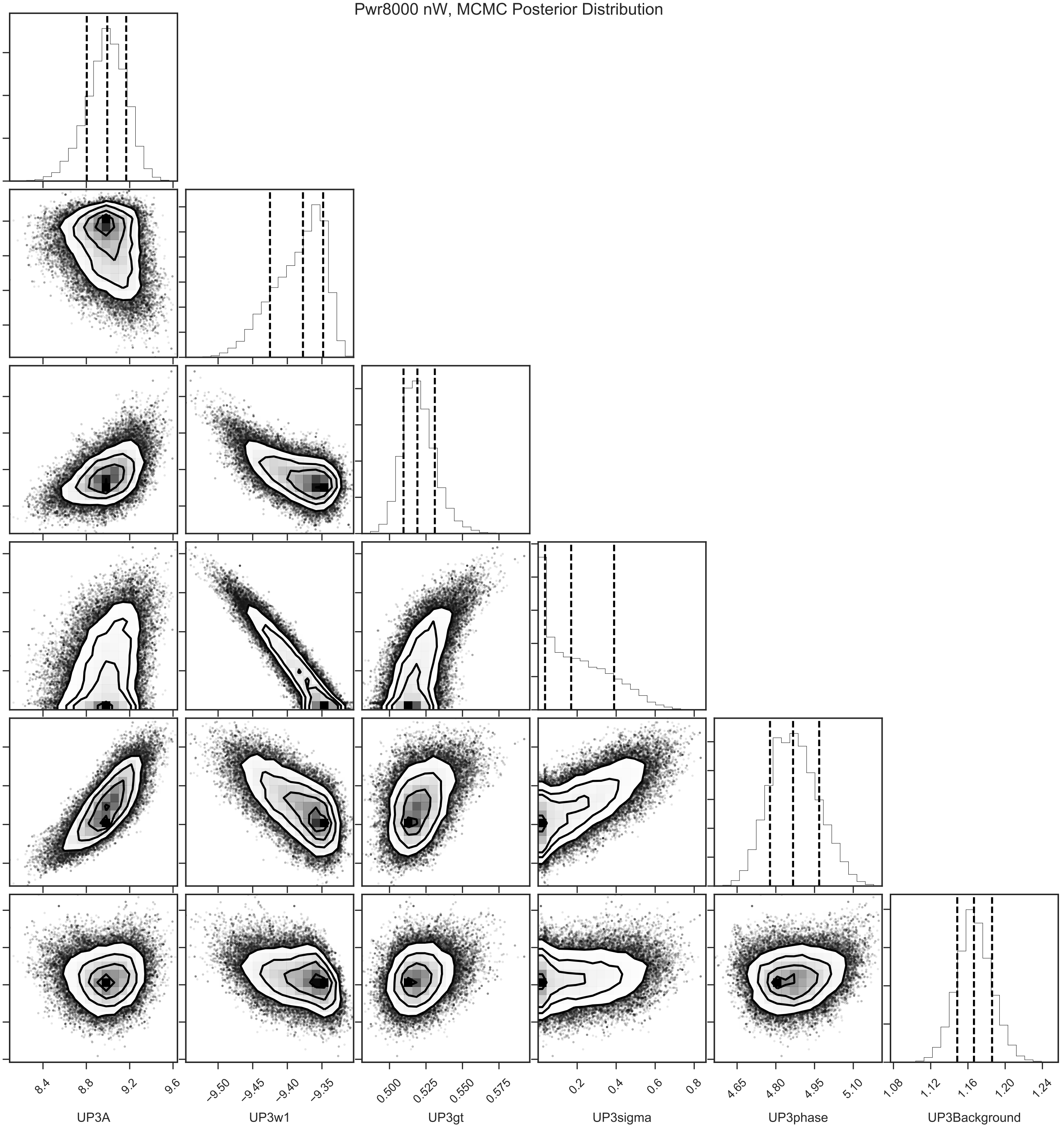
Pwr8000 nW, MCMC Posterior Distribution
UP3w1
−9.35
−9.40
−9.45
−9.50
UP3gt
0.575
0.550
0.525
0.500
UP3sigma
0.8
0.6
0.4
0.2
UP3phase
5.10
4.95
4.80
4.65
UP3Background
1.24
1.20
1.16
1.12
1.08
8.4
8.8
9.2
9.6
UP3A
−9.50
−9.45
−9.40
−9.35
UP3w1
0.500
0.525
0.550
0.575
UP3gt
0.2
0.4
0.6
0.8
UP3sigma
4.65
4.80
4.95
5.10
UP3phase
1.08
1.12
1.16
1.20
1.24
UP3Background

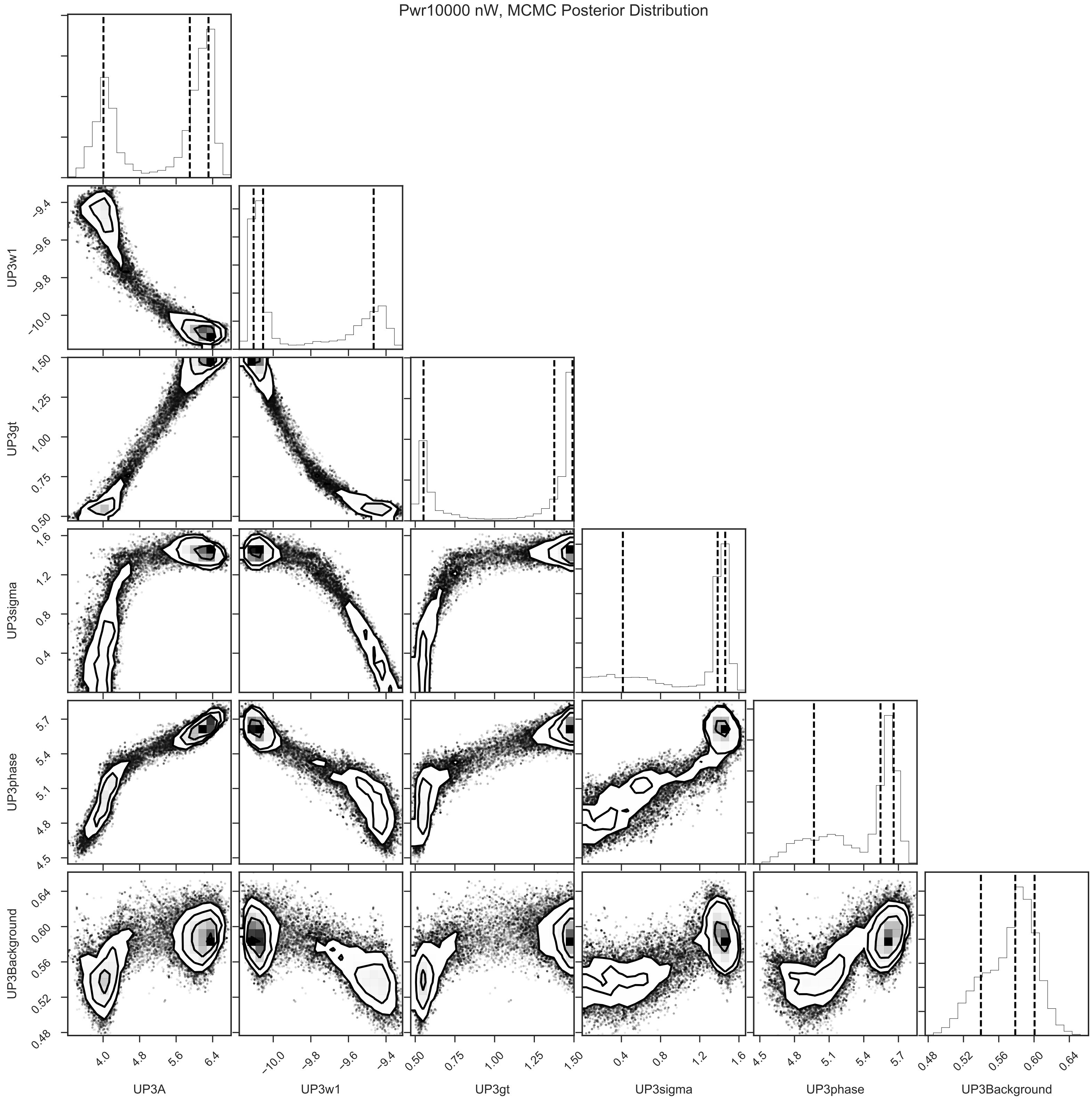
Pwr10000 nW, MCMC Posterior Distribution
UP3w1
-9.4
-9.6
-9.8
-10.0
UP3gt
1.50
1.25
1.00
0.75
0.50
UP3sigma
1.6
1.2
0.8
0.4
UP3phase
5.7
5.4
5.1
4.8
4.5
UP3Background
0.64
0.60
0.56
0.52
0.48
4.0
4.8
5.6
6.4
UP3A
-10.0
-9.8
-9.6
-9.4
UP3w1
0.50
0.75
1.00
1.25
1.50
UP3gt
0.4
0.8
1.2
1.6
UP3sigma
4.5
4.8
5.1
5.4
5.7
UP3phase
0.48
0.52
0.56
0.60
0.64
UP3Background

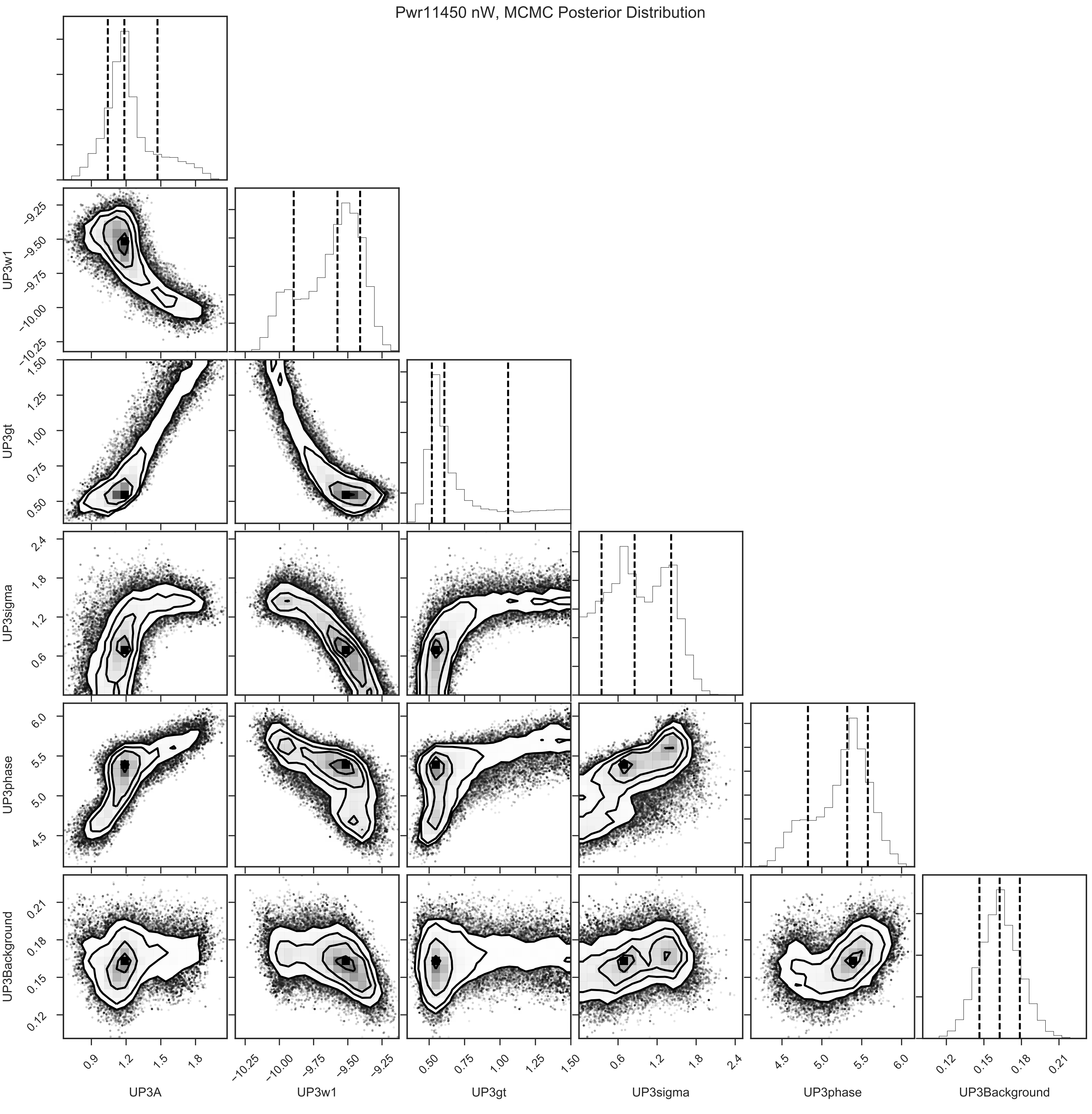
Pwr11450 nW, MCMC Posterior Distribution